Experimental analysis of the dynamics of gaseous and two-phase counterflow flames submitted to upstream modulations

Patrick Duchaine

Ecole Centrale Paris

THESE

présentée par

Patrick DUCHAINE

pour l'obtention du

GRADE de DOCTEUR

Formation doctorale : Energétique

Laboratoire d'accueil : Laboratoire EM2C, CNRS, Ecole Centrale Paris

Experimental analysis of the dynamics of gaseous and two-phase counterflow flames submitted to upstream modulations

Soutenue le 1 juillet 2010

Composition du jury :	**Mme**	**BAILLOT**	**Françoise**	**Rapporteur**
	M.	**GRISCH**	**Frédéric**	**Rapporteur**
	M.	**GUIBERT**	**Philippe**	**Président**
	M.	**HARDALUPAS**	**Yannis**	
	M.	**BÉRAT**	**Claude**	**Membre invité**
	M.	**SCHULLER**	**Thierry**	**Directeur de thèse**
	Mlle	**LACOSTE**	**Deanna**	**Co-encadrante de thèse**
	M.	**ZIMMER**	**Laurent**	**Co-encadrant de thèse**

Ecole Centrale des Arts et Manufactures
Grand Etablissement sous tutelle
du Ministère de l'Education Nationale
Grande Voie des Vignes
92295 CHATENAY MALABRY Cedex
Tél. : 33 (1) 41 13 10 00 (standard)
Télex : 634 991 F EC PARIS

Laboratoire d'Energétique Moléculaire et Macroscopique, Combustion (E.M2.C.)
UPR 288, CNRS et Ecole Centrale Paris
Tel. : 33 (1) 41 13 10 31
Fax : 33 (1) 47 02 80 35

2010 - xy

Contents

Remerciements

Les travaux présentés dans ce manuscrit ont été menés durant trois années au sein de l'équipe combustion du laboratoire EM2C. Je tiens ici à remercier l'ensemble des personnes qui ont contribué à la réussite de ce travail.

Je suis en premier lieu reconnaissant au directeur du laboratoire, Nasser Darabiha, pour m'avoir accueilli au sein du laboratoire. Je souligne également les soutiens financiers du ministère de la recherche et de l'ANR (Agence Nationale pour la Recherche) pour l'ensemble de ces travaux.

J'adresse ensuite tout naturellement mes remerciements à mes encadrants. Tout d'abord, mon directeur de thèse Thierry Schuller : fort de ses compétences et de son enthousiasme au travail, il a su me montrer les chemins à suivre et me faire apprécier le domaine de la combustion et le travail de recherche. J'adresse également de sincères remerciements à Laurent Zimmer, avec qui j'ai pu avoir des interactions très enrichissantes et fructueuses. Ses conseils avisés, sa constante disponibilité et sa grande expérience en matière d'expérimentation m'ont été précieux. Enfin, le travail effectué aux côtés de Deanna Lacoste a été profitable et formateur, car elle a su me transmettre ses connaissances en techniques expérimentales et partager son sens scientifique. Ce trio d'encadrants - complémentaire, disponible et exigeant - m'a permis de mener un travail rigoureux et d'affronter les joies et les difficultés du travail expérimental.

Je tiens ensuite à exprimer ma sincère gratitude envers les rapporteurs de thèse, Françoise Baillot et Frédéric Grisch, pour avoir pris autant d'attention à lire et évaluer mon manuscrit. J'adresse aussi mes remerciements à Philippe Guibert pour avoir accepté le rôle de président de mon jury. Je remercie de même Yannis Hardalupas pour avoir accepté de porter son regard expert sur mes travaux. Je remercie enfin chaleureusement Claude Bérat pour avoir participé à mon jury. Il est sincèrement gratifiant pour un thésard de voir son travail évalué par

un jury d'une telle qualité.

Mes remerciements vont chaleureusement à l'ensemble du personnel du laboratoire qui m'a largement épaulé durant toute ma thèse. Je pense biensûr aux chercheurs et ingénieurs de recherche dont les conseils précieux m'ont permis de mener ma barque à bon port. Ayant eu à réaliser d'importantes tâches expérimentales, je suis tout particulièrement reconnaissant au personnel technique du laboratoire: l'atelier mécanique (Erika, Yannick et Alain), l'atelier électronique (Samira) et le bureau d'études mécanique (Sid et Jérome, qui a d'ailleurs su m'enseigner, outre la mécanique des brûleurs à contre courant, celle du pédalier et du dérailleur, avec les mises en application associées). Je pense aussi au personnel adminitratif du laboratoire (Merryl, Anne-Cécile, Virginie, Jordan ...) qui m'a permis de travailler dans les meilleures conditions. Enfin, ces trois années de travail au sein de l'équipe des doctorants d'EM2C m'auront laissé des souvenirs formidables. Merci à tous pour ces moments d'entraide et de bonne humeur : Antoine (alors, c'est pour quand cette GTA ?), Paulo (il va finir par marcher notre proto, t'inquiètes), Ammar (et ses fantastiques récits de géopolitique), Théodore, Nicolas, Elodie, Xinjuan, et bien d'autres ...

Merci également à ma famille d'avoir fait le déplacement aussi nombreux le jour de ma soutenance, et à Séverine, pour son soutien constant et infaillible.

Abstract

Modern combustion systems benefit from constant technological advances which aim at reducing the emissions of chemical pollutants and at widening regimes of stable operation. Further progress in the combustion field requires a better understanding and modelling of the combustion dynamics. In these systems, the combustible is often injected as a liquid polydisperse spray. Experimental data are thus required to validate simulation tools in configurations with flames interacting with controlled structures in multi-phase flows.

This thesis aims at studying some of these fundamental interactions in well-controlled laminar flows submitted to upstream modulations. Two experimental configurations are investigated comprising counterflow flames and free inert jets, fed with gaseous or liquid combustibles. The flows may be submitted to upstream velocity modulations to reproduce effects of unsteadiness. Depending on the pulsation frequency, vortices of controlled sizes are shed from the burner lips and convected with the flow, while interacting with the spray and the flame.

In the first part of this thesis, the dynamics of a premixed stretched flame is analysed in a stagnation flow. The study focuses on determining the flow and flame structures under upstream modulations, and principally on studying the dynamics of flame/vortex interactions. Different responses of the flame are identified and analysed relative to the size of the vortex ring generated at the burner outlet. Two propagation modes for the velocity perturbations are identified, corresponding to a bulk oscillation of the entire reaction zone or to a flame perturbed only at its periphery. This leads to a discussion on the choice of velocity boundary conditions to conduct 1D simulations of these configurations. Comparisons between simulations and measurements of the velocity field illustrate these conclusions. Flame transfer functions between heat release rate and velocity perturbations imposed at the burner outlet are established for different flow conditions. These measurements relying on local and global chemiluminescence of the flame show again a distinct behaviour of the emission originating from the flame region close to the burner axis and

the whole flame. Mechanisms of sound production by partially and perfectly premixed flames are also identified and analysed relative to flame/vortex interactions.
In the second part, the dynamics of a spray convected by a free inert jet or impinging a diffusion flame submitted to velocity modulations is analysed. The originality of this work consists in characterizing the flow and spray dynamics using a set of advanced diagnostics. Phase-conditioned images at different instants in the modulation cycle are used to analyse the interactions between the gaseous phase and the spray. The spatial distribution of combustible vapour and liquid phases is determined using Laser Induced Exciplex Fluorescence (LIEF). Velocities and sizes distribution of droplets from the spray are determined locally by Phase Doppler Anemometry (PDA) and in a plane by Interferometric Particle Imaging (IPI). Laser Doppler Velocimetry (LDV) and Particle Image Velocimetry (PIV) are also used to determine the response of gaseous phase. These phase-conditioned analysis highlight some interactions between the gaseous and liquid phases and constitute an interesting database for detailed simulation of these two-phase flows.

Key words: *counterflow flame, two-phase flow, flame dynamics, combustion noise, laser diagnostics*

Résumé

La conception de chambres de combustion de nouvelles génération moins polluantes et fonctionnant sur des plages de stabilité plus grandes nécessite une meilleure connaissance et modélisation de la dynamique de la combustion. De nombreux systèmes sont alimentés avec des carburants liquides atomisés qui interagissent avec des grandes structures de l'écoulement d'air puis avec le front de flamme. Il existe cependant peu de données qui permettent de valider les outils de simulation dans des configurations mettant en jeu des flammes en interaction avec des structures contrôlées pour des écoulements polyphasiques.

Certaines de ces interactions fondamentales sont étudiées dans ce travail pour des écoulements laminaires soumis à des modulations de vitesse. Les configurations expérimentales correspondent à des flammes à contre-courant et à des jets inertes libres, avec une injection de combustible liquide vaporisé ou sous la forme de sprays polydisperses. Ces écoulements peuvent être soumis à des modulations de vitesse de manière à reproduire les effets d'instationnarité. En fonction de la fréquence de la pulsation, des tourbillons de tailles contrôlées sont générés à la sortie des brûleurs et sont convectés par l'écoulement. Ils interagissent avec le spray de combustible ou la flamme.

Une première partie de la thèse vise à caractériser la dynamique de flammes prémélangées dans des écoulements à point d'arrêt pour des combustibles gazeux. L'étude se concentre tout particulièrement sur l'interaction de structures tourbillonnaires avec une flamme plane. Différentes réponses de la flamme sont identifiées et analysées en fonction de la taille des tourbillons générés. Deux régimes de propagation des perturbations de vitesse sont mis en évidence correspondant à une oscillation en bloc de la zone de combustion ou à des perturbations limitées à la périphérie du front de flamme. Ces constatations remettent en cause le choix des conditions aux limites à imposer dans les simulations numériques unidimensionnelles de ces configurations. Des comparaisons entre des prévisions numériques et des mesures du champ de vitesse supportent nos conclusions. L'analyse de la réponse de ces flammes est ensuite

poursuivie par la détermination de leurs fonctions de transfert entre le dégagement de chaleur et les perturbations vitesses imposées à la sortie du brûleur. Ces mesures basées sur l'étude du signal de chimiluminescence rayonné par la flamme mettent à nouveau en évidence une différence de comportement entre la région restreinte au centre de l'écoulement à point d'arrêt et le comportement global de l'ensemble de la zone de combustion. Ces configurations sont ensuite utilisées pour identifier les mécanismes de production de bruit par des flammes parfaitement et partiellement prémélangées.
La deuxième partie des travaux est dédiée à la caractérisation de la réponse à des tourbillons d'un spray dilué convecté par un jet inerte ou d'un spray combustible alimentant une flamme plane de diffusion dans un écoulement à contre-courant lorsqu'ils interagissent avec des tourbillons. L'originalité du travail repose sur l'utilisation combinée de diagnostics optiques avancés pour caractériser la dynamique de la phase gazeuse et de la phase dispersée, ainsi que leurs interactions par une prise d'images en moyenne conditionnée à différents instants du cycle de modulation. La distribution de la vapeur de carburant injecté dans les phases gazeuses et liquides est notamment caractérisée grâce à la Fluorescence Exciplex Induite par Laser (LIEF). La distribution de vitesse et la granulométrie des gouttelettes du spray sont déterminées localement par effet Doppler (PDA) et dans un plan par Interférométrie par Imagerie de Particules (IPI). Ces diagnostics sont complétés par l'utilisation de la Vélocimétrie Laser Doppler (LDV) et la Vélocimétrie par Imagerie de Particules (PIV) pour déterminer la réponse de la phase gazeuse de ces écoulements. Les acquisitions aux différents instants du cycle permettent de mettre en évidence les interactions entre les différentes phases et constituent une base de données pour envisager la simulation fine de ces écoulements.

Mots clés : *flamme à contre-courant, écoulement diphasique, dynamique de flamme, bruit de combustion, diagnostics laser*

Introduction

Worldwide energy production constitutes one of the major challenges of our society in the current context of increasing demand for energy, shortage of fuel resources and growing environmental issues. Combustion remains a key conversion means of energy, providing with about 80% of the world consumption (IAE (2008)). The main advantages of chemical-energy conversion devices is that the raw materials (oil, coal, natural gas, biomass fuels) have a high energy density, are easily stored and may be burned on demand. While combustion has been used from prehistoric times, its technology has rapidly evolved since the first industrial revolution. Decisive advances have been made on the fundamental level and on their application to practical problems leading to the development of novel combustion processes, high performance devices and clean and efficient combustors. For instance, the fuel efficiency per passenger of today's subsonic aircraft has been increased by 70% compared to standards 40 years ago (Penner et al. (1999)), while NOx emissions have been reduced by a factor of 20 in the meantime (Correa (1998)). Further progress is still needed to convert energy via combustion in a more efficient, more reliable and safer way.

These progress have been made possible by the development of new concepts of combustion and by a better design of combustion chambers. Nowadays, during the development phase of a combustor, numerous tests on experimental benches are carried out in order to validate machine performances, to characterize the pollutant emissions and to determine operational and stability domains. Measurement techniques are in this context very helpful to reach quantitative information on the flow and the combustion. Flow and wall temperatures, flame structure and position, concentration of pollutants may be for instance characterized by modern experimental techniques.

These tests are nevertheless time consuming and onerous. The current trend aims at increasing the role of numerical simulations to partly replace these ex-

perimental test runs. Reynolds-averaged Navier-Stokes (RANS) simulations are, for instance, of a great help for the engineers in the design of combustion chambers. In addition, new numerical tools, like the currently developed Large Eddy Simulations (LES), are likely to play a growing role in the design of tomorrow's combustors. These advances mainly rely on a better understanding, and therefore a better modelling, of complex physical phenomena occurring in a combustion chamber.

In many practical burners, such as gas turbines, the liquid fuel is atomized and the disperse phase interacts with the air flow which is generally swirled to obtain compact turbulent flames. Complex physics like spray atomization and evaporation, mixing of incoming flows and combustion take place successively in a confined environment (figure 1).

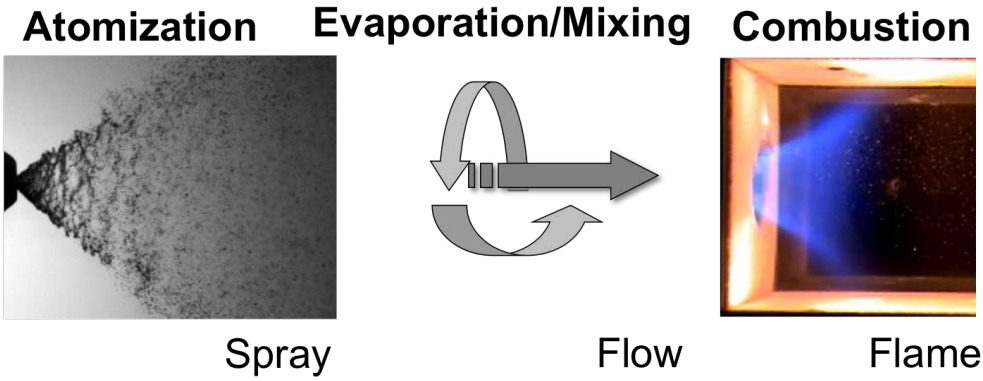

Figure 1: General mechanism taking place in a combustion chamber: the liquid fuel is atomized forming a spray, evaporating in the vicinity of a flame. Complex phenomena like the atomization and evaporation of the spray, its mixing with incoming oxidizer and combustion are involved (images from Laboratoire EM2C).

In order to model and simulate such complex configurations, experimental data are needed for the understanding of fundamental physics. They also serve as a benchmark for comparisons with simulation results. For all these reasons, there is a great need of accurate and quantitative data on flow and flame features in industrial systems as well as in laboratory-scale experiments. Non-intrusive laser diagnostics have accelerated developments by providing advanced measurements of many physical quantities. For instance, laser diagnostics can yield composition and temperature data in relatively simple flames, which motivate theoretical developments (Wolfrum (1998)). These also pro-

vide similar restricted data on more complex flames in practical combustors which are used to assess models.

Table 1 presents some laser based techniques setup in the scope of this thesis to investigate features of the flow, the flame and the spray. Laser Doppler Velocimetry (LDV) and Particle Image Velocimetry (PIV) developed in the 60's and 70's are widely used to measure velocity fields. The size distribution of droplets may be estimated using Phase Doppler Anemometry (PDA) or Interferometric Particle Imaging (IPI) techniques. Similarly, flame imaging, concentration and temperature field measurements via Laser Induced Fluorescence (LIF) are commonly used nowadays.

Study	Diagnostics	Measurement Features
Flow	LDV	Pointwise velocity
	PIV	Planar velocity
Flame	Chemiluminescence imaging	Flame front location and intermediate reactives
	LIF	Visualisation of intermediate reactives
Spray	PDA	Pointwise velocity and diameter of droplets
	Mie scattering	Planar signal proportional to d^2
	LIF	Planar signal proportional to d^3
	IPI	Planar velocity and diameter of droplets

Table 1: Some optical diagnostics commonly used in two-phase reactive flow to investigate features of the flow, the flame and the spray.

Combustion science and technology, concerning in particular gas turbines, face nowadays many challenges (Correa (1998)). Among them is the need to understand thoroughly the flame dynamics to avoid potential combustion instabilities in the design of combustors. A second major challenge in combustion field is to achieve an accurate modelling of two-phase reacting flows, widely used in industrial systems. These two main challenges motive this thesis research work, and therefore shape its architecture. Both subjects are introduced in details in the following paragraphs.

Flame dynamics

An important challenge in today's combustion field consists in understanding the flame dynamics, i.e. the interaction of the flame with the unsteady flow of reactants and the acoustics of the combustion chamber. The development of Lean Premixed Prevaporized burners (LPP) brings into light the problem of combustion instabilities (Candel (2002)). These instabilities are due to thermo-acoustic coupling resulting from a resonant feedback between the unsteady heat release rate produced by the flames and the acoustic eigenmodes defined by the system geometry and the mean temperature field. This phenomenon occurs when the acoustic oscillations in a combustion chamber cause oscillations in the reactants delivery system and subsequent oscillations in the heat release rate. If the heat release oscillations are in phase with the pressure oscillations, their amplitude grows and this often has severe consequences (Lieuwen and Yang (2005)). A better understanding of flame dynamics is a key element to predict such instabilities, and therefore to design stable combustors.

Since combustion in practical and industrial systems takes place most often in turbulent flows within a complex geometry where combustion and flow dynamics are strongly coupled, it is extremely difficult to focus on the structure and features of the flames. If one aims at better understanding fundamental phenomena of combustion dynamics, it is preferable to study a configuration with a relatively simple flow and a well-controlled flame. Counterflow laminar flames meet all these requirements. As represented in figure 2, a counterflow diffusion flame may be lighted on in a region where a fuel and an oxidizer stream jet impinge, while a premixed flame may be stabilized in a fuel-oxidizer stagnation flow. In such a configuration, the flow is well defined and well controlled from an experimental point of view. The flame is located close to a stagnation plane, with no wall in its vicinity and exhibits a temporal and spatial stability. The configuration can also be modelled with a great accuracy. This type of flames enables to carry out in parallel experiments and calculations, with the aim to validate hypothesis and models, or to collect information on the flame dynamics.
The configuration of a counterflow flame is an interesting generic configuration to study even though it is an idealization of many practical systems. The interest in features of stretched flames is not recent since Karlovitz et al. (1953) already focused on effects of a velocity gradient on the propagation of stretched flames in the 50's. Moreover, in turbulent combustion modelling, the development of flamelet theory (Peters (1986)) brought up the need of know-

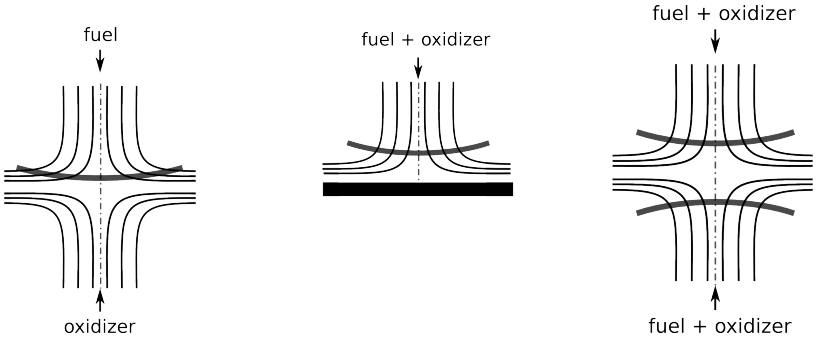

(a) Diffusion **(b)** Premixed **(c)** Twin-Premixed

Figure 2: Counterflow flames

ing some global parameters on stretched flat flames, and therefore sustained the interest in counterflow flame studies.

Another interesting feature of the counterflow configuration is the possibility to modulate the flow upstream of the flame via a loudspeaker. The acoustical excitation can be used to create periodical large vortical structures shed from the burner rim, which are representative of the dynamics of gaseous flows in more complex configurations. This enables to study the dynamics of the flame in well-controlled conditions. Many experimental studies were already conducted to investigate stretch oscillation effects on gaseous premixed and diffusion flames - via the interaction with a vortex ring (Brown et al. (1998); Lee et al. (2006)) or via burner oscillation (Hirasawa et al. (2000)).

The counterflow configuration is also compatible for analysis of two-phase flows combustion because the incoming flow may carry away a stream of droplets (Chen and Gomez (1992)). Note that

Two-phase flows

Another challenging subject is to deal with combustion in two-phase flows. Indeed, in many practical burners, such as gas turbines for instance, the fuel is introduced in a liquid form. The liquid fuel is atomized and the disperse phase interacts with the air flow which is generally swirled to obtain compact flames (figure 1). This two-phase turbulent reactive flow is characterized in the vicinity of the flame region by a polydisperse evaporating spray interacting with an unsteady flow and a flame. Therefore, one easily infers the key

role of evaporating sprays and spray interactions with vortices in the understanding of the dynamics of combustion systems. Burners fed by liquid fuels are also prone to instabilities which often feature large synchronized coherent flow structures carrying the disperse fuel phase periodically to the flame (Santoro et al. (2000); Lemaire et al. (2004)).
The challenges in modelling and simulating of such two-phase configurations are important. The modelling of two-phase combustion should take into account complex physical phenomena like the evaporation of sprays, droplet interactions, and the spray interaction with the flow and flame. Here again, measurements come as a key input in the understanding of fundamental physical mechanisms, and as a benchmark for comparisons with simulations in well-controlled configurations.

Fundamental experiments are valuable to collect quantitative data on interactions of sprays with vortices and flame. This also enables a better understanding of the different contributing mechanisms. Among them, the interaction of a vortex with a laminar flat flame can be used to investigate a number of features that are common in turbulent combustion such as stretch or extinction effects. In the literature, one finds some experimental studies dealing with the interaction of vortices with a two-phase flow and a laminar flame (see the by Li (1997)). There are also studies considering unsteady acoustically pulsated free laminar jets with a polydisperse spray injection in a 2-D axisymmetrical configuration (Freret et al. (2009)). For an appropriate choice of acoustic pulsation frequencies, periodical large vortical structures can be generated that modify the dynamics and the evaporation of the polydisperse spray. It thus provides a well-controlled configuration which is appropriate for the study of fundamental mechanisms.
Lemaire et al. (2004) investigate the interaction of a vortex with diffusion flat flame in a two-phase flow imaging the flame front with Laser Induced Fluorescence (LIF) on CH radicals. Mikami et al. (2002) shows that the extinction limit is affected by the droplet size distribution. Darabiha et al. (1993), Massot et al. (1998) and Laurent et al. (2004) carried out comparisons between measurements and simulations of a spray impinging a counterflow flame for different values of the stretch rate. Chen and Gomez (1992) studied the structure of quasi monodisperse heptane sprays by measuring their size, velocity and gas phase temperature distribution in two flames characterized by two different strain rates. Two types of spray structures were found depending on the Stokes number. If the strain rate remains relatively low and droplets suitably small, all the droplets are evaporated before the flame. On the opposite, when the Stokes number is sufficiently high, some droplets are able to cross

the flame. The former case supports a well defined flame where all droplets vanish at the vaporization plane, the latter develops significant relative motion between droplets and gas flow and thus a more complex droplets dynamics. In some other experiments, a monodisperse droplet generator device is used and vapour concentration and quantitative measurements of the temperature field were conducted inside and in the vicinity of the droplet via two-wavelengths LIF (Lavieille et al. (2001); Castanet et al. (2003); Castanet et al. (2007)). These studies are used to validate models of single droplet evaporation but do not intend to take into account droplets interactions.

In the experimental field, efforts have been made in the last decades to reach rapid and reliable measurements on the vapour and liquid phases of droplets simultaneously in sprays. Numerous laser-based techniques have been developed for the separate characterization of either vapour phase or the liquid phase of evaporating droplets. The vapour sensing techniques include laser Rayleigh scattering (Zhao and Ladommatos (1998)), spontaneous Raman spectroscopy (Zhao and Ladommatos (1998)), LIF (Zhao and Ladommatos (1998); Thurber and Hanson (2001)), spectrally resolved absorption spectroscopy (Ma et al. (2002)), and others. Droplet measurement techniques include measurements based on laser extinction (Dobbins and Jizmagian (1966)), laser phase Doppler anemometry (Bachalo (1994)) and interferometric particle imaging (Damaschke et al. (2005)). Each technique has its own advantages and disadvantages and is useful for a certain domain of applications. However, these techniques are generally not transferable to the simultaneous characterization of both vapour and liquid droplet properties. Some vapour sensing techniques based on elastic scattering such as the Rayleigh scattering technique or LIF can be extended to measure both vapour and liquid droplets quantities (Bazile and Stepowski (1995)). But, usually the scattering from droplets greatly exceeds that from the vapour, therefore jeopardizing or even prohibiting accurate estimated on the vapour measurements. A similar analysis makes tough the direct combination of one vapour and one droplet measurement technique discussed above for simultaneous vapour and droplet measurements. Despite these problems, a few laser-based diagnostics have been attempted for simultaneous characterization of the vapour and liquid phases originating from droplets. Laser Induced Exciplex Fluorescence (LIEF) developed by Melton (Melton (1983)) allowed two-dimensional imaging of the vapour and liquid phase simultaneously under limited conditions. Besides implementation difficulties, the LIEF signal is difficult to quantify, and quenching from oxygen limits most of the LIEF applications to nitrogen environments (Desantes et al. (2005)). Also, Chraplyvy (1981) proposed an

alternative technique and applied a method based on a two-wavelengths laser extinction strategy to measure vapour concentration and droplet volume fraction simultaneously in an evaporating fuel spray.

Thesis objectives and contents

This thesis aims at collecting knowledge on fundamental aspects of combustion dynamics in laminar flows submitted to upstream modulations. The objective is both to characterize the flame dynamics in a premixed counterflow configuration and to experimentally study via advanced diagnostics a two-phase flow in an inert and reactive configurations. The scope of this thesis concerning gaseous flows spans from the study of flame-vortex interactions to the understanding of fundamental mechanisms of sound production. Concerning two-phase flows, the focus is put on the interaction of droplets with vortices and flame, as well as the characterization of the spatial distribution of vapour and liquid phases under flow modulations.

This thesis is composed of three main parts. Part I introduces the experimental configurations and measurement methods used in this thesis. Part II consists in an analysis of the response of counterflow premixed gaseous flames submitted to incoming perturbations including investigations on the flame transfer function and combustion noise production. Part III deals with the study of the dynamics of an inert two-phase flow and a two-phase diffusion flame submitted to upstream modulations.

Gaseous and two-phase flow configurations and instrumentations (Part I)

Chapter 1 presents two configurations on which experiments presented in this thesis were carried out. The first experimental configuration is a gaseous stagnation flow impinging on a plate. The second one is a free jet carrying a polydisperse spray. In both configurations, the flow can be modulated so that the dynamical responses of the flow, the flame and the spray can be studied under well controlled forced flow conditions.

A collection of diagnostics are set up around the experimental bench to obtain detailed information on flow velocities, on droplets sizes and their velocities, and on vapour and liquid fuel concentration fields. Chapter 2 introduces these diagnostics including Laser Doppler Velocimetry (LDV) and Particle Image

Velocimetry (PIV) to characterize the velocity flowfield of the gaseous and vapour phases. The velocities and the size distribution of droplets are determined using Phase Doppler Anemometry (PDA), Particle Tracking Velocimetry (PTV) and Interferometric Particle Imaging (IPI). The concentration fields in the vapour and liquid phases are investigated by planar measurements of the Mie scattering and Laser Induced Exciplex Fluorescence (LIEF) signals. This latter method is originally adapted under well-controlled conditions of flow and modulations to perform quantitative measurements of the vapour phase concentration via a calibration procedure.

Flame dynamics in a gaseous stagnation flow (Part II)

Chapter 3 investigates the flow and flame structures of a premixed flame in a stagnation flow under modulation of the upstream flow. Tomographic images and PIV measurements put into evidence vortical rings shed from the burner lips. Their interactions with the flow and the flame are analysed in details. In particular, the focus is put on the propagation of velocity perturbations along the burner centreline, exhibiting convective and acoustic modes. Consequences are also drawn on the choice of appropriate boundary conditions for the simulation of this configuration.

Chapter 4 establishes the transfer function of the flame response to velocity perturbations in a premixed stagnation flow configuration for different equivalence ratios. Using an originally adapted measurement setup, it is shown that the global and the local on-axis responses of the flame may vary significantly. These transfer functions enable an analysis of the response of a planar flame over a set of frequencies.

Chapter 5 investigates the sound production by laminar premixed flames in a stagnation flow submitted to upstream modulations. The study identifies the different mechanisms of sound production, and qualitatively compares the level of sound produced when varying the distribution of fuel and oxidizer between a central and an annular outlets.

Dynamics of a spray in a jet and in a reactive flow (Part III)

The third part of this manuscript is devoted to the analysis of the dynamics of a polydisperse spray entrained by a free inert jet and burning in a reactive counterflow.

Chapters 6 and 7 deal with the experimental study of an inert hexane two-phase flow in steady and pulsated configurations. The aim of this work is to analyse effects of unsteadiness on the fuel vapour distribution originating from hexane evaporating liquid droplets injected in a free jet. This setup is chosen because it provides a well controlled configuration where large coherent vortices can be created by modulation of the outlet flow. These structures are then convected towards the reaction region and interact with the gas flow and the disperse evaporating phase. These experiments complete data obtained by Freret et al. (2009) where the velocity field and size distribution of droplets in a similar configuration were determined. These interactions encompass many challenges for numerical simulations with a polydisperse spray interacting with an unsteady reactive flow. The measurements of vapour fluorescence signal are successfully processed thanks to a calibration procedure at ambient temperature to yield the distribution of absolute vapour concentrations in the symmetry plane of the burner at different instants in the modulation cycle. The liquid phase is characterized using Mie scattering and LIEF measurements. The size distribution of the spray is also investigated in a region close to the burner outlet. The boundary conditions of both phases in the free inert jet flow configuration have been precisely determined to enable simulations of this configuration.

Chapter 8 deals with a spray of heptane burning in a counterflow diffusion flame. The use of chemiluminescence imaging and LIF measurements on the vapour phase enabled the study of the flame response to flow modulations and the characterization of the spatial distribution of the vapour phase.

In the last part of the manuscript, conclusions and perspectives relative to this research work are drawn.

Part I

Gaseous and two-phase flow configurations and instrumentations

Chapter 1

Experimental configurations

The experiments presented in this thesis were conducted on two configurations. The first one is a pulsated reactive flow impinging a plate which is presented in section 1.1. This setup is used to analyse the dynamics of a flat stretched premixed flame and its sound production mechanisms which are presented in part II. Afterwards, the experimental bench was modified to enable the study of two-phase flow dynamics, presented in part III. This second configuration and its adaptation to two-phase reactive flows are presented in section 1.2.

1.1 First setup: a pulsated reactive flow impinging a plate

The burner is sketched in figure 1.1. It corresponds to the upper part of a twin counter-flow burner designed by Pr J. C. Rolon at Laboratoire EM2C (Rolon (1988)). It is composed of two cylindrical concentric pieces both ended by smooth converging sections with a surface contraction ratio of 16. These elements are used to generate two coaxial laminar flows: a central jet flow of diameter $d_1 = 20$ mm surrounded by an annular flow of external diameter $d_2 = 39$ mm. These flows are separated by a $e = 1.5$ mm thick piece at the burner outlet section.
The central and annular parts of the burner can be independently fed with different mixtures of gases constituted by air, nitrogen and methane. Gases of central and annular flows are premixed upstream of the burner in a cylinder supplied by three lines which flowrates are controlled by three mass-flow controllers from Bronkhorst (see figure 2.3a). For the central and the annular flows, the set of flowcontrollers is identical: the nitrogen and air flowrates are each controlled by a flowcontroller with a maximum range of 2 $nm^3\ h^{-1}$, the

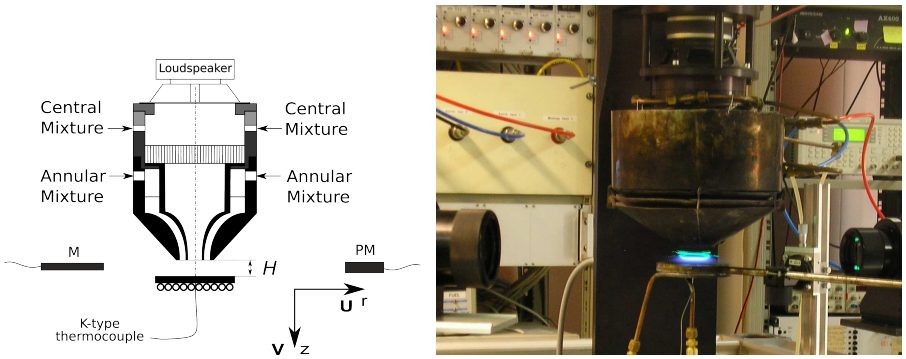

(a) Scheme of the burner configuration **(b)** Picture of the flame in the stagnation flow. LDV system is set up around the burner

Figure 1.1: Experimental setup. The burner to plate distance is fixed in all experiments to $H = 24.2$ mm - The origin O of the local coordinate system (O, r, z) is fixed on axis at the burner outlet

methane flowrate is controlled by a flowcontroller with a maximum range of 200 nL h^{-1}. The accuracy of the flowcontrollers is 1% of the full scale. The letter *n* in *nL* or nm^3 refers to normal conditions of pressure and temperature, i.e. $T = 0$ °C and $P = 101{,}325$ Pa. These mixed flows are simultaneously injected by four inlets into the burner (figure 1.1). The annular flow is mainly used to produce a controlled coflow to modify the mixing layer between the central reactive jet and the surrounding coflow. It is also used to diminish external disturbances on the central flow.
A set of grids and a honey comb in the central flow and a grid in the annular flow are placed upstream of the converging sections to produce a laminar flow at the central and annular outlets. The whole system is mounted on an automated three axis displacement system accurate beyond 0.1 mm.
A plate made of copper, of diameter $D = 100$ mm, can be approached to the burner outlet using a micrometric displacement system. The plate to burner outlet distance was fixed in this thesis to $H = 24.2$ mm producing a laminar stagnation flow impinging the plate. Note that for reacting conditions, the plate is cooled down using a water heat exchanger welded on the bottom side of the plate. The temperature in the center of the plate is controlled with a K-type thermocouple. The bottom part of the burner is insulated with deflecting panels protecting the burner from the hot gases of the flame and to a water heat exchanger enrolled around the burner tip. The temperature of the burner is controlled with a K-type thermocouple inserted in the external part of the burner at about 80 mm from the burner outlet.

A loudspeaker placed at the top of the burner is used to produce harmonic modulations of the central flow at various forcing frequencies, lying between $f = 10$ Hz and $f = 200$ Hz, and with different amplitudes ranging from $(v_{rms}/\overline{v}) = 5\%$ and 20% measured at burner outlet. The loudspeaker reference is Seas P14-RCY 8 Ohms and has polypropylene membranes. The annular flow was not modulated in this work.

In the whole thesis, a system of cylindrical coordinates (O,r,z) is adopted. The reference point O is located on the burner axis at the nozzle outlet, the coordinate r is the radial distance to the burner axis and z is the vertical distance from the burner outlet. When needed, this system of coordinate is replaced by the planar coordinate system (O,x,z) where x is the algebraic distance to the burner axis along a given diameter.

1.2 Second setup: a pulsated two-phase flow

The geometry of the burner has been modified to adapt it to two-phase flow configurations. In this second configuration, liquid fuel can be injected either in the liquid phase via an atomizer generating a cloud of droplets, or in the vapour phase via an evaporator. The burner with its modified geometry is sketched in figure 1.2. A picture of the setup is presented in figure 1.3.

A six-branch cross is mounted on the converging unit of the burner described in figure 1.1. Two loudspeakers with proofed polypropylene membranes resisting to liquid fuel are mounted on the lateral branches of the cross. They are supplied by an amplified signal in order to pulsate the central flow. On the two other horizontal branches, glass-windows are mounted to enable optical access to the burner center where the tip of the atomizer is located. This can be used to check its normal operating conditions. On top of the cross, an ultrasonic atomiser A7500H from Fisher Scientific Instruments is mounted on a rubber ring. This mounting prevents the transmission of vibrations to the burner setup. An additional inlet is available for supplying the reactants to the central flow.

In this configuration, the liquid fuel can be simultaneously injected as liquid and vapour. On top of the setup, the ultrasonic atomizer is fed by a syringe pushed by a continuous step motor to supply a constant liquid flowrate ranging from 30 g h^{-1} to 200 g h^{-1} with a 5% accuracy. The atomizer operates with a 20 kHz frequency voltage, creating high frequencies vibrations of its tip. The

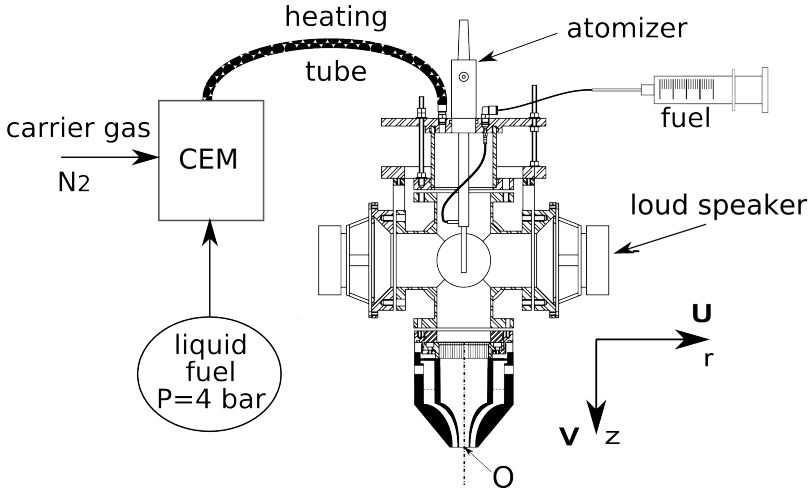

Figure 1.2: Scheme of the experimental setup used for two-phase flows: the liquid fuel is injected either as vapour via the Controlled Evaporator Mixer (CEM) or as a cloud of droplets via the atomizer. The origin O of the local coordinate system (O, r, z) is fixed on axis at the burner outlet.

liquid fuel pushed through the tip is atomized by the vibration of the atomizer tip into a cloud of droplets of 30 to 90 µm diameter. The angle of the spray cone generated is about 40 °.

In parallel, another injection system is set up. A Controller Evaporator Mixer (CEM W-303-333-K) from Bronkhorst mixes the liquid fuel with a carrier gas. The liquid fuel flowrate is controlled by a Coriolis massflow controller supplying from 30 g h^{-1} to 9,000 g h^{-1}. The precision of flowrate measurements are certified at 1.5 % of the measured value by the manufacturer. The carrier gas is in this case nitrogen and its flowrate is controlled by a massflow controller of maximum range 2 nm^3 h^{-1} with an accuracy of 1% of the full range. The liquid fuel and carrier gas then enter a thermo-regulated cell and travel inside during a time long enough so that the fuel is totally evaporated at the outlet. The vapour is then carried away in a heating tube ensuring a temperature sufficiently high to avoid any condensation. This mixture is injected using an inlet located at the top of the burner in the central flow. The annular flow is composed of pure nitrogen and its flowrate is regulated by a mass flow controller of maximal range 2 nm^3 h^{-1}.
The top part of the burner is thermostated with heating tapes. On the bottom part, a radiating panel is also used to deflect the burnt gases, and a water flowing system to cool down the burner outlet when needed. K-type thermocouples

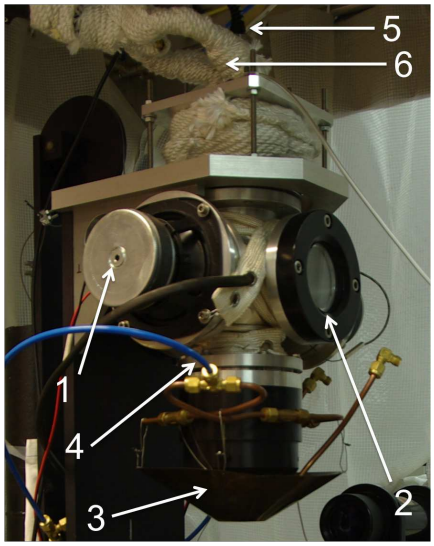

Figure 1.3: Picture of the burner in the two-phase configuration: one identifies on the side a loudspeaker (1) and a glass window (2), on the bottom a radiating panel (3) and the feeding lines of annular flow (4), on top the atomiser (5) and the feeding lines of the central flow (6).

are placed at three positions along the burner to ensure that the temperature remains constant at a value of about 70 °C. In this configuration, laminarization grids in the central flow are removed so that droplets can travel freely from the atomizer tip to the burner outlet without solid obstacles along their path. The honey comb featuring large holes is kept in place because it does not interact with droplets and ensures a good laminarity of the central flow. The grid in the annular flow also remains. Airtightness is proofed thanks to Viton gaskets resisting to temperatures up to 100 °C.

The same systems of cylindrical coordinates (O,r,z) and planar coordinates (O,x,z) are used with this second experimental setup. The origin O is located at the burner outlet on the axis.

This setup can be used for different purposes. In chapters 6 and 7, it is used to study a two-phase jet flow released in a free environment in steady conditions and under flow modulations. Hexane is used as liquid fuel and is pushed entirely through the atomizing system. In chapter 8, a second burner similar to the one described in section 1.1 is placed below this second configuration at a distance $H = 24.2$ mm. This lower burner is fed with a nitrogen annular flowrate and an air central flowrate. In the upper burner, heptane is injected

both with a fluorescent tracer via the atomizer to produce a cloud of droplets and the fuel is also injected without any tracer into an evaporating system in the upper burner. A diffusion two-phase flame can be stabilized in the vicinity of the stagnation plane.

Chapter 2

Measurements methods

Different diagnostics were used for velocity, particle sizes and concentration measurements. An overview of these methods is presented in this chapter. They are briefly introduced and their specific features relative to the present work are also given. The Laser Induced Exciplex Fluorescence (LIEF) method used in this study in order to get quantitative fuel concentration measurements has led to an important literature analysis which is presented in details in this chapter.

2.1 Velocimetry techniques

2.1.1 Laser Doppler Velocimetry (LDV)

The Laser Doppler Velocimetry (LDV) technique is a means by which velocity can be determined using small particles seeded within the flow. The process involves measuring the Doppler shift of the laser radiation that is scattered by the moving particles seeded in the flow. The technique was first developed by Yeh and Cummins (1964). The details on fundamental principles of the measurements are given in Albrecht et al. (2003).
In this thesis, LDV is used for different purposes. The velocity boundary conditions of the different configurations studied are characterized under forced and unforced flow conditions. The propagation of velocity fluctuations along the burner centreline is also investigated in chapter 3 via LDV measurements. In addition to this, the LDV technique was also used to control the fluctuation level at the burner outlet set by the loudspeaker during all experiments.
The measurement setup is a Dantec Flow Dynamics commercial system consisting of a continuous 2 W Argon laser, a Bragg cell, an emitting head with a 250 mm achromatic focal length lens and a collecting head with a 300 mm

focal length lens. The setup is schemed in figure 2.1. Both optical heads are set on translational bars around the burner. The lasing signal at $\lambda_1 = 514.5$ nm and $\lambda_2 = 488$ nm wavelengths emitted by the Argon laser are split into two beams sent parallel into the emitting head. The pairs of beams focus respectively along a vertical plane and along an horizontal plane into a single location, referred as the measurement volume. The flow, seeded with micronic oil droplets (see details in section 2.1.3) passes through the measurement volume. The detection of scattered light at both wavelengths λ_1 and λ_2 when a droplet crosses the measurement volume yields two analog signals featuring a frequency proportional respectively to the z- and the x-components of the droplet velocity. A frequency counter converts these signals into analog signals comprised between 1 and 10 V, proportional to the velocity component. A Bragg cell, set at 40 MHz, is used to shift the Doppler frequency, and enables to measure positive and negative velocity components.

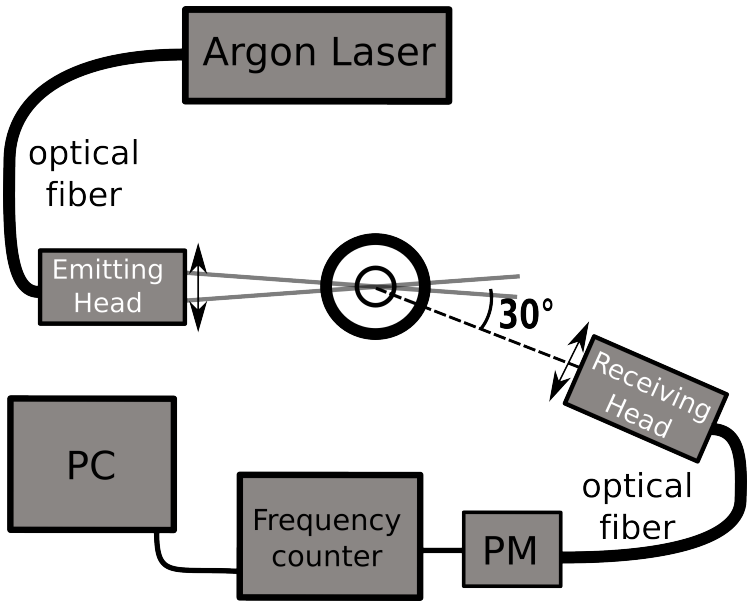

Figure 2.1: Experimental setup for the LDV measurements. Two coherent laser beams ($\lambda_1 = 514.5$ nm and $\lambda_2 = 488$ nm) focus through an emitting head. The laser beam scattered by particles passing through the measurement volume is collected by a lens located at 30° from the laser initial direction. Thanks to the measurement of the signal by photomultipliers, the frequency counter delivers an analog signal proportional to each velocity component.

Phase-conditioned measurements are carried out in pulsated flow configura-

tions using a TTL reference signal coming from the signal synthesizer, used to drive the loudspeakers. This reference signal is recorded simultaneously on the computer via the same acquisition card. Post-processing of the different recorded signals enables to determine phase conditioned averages of measurements with respect to this TTL reference signal. One ensures that the signal from the frequency counter is sampled at a frequency $f_s = 4{,}096$ Hz or $f_s = 16{,}384$ Hz so that at least 20 data per modulation period were recorded. During all measurements carried out in this work, the detected data rate is greater than the sampling frequency to avoid any bias. The duration of the acquisition is sufficiently long to record at least 100 periods of the forcing signal.

2.1.2 Particle Image and Particle Tracking Velocimetry (PIV and PTV)

The Particle Image Velocimetry (PIV) is a technique providing velocity vector measurements in a laser sheet illuminating a gaseous flow seeded with micronic particles (Raffel et al. (1998)). It consists in taking successively two images of the Mie scattering signal (details on the Mie theory are given in section 2.3.1) from the seeders in a flow split by a laser sheet as schemed in figure 2.2. First, the pairs of raw images are divided into several windows, called interrogations areas. Then, each pair of corresponding interrogation areas are cross-correlated using Fast Fourier Transform algorithms (Scarano (2002)). A high cross-correlation value is observed where many particles match up within an interrogation area with their corresponding spatially shifted partners, and small cross-correlation peaks may be observed when individual particles match up with other particles. Only the highest correlation peak is interesting as its position in the correlation plane directly corresponds to the average particle displacement within the interrogation area investigated. The velocity can be deduced because the time separation between the two pictures of one image pair is known. A calibration with a grid is used to obtain the scaling factor relating the pixel displacement to the velocity vector in m s^{-1}. The signal to noise ratio (SNR) of a PIV measurement can be defined as the ratio between the amplitude of the first and second peaks of crosscorrelation. A minimum SNR value of 2, ensuring a reliable crosscorrelation, has been respected for all measurements presented in this thesis. Vectors featuring a lower signal to noise ratio were rejected.

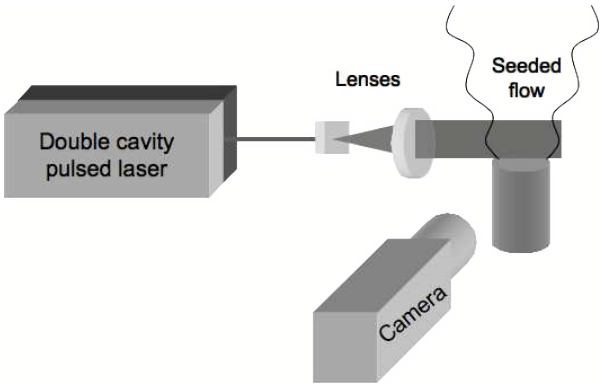

Figure 2.2: Generic setup of Particle Image Velocimetry

PIV processing of Mie scattering images was performed with the Dantec Flow Manager v4.1 software. For PIV measurements, the flow is seeded with liquid or solid micronic particles (details are given in section 2.1.3). One ensures that at least 20 particles are detected in each interrogation area constituted typically by 32x32 pixels^2. The time delay between two images is set so that the mean displacement of the seeding particles corresponds to about one fourth of the interrogation area. This limitation might be avoided using an adaptive correlation (Scarano (2002)), but this was not necessary here since the flow structure remains relatively smooth. All the parameters relative to PIV acquisition and post-processing are reported before each PIV campaign in the corresponding chapter. The sets of seeded gaseous flow images have been cross-correlated by pairs and then averaged over the total number of acquisitions (typically 100 pairs).

When dealing with images obtained for measurements of the droplets velocity from the spray, the PIV processing is often inefficient because the number of particles per interrogation area is too small. Furthermore, there may be two droplets within a small distance having different velocities due to their respective diameters leading to non predominant peaks in the cross-correlation function. In this case, a Particle Tracking Velocity (PTV) processing technique is applied. PTV consists in tracking individual particles from pairs of Mie scattering images. In a spray, when a droplet is successfully localized on both images, a displacement and thus a velocity can be attributed to the individual droplet. Contrary to the PIV algorithms, PTV is not a statistical method and deals with droplets individually. PTV post-processing of Mie scattering images has also been performed with the Dantec Flow Manager v4.1 software. The signal to noise ratio (SNR) is not really defined in this context and an im-

portant source of error may be attributed to the correct measurement of the particle position. Often a 3-point Gaussian scheme is applied on the intensity to retrieve the position at sub-pixel accuracy. Using identical schemes on both images reduces systematic error.

A calculation of particle trajectories is conducted in chapters 6 and 7 using the same average correlation algorithm applied to the sets of images of Mie scattering of the seeded flow and the spray. This algorithm consists in cross-correlating particle-image fields from the sets of instantaneous realizations, then an ensemble-averaging procedure of the cross correlation functions is carried out. This enables to determine the peak of the ensemble-averaged correlation function (Meinhart et al. (1999)). This process is repeated for each velocity vector in the measurement domain. The signal-to-noise ratio is significantly increased by this ensemble averaging of the correlation function before peak detection, as opposed to either ensemble averaging the velocity vectors after peak detection, or ensemble averaging the particle-image field before correlation. The ensemble-averaging correlation technique is though limited to steady or periodic flows since it only yields one velocity vector per interrogation window for the ensemble of Mie images. This algorithm applied both to determine the fluid particles velocity for the vapour and liquid phases yield smooth velocity fields while keeping the exact same nature of the flow. The calculation of trajectories of vapour and liquid fluid particles were done from these velocity fields.

The setup for PIV and PTV measurements consists in a double pulsed Continuum 400 mJ Nd:YAG laser at 532 nm working at shooting frequencies around 10 Hz. A laser sheet (0.5 to 1 mm thick) is focused on the central plane of the burner nozzle. The particle Mie scattering signal is collected on a Dantec Hi-Sense CCD camera 1600x1186 pixels^2 equipped with a Nikkor 60 mm lens and an interferential 532 nm filter. In pulsated flow conditions, in order to perform phase-locked acquisitions, the laser is triggered by the TTL reference signal from the synthesizer driving the loudspeakers. The laser then triggers the camera.

In each set of experiments it has been checked that measurements did not suffer from peak locking (Westerweel (1997)). This phenomenon inducing a loss in sub-pixel accuracy can occur when the scattering images of particles reach the saturation level of the camera. To avoid such phenomena, the aperture of the camera was adjusted so that the light collected from the particles remained below the saturation level. In addition to this, the post-processing of the ob-

tained velocity vectors revealed no bias in the sub-pixel displacement, a proof that measurements were fully reliable.

2.1.3 Flow seeding

Both LDV and PIV methods consist in measuring the velocities of small particles seeded in the flow that are supposed to follow the flow pattern. This section aims at describing the flow seeding with liquid and solid particles used in this thesis. For LDV and PIV measurements, the central and annular flow mixtures are each seeded with micronic oil droplets generated in an atomizer. This liquid seeding is very convenient to use for measurements of velocity in the fresh gases. The velocity flowfield in the burnt gases is though not available with liquid because the droplets evaporate at the flame front. In chapter 5, the velocity field downstream of the flame was though needed. For this purpose, the central flow has also been seeded with solid particles, resistant to the flame front.
Both seeding systems are sketched in figure 2.3. Liquid or solid seeders are mounted upstream of the burner on a by-pass of the central flow as shown in figure 2.3a. The quantity of seeding particles is tuned by adjusting the main and by-pass flowrates.

The liquid atomizer is sketched in figure 2.3b. It is mainly composed of a glass vessel filled with vacuum oil pump (Edwards oil n°15). A system of two valves mounted upstream of the vessel enables to deviate part of the main stream into the atomizer. The flow is accelerated in a converging glass unit and creates a depression around a capillary tube filled with oil. This produces a suction of oil which is atomized by the high velocity gas jet impinging on the liquid flow. This interaction generates a cloud of droplets. An obstacle made of glass blocks the largest droplets. The whole system produces a monodisperse stream of droplets with a mean diameter of about $D_{10} = 2.6$ µm (Durox et al. (1999)).

The solid seeding system is sketched in figure 2.3c. Solid particles of zirconium dioxide (ZrO_2) are stored in a hermetically closed cylinder. Part of the central flow is by-passed and sent into a swirling pipe at the bottom of the cylinder. The swirling flow carries away some solid particles up to the exit. Only one solid seeding system was used for the central flow, the annular flow being seeded with oil particles in these experiments.

Velocity measurements with LDV and PIV rely on the hypothesis that the seeding particles strictly follow the flow. This hypothesis is discussed here in

details. Assuming that vaporization can be neglected, the droplet dynamics can be described using the Stokes number Stk (Rosner (1986); Mikami et al. (2002)), which is the ratio of characteristic time of the droplet response (so-called characteristic "stopping time"), τ_p, to the characteristic time of gas flow, τ_{flow}.

$$\text{Stk} = \frac{\tau_p}{\tau_{flow}} = \frac{\rho_p d_p^2 v}{18 \mu_{air} \rho_{air} L_c} \tag{2.1}$$

where ρ_p and d_p are respectively the volumetric mass and the diameter of the solid particles, v is the flow velocity ($\simeq$ 1.5 m s^{-1}), μ_{air} is the dynamic viscosity of air (18-56 10^{-6} kg m^{-1}s^{-1} for temperatures between ambient and 1300 $^\circ$) and L_c is a characteristic length of the system which was taken here equal to the nozzle-to-plate distance $H \simeq 24.2$ mm.

If the Stokes number remains small ($\text{Stk} \ll 1$), the droplet follows the flow. If this number is of the order of unity ($\text{Stk} \sim 1$) there is a slip velocity between the droplet and the flow. For large values ($\text{Stk} \gg 1$), the droplet has a large penetration into the flow. Table 2.1 presents estimations of Stokes numbers for the liquid and solid seeding systems used in this thesis.

	ρ_p [kg m^{-3}]	d_p [µm]	Stk
Oil	910	2.6	$\simeq 3 \times 10^{-4} - 10^{-3}$
ZrO_2	6500	1	$\simeq 3 \times 10^{-4} - 1.1 \times 10^{-3}$

Table 2.1: Stokes numbers Stk for liquid and solid seeding. The volumetric mass ρ_p and the mean diameter d_p used for the estimation of the Stokes numbers are also reported.

For oil particles and solid particles, this yields values of the order of $\text{Stk} \simeq 10^{-3}$. In both cases, $\text{Stk} \ll 1$, so the oil and solid particles have very low inertia and can be assumed to follow the flow. As a conclusion, the oil droplets and the Zirconium oxide particles constitute good tracers for velocimetry measurements in the present configurations.

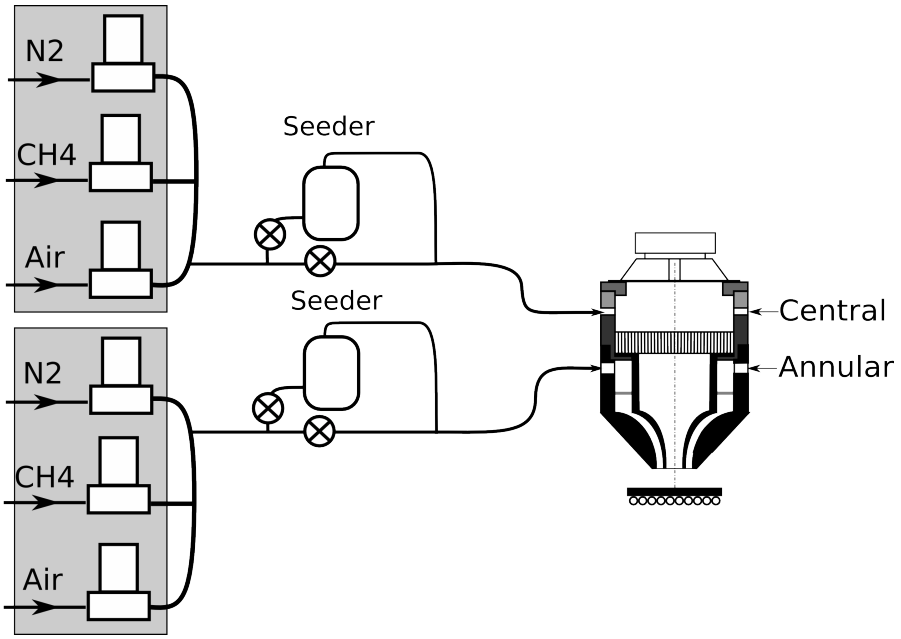

(a) Position of the seeders in the fluids lines feeding the central and annular flows: the seeders are placed on the feeding lines upstream of the burner

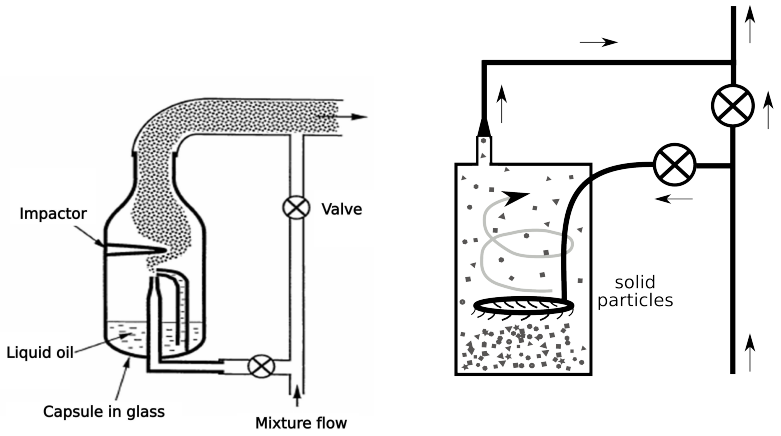

(b) Sketch of the oil atomizer: by-pass flowrate, accelerated in a converging unit, atomizes an oil jet - large droplets are blocked by a glass obstacle (Durox et al. (1999)).

(c) Sketch of the solid seeder: by-pass of the incoming flow is swirled at the base of the cylinder filled with solid particles, and it carries away solid particles.

Figure 2.3: Oil and solid particles seeding systems.

2.2 Size measurement techniques

2.2.1 Phase Doppler Anemometry (PDA)

The Phase Doppler Anemometry (PDA) is a an optical method used to measure the velocities and sizes of droplets passing through the measurement volume (Albrecht et al. (2003)). The setup is identical to the one described for LDV measurements (section 2.1.1) and the software is Dantec Flowsizer v2.0. Measurement of droplets velocities is performed by the LDV method as described earlier. The measurement of droplet diameter is carried out from the measurement of the phase shifts between scattered lights from the same particle but collected in the receiving head at three different locations. The phase shift between these signals can be directly related to the diameter of the particle crossing the measurement volume. In theory, the measurement of phase shift between two different locations is sufficient to deduce the droplet diameter. In practice, phase measurements at three different locations enables a greater precision and a wider measurement range. A calibration procedure is first carried out to subtract an intrinsic phase shift dependent on the optical apparatus. This calibration procedure consists in measuring the phase shift from the light emitted by a diode situated in the receiving head. The calibration is performed before each set of PDA measurements.

The PDA emitting and collecting heads are set on translational bars around the burner. The collecting head is placed in the horizontal plane comprising the measurement volume at an angle $\theta = 30^{o}$ relative to laser beams direction. A scheme of the setup is presented in figure 2.4.

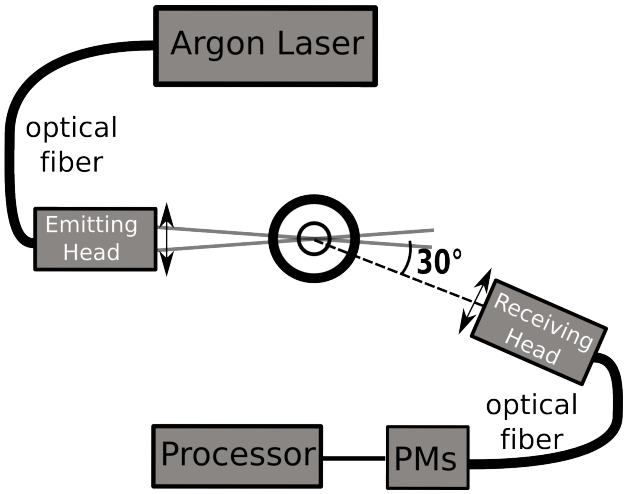

Figure 2.4: Experimental setup for the PDA measurements. Two coherent laser beams ($\lambda_1 = 514.5$ nm and $\lambda_2 = 488$ nm) focus through an emitting head, the laser beam scattered by particles passing through the measurement volume is collected by a lens located at 30° from the laser initial direction. The scattered signal is collected by a set of photomultipliers, the processor estimates velocities and sizes of individual droplets.

A set of parameters have to be given to the Dantec Flowsizer software to perform accurate calculations of the droplet size distribution. Among them are the angle θ between the emitting and receiving heads and the optical index $n = c/v$ of the liquid particles. Optical index values of $n = 1.372$ and $n = 1.385$ have been considered for experiments with respectively hexane and heptane droplets.

2.2.2 Interferometric Particle Imaging (IPI)

The Interferometry Particle Imaging (IPI) technique aims at determining the size of transparent droplets, flowing through the light sheet of a laser plane and scattering light towards a camera. This technique is based on the interferences created in a voluntarily defocused image between reflected and refracted light rays, travelling through a transparent droplet. Using the geometrical approach (Konig et al. (1986); Glover et al. (1995)), the interference pattern between reflected and first order refracted light ray paths can be expressed by a simple linear relation between N_f the number of fringes and d_p the particle diameter $N_f = \kappa d_p$. The geometrical factor κ is function of the light source wavelength λ, the angle of collection relative to the laser sheet ϕ, the lens aperture diameter d_a, the optical index of the liquid n and the distance from the lens to the light

sheet z_l. The complete expression of κ is (Damaschke et al. (2005)):

$$\kappa = \frac{\arcsin(d_a/2z_l)}{\lambda}\left(\cos\left(\frac{\phi}{2}\right) + \frac{n\sin\left(\frac{\phi}{2}\right)}{\sqrt{n^2+1-2n\cos\left(\frac{\phi}{2}\right)}}\right) \tag{2.2}$$

Experiments presented in part III are carried out with two CCD cameras collecting the scattered light at a right angle $\phi = \pi/2$ rad relatively to the laser light source as sketched in figure 2.5. The camera B focuses through a semi-reflective blade on the laser sheet. Its images are used to locate the droplet position and to obtain its velocity. The camera A images directly the scene. Its lens is defocused to generate interference fringes. This image is then used to infer the droplet diameter after processing.

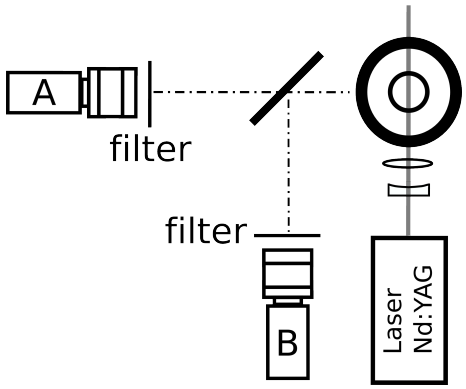

Figure 2.5: Experimental setup for the IPI measurements: CCD camera A records unfocused images of the scene directly - CCD camera B records focused images of the scene through a semi-reflective blade, its images are horizontally mirrored

In the present experimental configuration, the relations $\phi = \pi/2$ and $n \simeq 1.4$ yield $|n^2 - 2n\cos(\frac{\phi}{2})| \ll 1$ and the equation 2.2 can be simplified (Lacour et al. (2010)):

$$\kappa = (1+\frac{\sqrt{2}}{2})\frac{1}{\lambda}\arcsin\left(\frac{d_a}{2z_l}\right) \tag{2.3}$$

The constant κ linking the number of stripes N_f from a defocused droplet and the measured droplet diameter equals 1.53 10^5 fringes m^{-1} in the present

setup.

The camera A is defocused so that the apparent size of droplets spans over 35 pixels. This value is high enough to ensure a good accuracy on the determination of number of stripes and is small enough to limit the overlap between different droplets from the spray. The range of detectable number of stripes spans from 1 to half the number of pixels of the apparent size, i.e. 17.5 fringes. The range of measurable diameters via IPI can thus be deduced from the linear relation $N_f = \kappa d_p$. The measurable diameters actually range between 6.5 and 110 µm. The laser and camera are synchronized using the TTL reference signal to perform phase-locked acquisitions. For each of 20 phases equally distributed in the modulation cycle, 100 phase-locked acquisitions are recorded, ensuring the measurement of velocity and diameter of at least 6,000 droplets. During steady operations, 500 acquisitions are recorded, ensuring the detection of at least 30,000 droplets.

An example of defocused IPI image of a pulsated inert flow presented in part III and recorded by the camera A is shown in figure 2.6. Colours have been inverted in this image to improve the contrast. This image shows vertical interference stripes inside the droplet and gives a good idea of the overlap ratio between unfocused droplets.

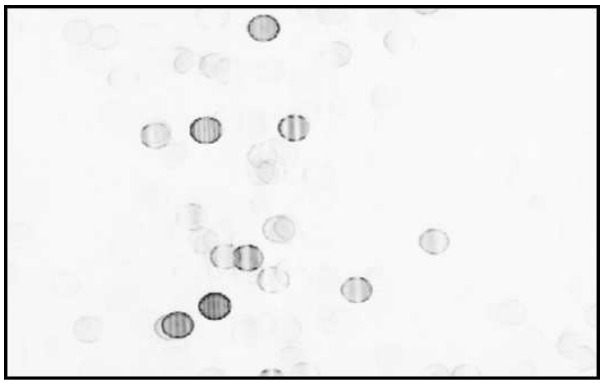

Figure 2.6: Zoom of an instantaneous image taken by the unfocused camera A of a pulsated inert flow. All droplets have the same apparent size of 35 pixels width containing a number of stripes related to the real diameter. Colours have been inverted to improve the contrast.

2.3 Mie scattering and laser induced fluorescence techniques

2.3.1 Mie scattering

A straightforward technique to visualize the spray is to collect the light scattered by individual transparent droplets cut by a laser sheet. The dimensions of the droplets being superior to the wavelength of the incident light induce that the scattered light is a Mie solution of the Maxwell's equations. The scattered light is anisotropic, and is distributed according to lobes in the 3D environment (Van de Hulst (1981)). The main lobe is in the forward direction and the second one has a 30° angle with respect to this direction. It is also an elastic wave-matter interaction and the reflected beam has the same wavelength as the incident light. The Mie theory yields that the amplitude of the scattered light is proportional to the square of the droplet diameter. However, this feature does not enable truly quantitative measurements because the response of the camera pixels should also be calibrated. Other techniques can be used to estimate surface diameter of the spray. This technique was widely used in reactive flows (Domann et al. (2002); Zimmer et al. (2003); Adam et al. (2009)). The scattered light is collected in the perpendicular direction to the laser sheet where the signal is not maximal but sufficiently high. The whole setup used for this thesis is presented further in section 2.3.4.

2.3.2 Laser Induced Fluorescence techniques

Laser Induced Fluorescence (LIF) techniques are commonly used for the investigation of concentration in flows. The present chapter introduces the principles of this technique in a planar configuration: Planar Laser Induced Fluorescence (PLIF).
The principle of planar laser-induced fluorescence is illustrated in figure 2.7.

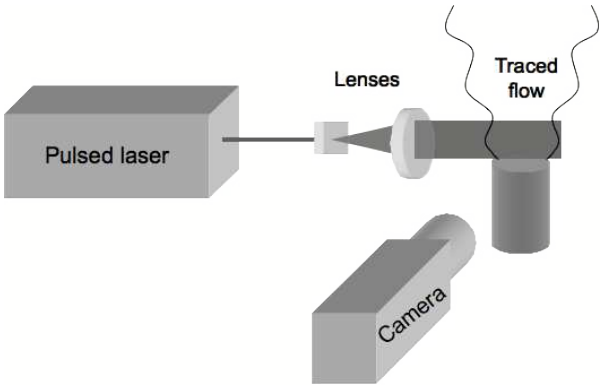

Figure 2.7: Generic setup of Laser Induced Exciplex Fluorescence

A laser beam, typically coming from a pulsed laser with high peak energy, is formed into a thin sheet and passes through the flow of interest, exciting an absorption transition of a tracer seeded in the flow or a naturally present specie in the plane of the sheet. The fluorescence phenomenon can be briefly explained as the re-emission, at a different wavelength, of part of the radiation incident on the substances under examination (Eckbreth (1996)). The fluorescence signal from this tracer is captured by a digital camera, most commonly onto an array of charge-coupled device (CCD) elements sensitive at the wavelengths of interest. An image intensifier can be added in front of the array to improve the sensitivity of the system, particularly in the ultraviolet, and also to increase the gain and the gating performances.
To provide useful information, the fluorescence image must be related either qualitatively or quantitatively to a fluid property of interest. For example, the fluorescence signal from acetone excited with a weak laser energy (linear excitation) and in conditions of uniform pressure and temperature is reported as approximately proportional to the acetone number density in Lozano et al. (1992). Temperature can be measured using fluorescence by considering the dependence of the fluorescence efficiency and the population of the laser-excited lower state of a tracer molecule on temperature (Seitzman et al. (1985); Einecke et al. (2000); Morin et al. (2008)). Even, velocity can be imaged based on an examination of the Doppler shift of the absorption line (McDaniel et al. (1983); Hiller and Hanson (1988)), while pressure broadening effects on the line can additionally be evaluated to infer pressure (Hiller and Hanson (1988)).

Laser induced fluorescence signal S_F may be dependant on the duration τ_{pulse} and the energy density E of the laser pulse (Eckbreth (1996)). Given the typi-

cal durations of laser pulse used in these kinds of applications ($\tau_{pulse} \simeq 7$ ns), the fluorescence signal S_F has reached the saturated regime versus the durations of laser pulse (Eckbreth (1996)), meaning that the fluorescence signal does not vary from shot to shot due to fluctuations in laser pulse durations. The dependence with respect to the energy density E is more complex. The fluorescence signal S_F may be either proportional to the energy of the laser pulse per unit of surface (linear regime), or very little dependant on it (saturated regime) as schemed in figure 2.8. In the linear regime, the fluorescence signal varies from shot to shot with the fluctuations of the laser energy. In the saturated regime, the fluorescence signal does not depend anymore on the laser energy fluctuations.

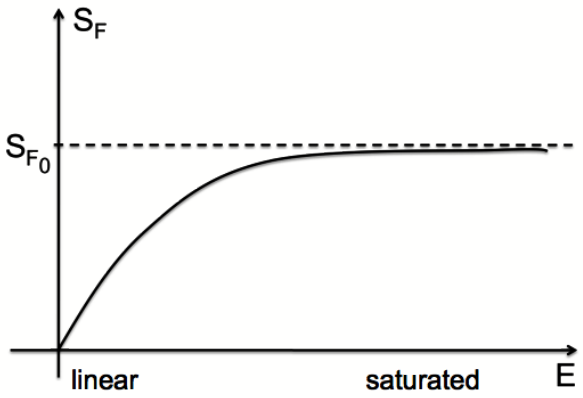

Figure 2.8: Laser induced fluorescence signal S_F versus the energy density E. Two distinct regimes are put into evidence. The linear regime prevails at low energy densities and the saturated regime establishes for high energy densities.

A precise characterization of the regime of the fluorescence signal versus the laser energy was carried out (see section 6.2.3) to know if one can free oneself from fluctuations of the laser energy in the experimental conditions explored.

The advantage of PLIF-based diagnostics is their ability to non-intrusively provide instantaneous information in an entire plane of the flowfield, without line-of-sight averaging effects inherent to schlieren or shadowgraph techniques. The main advantages of these techniques are the relatively high intensity of the fluorescence radiation, its proportionality to the concentration of the substance under study and its red shift. Signals levels are generally higher than for Rayleigh or Raman scattering. The use of atomic or molecular fluorescent species also generally ensures that the tracers track the flow. Since its initial

development in the late 1970's and early 1980's (Epstein (1977); Kychakoff et al. (1984)), the potential of PLIF techniques has been demonstrated in a wide variety of flows (see, for example, reviews by Hanson et al. (1990)).

However, the absorption characteristics and the fluorescence spectra of different molecules present or dissolved in a fuel are almost identical for both liquid and vapour phases, the latter fluorescence signal being several orders of magnitude lower, which usually makes PLIF techniques inappropriate for the study of evaporating sprays (Pastor et al. (2002)).

2.3.3 Laser Induced Exciplex Fluorescence (LIEF)

The use of a LIF technique in a two-phase flow faces many difficulties. Due to differences in density between the vapour and the liquid of the same substance, the amplitude of the fluorescence signal emitted by the liquid phase is usually two to three orders of magnitude higher than the one radiated from the vapour phase. Visualisation of both signals with different dynamics requires a great amplitude of detection, usually not available even with a 16-bit camera. The Laser Induced Exciplex Fluorescence is an alternative method to circumvent this problem. Its fundamental principles are introduced in the present section.

Fundamentals and state of the art

The Planar Laser-Induced Exciplex Fluorescence (PLIEF) technique, was proposed by Melton in the early 1980s (Melton (1983)). It is based on the spectral separation of the liquid and vapour phases fluorescence signals by adding two tracer species to the investigated specie, which act as a monomer (M) and a reacting partner (Q) pair. The fundamental principles of LIEF are summarized in figure 2.9. In the vapour phase, the incident laser pulse brings up the monomer to an excited state (M*), which thereafter fluoresces in emitting a laser photon of energy $h\nu_0$. In the liquid phase, the monomer (M) and the reacting partner (Q) easily form together a loosely bound excited complex, designated as exciplex (E*), due to the reactive collision of both molecules in a high density media such as the liquid phase. The exciplex molecules feature a fluorescence emission at a longer wavelength than the emission from the respective excited monomer (M*), which is mainly present in the vapour phase due to its lower reaction probability. The released photon has thus an energy $h\nu_1$ lower than the photon released in the vapour phase. This additional red-shift of the exciplex fluorescence occurs because part of the incident photon radiation is used to maintain the bound excited complex.

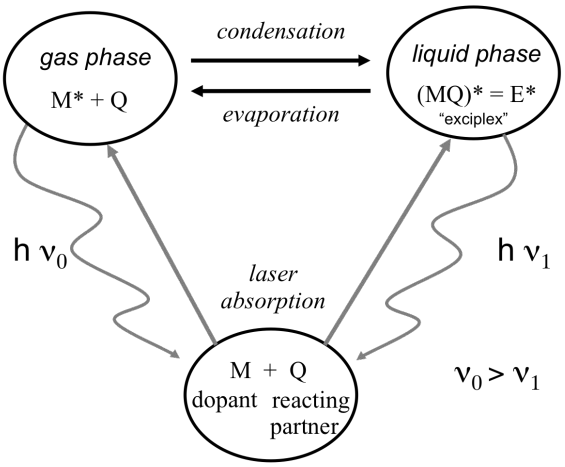

Figure 2.9: Scheme of the fundamental principles of LIEF: in the vapour phase, the incident laser pulse brings up the monomer to an excited state (M*), which fluoresces in emitting a photon of energy $h\nu_0$. In the liquid phase, the monomer (M) and the reacting partner (Q) easily form together a loosely bound excited complex, designated as exciplex (E*). The exciplex molecules show fluorescence at a longer wavelength than the monomer, i.e. releases a laser photon of energy $h\nu_1 < h\nu_0$.

These particular properties of some couples of tracers, called exciplex tracers, enable the discrimination the fluorescence signal from the vapour and the liquid phase based upon the bandwidth of their fluorescence signal. The basic idea of LIEF is to image the scene with adequate band-pass filters, recording separately the vapour and the liquid fluorescence signals. The challenge of measuring different amplitudes of signals coming from different phases can be faced up this way.

The original idea, first suggested by Melton (1983) and further explored by Melton and Verdieck (1985), paved the way for several studies on the spray evaporation characterization with focus on injection in internal combustion engine. First studies (Bardsley et al. (1988); Bardsley et al. (1989); Hodges et al. (1991); Senda et al. (1992); Kashdan and Bruneaux (2006)) were carried out in transparent cylinders to characterize the atomization process of fuel jets evaporating sprays into inert atmospheres. These studies yield information on the spatial distribution of vapour and liquid phases during an engine cycle. Later on, some more studies tend to reach quantitative information on both phases (Felton et al. (1993); Schafer et al. (1994)) using different calibration procedures. However, it is difficult to obtain accurate measurements because of the need to take into account several aspects, such as the dependency of

the fluorescence signal on the mixture temperature and pressure, the different evaporation rates of the tracers and the fuel, incident and fluorescent radiation attenuation due to absorption and Mie scattering (Rotunno et al. (1990); Kim and Ghandhi (2001)).
The couple of tracer N,N,N'N'-tetramethyl-p-phenylene diamine /naphthalene (TMPD/naphthalene) was used in many studies because of its coevaporation with gasoline. Other couples of tracers were also suggested and explored in some experimental studies (Kim et al. (1997); Froba et al. (1998)). A bibliographic study of exciplex tracers is presented thereafter.

Limitations

Several limitations are associated with the use of Laser Induced Exciplex Fluorescence. To counteract as much as possible these limitations, the setup for LIEF experiments should comply with some important conditions. In the present paragraph, these limitations are examined and the respective solutions chosen for the present experimental setup are presented and discussed.

O_2 Quenching Quenching is a de-excitation of excited molecules by collisions. The presence of O_2 molecules favours of a strong quenching and the LIEF signal can be reduced by several orders of magnitude (Desantes et al. (2005)). Indeed using exciplex dopants in presence of O_2 will cause such a drastic reduction of the emitted signal that detection becomes very difficult. As a consequence, the LIEF diagnostic may generally only be used in inert configurations, replacing O_2 of air by N_2. This is what is done in most studies (Diwakar et al. (1992); Fujimoto and Tabata (1993); Ghandi et al. (1994)). LIEF may also be used to investigate non-premixed flames, a configuration in which, thanks to a protecting inert annular flow, tracers on the fuel side are not in contact with O_2 molecules. Two configurations corresponding to an inert flow and a counterflow diffusive flame are investigated in chapters 6 to 8. Note that this quenching mechanism, which is here restrictive, can be useful to measure the mixture fraction (Orain et al. (2006)).

Coevaporation of tracers and fuel To proceed to quantitative measurements using LIEF, a convenient assumption is to consider that the tracers behave the same way as the investigated fuel in terms of evaporation properties. In this case, the measured evaporation rates are equal to the fuel ones without any correction. Such a mixture is called an azeotropic mixture, i.e. the vapour forms with the same concentration as the solution, in other words the distillation occurs without a change in concentration. This condition is satisfied if

the boiling points of fuel and tracers are the same or at least they belong to the same temperature range. Values of boiling points of some exciplex dopants and fuels are reported in table 2.2. In the study carried out in part III, the coevaporation of tracers and fuel has been carefully checked.

	Molecular weight (g mol^{-1})	Boiling point (°C)
Fuels		
n-hexane C_6H_{14}	86	69
n-heptane C_7H_{16}	100	98
Isooctane C_8H_{18}	114	99
n-decane $C_{10}H_{22}$	142	174
Hexadecane $C_{16}H_{34}$	226	287
Gasoline	-	20-215
Exciplex tracers		
Benzene	76	81
TEA	101	99
TMPD $C_{10}H_{16}N_2$	174	260
Naphthalene $C_{11}H_{10}$	142	240
DMA	122	193
FB C_6H_5F	96	84-85
DEMA $C_5H_{13}N$	87	63-65

Table 2.2: Molecular weight and boiling points of some fuels and exciplex tracers

Tracers' behaviour at high temperatures Close to the flame, most tracers are very likely to undergo complex transformations like pyrolysis or cracking. As a consequence, in the preheated zone of a flame ($\simeq$ 1 mm), the fluorescence signals may be strongly modified. Quantification in this region is more difficult to obtain.

Temperature and pressure dependence of fluorescence signals Fluorescence signals are in general highly dependent on temperature and pressure conditions (Desantes et al. (2005); Modica et al. (2007)). As a consequence, the respective influences of pressure and temperature needs to be studied thoroughly to get reliable quantitative results.

In the context of this research work, experiments are carried out in open environments at ambient pressure, so the pressure does not have any significant influence on fluorescence signal. Concerning the influence of the temperature, the study of the inert spray in chapters 6 and 7 is carried out at ambient temperature, and therefore simply requires a calibration of fluorescence signal versus concentration at ambient temperature. On the contrary, the study of the reactive configuration in chapter 8 would indeed require the measurements of temperature maps and a calibration over the whole range of temperatures. This whole process has not been carried out this thesis and measurements are only considered in that chapter as qualitative data. This was further induced by the choice of tracers in that chapter, which do not have identical evaporation properties as the fuel used in these experiments.

Fluorescence signal crosstalking The liquid and vapour fluorescence signals are emitted on different bandwidths. Nevertheless, these bandwidths may partially overlap as shown for example in figure 2.10. This induces that, on

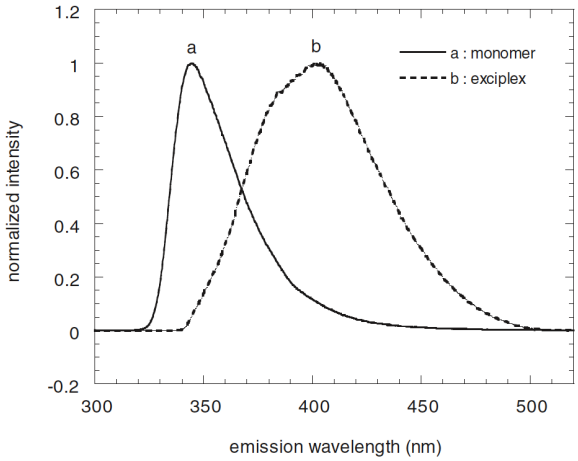

Figure 2.10: Emission fluorescence spectra from the monomer (a) and exciplex (b) with couple of tracers DMA (N,N-dimethylaniline) and 1,4,6-TMN (trimethylnaphthalene). The vapour phase can be tracked by the monomer fluorescence and the liquid phase can be tagged by the exciplex fluorescence. The both spectra do overlap for wavelengths between $\lambda = 350$ nm and $\lambda = 400$ nm. Data are extracted from Kim and Hong (2001).

a given range of wavelengths, the fluorescence signal may result both from liquid and vapour phases. This phenomenon is called crosstalking. Due to differences in density between the vapour and the liquid, the amplitude of

the fluorescence signal from the liquid phase is usually two to three orders of magnitude higher than the one emitted by the vapour phase. It can thus occur that on given wavebands the fluorescence signal coming from the vapour and liquid phases are of the same order of magnitude. In such a configuration, visualization and quantification of the vapour concentration is prohibited. Limiting crosstalking is therefore important because it could deprive LIEF of its main interest, i.e. simultaneous visualizations of fuel under vapour and liquid phases. The choice of relevant filters may help to tackle this issue.
In the present thesis, it was checked that by imaging the different dilute sprays under investigation with the filters indicated in table 2.4, no crosstalking effect could be observed on both the vapour and liquid phases (see section 6.2.3).

Tracers

This section aims at presenting exciplex tracers commonly reported in the literature. Table 2.3 lists a set of studies carried out using eight chemical couples composed of a monomer and a reacting partner. For each couple, the mass ratio of respectively the monomer and the reacting partner are given in the first column when available. The laser source and liquid fuel are given when available in columns 2 and 3. The reference is given in the last column. In most cases, experiments were carried out in high pressure vessels, but some articles relate on atmospheric pressure experiments.

Mass ratio	Laser source	Fuel	Reference
TEA / Benzene			
	Kr-F 248nm	Benzene	Froba et al. (1998)
4.1-2.9%	Nd:YAG	Isooctane	Mounaim-Rousselle et al. (1999)
0.75-5.25 %	Kr-F 248 nm	Benzene	Kornmesser et al. (2001)
4.1-2.9%	Nd:YAG 266 nm	Isooctane	Gervais and Gastaldi (2002)
4.1-2.9%	Nd:YAG 266 nm	Isooctane	Le Coz et al. (2003)
TEA / Fluorobenzene			
10-0.5%	Xe 351 nm	Isooctane	Schafer et al. (1994)
DMA / Naphthalene			
5-5%	Xe-Cl 308 nm	Gasoline	Shimizu et al. (1992)
7-7%	Xe-Cl 308 nm	Isooctane	Leach (2004)
DMA / TMN			
5-7%	Xe-Cl 308nm	Isooctane	Kim et al. (1996)
1-2.5%	Xe-Cl 308nm	Isooctane	Kim et al. (1997)
5-5%	Xe-Cl 308nm	Isooctane	Kim and Hong (2001)
5-5%	Xe-Cl 308nm	Isooctane	Kim et al. (2002)
FB / DEMA			
0.5-9%	Nd:YAG 266 nm		Ghandi et al. (1994)
0.5-9%	Nd:YAG 266 nm	Hexane/MTBE	Wieske et al. (2006)
2-9%	Nd:YAG 266 nm	Hexane	Duewel et al. (2007)
Pyrene			
	354.7 nm	Decane	Stufflebeam (1989)
TMPD / Naphthalene			
1%-10%		Hexadecane	Melton (1983)
1-2.5%	Nd:YAG 266 nm	Hexadecane	Melton and Verdieck (1985)
2.5-1%	Xe-Cl 308 nm	Hexadecane	Murray and Melton (1985)
1%-9%	Nd:YAG	Decane	Bardsley et al. (1988)
1-9%	Nd:YAG	Decane	Senda et al. (1992)
10-1%	Nd:YAG 355 nm	Decane	Diwakar et al. (1992)
1-9%	Nd:YAG 355nm	Octane	Fujimoto and Tabata (1993)
1-9%	Nd:YAG 355 nm	Decane	Felton et al. (1993)
1-9%	Nd:YAG 355 nm	Dodecane	Yeh et al. (1994)
1 - 9%	Nd:YAG 355 nm		Tabata et al. (1995)
1-9%	Nd:YAG 355 nm	Decane	Campbell et al. (1995)
0.3-1%	Nd:YAG 266 nm	Hexadecane	Chojnacki and Feikema (1998)
	Kr-F 248 nm		Kornmesser et al. (2001)
1-9%	Nd:YAG 355 nm	Dodecane	Kim et al. (2002)
1-9%		Hexadecane	Desantes et al. (2005)
0.2-30%		Decane	Andersson et al. (2006)

Table 2.3: Exciplex fluorescence studies reported in the literature: the nature and mass ratios of dopants, the laser source and the fuel are indicated

The couple of tracers TMPD/Naphthalene appears as the most frequently used for studying evaporating gasoline sprays. This couple of tracers is though not convenient to manipulate and its coevaporation with gasoline has not been fully proven.
The choice made in the scope of this thesis is another less investigated couple of tracers: Fluorobenzene/Diethylmethlamine (FB/DEMA). This couple has the advantage of being perfectly coevaporative with hexane as investigated by Duewel et al. (2009). Moreover, these tracers are naturally liquid at room temperature and pressure and safer to manipulate than TMPD and naphthalene. The spectroscopic characterization of these tracers, presented in details in Duewel et al. (2009), shows that submitted to a laser pulse at 266 nm, the vapour fluoresces on a waveband centred around 290 nm and the liquid fluoresces around 350 nm. These wavebands are separated enough to allow the spectral discrimination with adapted interference filters.

Considering the advantages cited above, the couple of tracers FB/DEMA with hexane fuel is chosen for quantitative characterization of an evaporating hexane spray. Results are presented in chapters 6 and 7. In these experiments, the mass ratio of the mixture fuel/tracers is the following: fluorobenzene 2%, diethylmethlamine 9% and n-hexane 89%. These ratios are the same as the one used by Duewel et al. (2007). In order to improve the sensitivity of the vapour channel, the fluorobenzene was mixed in excess, meaning that the liquid phase may contain some FB too. The mixture has been checked as coevaporative with hexane within an accuracy of 1.5% for different operating temperatures ranging from ambient to 70 °C (Duewel et al. (2007)), meaning that the composition of the vapour remains constant in this temperature range. These tests ensure that measurements carried out in chapter 6 and 7 on hexane traced with FB/DEMA are quantitative. Measurements carried out with a heptane diffusion counterflow flame in chapter 8 cannot yield quantitative results for the vapour concentration because heptane was used instead of hexane with the same couple of tracers. In this latter case, only qualitative results may be retrieved because n-heptane and FB/DEMA features different evaporation characteristics (table 2.2).

2.3.4 Mie scattering and LIF setups

The experimental setups used for Mie scattering and LIF measurements are presented hereby. A Nd:YAG laser Spectra Physics Quanta Ray INDI is equipped with a quadrupler crystal to lase a beam at $\lambda = 266$ nm. The laser can be triggered from an external synchronisation signal with a frequency comprised

between 9 and 11 Hz. It yields a maximal energy of 35 mJ per pulse at $\lambda =$ 266 nm. The power is regularly measured via a power meter to ensure constant lasing conditions during the experiments. A vertical laser sheet cutting the burner exactly on its axis is formed from the laser beam using a system of a cylindrical and a spherical lenses. The laser sheet is about 50 mm high and 1 mm thick which yields a mean power per unit of area of about 0.7 mJ/mm^2 per pulse. A 16-bit ICCD camera Princeton Instruments - Ropers Scientific equipped with a UV 105 mm objective (maximum aperture 4.5) is placed perpendicularly and images the laser sheet around burner axis.

Since the flow is laminar and modulated by perfectly periodic signals, it was more convenient during the LIEF experiments to take phase-averaged images of vapour and liquid phases alternatively, and not simultaneously. As a consequence, only one ICCD camera was necessary, which was equipped alternatively with interference filters to collect the vapour and liquid exciplex fluorescence signals.

Different experiments were conducted for a set of forcing frequencies. An example of the triggering system used to perform phase locked images of the flow is detailed below. Other triggering systems used in the scope of this thesis are similar to the one described. Figure 2.11 presents the triggering system used for the Mie scattering and LIEF experiments in chapters 6 and 7. For phase-locked measurements in pulsating conditions, the laser and the ICCD camera were triggered relative to the TTL reference signal. The loudspeaker is supplied with an amplified $f = 28.125$ Hz sine signal from channel 1 of the wave generator. Its amplitude is tuned to generate the desired velocity fluctuations level at the burner outlet. The channel 2 is interlocked to channel 1 and its frequency is set to $f/3 = 9.375$ Hz. The corresponding TTL signal is sent to the Nd:YAG laser for the synchronisation. The laser sends also a signal to the PTG device, triggering the aperture of the ICCD camera. The relative phase shift of the two channels can be tuned easily so that each phase position can be investigated. The trigger frequency of the laser should be comprised between 9 and 11 Hz. This explains the choice of triggering frequency of channel 2 at $f/3 = 9.375$ Hz.

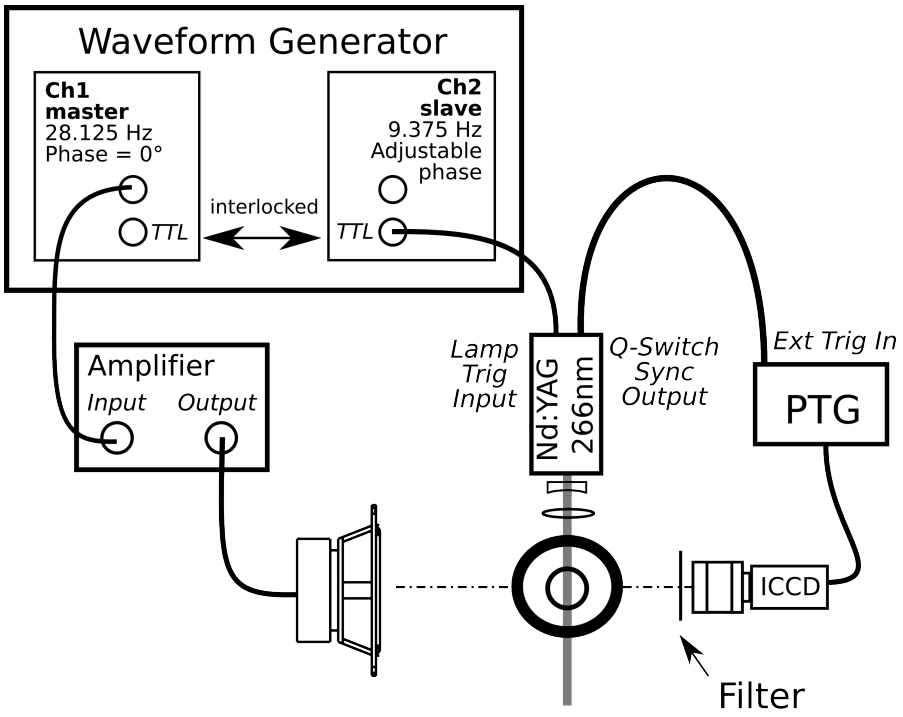

Figure 2.11: Experimental setup for Mie scattering and LIEF measurements - The loudspeaker is supplied by an amplified sine signal at a frequency $f =$ 28.125 Hz from channel 1 of a wave generator - A TTL signal at $f/3 =$ 9.375 Hz from channel 2 is used to trigger the laser and the camera via the controller PTG - The relative phase shift between the two channels can be tuned

Figure 2.12 presents the chronogram of the laser pulse, the aperture of the ICCD camera for the Mie scattering and fluorescence acquisitions. The laser signal was characterized and was found to last about 4 ns (full width half maximum) and is precisely localised in time relative to the camera timing at $t =$ 25 µs. As a consequence, the ICCD camera conditions of aperture are tuned relatively. The gate delay gd corresponds to the instant of aperture of the camera and the gate width gw corresponds to the duration of the aperture of the camera. The values of gate delay $gd = 31$ ns and gate width $gw = 50$ ns were used for LIEF measurements for both phases. This set of parameters ensures the aperture of the camera right after the laser pulse, so that the camera is not affected by the scattered signal from the laser pulse but only images the fluorescence signal. Using these aperture conditions, it has been checked with non-traced droplets that the camera does not record any scattered signal. For the Mie scattering acquisitions, the gate delay parameter is set to $gd =$

21 ns and gate width $gw = 10$ ns so that the camera images the scene during the whole laser pulse duration. The gain of the camera can be tuned between 100 and 250 over 255 depending on the configuration so that the signal in the viewfield remains well below the saturation level.

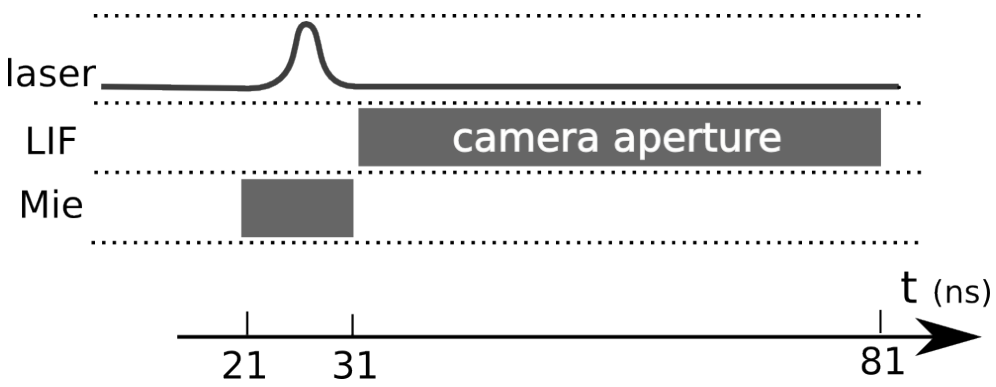

Figure 2.12: Aperture of the ICCD camera for the Mie and LIF acquisitions relative to the laser pulse. Laser pulse lasts 6 ns around $t = 25$ ns. ICCD camera is opened from $gd = 31$ ns during $gw = 50$ ns for the fluorescence acquisitions. ICCD camera is opened from $gd = 21$ ns during $gw = 10$ ns for the Mie scattering acquisitions. The triggering signal is a TTL signal emitted from channel 2 of the waveform generator.

The fluorescence signals are collected on given span of wavelengths with a set of optical filters which are alternatively mounted in front of the lens of the ICCD camera. The optical characteristics of the filters used for the acquisitions of Mie scattering, vapour and liquid fluorescences are reported in the table 2.4. They correspond to high-pass 266nm Semrock LP02-266RS (HP266), band-pass 290nm Melles Griot F10-289FWHM10 (BP290), band-pass 360nm Melles Griot F10-360FWHM10 (BP360) and band-pass 532nm Melles Griot 93/XB90/505 (BP532) filters. The HP266 filter aims at reducing the laser energy level at 266 nm. The BP290 and BP360 filters aim at collecting the fluorescence signals coming from the liquid and vapour phase. The BP532 collects the Mie scattering signal from the remaining laser energy at 532 nm. The laser energy at this wavelength is much smaller than the laser energy at 266 nm but it is enough to get good images of Mie scattering of the spray.
The choice of the optical filters is important to get a good quality of the fluorescence signal collected. A special care has been paid to choose optical filters preventing any crosstalking effects (Desantes et al. (2005)). For instance, an interference band-pass filter centred on 340 nm was first used to collect the

Filter reference	Type	λ_0 [nm]	FWHM	Strength
HP266	High-Pass	266 nm	-	10^{-5}
BP290	Band-pass	290.7 nm	10.8 nm	10^{-2}
BP360	Band-pass	361.5 nm	10.1 nm	10^{-3}
BP532	Band-pass	532 nm	10 nm	10^{-2}

Table 2.4: Interference filters used in front of the ICCD camera for Mie scattering and fluorescence acquisitions: type, characteristic wavelength λ_0, full width half maximum (FWHM) and strength of the filters are indicated

liquid fluorescence signal. Unfortunately, a too strong crosstalk signal coming from the vapour phase was also collected with this filter. The use of the BP360 filter solved this problem (see section 6.2.3).

Table 2.5 sums up the different sets of acquisitions that have been carried out in steady flow conditions and for four phase positions equally distributed during a modulation cycle in pulsating conditions.

Visualisation	gd / gw nb of acquisitions	Filters
Vapour Fluorescence	31 ns / 50 ns 100	HP266 + BP290
Liquid Fluorescence	31 ns / 50 ns 4,000	HP266 + BP360
Mie Scattering	21 ns / 10 ns 2,000	HP266 + BP532

Table 2.5: Characteristics of the acquisitions performed in the steady configuration and for 4 phase positions equally distributed in the modulation cycle in the pulsated configuration: temporal acquisition parameters gw and gd, number of acquisitions and filters used in front of the ICCD camera

A large number of acquisitions was performed in each case to reach a good signal to noise ratio and a statistical convergence of measurements: 100 acquisitions for the vapour fluorescence, 2,000 acquisitions for the Mie scattering and 4,000 for the liquid fluorescence.

The calibration process of the vapour fluorescence signal and a study of statistical convergence on sets of vapour acquisitions are presented in details in chapter 6.

Part II

Flame dynamics in a gaseous stagnation flow

Chapter 3

Flow and flame structure

The dynamics of an inert and a reactive stagnation flows is investigated in steady and pulsated configurations for different forcing frequencies. Flow and flame structures are characterized by tomographies and chemiluminescence images. The velocity flowfield is characterized by PIV measurements and LDV is used to determine precisely the boundary conditions at the burner outlet and the velocity evolution along the burner centreline. The structure of the flow and the flame feature periodical vortex rings shed from the burner lip, that are analysed for different forcing frequencies. In particular, different propagation modes of velocity perturbations along the burner axis are identified depending on the Strouhal number St *of the flow. They can be of acoustic or convective types. These propagation modes are analysed relative to the influence of the vortex ring on the burner centreline, with the support of a decomposition of velocity components on this axis. It is also shown that the set of boundary conditions commonly used for 1D modelling of such a configuration should be reconsidered when a convective propagation mode settles.*

3.1 Introduction

Combustion dynamics is a topic of standard interest. Many studies in different experimental configurations are carried out. For instance, Wyzgolik and Baillot (2007) investigated the responses of jet flames to axial jet mixing layers. Other studies have been carried out for stretched flames in steady flows. Unsteady stretched effects have also been analysed but mainly using numerical tools, because of the difficulty to reproduce unsteady stretch in the experiments. Some studies have been carried out in stagnation flows by physically moving the wall position to induce stretch modulations(Hirasawa et al.

(2000)). In such configurations, the stretch is modulated with no vortex rings shed at burner mouth since the upcoming flow is not pulsated. Results obtained are however limited to low frequencies because of technical difficulties to set an oscillatory motion to the moving plate. In this study, an impinging flow with upstream velocity modulations produced by acoustic excitation of the incoming flow has been chosen to analyse unsteady stretch effects.
Investigations of unsteady effects on gaseous premixed flame is actually a necessary first step before studying two-phase configurations. It is important to understand in details governing mechanisms of these interactions. In this chapter, the focus is placed on premixed planar flames in a stagnation flow. Different diagnostics are used to characterize and analyse the flame response to incoming flow perturbations produced at the burner outlet. The configuration explored is a gaseous premixed plane laminar flame stabilized in a stagnation flow near a wall and submitted to upstream velocity modulations. The velocity flow field is characterized using Particle Imaging Velocimetry (PIV) and flame chemiluminescence is imaged with an ICCD camera.

3.2 Experimental configuration

Experimental setup

Experiments were carried out with the burner described in Chapter 1. A schematic view of the setup and notations used in this section are presented in figure 3.1.

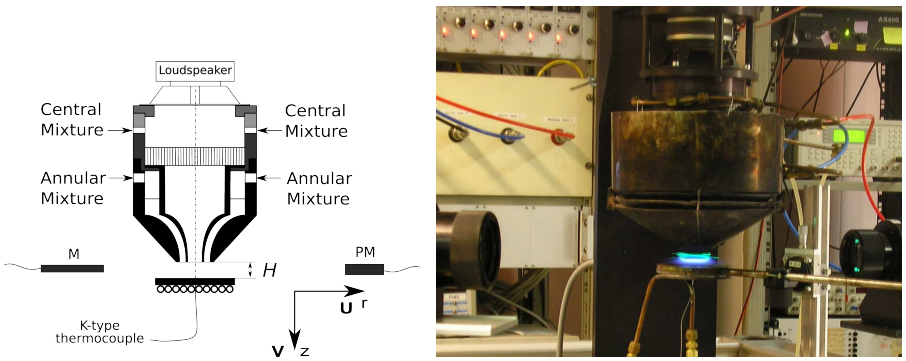

(a) Scheme **(b)** Picture

Figure 3.1: Experimental setup. The burner to plate distance is fixed in these experiments to $H = 24.2$ mm - The origin O of the local coordinate system (O, r, z) is fixed on axis at the burner outlet.

Two axi-symmetric flows originating from the burner outlet are directed towards a thermalized plate: a central jet corresponding to a mixture of air and methane and an annular flow of nitrogen encompassing the latter. The presence of a grid and a honey comb in the central flow ensures a perfectly laminar flow at burner outlet. The plate to burner distance is kept constant and equal to $H = 24.2$ mm and the central jet has a diameter $D = 20$ mm at the burner outlet. In this section, the velocity flowfield is characterized using cylindrical coordinates (r,z), where r is the distance to the burner axis and z is the vertical distance measured from the burner outlet.

One inert and three reactive configurations (flames P, Q and R) are investigated in chapters 3 and 4. Values for the central and annular flowrates, equivalence ratios Φ, flame velocities S_L (Vagelopoulos and Egolfopoulos (1998)), fuel mass fractions Y_F of central flow and mean central plug flow velocities V are indicated in table 3.1. Other flowrate conditions will be explored for the study of sound production mechanisms. These conditions will be presented later in chapter 5.

nL h^{-1}		Inert	Flame P	Flame Q	Flame R
central flow	CH_4	0	155	127	186
	Air	1639	1484	1511	1452
annular flow	N_2	698	698	698	698
Φ		0	0.99	0.80	1.22
S_L [m s^{-1}]		-	0.38	0.27	0.27
Y_F		0	0.055	0.044	0.066
V [m s^{-1}]		1.55	1.55	1.55	1.55

Table 3.1: Flames P, Q, R and inert configuration: definition of mass flow rates, values of equivalence ratio Φ, flame speed S_L, fuel mass fraction Y_F of central flow and mean central mean flow velocity V.

For the three reactive configurations P, Q and R, the sum of central flowrates of air and methane is kept constant and equal to $q_c = 1639$ nL h^{-1} in these experiments with mixtures featuring different equivalence ratios. Flame P is near stoichiometry, flame R is rich and flame Q is lean. Note that flames Q and R have the exact same flame velocity $S_L = 0.27$ m s^{-1} (Vagelopoulos and Egolfopoulos (1998)). The inert configuration explored features also a central mass flowrate of air of $q_c = 1639$ nL h^{-1}.
The four configurations have indeed the exact same central volumetric flow

rate at ambient conditions, as shown in following equation:

$$\begin{aligned}\dot{Q}_{air}(T,P) &+ \dot{Q}_{CH_4}(T,P) \\ &= \frac{\rho_{air}(T_0,P_0)}{\rho_{air}(T,P)}\dot{Q}_{air}(T_0,P_0) + \frac{\rho_{CH_4}(T_0,P_0)}{\rho_{CH_4}(T,P)}\dot{Q}_{CH_4}(T_0,P_0) \\ &= \frac{P_0}{P}\frac{T}{T_0}\underbrace{\left[\dot{Q}_{air}(T_0,P_0) + \dot{Q}_{CH_4}(T_0,P_0)\right]}_{=1639 \text{ nL h}^{-1}}\end{aligned}$$

with T, P being the temperature and pressure of the flow in the experimental conditions and $T_0 = 0$ °C and $P_0 = 101{,}325$ Pa being the temperature and pressure of the flow in normal conditions.

An annular flowrate of $q_a = 698$ nL h^{-1} of nitrogen is used in the four configurations. These flowrates correspond to plug flow with a mean velocity of $V = 1.55$ m s^{-1} in the central outlet and $V = 0.66$ m s^{-1} in the annular outlet. In the present chapter, only the inert flow and the flame P are investigated. Flame P configuration is often simply referred as the reactive configuration. Flames Q and R will be used in the chapter 4.

Note that for reacting conditions, the plate is cooled down using a water heat exchanger welded on the bottom side of the plate. The temperature in the center of the plate is controlled with a K-type thermocouple and fixed to about 80°C. In reacting conditions, the burner temperature is controlled at three different locations: it is about 65°C at the bottom, 55°C in the middle and about 50°C at the top of the burner. The flow temperature has also been measured at the burner in the central jet. Inserting a thermocouple upstream of the flame modifies the flame stabilization location, it was thus only possible to measure the flow temperature at the burner outlet just after blowing off the flame and results yield a temperature of about T = 65°C.

Analysis of the steady and pulsated flows of the inert and flame P configurations are respectively presented in sections 3.3 and 3.4. The different techniques and forcing conditions used to characterize these indications are first introduced.

Flow forcing conditions

When the flow is modulated by an harmonic excitation, the shape of the flame responds to the modulation. The forcing frequency was kept within the frequency band [10 Hz-150 Hz] over which the flame features different patterns. Below $f = 10$ Hz, modulations of velocity are more difficult to obtain with

the loudspeaker and for frequencies higher than $f = 150$ Hz, the flame seemed motionless.
Six different driving frequencies were chosen to explore the flow and flame responses $f = 10$, 35, 51.282, 63, 75 and 102.564 Hz. They were chosen because the CCD camera used in this study is operating at a fixed rate of 50 Hz. Using these settings, it is possible to image a whole cycle of excitation with respectively 5, 11, 40, 63, 26 and 40 images separated by a constant phase shift. These images are used in the following to get insight on the flow and flame dynamics. For the particular forcing frequency $f = 10$ Hz, only 5 images per cycle could be recorded. As a consequence, images of the flow at a slightly shifted forcing frequency $f = 11$ Hz yielding 51 shots per modulation cycle were taken in order to get more details on the flow and flame dynamics. For the determination of flame transfer functions, more forcing frequencies were investigated, typically from 10 to 150 Hz separated by 10 Hz increments.

For each forcing frequency, the signal amplitude from a sine wave synthesizer supplied to a stereo-amplifier and to the loudspeakers was tuned to keep constant the velocity fluctuation level measured by LDV. The amplitude of velocity fluctuations v_{rms} is controlled at point R located on the burner axis, at $z_R = 3.5$ mm away from the nozzle outlet. It has been set during these experiments at a constant value of:

$$v_{rms,R} = \frac{1}{T}\int_0^T (v_R(t) - \overline{v}_R)^2 dt \simeq 0.20\,\overline{v}_R \tag{3.1}$$

Using this modulation level, the flame executes a periodic motion and perturbations are sufficiently strong to cause noticeable interactions of the flow and the flame. For higher modulation levels, the flame could extinguish and the quality of the perturbations generated by the loudspeaker worsen.

Measurement techniques

Different diagnostics are used to study the flow and flame interactions produced by the modulation. A CCD camera is used to record phase conditioned images of flame chemiluminescence during the modulation period. An Argon laser with a cylindrical and spherical lenses system are used to get tomographic images in the symmetry plane of the burner. Laser Doppler Velocimetry (LDV) and Particle Imaging Velocimetry (PIV) techniques are used to characterize the velocity field along the burner axis and between the burner outlet and the plate. A photomultiplier PM equipped with interference filters was also used to record fluctuations of light intensity in CH^* and OH^* emission

bands. A microphone M is also used to measure sound pressure fluctuations in the vicinity of the flame region. The reader should refer to chapter 2 for a detailed description of all these diagnostics.

The microphone M, photomultiplier PM and LDV temporal signals are all recorded on a computer via a 12-bits A/D converter. During all experiments, the analog signal delivered by the frequency counter from the LDV system is sampled at a frequency $f_s = 4096$ Hz or $f_s = 16384$ Hz so that at least 20 points per modulation period were recorded. All signals are synchronized using the TTL output from the wave synthesizer supplying the loudspeakers. This provides a temporal reference for all signals with respect to the modulation cycle.

LDV settings

The LDV technique and its setup are presented in chapter 2. The central and annular flows are seeded with micronic oil droplets using the system presented in chapter 2. It was ensured during all experiments that the particles detection data rate is well above the sampling frequency to avoid any bias. Acquisition duration was sufficiently long to record at least 100 periods of the forcing signals.

LDV measurements are carried out at regular increments (see figure 3.2) every $\Delta z = 0.2$ mm in the vertical direction along the burner axis from $z_R = 3.5$ mm (point R) away from the burner outlet down to the flame front location and every $\Delta r = 0.2$ mm in the horizontal direction at respectively $z = 3.5$, 6.5, 9.5, 13 and 16 mm to cover the entire flow field between the nozzle outlet and the flame location.
In addition, LDV was also used to control the fluctuation level at the burner outlet in all experiments. For each forcing frequency and flow condition, the amplitude of the signal synthesizer feeding the loudspeaker has been chosen to keep this oscillation level constant at point R indicated in figure 3.2.

PIV settings

The PIV technique was presented in chapter 1. Similarly to LDV, the central and annular flows are also seeded with micronic oil droplets. A calibration based on a background grid image is used to scale the PIV data with a resolution of 16.2 pixels/mm in each direction. The aperture of the camera is set to avoid saturation from the light scattered by the seeding particles. A too

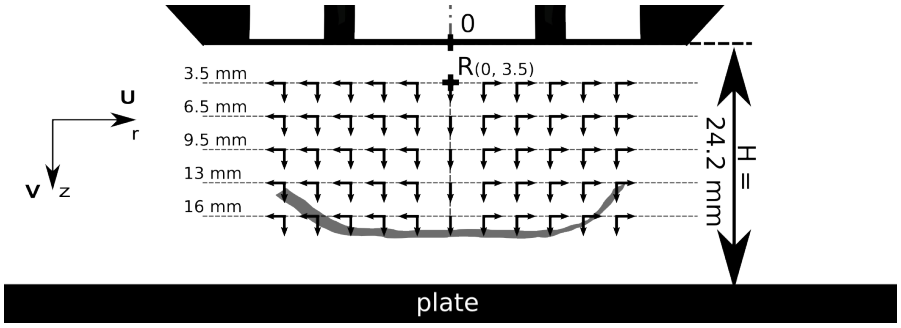

Figure 3.2: LDV measurement grid: axial and radial velocities have been measured along burner axis from point R to the flame location and along diameters at $z = 3.5$, 6.5, 9.5, 13 and 16 mm. Increments Δz and Δr equal to 0.2 mm in both directions.

small aperture decreases the quality of image and consequently the quality of cross-correlation results. One hundred pairs of images were taken at twenty successive instants separated by a constant phase shift to describe a complete modulation cycle. Cross-correlation is calculated for each pair of images on windows of 16×16 pixels^2 with an overlap of 25%. Velocity vectors obtained with a signal to noise ratio (SNR) below 2 have been rejected.

3.3 Analysis of flow and flame structure in steady state conditions

3.3.1 Tomographic and chemiluminescence images

Tomographic views of the flow and flame combined with chemiluminescence images are presented for the inert configuration and for flame P in absence of modulations in figure 3.3. For this purpose, an Argon laser generates a vertical light sheet cutting the seeded flow along the burner axis. A CCD camera, placed perpendicular to the sheet, records images of the scene. The technique yields snapshots of the flow patterns in the plane of the laser sheet and records also the flame chemiluminescence intensity integrated in the line of sight. This explains some blurred effects on the shape of the flame front which is not perfectly flat over the burner radius. The position of the plate and the burner outlet can be inferred from laser reflections.

The flow pattern is symmetric with respect to the burner axis and features no perturbation. The flame is plane around the burner axis, horizontal and stable.

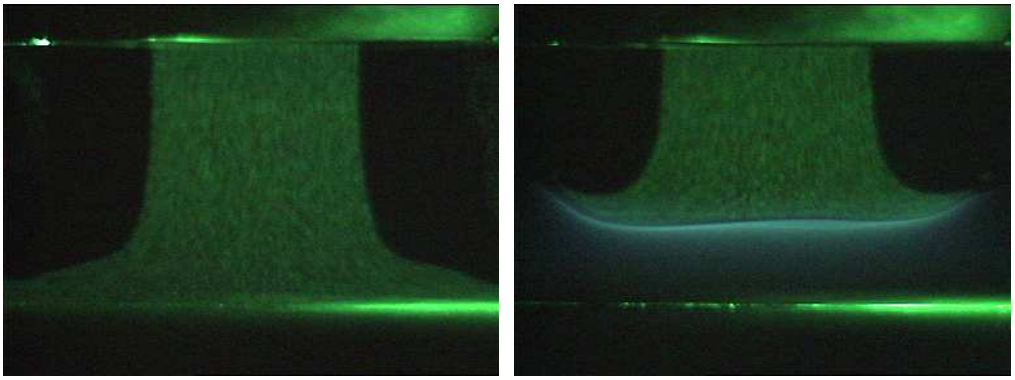

(a) inert flow **(b)** flame P

Figure 3.3: Tomographic views in steady conditions. Distance between the plate and the burner outlet $H = 24.2$ mm.

The stability of this configuration was analysed by measuring the flame front position at different instants from ignition. An experience with a background grid was conducted to scale precisely the images. It was found that the reaction zone is located between $z = 16.5$ and $z = 17.2$ mm from the burner outlet. The flame reaches this steady position within one minute after ignition. Using the scale factor 14.4 pix/mm, the flame luminosity thickness is estimated at about $\delta = 0.6$ mm. Fluctuations of the flame location in the different snapshots can be estimated of about 0.3 mm, indicating that the flame is extremely stable versus time.

3.3.2 Velocity flowfield

The velocity flow fields for the inert and flame P configurations are plotted in figure 3.4. Only half burner is represented to improve clarity it was checked that all configurations explored feature a perfect symmetry around the burner axis. In these figures, scaled black arrows indicate the mean velocity calculated in each cross-correlation window. In the inert configuration, the velocity field is available in the whole view field. In the reacting case, only the fresh reactants field can be imaged with oil particles and therefore the velocity flow field is restricted to the region upstream of the flame.

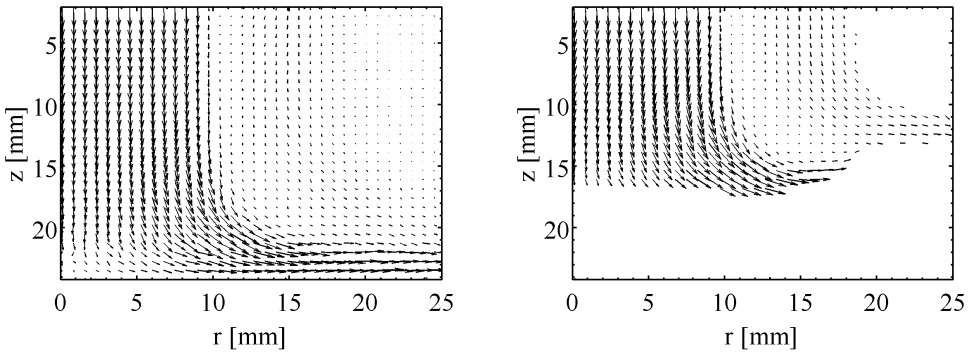

(a) inert flow **(b)** flame P

Figure 3.4: Steady velocity fields in the central and surrounding jet flows impinging on the plate. Scale is given by the vectors at burner outlet corresponding to about 1.55 m s^{-1}

The inert velocity flowfield exhibits parallel streamlines for $z \leq 15$ mm. Further down, the velocity vectors deviate from the burner centreline due to the presence of the plate. In the reactive configuration, the velocity flowfield is modified upstream of the flame. The flame stretches the flow from $z = 10$ mm where velocity vectors exhibit radial expansion. The flame shape can be inferred from the boundary between seeded and unseeded flows corresponding to the evaporation front of micronic oil droplets evaluated at about $T \simeq 600$ °C.

Axial velocity profiles along the radial direction are plotted in figure 3.5 using LDV and PIV data in the inert and reactive configurations at different axial locations $z = 3.5$, 9.5 and 16 mm. For PIV data, measurements at the closest mesh point have been considered.

The axial velocity is symmetric around the burner axis for all vertical distances explored. This is a guarantee of the symmetry of the flow at the burner exhaust. There is also a good match between LDV and PIV data. The slight differences between LDV and PIV measurements might explained by the fact that PIV measurements are spatially averaged over an interrogation window while LDV measurements are relative to the volume where two laser beams cross. In the inert and reactive configurations, the velocity profile at the central outlet nozzle is quite flat over 80% of the outlet diameter. A dead zone is easily noticeable between the central and annular flows at burner lips. Close to the burner axis, velocity profiles have a concave shape due to the presence

of the plate that induces a counterflow pressure gradient. The presence of the plate stretches the flow in the horizontal direction with a decrease of the axial velocity. This is a typical shape of impinging flow. At burner exit, the fluctuation levels indicated by root mean square values of the velocity are typically less than 2% of the mean axial velocity.

The inert and the reactive flows feature some noticeable differences. In the reactive conditions, the flow widens more in the radial direction due to the presence of the flame and the mean axial velocity on the burner axis decreases faster than in the inert configuration for the same flowrate. Close to the burner, PIV and LDV measurements in inert and reactive configurations fit exactly. The situation is not the same at $z = 16$ mm, RMS values from PIV measurements become significantly higher and PIV measurements differ from LDV measurements in the reactive case. This is caused by interrogation windows of PIV that cover both seeded and unseeded areas close to the flame and as a consequence the crosscorrelation features some bias. LDV yields more reliable data in this region because the measurement volume is smaller.

It should also be noted that the potential influence of flow seeding on the combustion has been evaluated by accurately imaging the flame chemiluminescence with and without seeding particles. Using a resolution of about 16 mm/pixel, no noticeable difference has been observed. As a result, the seeding of the flow with liquid oil droplets for velocity measurements purposes can be considered as non influencing the combustion.

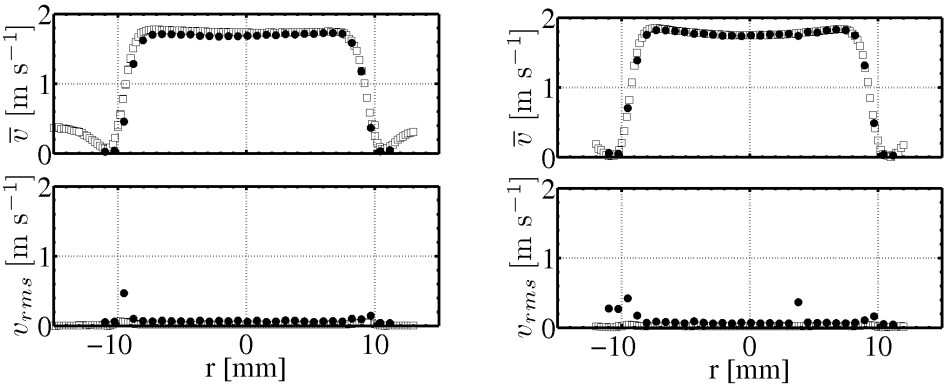

(a) $z = 3.5$ mm

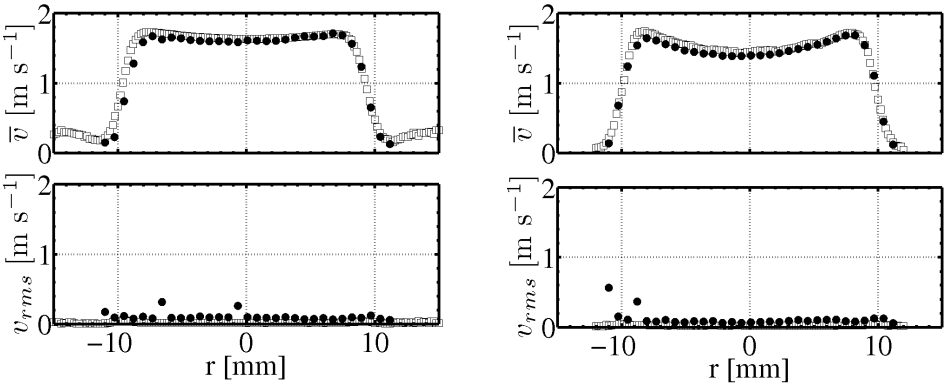

(b) $z = 9.5$ mm

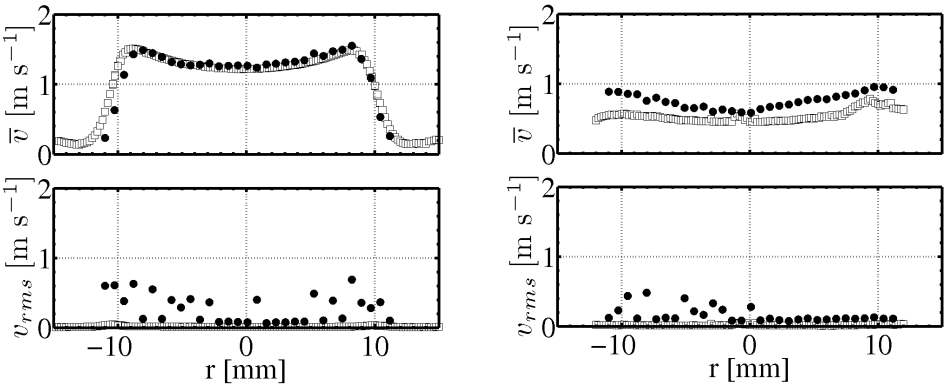

(c) $z = 16$ mm

Figure 3.5: Profiles of mean and fluctuation levels of axial velocity in steady configuration at $z = 3.5$ mm, 9.5 mm and 16 mm from LDV measurements (filled disks) and PIV measurements (empty squares) - left: inert configuration - right: flame P.

3.3.3 Comparisons with simulations

Velocity measurements are compared with 1-D simulations using a reacting flow solver with detailed chemistry developed at laboratoire EM2C (Darabiha (1992); Aguerre (1994)). The calculations have been performed by Dr F. Laurent. In this solver, the symmetry of the flow near the burner axis is used to simplify the set of equations by considering the following structure of the flow field in the axisymmetric base (O,r,z) (Kee et al. (1988); Dixon-Lewis (1991)):

$$\begin{aligned} T(z,t), \quad Y_k(z,t), \quad \rho(z,t), \quad v(z,t), \quad u(r,z,t) = rU_r(z,t) \\ p(r,z,t) = p_{atm} - J(t)\frac{r^2}{2} + \hat{p}(z,t). \end{aligned} \tag{3.2}$$

with T the temperature, Y_k the mass fraction of the kth specie, ρ the density of the gaseous mixture, v the vertical velocity component, u the horizontal velocity component, U_r the radial reduced velocity and p pressure field.

The following boundary conditions are imposed at the plate location $z = H$:

$$\begin{aligned} \frac{\partial T}{\partial z}(H,t) = \alpha(T - T_{plate}), \quad \frac{\partial Y_k}{\partial z}(H,t) = 0, \\ v(H,t) = 0, \quad U_r(H,t) = 0 \end{aligned} \tag{3.3}$$

with $\alpha = 700$ cm^{-1} and the plate temperature $T_{plate} = 80$ °C.

In the steady configuration, the following boundary conditions are imposed at $z_R = 3.5$ mm from burner outlet:

$$T(z_R,t) = T_R \quad , Y_k(z_R,t) = Y_{k,R} \tag{3.4}$$

with T_R the temperature of flow at burner outlet, and $Y_{k,R}$ the mass fractions of methane and oxidizer corresponding to $\Phi = 1$ (flame P), $\Phi = 0.80$ (flame Q) and $\Phi = 1.22$ (flame R).

Under steady operating conditions, the velocity is imposed at burner outlet at $z = z_R$:

$$v(z_R,t) = \overline{v}_R, \quad u(z_R,t) = 0 \tag{3.5}$$

where $\overline{v}_R$ is the axial velocity measured at point R by LDV.

Figure 3.6 presents the results for several possible incoming flow temperatures T_R. The calculated axial velocity v and reduced radial velocity $U_r = u/r$ are presented along the burner axis from $z = 0$ to 24.2 mm. Gray levels indicate predictions obtained for different inlet temperatures varying from $T_R = 52$ °C (black line) to $T_R = 102$ °C (gray line) with $\Delta T_R = 10$ °C increments. Data extracted from PIV measurements with oil particles are also indicated using square symbols.

Numerical results and measurements fit reasonably well upstream of the flame. The last plotted symbol indicates roughly the beginning of the preheated zone where oil particles are vaporized ($T \simeq 600$ °C). The position of the flame front is shown to be sensitive to the inlet temperature. An inlet temperature of $T_R = 82$ °C yields the best match for the estimation of the flame front location. It is worth noting that this value is a bit higher than that measured at the burner outlet $T_R = 65$ °C after blowing the flame. This value $T_R = 82$ °C is chosen for simulations in pulsating conditions, presented in the next section.

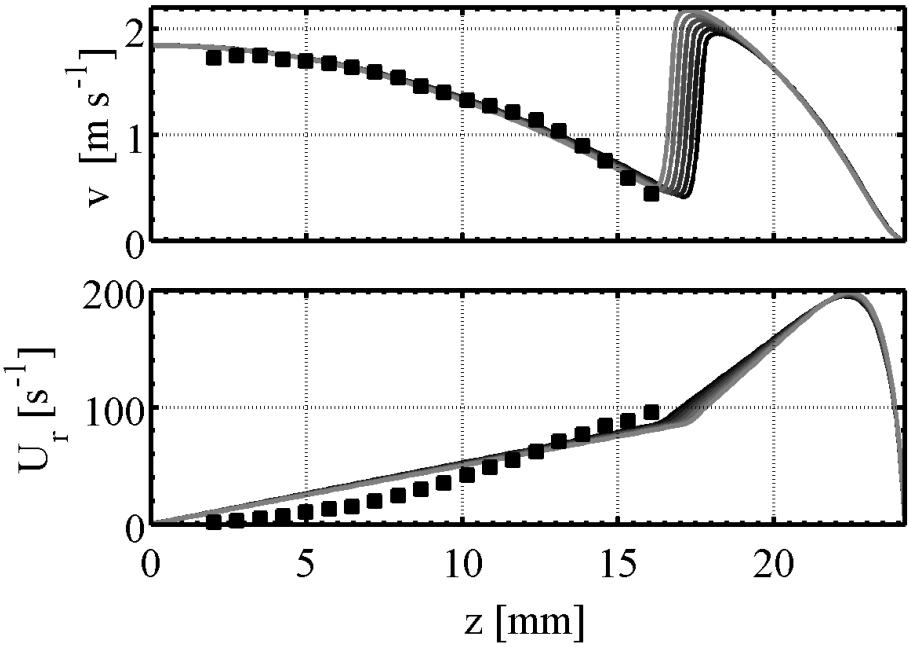

Figure 3.6: Simulations of axial velocity v and reduced radial velocity $U_r = u/r$ along the burner axis from $z = 0$ mm to $z = 24.2$ mm for flame P. Gray levels indicate different inlet temperature conditions from $T = 52$ °C (black line) to $T = 102$ °C (gray line) with $\Delta T = 10$ °C increments. Data extracted from PIV measurements are added as square symbols.

3.4 Flow and flame structures under pulsating conditions

3.4.1 Tomographic and chemiluminescence images

Tomographic views of the light scattered by the oil particles and flame chemiluminescence are presented for three different forcing frequencies $f = 10$, 51 and 102 Hz in figures 3.7, 3.8 and 3.9. For each forcing frequency, six images describing a whole cycle of modulation are shown. A whole cycle is read clockwise, i.e. from top left image to top right image, then down to bottom right image, then left to bottom left image, and back up to top left image.

These snapshots provide an insight on the flow and flame patterns when the flow is modulated. For a low modulation frequency, at $f = 10$ Hz, the flow

and flame feature a bulk vertical oscillation accompanied by a stretch in the radial direction (Figure 3.7). When the forcing frequency is increased, one notices large structures shed from burner lip and enrolling the flame. Due to the axial symmetry, the traces of the left and right vortices in the vertical plane correspond to a single vortex ring. This ring is created by velocity fluctuations at burner lips in the shear layer between the central jet and the surrounding coflow. It is then convected towards the plate by the flow. The size of this vortex ring depends on the forcing frequency. At $f = 10$ Hz, the width of the central flow at burner outlet slightly fluctuates during the modulation period but no vortex is generated. At $f = 51$ Hz, one large vortex ring is shed from the burner mouth and is convected in the viewfield (Figure 3.8). At $f = 102$ Hz, smaller vortices are shed at the burner lip and two of them are clearly visible between the burner and the flame (Figure 3.9).
Chemiluminescence images of the flame show that these disturbances strongly modify the shape of the flame. At low frequency, the shape of the flame remains planar during the modulation period but the flame location features a large vertical oscillation. It is also stretched in the horizontal direction. At higher forcing frequencies, the central region of the flame close to the burner axis does not move anymore while flame tips are strongly perturbed. The flame enrols around the vortex ring. The amplitude of the flame motion on the vertical axis has been measured precisely. At $f = 10$ Hz, flame P oscillates along the axis between $z = 12.8$ mm and $z = 18.5$ mm $\pm$ 0.5 mm, while at $f = 51$ Hz, the motion amplitude is reduced between $z = 16.3$ mm and $z = 17.2$ mm. At $f = 102$ Hz, almost no oscillation on the axis is noticeable and the flame is located at about $z = 17.1$ mm, a position corresponding approximately to the steady location of the flame in absence of modulation.

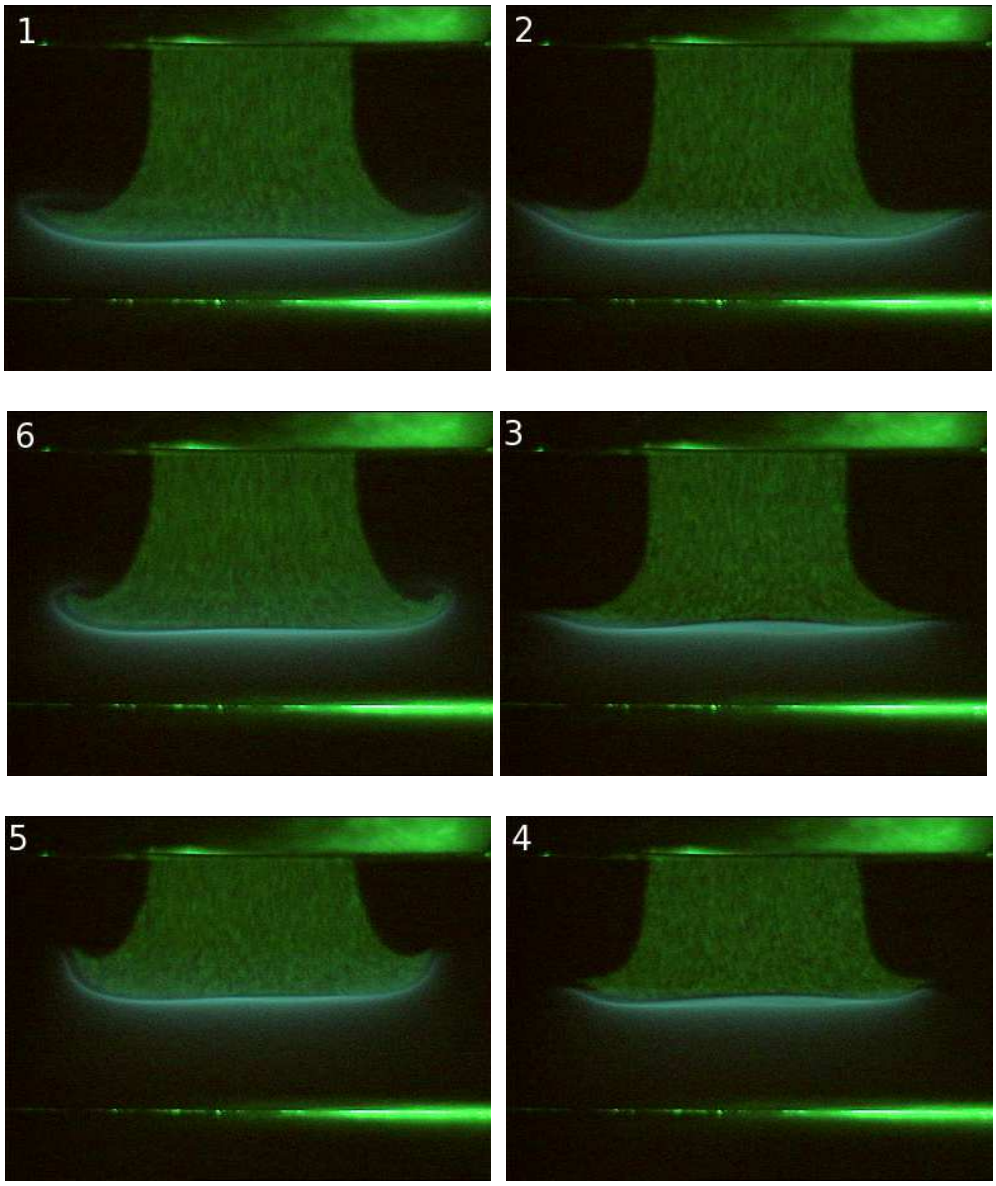

Figure 3.7: Tomographic views of the flow and flame structures in flame P configuration for a forcing frequency $f = 10$ Hz and a fluctuation level $(v_{rms}/\overline{v})_R = 0.20$ - Six images taken at instants separated by an equally phase shift describe a whole cycle clockwise. Distance between the plate and the burner outlet $H = 24.2$ mm.

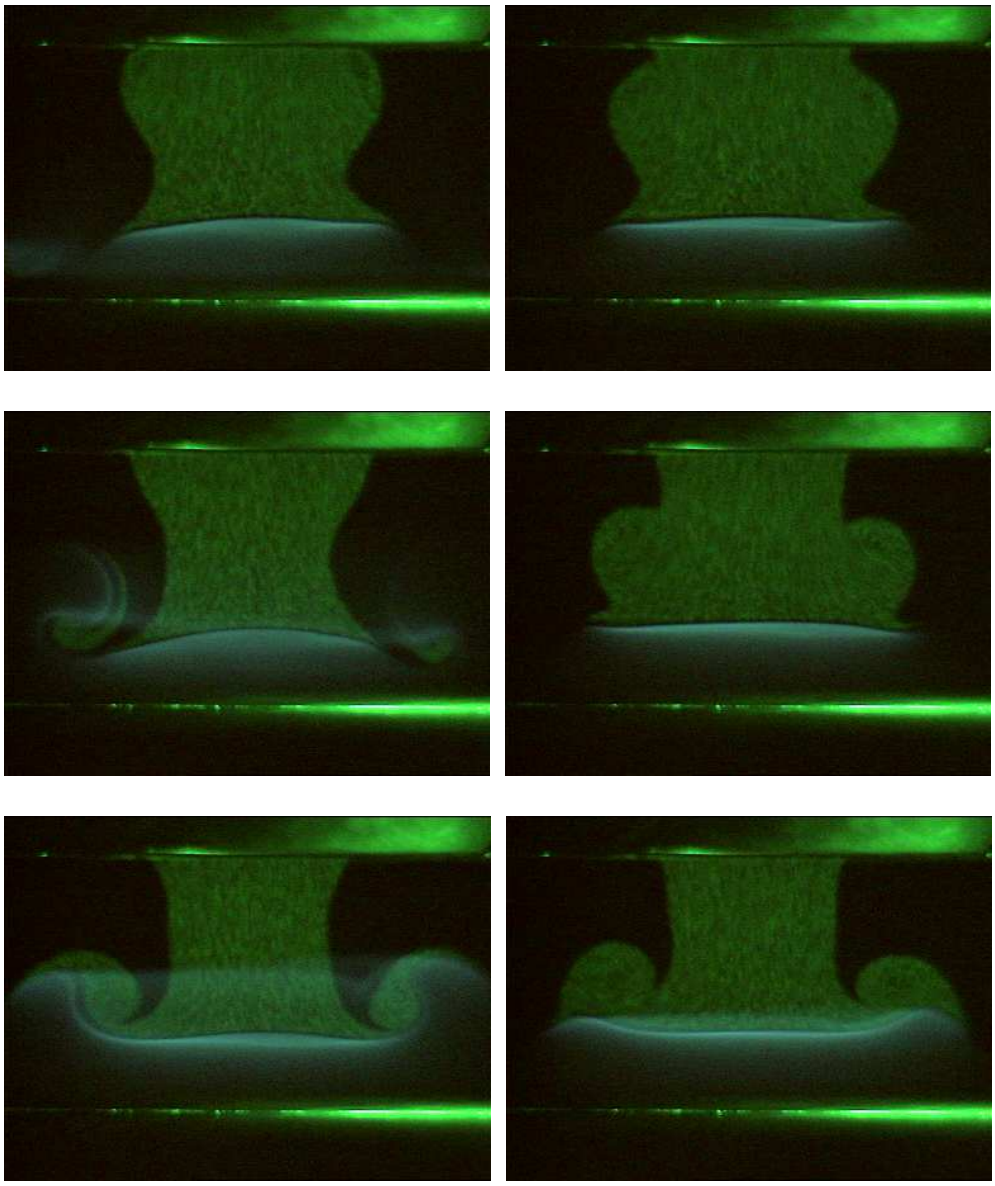

Figure 3.8: Tomographic views of the flow and flame structures in flame P configuration for a forcing frequency $f = 51$ Hz and a fluctuation level $(v_{rms}/\overline{v})_R = 0.20$ - Six images taken at instants separated by an equally phase shift describe a whole cycle clockwise. Distance between the plate and the burner outlet $H = 24.2$ mm.

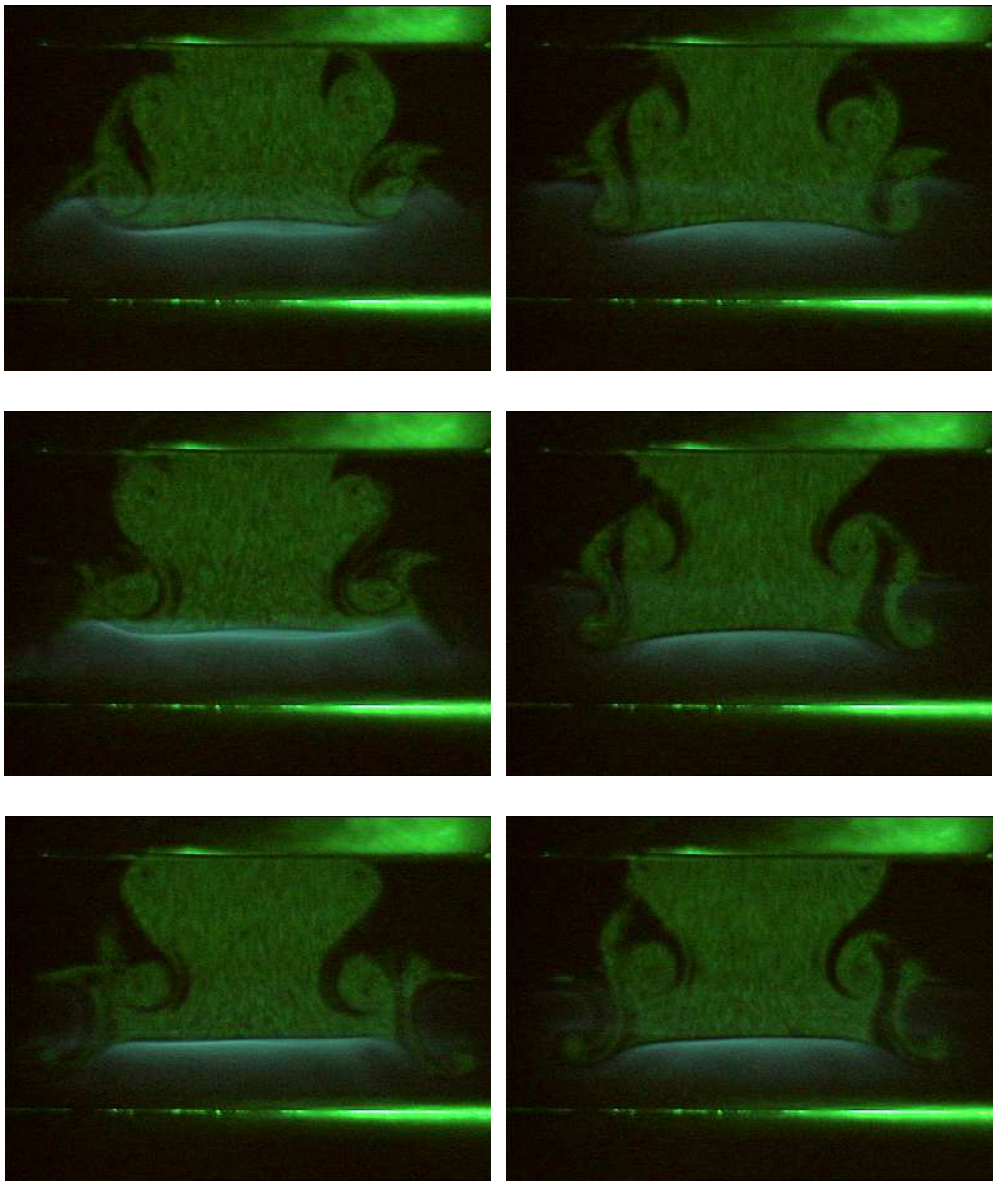

Figure 3.9: Tomographic views of the flow and flame structures in flame P configuration for a forcing frequency $f = 102$ Hz and a fluctuation level $(v_{rms}/\overline{v})_R = 0.20$ - Six images taken at instants separated by an equally phase shift describe a whole cycle clockwise. Distance between the plate and the burner outlet $H = 24.2$ mm.

3.4.2 Velocity and swirling strength flowfields

Tomographic and chemiluminescence images were completed by PIV measurements in the fresh reactants. Figures 3.10 to 3.15 present velocity and swirling strength fields in the inert and reactive configurations when the central flow is modulated. Six velocity fields determined at equally separated instants describe a whole cycle of modulation clockwise. In these experiments, the counterflow and the coflow were both seeded with oil particles. The local flow velocity vector is represented by an arrow which length is proportional to the velocity modulus.
The local swirling strength λ_{ci} is also superimposed in these figures using gray contour plots. This is estimated using the D^2 criterion (Adrian et al. (2000)), where D is the local velocity gradient tensor: $D_{ij} = \partial u_i/\partial x_j$, $i, j = 1, 2$, u_i being the velocity component associated to x_i. The swirling strength λ_{ci} is defined as the imaginary component of the complex eigenvalue of the local velocity gradient tensor. The inverse of the complex eigenvalue of the tensor of velocity gradients can be taken as being the time required for the local streamlines to have one turnover. This is estimated here using two-dimensional PIV fields. This criterion is not sensitive to shear stress and is representative of the swirling motion only (Adrian et al. (2000)).
Results are successively presented for a modulation at $f = 10$ Hz in the inert configuration (figure 3.10) and in the reactive configuration flame P (figure 3.11), then for a modulation at $f = 51$ Hz in figures 3.12 and 3.13, and finally for a modulation at $f = 102$ Hz in figures 3.14 and 3.15. The scale remains the same between all these plots.

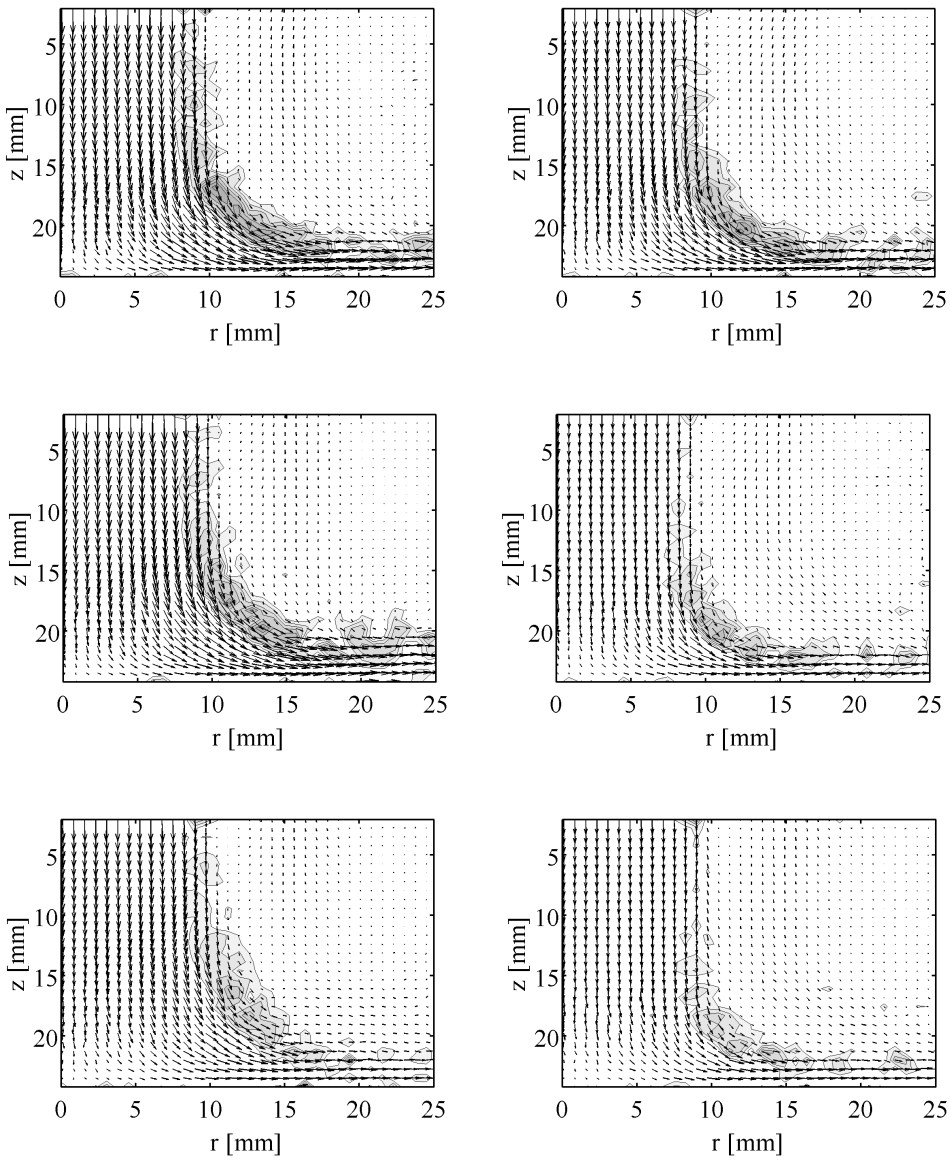

Figure 3.10: Velocity and swirling strength λ_{ci} fields calculated in the inert configuration for a forcing frequency $f = 10$ Hz - A whole cycle is described clockwise.

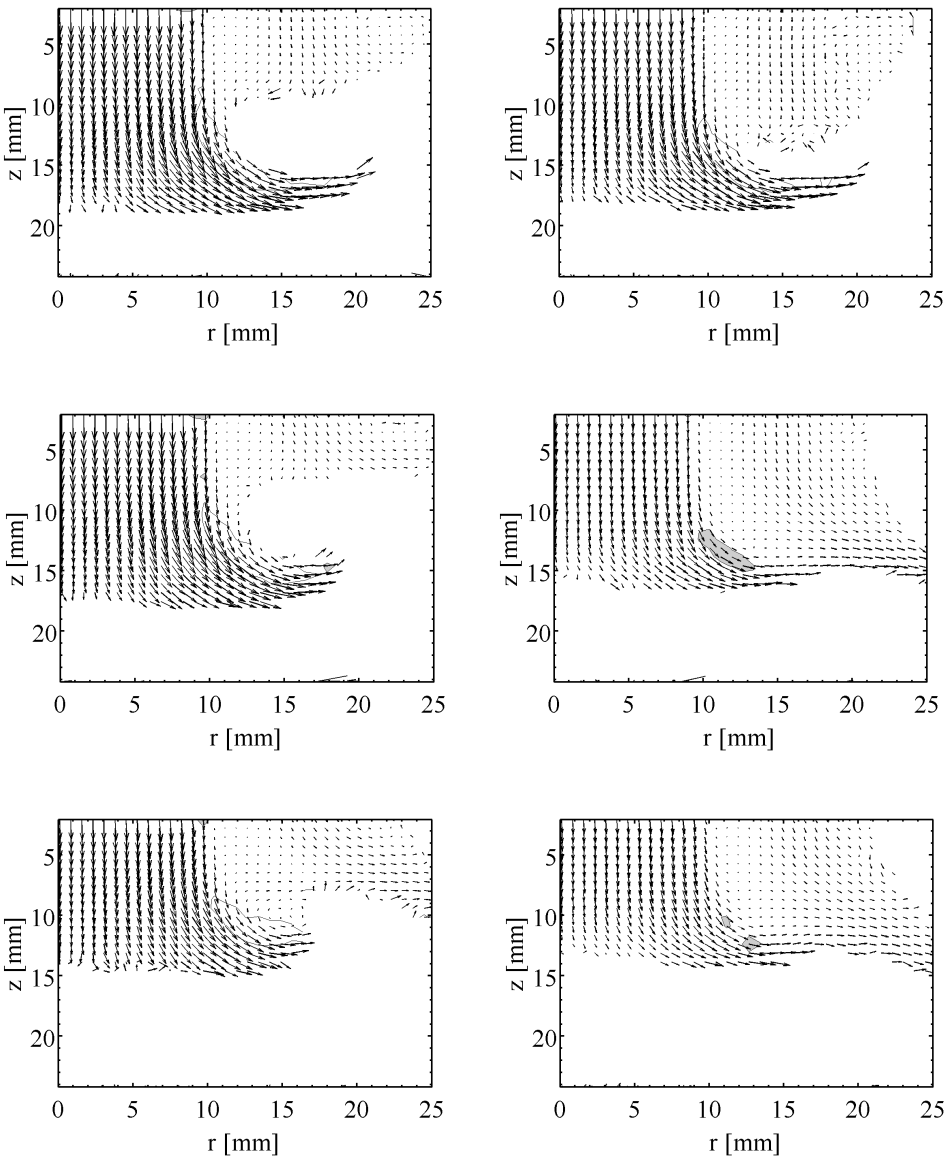

Figure 3.11: Velocity and swirling strength λ_{ci} fields calculated in the flame P configuration for a forcing frequency $f = 10$ Hz - A whole cycle is described clockwise.

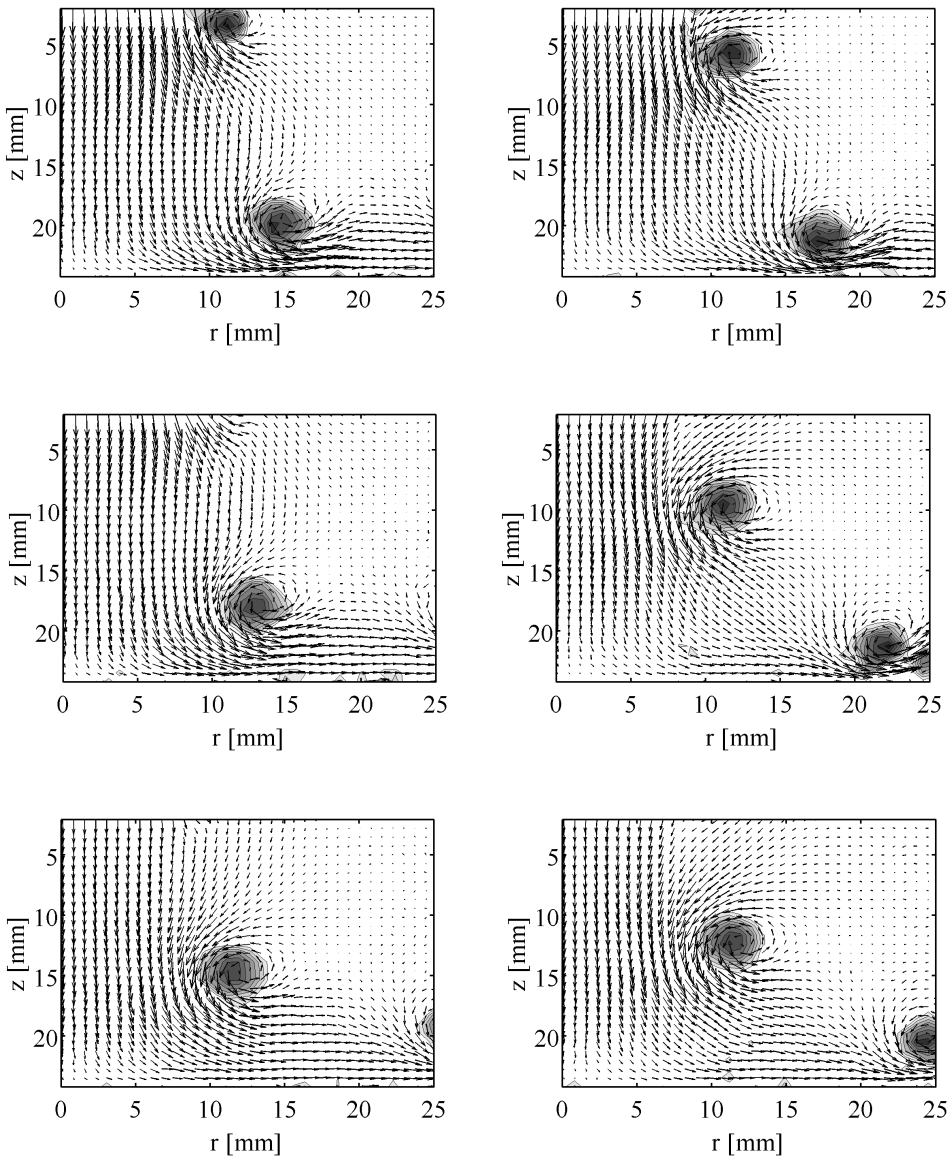

Figure 3.12: Velocity and swirling strength λ_{ci} fields calculated in the inert configuration for a forcing frequency $f = 51$ Hz - A whole cycle is described clockwise.

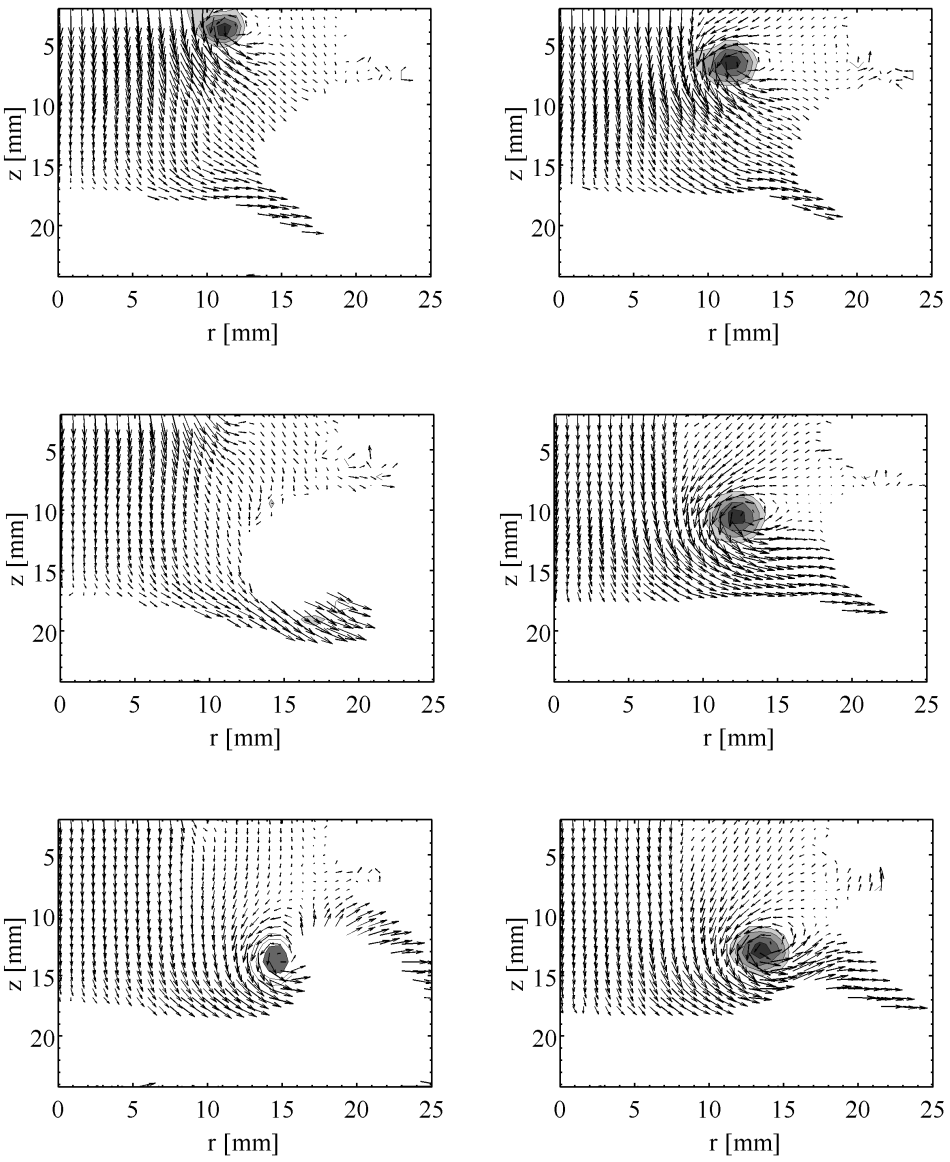

Figure 3.13: Velocity and swirling strength λ_{ci} fields calculated in the flame P configuration for a forcing frequency $f = 51$ Hz - A whole cycle is described clockwise.

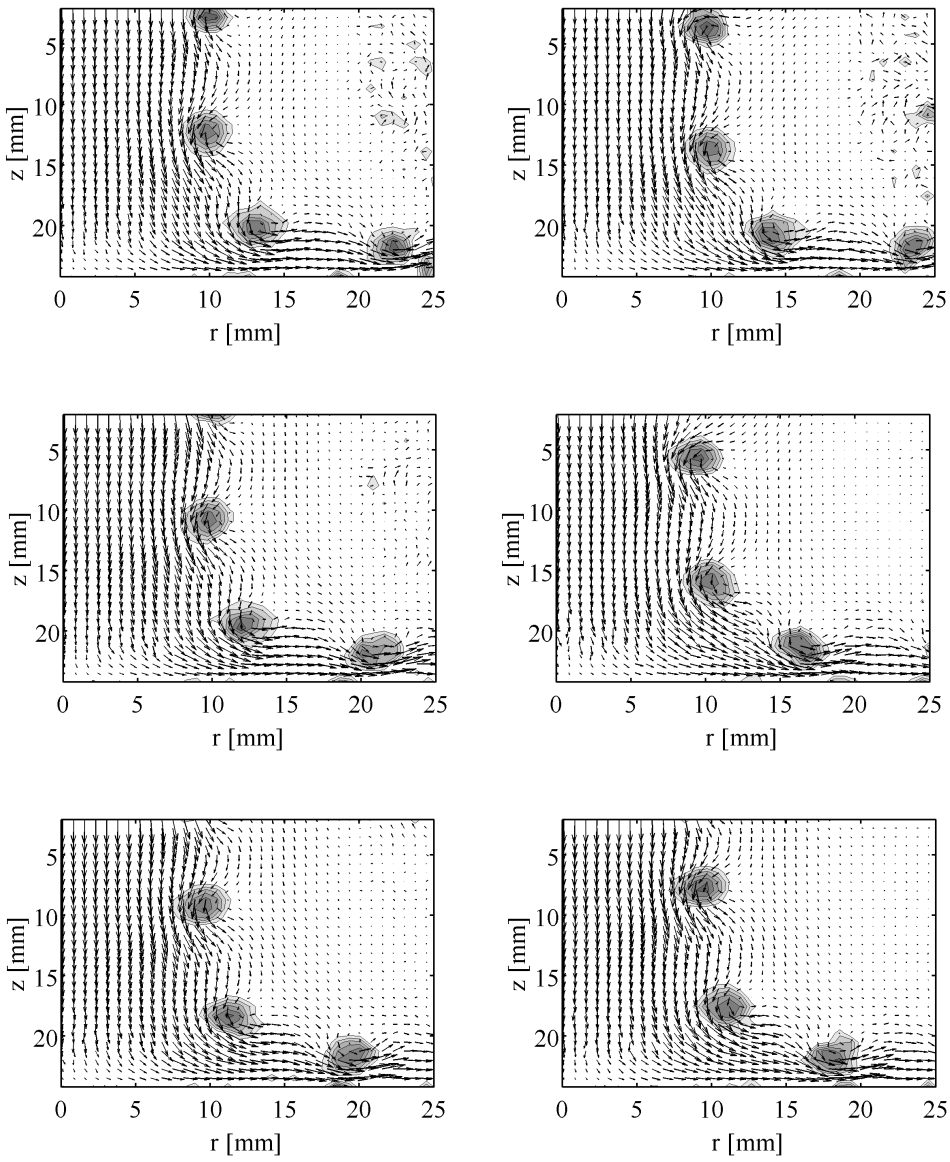

Figure 3.14: Velocity and swirling strength λ_{ci} fields calculated in the inert configuration for a forcing frequency $f = 102$ Hz - A whole cycle is described clockwise.

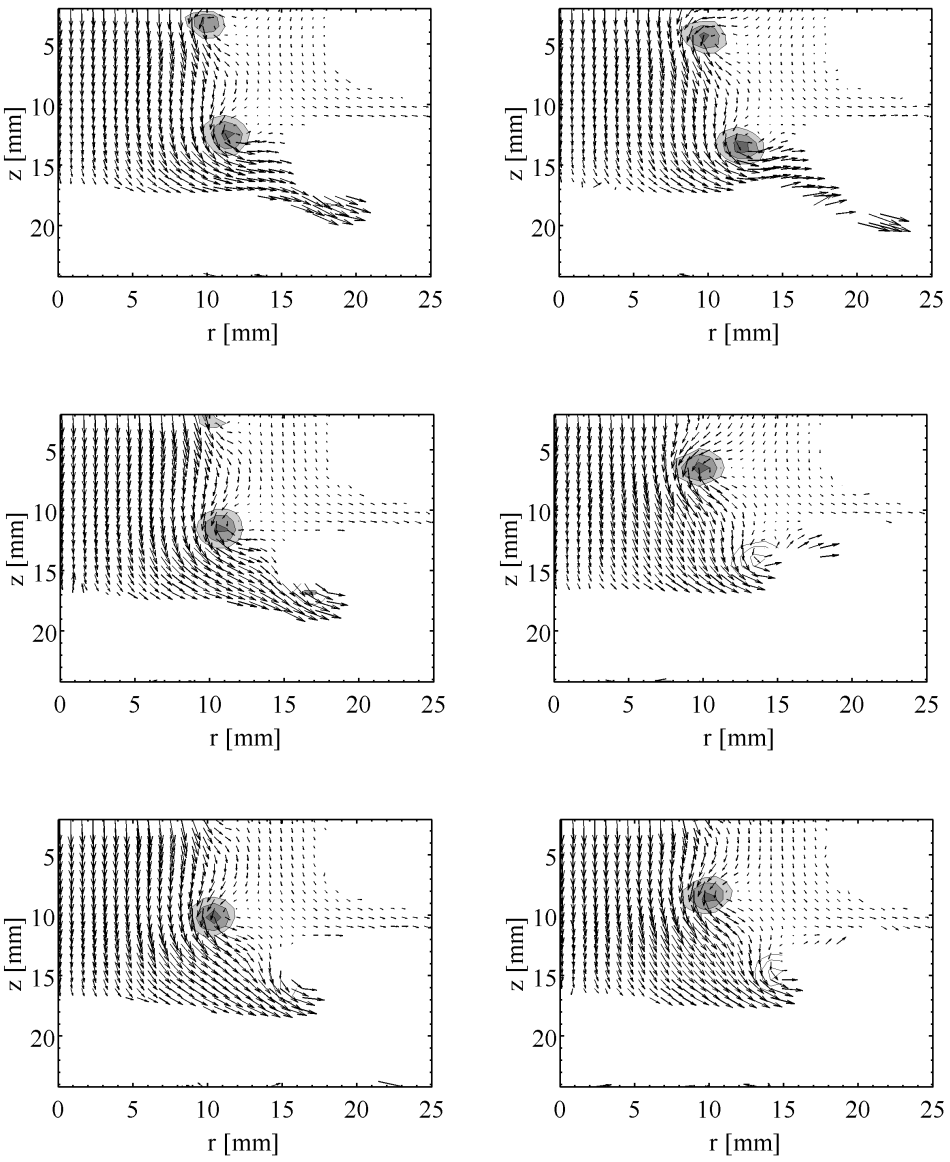

Figure 3.15: Velocity and swirling strength λ_{ci} fields calculated in the flame P configuration for a forcing frequency $f = 102$ Hz - A whole cycle is described clockwise.

Measurements for a modulation at $f = 10$ Hz in figures 3.10 and 3.11 in the inert and reactive configurations show that there is no coherent structure in this case. The flow field keeps the same general structure with vectors lined up in the same direction with a slightly varying amplitude during the modulation cycle. For a higher forcing frequency $f = 51$ Hz, one or two large vortices are present in the flowfield and are convected along the shear layer between the central flow and the surrounding annular flows (figures 3.12 and 3.13). The velocity vectors enrol around these pockets which symbolize the center of the vortex ring. For higher forcing frequency $f = 102$ Hz, three to four structures of smaller sizes are convected from the burner tip towards the plate as shown in figure 3.14.

Figures 3.11, 3.13 and 3.15 show the interactions of these vortex rings with flame P. In these images, the boundary between seeded and unseeded flows corresponds to the evaporation front of micronic oil droplets. The temperature gradient close to the flame front is very sharp and the flame position can be estimated using this location. The same observations can be made as for the tomographic and chemiluminescence images. For example, one notices that at $f = 10$ Hz, the vertical position of the flame features large oscillations but its shape remains quite flat. PIV data bring some more pieces of information on the interaction of vortices with the flame. For a modulation at $f = 51$ Hz, a vortex ring is shed from the burner lips. It is then convected by the flow, it interacts with the flame front where it bends the flame at the periphery towards the top and it also modifies the local flow structure near the burner axis. For a higher modulation frequency $f = 102$ Hz, vortex rings of a smaller size are shed away and their influence at the flame periphery is reduced. For this forcing frequency, the flame front close to the burner axis feature no vertical motion.

These PIV data are now used to obtain some quantitative information on the sizes of vortex cores generated. The definition of the radius of a vortex core can be introduced using the Lamb-Oseen vortex model (Saffman (1995)). In this model, a vortex is characterized by two parameters: a circulation Γ (m^2 s^{-1}) and an effective radius σ (m) related to the core radius σ_c. The azimuthal velocity v_θ and vorticity Ω induced at a distance r from the vortex center can be written in a polar coordinates system as:

$$\begin{cases} v_\theta(r) &= \dfrac{\Gamma}{2\pi r}\left[1-\exp\left(-\dfrac{r^2}{\sigma^2}\right)\right] \\ \Omega(r) &= \dfrac{\Gamma}{2\pi\sigma^2}\exp\left(-\dfrac{r^2}{2\sigma^2}\right) \end{cases} \tag{3.6}$$

These normalized components are plotted in figure 3.16.

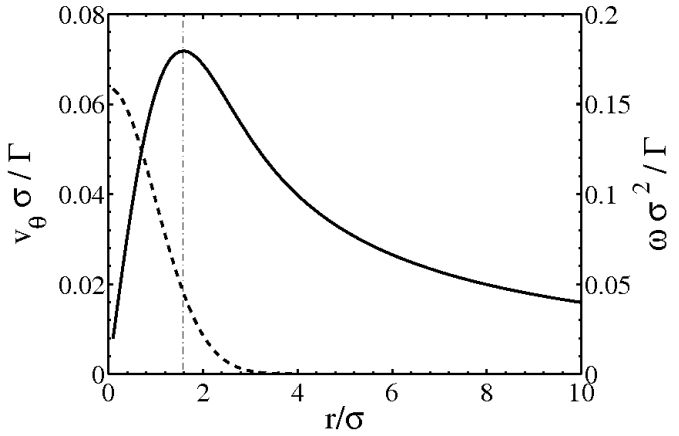

Figure 3.16: Profiles of azimuthal velocity (solid line) and vorticity (dashed line) induced by a Lamb-Oseen vortex.

A commonly used convention is to define the radius of the vortex core σ_c as the radial location corresponding to the maximal azimuthal velocity v_θ. The core radius σ_c is indeed the distance over which the hydrodynamical influence of the vortex is maximal. At a distance of three to four core radii σ_c, the influence of the vortex has significantly decreased.
In the present configuration, estimations of vortex core radii σ_c are obtained from the swirling strength maps (figures 3.10 to 3.15) by taking the distance where the swirling strength λ_{ci} has been reduced by half compared to its maximal value. The measured values are gathered in table 3.2.

In the present configuration, the vortex radius core is constrained by several characteristic dimensions of the setup. An upper limit of the vortex core radius can easily be estimated for pulsating flows. Vortices convected by the flow with a mean velocity $\overline{v}_c$ are separated by a wavelength $\lambda = \overline{v}_c/f$ where f is the forcing frequency. The vortex core radius must therefore satisfy $2\sigma_c \leq \lambda$ (Birbaud et al. (2007)).

A rough estimate of the vortex convection velocity can be obtained for perturbed jets: $\overline{v}_c \simeq V/2$ where V is the mean flow velocity of the central outlet (Crow and Champagne (1971)). This yields the following condition for the maximal size:

$$\sigma_c^{th.} = \frac{\lambda}{2} = \frac{V}{4f} \tag{3.7}$$

Table 3.2 summarizes results obtained for three forcing frequencies $f = 10$, 51 and 102 Hz. Strouhal numbers $\mathrm{St}_D = fD/V$ are evaluated in this table using the mean flow velocity V and the central jet outlet diameter D. The maximal value of the vortex core radius $\sigma^{th.}$ that can be generated in this setup is also reported. The value of the vortex core radius σ^{exp} measured from the swirling strength maps presented in figures 3.10, 3.12 and 3.14 is indicated in the last column.

f (Hz)	St_D	$\sigma_c^{th.}$ (mm)	σ_c^{exp} (mm)
10	0.13	40	-
51	0.65	8	5
102	1.3	4	3

Table 3.2: Strouhal number St_D of the central flow and core radius σ_c of the vortex ring for the three investigated forcing conditions - Estimation of core radius σ_c^{exp} is also given from PIV measurements.

At $f = 10$ Hz, the burner diameter $D = 20$ mm and the interspace $H = 24.2$ mm between the burner nozzle and the plate are too small and a vortex of radius $\sigma_c^{th.} = 40$ mm cannot develop. For a higher forcing frequency $f = 51$ Hz, a vortex may fully develop and the size of this vortex measured via PIV is a bit smaller than the maximal value expected. At $f = 102$ Hz, the diameter of the generated vortex is similar to the one expected. These values will be used later for further analysis.

Stretch modulation

Figure 3.17 shows the evolution of the radial velocity profiles along the radial direction. These measurements were conducted near the flame at a distance $z = 13$ mm away from the burner outlet and are also compared with measurements at the same location in the inert configuration. The flame remains below the location $z = 13$ mm during the whole modulation cycle, and consequently the flow is always seeded around this location.

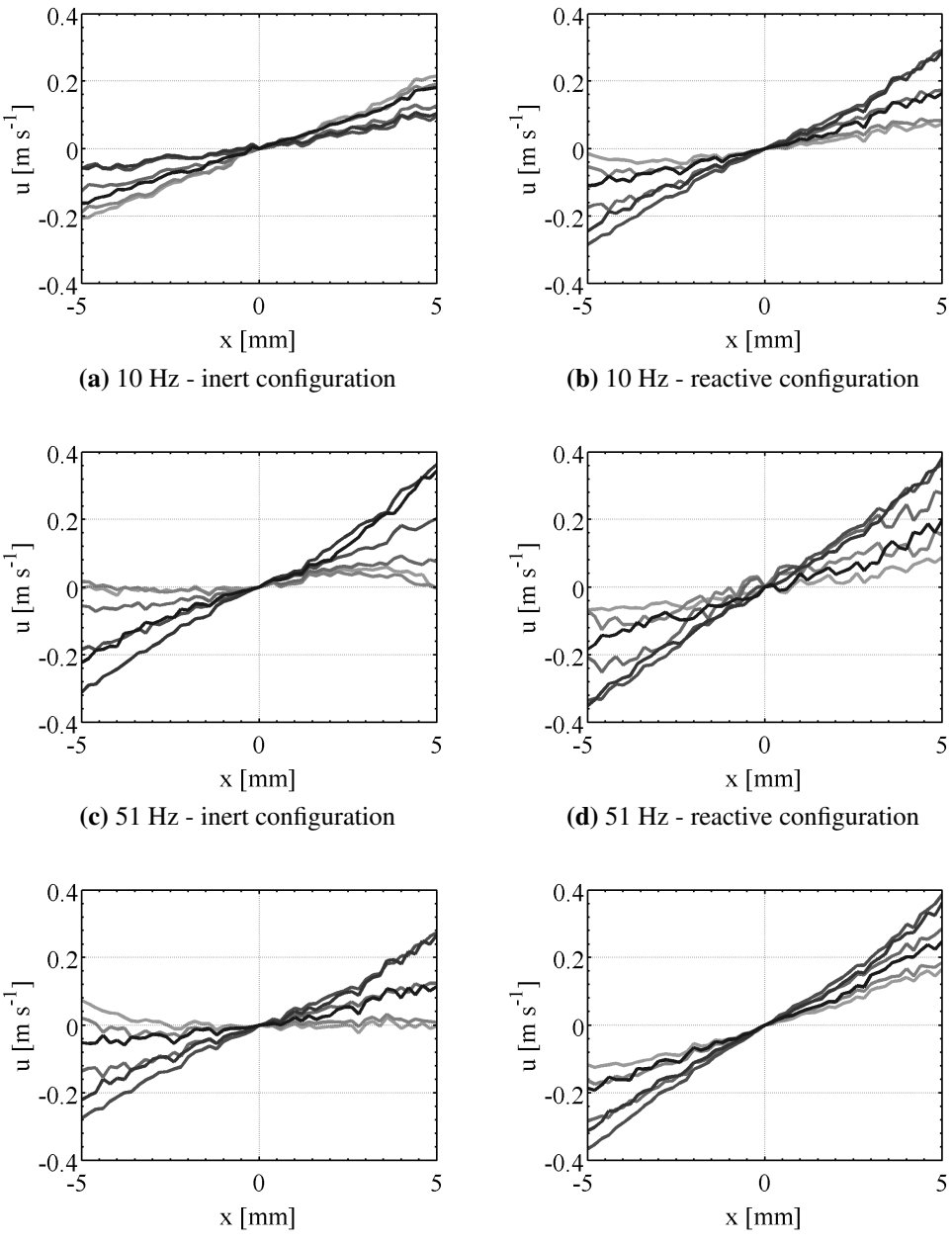

(a) 10 Hz - inert configuration

(b) 10 Hz - reactive configuration

(c) 51 Hz - inert configuration

(d) 51 Hz - reactive configuration

(e) 102 Hz - inert configuration

(f) 102 Hz - reactive configuration

Figure 3.17: Radial profiles of the radial velocity component around the burner axis at $z = 13$ mm - Different grayscales (from light to dark) represent phased-averaged values at six equally distributed instants in the modulation cycle.

Figure 3.17 shows that the instantaneous radial velocity is almost proportional to the burner distance. The amplitude of stretch modulation along a cycle is closely dependent on the forcing frequency and on the configuration. These data are now used to estimate the local stretch rate. The stretch rate ε for a planar flame is defined as the rate of change of the flame area A:

$$\varepsilon = \frac{1}{A}\frac{dA}{dt} \tag{3.8}$$

In a stagnation flow configuration, the stretch rate can be expressed as (Sun et al. (1999)):

$$\varepsilon(t) = \frac{du}{dr}(t) \tag{3.9}$$

Using the assumptions made on the flow structure in equation 3.2, the stretch can also be expressed as the radial reduced velocity:

$$\varepsilon(t) = U_r(t) \tag{3.10}$$

One can estimate the values of the stretch rate ε for the different configurations explored at $z = 13$ mm using figure 3.17. These data can be used to calculate the mean value $\overline{\varepsilon}$ and the relative root mean square fluctuation levels ε_{rms} / $\overline{\varepsilon}$ in the inert and reactive configurations for the three forcing frequencies $f = 10$, 51 and 102 Hz and also for the steady reactive flow. These values are reported in table 3.3.

Configuration	f [Hz]	$\overline{\varepsilon}$ [s^{-1}]	ε_{rms} / $\overline{\varepsilon}$	ε_{rms}[s^{-1}]
Inert	0 Hz	30.8	1.3 %	0.4
	10 Hz	28.1	36 %	10.1
	51 Hz	30.6	57 %	17.4
	102 Hz	22.9	76 %	17.4
Reactive	0 Hz	79.5	1.5 %	1.2
	10 Hz	33.1	32 %	10.6
	51 Hz	44.1	45 %	19.8
	102 Hz	49.1	26 %	12.8

Table 3.3: Mean values and fluctuation levels of the stretch rates in the inert and the reactive configurations for three forcing frequencies $f = 10$, 51 and 102 Hz and in the steady flow

One first notices that the presence of the flame stretches the flow as already indicated in figure 3.5. Values of the stretch rates are significantly higher in the reactive configuration than in the inert configuration. The significantly higher value found for the stretch rate in the steady configuration, $\varepsilon = 79.5$ s^{-1}, compared to the mean values found in the pulsated configuration can be linked to the position of the flame. The steady flame is located a bit closer to the burner outlet than its mean position in the pulsated flow. For the modulated cases at $f = 10$, 51 and 102 Hz, the relative fluctuation levels are of the same order of magnitude in the inert and reactive conditions.

Axial velocity profiles

Figure 3.18 presents axial velocity profiles measured by LDV in the fresh gases for flame P along a modulation period for the three forcing frequencies $f = 10$, 51 and 102 Hz.

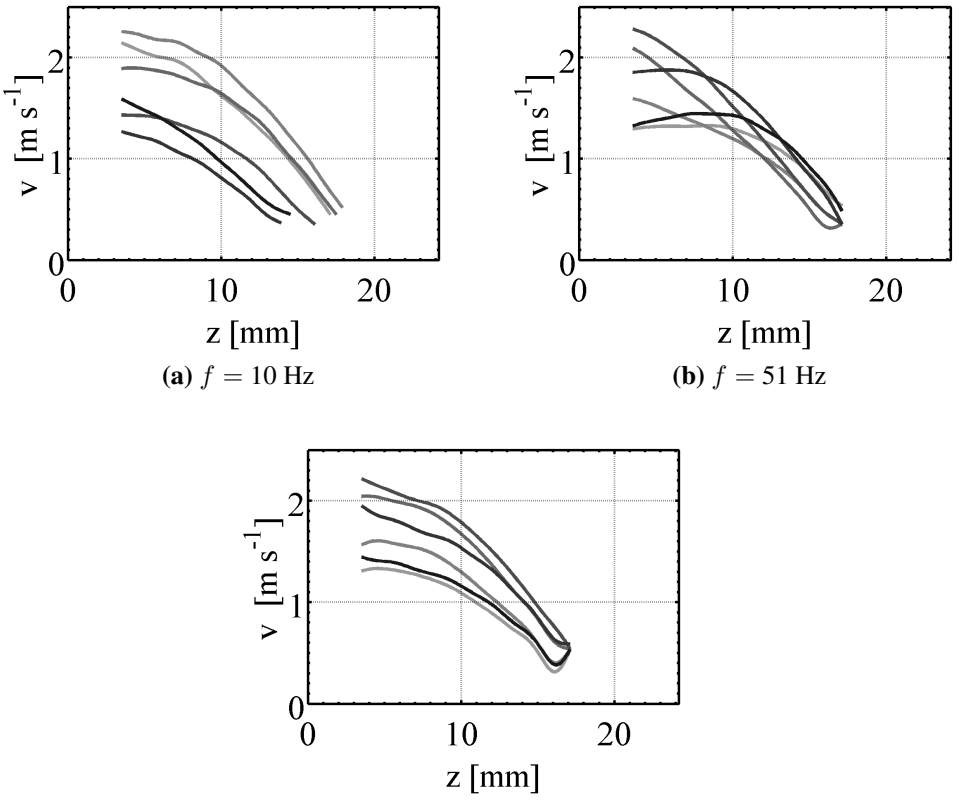

(a) $f = 10$ Hz **(b)** $f = 51$ Hz

(c) $f = 102$ Hz

Figure 3.18: Axial velocities measured by LDV in the fresh gases of flame P along a modulation period for a fluctuation level of $(v_{rms}/\overline{v})_R = 0.20$ measured at burner outlet - Different grayscales (from light to dark) represent phased-averaged values at six equally distributed instants in the modulation cycle.

Data are available from the burner outlet ($z_R = 3.$ mm) to the flame front location where micronic oil droplets evaporate. At $f = 10$ Hz, it can be inferred from figure 3.18a that the flame position varies significantly from $z = 14$ mm to $z = 18$ mm along the modulation cycle. The flow features a bulk oscillation without significant phase shift for velocity fluctuations along the burner axis because phase-averaged profiles are almost homothetic to the z-axis. At $f = 51$ Hz, the flame position remains almost steady and unaffected by the velocity perturbations generated at the burner outlet and the different phase-averaged profiles cross themselves indicating that flow perturbations features a phase difference from the burner outlet to the flame region. At $f = 102$ Hz,

the flame is steady and the phase-averaged profiles are here again homothetic along the x-axis indicating a bulk oscillation.

3.4.3 Propagation of flow velocity perturbations

It is interesting to analyse the propagation of the flow perturbations along the burner centreline. This aspect is indeed of interest for the choice of the boundary conditions to impose at the domain inlet for 1-D simulations. In many works (Darabiha (1992); Egolfopoulos (1994); Sung and Law (2000); Im and Chen (2000)), the axial velocity v at the domain inlet is set as a temporal harmonic fluctuation with a pulsation and an amplitude corresponding to the forcing condition and the reduced radial velocity $U_r = u/r$ is set to zero at this location.

$$\left\{ \begin{array}{rcl} v(z_R,t) & = & \overline{v}_R \left(1 + a \sin\left(\dfrac{2\pi t}{T}\right)\right) \\ U_r(z_R,t) & = & 0 \end{array} \right. \tag{3.11}$$

In this equation, $\overline{v}_R$ is the mean velocity at point R, a is the relative amplitude of oscillation and $T = 1/f$ their temporal period. Values for these parameters are deduced from velocity measurements carried out by LDV at point R. This type of boundary conditions sets a particular form for the propagation of the perturbations originating from the burner outlet. The present study brings into question this choice of boundary conditions. It is shown using detailed experiments that different propagation modes may be identified and consequences on the choice of adequate boundary conditions used to model these propagation modes are drawn. A comprehensive analysis about propagative modes is presented in this section.

Velocity measurements

The evolution of the axial velocity is characterized from the reference point R located on the burner axis at $z_R = 3.5$ mm (see figure 3.2) every $\Delta z = 0.2$ mm downstream on the burner axis using LDV. Measurements closer to the burner outlet cannot be performed with this technique because of the reflection of the laser beams on the solid parts of the burner. This is used to determine the propagation modes of velocity fluctuations generated at the burner outlet.

Time traces of the velocity signal are presented for the inert configuration in figure 3.19 for several driving frequencies $f = 10$, 35, 51, 63, 75 and 102 Hz

and at different locations along the z-axis. Measurements are synchronized together with the TTL signal from the signal synthesizer output. The bold curve indicates the velocity signal at point R. The other curves refer to axial velocity signals every $\Delta z = 2$ mm along the z-axis. For visual clarity, each curve in these plots is positively offset by 0.4 m s^{-1} relative to the previous one.
Measurements at a forcing frequency $f = 10$ Hz show that the fluctuation level imposed at the burner outlet (point R, $z_R = 3.5$ mm) slightly decreases along the z-axis in figure 3.19a. A slight positive phase shift between the different signals can also be noticed when the distance z increases. For a higher modulation frequency $f = 35$ Hz, a larger positive phase shift between these signals is observed with a higher attenuation of the fluctuation amplitude along the z-coordinate. At a forcing frequency of $f = 51$ Hz, time traces indicate a different behaviour. The velocity fluctuation level starting from a ratio of $(v_{rms}/\overline{v})_R = 0.20$ decreases dramatically down to the background noise level at about $z = 9$ mm. It then increases again to a significant higher value closer to the plate. Moreover, a slight positive phase shift between the velocity signals can be observed along the z-axis. Close to $z = 9$ mm where fluctuations cancel, a phase distortion occurs. The signal at $z = 11$ mm is nearly in phase opposition with that measured at $z = 7$ mm. A phase jump to about π can be observed. For higher distances, the regular increase of the phase shift takes place again. In figure 3.19d, measurements for a forcing frequency $f = 63$ Hz show that the fluctuation level reaches a minimum at about $z = 9$ mm from the burner outlet. In this case, the phase lag between successive velocity signals first decreases up to about $z = 9$ mm and then increases for larger distances $z \geq 11$ mm. For higher modulation frequencies $f = 75$ Hz and $f = 102$ Hz, this phase shift is very small and the fluctuation amplitudes decrease gradually along z-axis.

Results in the reactive configuration indicate the same general trend with similar regimes. The transition occurs in this case for a slightly higher forcing frequency $f = 63$ Hz than in the inert configuration $f = 51$ Hz.

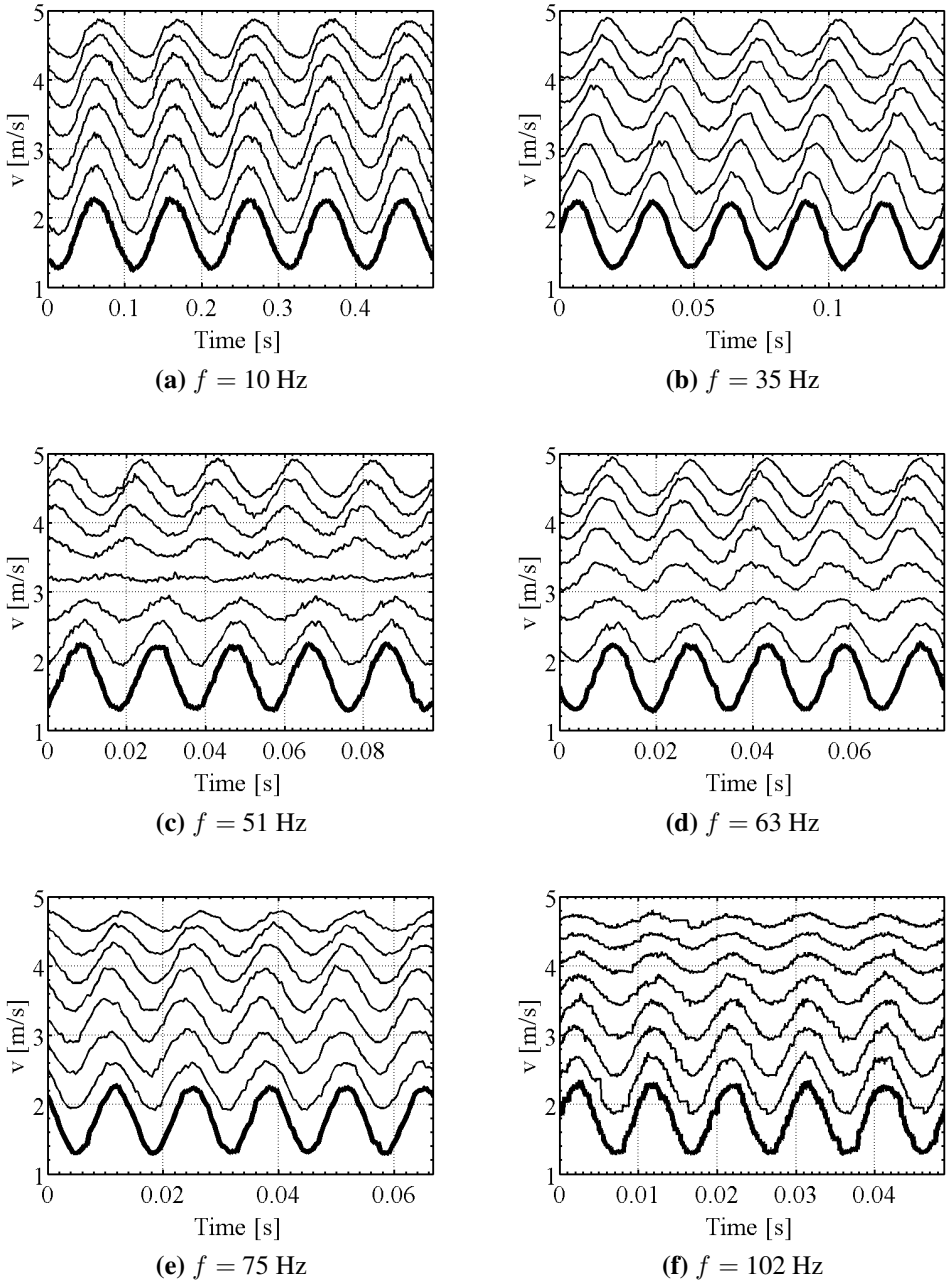

Figure 3.19: Samples of temporal velocity signals along burner z-axis in the inert configuration when the flow is modulated at different forcing frequencies $f = 10$, 35, 51, 63, 75 and 102 Hz. The bold curve indicates the velocity signal at point R ($z_R = 3.5$ mm). Each following curve refers to measurements separated by steps $\Delta z = 2$ mm along z-axis with a positively offset of 0.4 m s^{-1} relative to the previous one for clarity purposes.

This analysis is completed by an examination of the axial velocity profile along the z-axis for the different forcing frequencies. The evolution of the mean axial velocity $\overline{v}$ and the velocity fluctuation level v_{rms} are plotted in figure 3.20 as a function of the distance z from burner in the reactive and inert configurations. Mean velocity profiles are insensitive to the driving frequency. In the inert and reactive configurations, pulsated mean velocities along the axis exactly fit with the steady axial velocity profile as shown by the top plots in sub-figures 3.20a and 3.20b. In the reactive configuration, mean axial velocities decrease globally faster than in the inert configuration due to the presence of the flame.

Velocity fluctuations profiles feature different behaviours depending on the forcing frequency. One can observe two types of regimes. In the inert configuration, for a forcing frequency $f = 10$ Hz, the mean oscillation level decreases monotonically. At $f = 35$ and 51 Hz, the fluctuation level first decreases and reaches a minimum value respectively at $z = 8$ mm and $z = 10$ mm and then increases again with the z-coordinate. For higher forcing frequencies $f = 63$, 75 and 102 Hz, the evolution of the oscillation level is again monotonically decreasing with z-coordinate. In the reactive configuration, the same type of behaviour can be noticed with a shift of the mode transition frequency. For $f = 10$ Hz, the oscillation amplitude stays roughly constant till $z = 14$ mm before decreasing very sharply. For modulations at $f = 35$ Hz and 51 Hz, fluctuation levels decrease monotonically along z-axis. A transition occurs for the frequencies $f = 63$ and 75 Hz where the fluctuation levels reach a minimum at respectively $z = 8$ mm and $z = 10$ mm. Forcing at $f = 102$ Hz, the evolution of the fluctuation level is again monotonically decreasing. These different behaviours will be further analysed in the following sections.

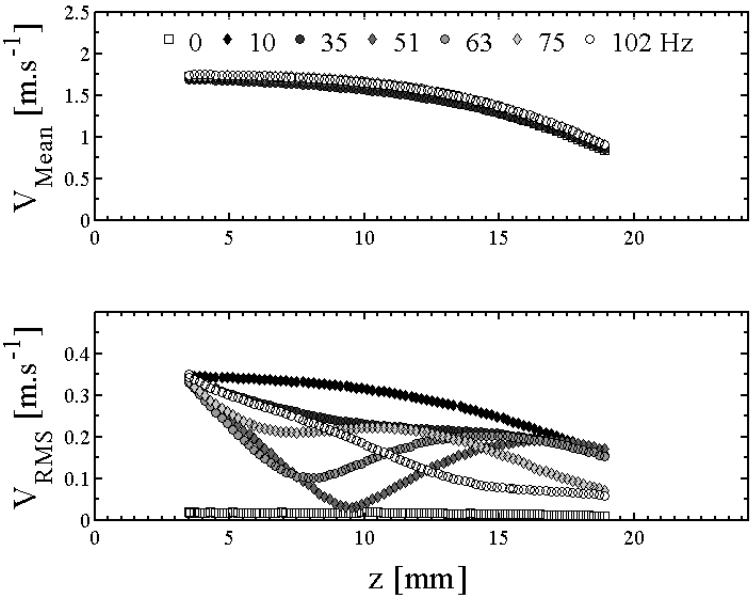

(a) inert configuration

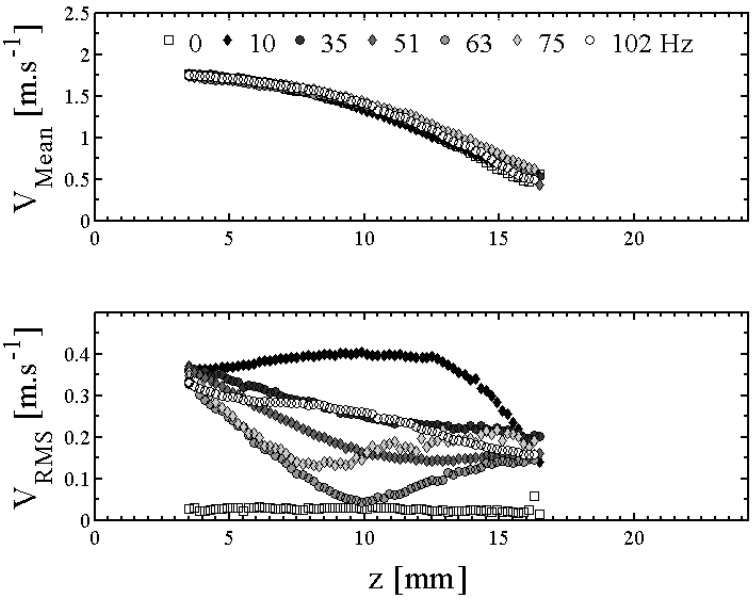

(b) reactive configuration

Figure 3.20: Evolution of mean value and fluctuation level of axial velocity for different driving frequencies $f = 10$, 35, 51, 63, 75 and 102 Hz along z-axis (measured by LDV) in an inert (a) and flame P (b) configurations. Measurements are carried out with $\Delta z = 0.2$ mm increments

Velocity transfer function

The analysis of the axial velocity along the burner centreline can be pushed forward by examining the transfer function between the velocity fluctuations along the burner axis. At each measurement point, a velocity transfer function F is defined between the velocity signal at the current point P at $z = z_P$ and the reference point R at $z = z_R$.

$$F(f) = \frac{S_{PR}(f)}{S_{RR}(f)} \tag{3.12}$$

where S_{PR} is the cross power spectral density between the velocity signals at locations R and P and S_{RR} is the auto power spectral density of the velocity signal at point R. These quantities are examined at the forcing frequency f to define the transfer function F.

The modulus of the power spectral density, often simply called spectrum of the signal, determines the power of the signal contained within a frequency band. In these experiments, the cross power spectral density of the discrete-time signals were calculated using the Welch's averaged, modified periodogram method with Hanning windows (Welch (1967)). In each window, a Fast Fourier Transform (FFT) is computed over at least 20 periods of the forcing signals. A 50 % overlap of windows was used to further improve statistic convergence. The Welch's averaged periodogram method is used for the estimations of these quantities to reduce the incoherent noise level. The gain G and phase φ at the forcing frequency f are defined by:

$$G = |F(f)| \text{ and } \varphi = \arg(F(f)) \tag{3.13}$$

If one considers purely harmonic velocity fluctuations at points R and P with a frequency f, respective amplitudes A_R and A_P and respective phases φ_R and φ_P, one can write:

$$\begin{aligned} v_R(t) &= A_R(t)\cos(2\pi f t + \varphi_R) = \Re\mathrm{e}\{A_R(t)\exp(-i(\omega t + \varphi_R))\} \\ v_P(t) &= A_P(t)\cos(2\pi f t + \varphi_P) = \Re\mathrm{e}\{A_P(t)\exp(-i(\omega t + \varphi_P))\} \end{aligned} \tag{3.14}$$

where $\Re\mathrm{e}\{\}$ denotes real part of the complex. The auto and cross power spectral density then simply write in the complex plane:

$$\begin{aligned} S_{RR}(f) &= A_R^2 \\ S_{PR}(f) &= A_R A_P e^{-i(\varphi_R - \varphi_P)} \end{aligned} \tag{3.15}$$

and the velocity transfer function $F(f)$ reads:

$$F(f) = \frac{A_P}{A_R} e^{-i(\varphi_R - \varphi_P)} \tag{3.16}$$

Consequently, the gain G and the phase φ respectively indicate the amplitude ratio and the phase lag of the velocity fluctuations examined at the forcing frequency f between points R and P.

$$G = |F| = \frac{A_P}{A_R} \text{ and } \varphi = \arg(\varphi_P - \varphi_R) \tag{3.17}$$

The evolution of the gain of the velocity transfer function is plotted in figure 3.21 along the z-coordinate in the inert and the flame P configurations. These plots have the same shape as for the evolution of the velocity fluctuation presented in figure 3.20. The only significant difference is that the gain value at $z_R = 3.5$ mm is now equal to 1, which is due to the definition of the transfer function.

It is more interesting to examine the phase of the velocity transfer function plotted in figures 3.22 and 3.23 versus z-axis for the six forcing frequencies in respectively inert and reactive configurations.

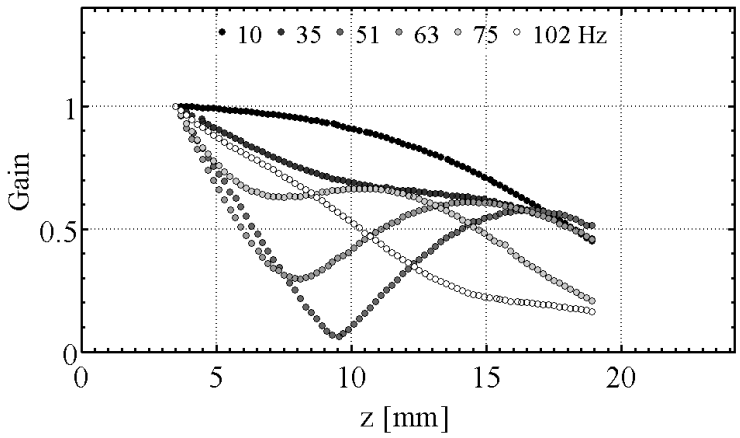

(a) Inert configuration

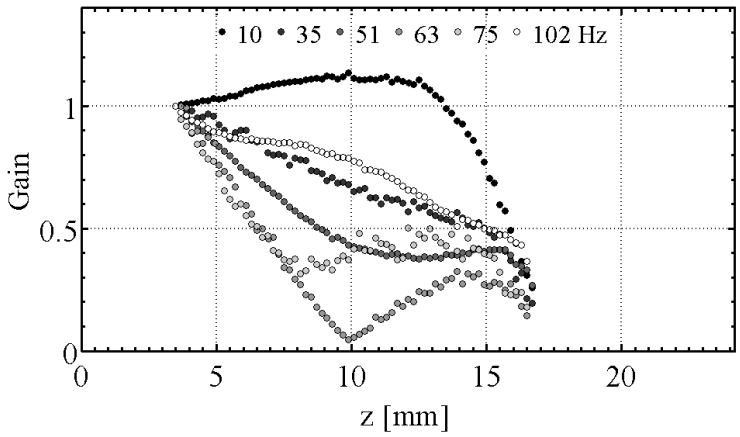

(b) Flame P configuration

Figure 3.21: Evolution of the gain of velocity transfer function versus z-coordinate at different driving frequencies in the inert (a) and flame P (b) configurations for a modulation level $(v_{rms}/\overline{v})_R = 0.20$.

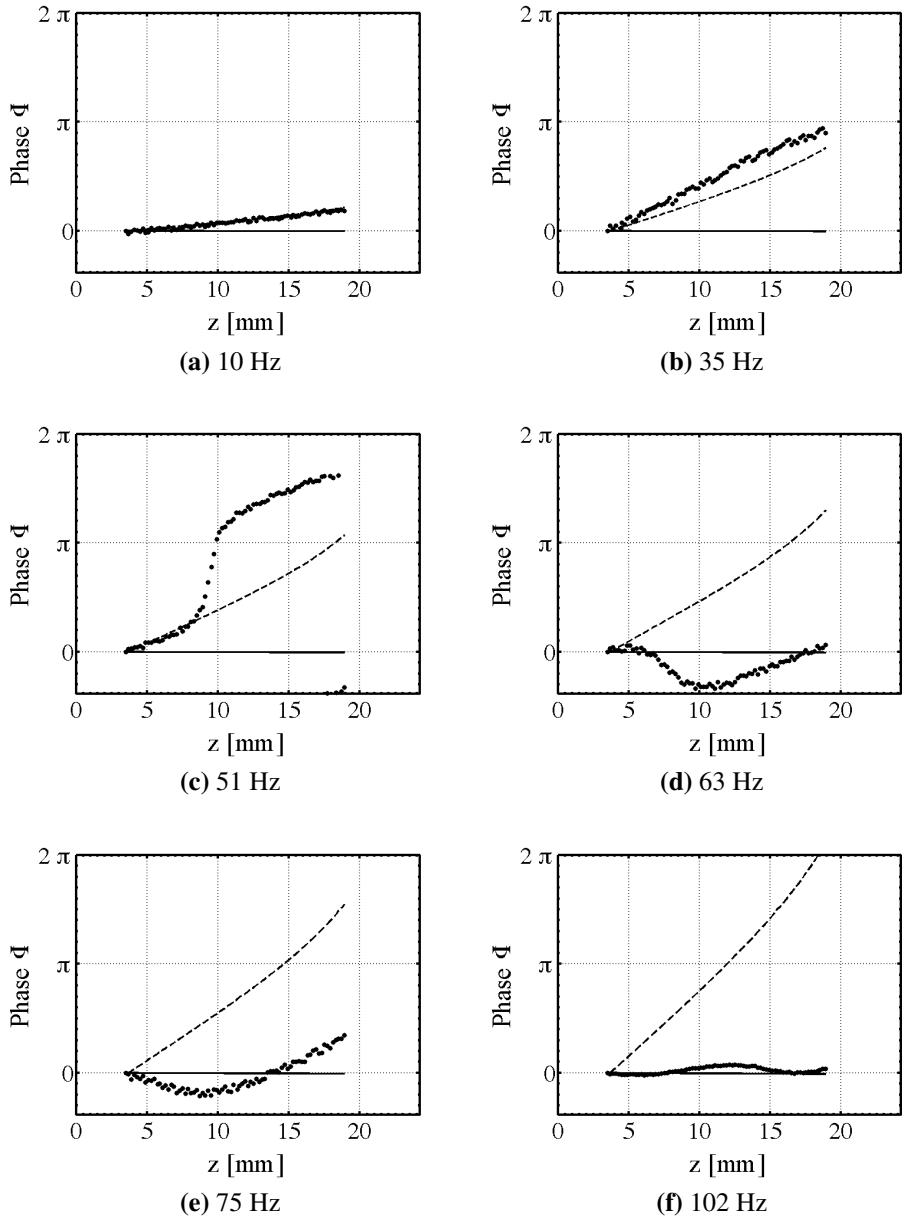

(a) 10 Hz **(b)** 35 Hz **(c)** 51 Hz **(d)** 63 Hz **(e)** 75 Hz **(f)** 102 Hz

Figure 3.22: Phase of velocity transfer function versus z-coordinate at different driving frequencies in the inert configuration (black dots). Pure acoustic propagation mode (solid line) and pure propagation convective mode (dashed line) are added.

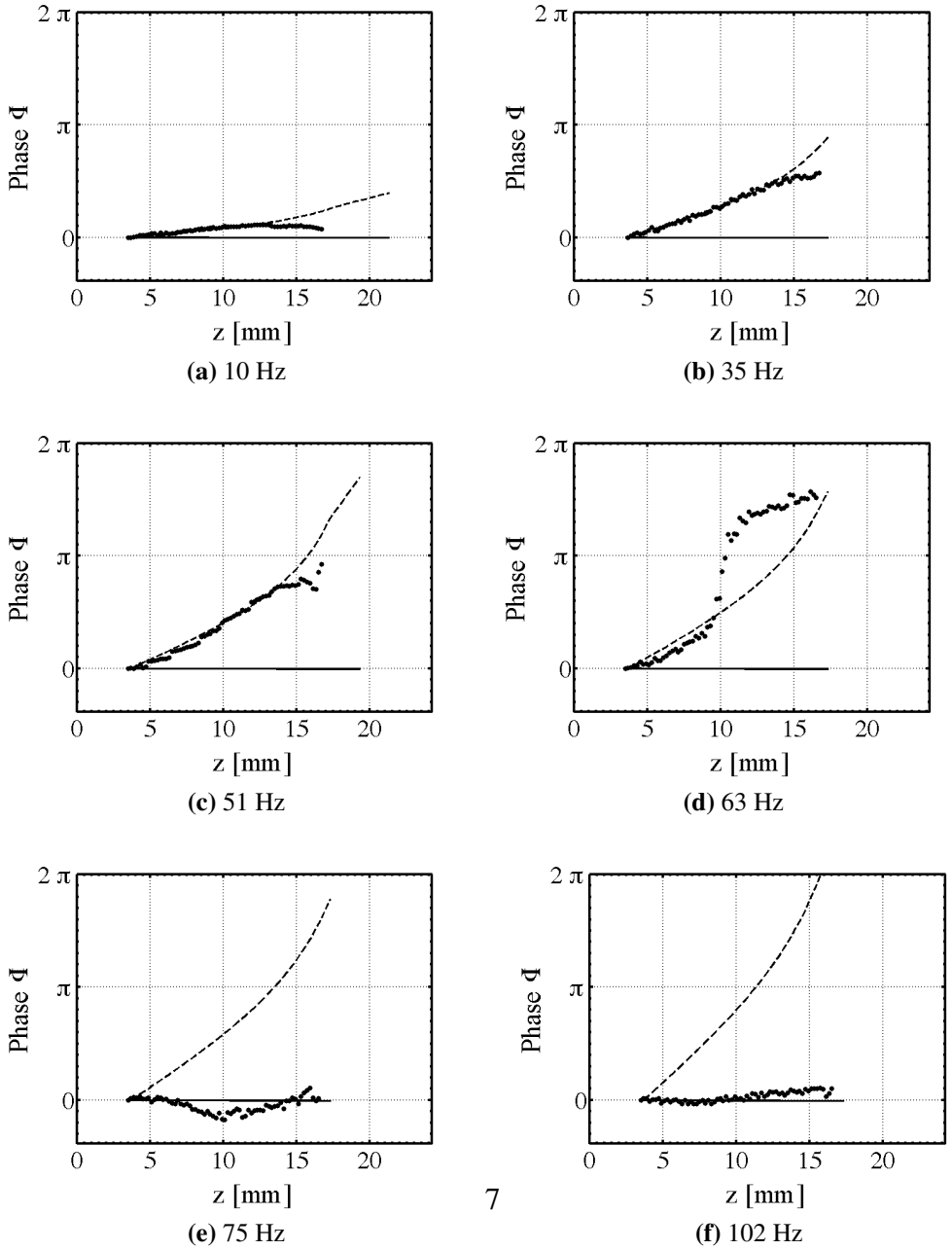

Figure 3.23: Phase of velocity transfer function versus z-coordinate at different driving frequencies in the flame P configuration (black dots). Pure acoustic propagation mode (solid line) and pure propagation convective mode (dashed line).

In the inert configuration, figure 3.22 shows that the phase lag between the velocity signals increases regularly with distance from the burner outlet for the forcing frequencies $f = 10$ and 35 Hz. This is well highlighted by an estimation of the convective phase lag $\Delta\varphi_{cv}$:

$$\Delta\varphi_{cv} = 2\pi f \int_{z_R}^{z_P} \frac{dz}{\overline{v}(z)} \tag{3.18}$$

where $\overline{v}(z)$ is the local mean axial velocity. These phase lags are indicated by the dashed lines in figures 3.22 and 3.23. It is worth noting that the reference phase is arbitrary and $\Delta\varphi_{ac}$ was set to zero at $z = z_R$. Data fit well these predictions $f = 10$ and 35 Hz.

For a modulation at $f = 51$ Hz, the phase lag follows the same trend for z-coordinate smaller than $z = 9$ mm. Between $z = 9$ and $z = 10$ mm, suddenly a transition occurs and the phase is rapidly shifted to a value close to π. After this transition, the phase evolves again regularly. This behaviour ceases at high frequencies. For $f = 63$ Hz, 75 Hz and 102 Hz, the phase lag roughly remains constant. It can be inferred for high modulation frequencies that the phase lag is principally determined by an acoustic time lag near the burner region determined by:

$$\Delta\varphi_{ac} = 2\pi f \int_{z_R}^{z_P} \frac{dz}{c} = 2\pi \frac{z_P - z_R}{\lambda_{ac}} \tag{3.19}$$

In this last expression, it is assumed that the temperature remains constant and consequently the sound speed $c(T)$ is also constant. These estimated acoustic phase lags are indicated by the solid lines in figures 3.22 and 3.23. Since the dimensions of the system are much smaller than the acoustic wavelength $H \ll \lambda_{ac}$, the phase lag $\Delta\varphi_{ac}$ takes vanishingly small values.

In the reactive configuration at forcing frequencies $f = 10$, 35 and 51 Hz, fluctuations of velocity roughly propagate according to the convective hypothesis as shown in figure 3.23. At $f = 63$ Hz, a similar behaviour as the one noticed at $f = 51$ Hz in the inert configuration appears. Velocity fluctuations propagate with a convective velocity close to the burner and close to the plate region while around $z = 9$ mm, a sudden phase shift close to a value of π occurs. At higher frequencies, at $f = 75$ and 102 Hz, the propagation of the velocity fluctuations fit to the acoustic model.

To sum up, the evolution of the phase of the velocity transfer function is very similar in the inert and reactive configurations. The general trends concerning

the propagation modes of velocity perturbations - convective at low frequency, acoustic at high frequency - remain the same. This type of behaviour has already been examined by Birbaud et al. (2007) for perturbed jet flow but the structure is here more complicated. The mode transition occurs for a higher forcing frequency in the reactive case due to the fact the flame modifies the flow structure.

These conclusions may be related to the plots of the axial velocity v along the burner centreline examined at different forcing frequencies presented earlier in figure 3.18. At $f = 102$ Hz, the acoustic wave is predominant, which explains the bulk oscillations upstream of the flame. At $f = 51$ Hz, the convective wave becomes significant and its wavelength is of the same order of magnitude as the dimensions of the system ($\lambda_{cv} = \overline{v}_c/f \simeq 25$ mm) and non uniform flow perturbation may settle. At $f = 10$ Hz, the convective wave is dominant but its wavelength is larger than the dimensions of the system ($\lambda_{cv} = \overline{v}_c/f \simeq 125$ mm). As a consequence, it is expected that the flow moves uniformly in the viewfield as observed in figure 3.18a. These plots show that the different modes of propagation identified for the velocity perturbations have noticeable consequences on the flow structure in the central flow region between the burner outlet and the plate.

3.4.4 Mode decomposition

This section aims at explaining the different propagation modes observed along the burner centreline. For this purpose, the velocity is decomposed into several components. The focus is first put on the mechanisms of vortex shedding at the burner outlet.

Vortex shedding at burner outlet

It is known from studies on jet dynamics that vortices are more likely to develop at preferential frequencies corresponding to a Strouhal number of about 0.5 (Crow and Champagne (1971)). In more recent works of Gutmark and Ho (1983), preferential frequencies of an axisymmetric jet are found to occur for jet Strouhal numbers St_D varying between 0.24 and 0.64. This mechanism is similar to the one identified in Birbaud et al. (2007) for the response of air jet to acoustic modulation. The authors have shown that the different regimes for the flow perturbations can be analysed as a function of two Strouhal numbers, one is the jet Strouhal number $\mathrm{St}_D = fD/V$ based on the nozzle diameter D and the second one is the shear layer Strouhal number $\mathrm{St}_\theta = f\theta/V$ based on

shear layer momentum thickness θ. They found that in the low jet Strouhal limit, the motion is dominated by a convective mode associated with large coherent structures induced by the modulation. In an intermediate range, the motion is of mixed type featuring an acoustic mode in the vicinity of the nozzle and then a convective mode further from burner lips. This is because the shear layer thickness between the jet and the surrounding flow increases with distance to burner outlet. For high jet Strouhal numbers St_D, a pure acoustic propagation is observed.

In the present configuration, considerations on the flow structure lead to similar conclusions. The focus is put on the available space for the development of coherent structures in the present experimental setup. The growth of vortex rings is limited by the outlet diameter D, by the distance λ between two successive vortex ring and by the presence of a plate located at a distance H from the burner nozzle. In figure 3.24, a train of vortex rings shed at burner mouth is represented. The center of the vortex ring moves with a velocity v_c, the induced azimuthal velocity by the vortex at a given distance from vortex center is noted as v_θ, the radius of the vortex core is noted σ_c.

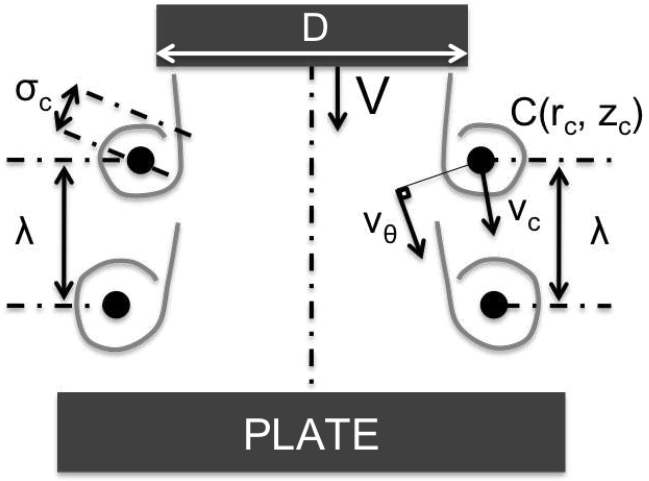

Figure 3.24: Vortex rings shed from the burner rim - The radius of vortex σ_c is limited both by the distance between two successive trains of vortices λ, by the outlet diameter D and by the distance H between the burner and the plate.

As explained in the previous section, the radius of vortices is limited by the available space between two successive vortex rings shed from the burner

when the flow is modulated at a forcing frequency f. Two vortices centers are indeed separated by a distance $\lambda_{cv} = \overline{v}_c/f$ with $\overline{v}_c$ being the mean velocity of the vortex ring. This condition implies: $\sigma_c \lesssim \overline{v}_c/(2\,f)$. As an approximation, one can set $\overline{v}_c$ as half of the mean flow velocity: $\overline{v_c} \sim 0.5\,V$ (Crow and Champagne (1971)). This yields the first condition:

$$\sigma_c \lesssim \frac{V}{4\,f} \tag{3.20}$$

Simultaneously, the size of a vortex ring is also limited by the size of the nozzle of diameter D:

$$\sigma_c \lesssim D/2 \tag{3.21}$$

In a flow stagnation configuration, the presence of the plate also limits the development of vortex:

$$\sigma_c \lesssim H/2 \tag{3.22}$$

The largest periodic structure that may settle should comply with these different constrains: $\sigma_c \lesssim min(V/(4f), H/2, D/2)$. In this setup, the relation $D/2 < H/2$ implies that the largest vortex cores are likely to develop in a flow where the relation $V/(4f_0) \simeq D/2$ is respected, i.e. for a Strouhal number:

$$\mathrm{St}_D = \frac{f_0\,D}{V} \sim 0.5 \tag{3.23}$$

In the present configuration, this yields a transition frequency f_0 between a bulk flow and a flow with periodically vortex rings shed at burner mouth for:

$$f_0 = \frac{\mathrm{V}}{2D} \sim \text{ 40 Hz} \tag{3.24}$$

It is difficult to get a more precise value for this transition. An improved analysis should include the true vortex convection velocity which can significantly differ from the previous estimation when the nozzle to plate distance is reduced. It should also take into account the flame inhibiting effect on the vortex formation. These parameters are difficult to model and this is beyond the scope of the present study.

As a conclusion, for frequencies smaller than the transition frequency $f \lesssim f_0$, i.e. for St $\lesssim$ 0.5, the development of a vortex interferes with the limited dimensions of the system and no vortex can not fully develop. For frequencies higher than the transition frequency $f \gtrsim f_0$, i.e. for St $\gtrsim$ 0.5, a vortex ring can fully develop and be convected by the flow.

Velocity field structure

This subsection aims at explaining the different propagation modes observed along the burner centreline. For this purpose, it is assumed that the axial velocity on the burner axis can be decomposed into three contributions: the steady velocity, an acoustic wave and a convective wave. The velocity $v(z,t)$ at time t and located at point P(0, z) is the sum of these three contributions:

$$v(z,t) = \overline{v}(z) + v_{cv}(z,t) + v_{ac}(z,t) \tag{3.25}$$

with:

$\overline{v}(z)$ being the velocity at P(z) of the steady flow

$v_{cv}(z,t)$ being the velocity induced by a convective wave at P(z) at instant t

$v_{ac}(z,t)$ being the velocity induced by the acoustic wave at instant t

The convective wave on the centreline axis results from the influence of the vortex ring shed at the burner outlet and convected along the burner axis. This wave has thus a propagation velocity along the z-axis corresponding to projection of the axial ring velocity along this axis. The acoustic component v_{ac} should be very little dependent on z-coordinate because acoustic wavelengths are much larger than the different dimensions of the system. Therefore, this component can be considered constant in the frequency range explored. The possible reflection of the acoustic wave on the plate would also generate a constant wave along the z-axis. As a result, this reflected wave may also be included in the acoustic contribution v_{ac}.

Two limit cases can be pointed out. In the first mode, acoustic perturbations prevail $v_{ac} \gg v_{cv}$. In the second, convective perturbations prevail when $v_{cv} \gg v_{ac}$. This decomposition is used to analyse the propagation of velocity perturbations along the burner axis in the present section.
The case for a modulation frequency $f = 10$ Hz is first examined. The maximum vortex core radius produced at each modulation period was estimated about $\sigma_c \simeq 40$ mm (see table 3.2), indicating that the vortex is large compared to the exhaust diameter $D = 20$ mm. It cannot therefore fully develop but has however an important influence on the flow along the burner axis. In this case, the convective contribution on the burner axis is predominant over acoustic contribution $|v_{ac}| \ll |v_{cv}|$ and equation 3.25 can be simplified as:

$$v(z,t) \simeq \overline{v}(z) + v_{cv}(z,t) \tag{3.26}$$

A convective propagation mode takes place on the burner axis for modulation at low frequencies, i.e. for Strouhal numbers St $\ll 0.5$.

For a higher forcing frequency of $f = 102$ Hz, the radius of vortices generated is about $\sigma_c = 4$ mm (see table 3.2), and is much smaller than the exhaust diameter $D = 20$ mm. Consequently the vortex ring produced in the shear layer has a minor, if not negligible, impact on the velocity flow field near the burner axis. As a result, the acoustic mode is prevailing ($|v_{ac}| \gg |v_{cv}|$). Equation 3.25 can be written as:

$$v(z,t) \simeq \overline{v}(z) + v_{ac}(z,t) \tag{3.27}$$

An acoustic propagation mode takes place on the burner axis at high forcing frequencies, i.e. for Strouhal numbers St $\gg 0.5$.

For intermediate modulation frequencies, contributions of the convective and acoustic components are of the same order of magnitude and can therefore create constructive or destructive interferences. These regimes occur for Strouhal numbers St ~ 0.5.

In the reactive case, the conclusions are slightly modified. As commented earlier in figures 3.17, the flame increases the mean stretch rate and it has globally the same effect as if the plate was closer. The transition frequency f_0 in the case of combustion is consequently higher than in the inert configuration. The evolution of the phase of the velocity transfer function is also shifted to higher frequencies in the reactive case. The phase shift of a value close to π, observed at $f = 51$ Hz without combustion, occurs at $f = 63$ Hz for the reactive flows (figures 3.22 and 3.23).

The scenario proposed in the present section is further investigated by decomposing the velocity fluctuation signals into their acoustic and convective contributions for the different forcing frequencies. The objective is to estimate the corresponding amplitudes and wavenumbers for the different contributions. These results are then discussed in relation to the flame transfer function.

First of all, it is worth examining whether a resonant mode may settle between the plate and the burner to explain the evolution of velocity fluctuations around $f = 51$ Hz in the inert configuration (see figures 3.20). Two types of low frequency resonances must be considered. The first one is a bulk oscillation when the burner responds as a Helmholtz resonator cavity featuring a bulk oscillation at $f_H = \omega_H/(2\pi)$ (Munjal (1987)):

$$\omega_H^2 = \frac{c^2.S}{V_c.L_c} \tag{3.28}$$

where $V_c = 0.7$ L is the volume of the cavity, $L_c \simeq 70$ mm is the length of the converging unit, $S = 314$ mm^2 is the surface of the burner exhaust and $c \simeq 330$ m s^{-1} is the celerity of the sound in the ambient air. This yields an oscillation frequency $f_H = \omega_H/(2\pi) \simeq 125$ Hz which is a value higher than the forcing frequency $f = 51$ Hz at which non monotonous evolutions of fluctuation level along the burner centreline is observed. As a consequence, Helmholtz resonance should not be invoked to explain the observed feature.

One could also consider that half- or quarter-wavelength modes set up between the plate and the top of the burner. The corresponding oscillation frequencies can easily be estimated knowing the system dimensions $f = c/(4L_b)$ or $c/(2L_b)$ where L_b is the distance between the plate and the bottom of the burner. For the three investigated frequencies $f = 10$, 51 and 102 Hz, the corresponding lengths L of the resonant tubes featuring a half- or a quarter-mode are reported in table 3.4.

f (Hz)	$L = c/(2f)$ (m)	$L = c/(4f)$ (m)
10	17	8.5
51	3.3	1.6
102	1.6	0.83

Table 3.4: Lengths of resonant tube versus the resonance frequency f for quarter- and half-wavelength modes.

These dimensions L are much larger than the distance from the plate to the burner outlet $H = 24.2$ mm or the distance between the plate and the bottom of the burner $L_b \simeq 20$ cm. These types of resonance can not therefore be evoked to explain the structure of the pulsated field observed in the region between the nozzle and the plate outlet for forcing frequencies lower than a few hundred Hertz.

Mode decomposition

The possibility of interferences between different propagating waves generated at the burner outlet is now investigated since resonance mechanisms based on the burner acoustic response cannot be responsible for the evolution of the gain of the transfer function. Inside the burner, the modulation with the loudspeaker generate fluctuations of the flow velocity which are of acoustic type only. Outside of the burner, the propagation mode is of mixed type with an

hydrodynamic field superimposed to the acoustic fluctuations. A part of the incident acoustic energy serves to generate a train of vortices in the shear layer between the central jet and the surrounding coflow, but the energy conversion is not complete and a substantial but unknown amount of acoustic energy remains in this flow (Noiray et al. (2009)). It is then logical to try to sort out the convective and acoustic components which form the velocity perturbation. Following a method proposed by Noiray et al. (2009), LDV measurements along the burner centreline are used to determine the respective convective and acoustic contributions. This method is briefly introduced.

The relative axial velocity fluctuation ratio $v'/\overline{v}$ on the centreline axis is considered in the following developments. The convective fluctuating component v_{cv} is induced by the vortex rings and is characterized by a convective wavenumber $k_{cv} = \omega/\overline{v}_{cv}$. The acoustic component v_{ac} features an acoustic wavenumber $k_{ac} = \omega/c$ and both perturbations are assumed to be harmonic $a' = \|a'\|e^{-i\omega t}$, ω being the forcing pulsation $\omega = 2\pi f$. The total velocity fluctuation is then given in the complex plane by:

$$\begin{aligned} v'/\overline{v}(z) &= v'_{ac}/\overline{v}(z) + v'_{cv}/\overline{v}(z) && (3.29)\\ &= A_{ac}e^{-i\omega t+ik_{ac}z+\varphi_{ac}} + A_{cv}e^{-i\omega t+ik_{cv}z+i\varphi_{cv}} && (3.30)\end{aligned}$$

In this expression, A_{ac} and A_{cv} stand for the acoustic and the convective fluctuation amplitudes and ϕ_{ac} and ϕ_{cv} stand for the acoustic and the convective phases. In this configuration, the mean axial velocity $\overline{v}(z)$ is strongly modified along the burner centreline. It is then preferable to work with relative velocity fluctuations $v'/\overline{v}(z)$. In the present situation, the geometrical dimensions are so small that the acoustic component can be considered uniform ($k_{ac}H \ll 1$). One can write:

$$v'(z,t)/\overline{v}(z) = A_{ac}e^{-i\omega t+i\varphi_{ac}} + A_{cv}e^{-i\omega t+ik_{cv}z+\varphi_{cv}} \quad (3.31)$$

Using this formulation, the objective is to extract the acoustic and convective components v'_{ac}, v'_{cv} and the convective wavenumber k_{cv} from measurements of the velocities $v'(z,t)$ and $\overline{v}(z)$ along the burner centreline. This may be done with the procedure summarized below and sketched in figure 3.25:

1. At several streamwise locations z_i on the central axis, the complex axial velocity v_i is reconstructed by taking the Hilbert transform of the real velocity signal.
$$v'_i = (A_{i,ac}e^{i\varphi_{ac}} + A_{i,cv}e^{ik_{cv}z_i+i\varphi_{cv}})e^{-i\omega t} \quad (3.32)$$
2. The resulting complex relative velocity fluctuation ratio is divided in a second step by $e^{-i\omega t}$ to obtain
$$v'_i/\overline{v}_i = A_{i,ac}e^{i\varphi_{ac}} + A_{i,cv}e^{ik_{cv}z_i+i\varphi_{cv}} \quad (3.33)$$

3. Taking values of the relative velocity fluctuations at three neighbouring points $v'_{i-1}/\overline{v}_{i-1}$, $v'_i/\overline{v}_i$ and $v'_{i+1}/\overline{v}_{i+1}$, and assuming that their acoustic and convective amplitudes as well as the convective wavenumber remain constant over the distance $z_{i+1} - z_{i-1}$, it is possible to analytically retrieve the amplitudes $A_{i,ac}$ and $A_{i,cv}$ by noting that the three values of $v'_i/\overline{v_i}$ belong to a common circle in the complex plane of center $A_{i,ac}$ and of radius $A_{i,cv}$. The center and radius of this circle can also be determined by means of the coordinates of three points that belong to the circle (figure 3.25).
4. The last unknown parameters $k_{i,cv}$, $\varphi_{i,cv}$, $\varphi_{i,ac}$ are easily calculated by substituting the values obtained in the previous step at three data points.

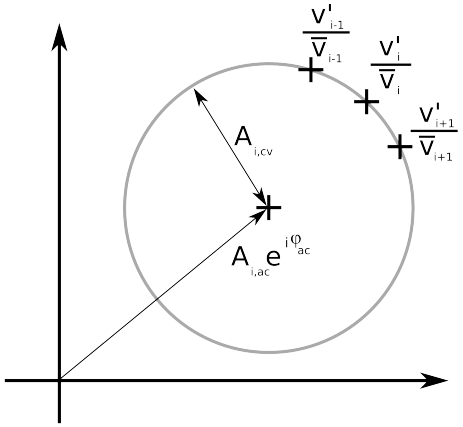

Figure 3.25: Mode decomposition for the convective and acoustic components. Three consecutive points are represented in the complex plane. The center of the circumscribed circle corresponds to the complex acoustic component $A_{i,ac}e^{i\varphi_{ac}}$ while its diameter corresponds to the modulus of the complex convective component $A_{i,cv}$.

This method can be used to obtain the acoustic and convective fluctuating velocity amplitudes as a function of the axial coordinate z. It is important to note that the choice of the axial locations z_i results from a compromise. On one hand if the spatial sampling z_i is too coarse, the assumption made at the third step of the process is not valid. On the other hand if the spatial sampling is too refined, the three points $v'_{i-1}/\overline{v}_{i-1}$, $v'_i/\overline{v}_i$ and $v'_{i+1}/\overline{v}_{i+1}$ are too close on the common circle and severe errors can be made in the determination of amplitudes of $A_{i,ac}$ and $A_{i,cv}$. It is not too difficult to adjust the parameters to obtain reliable results. The spatial increment was set constant and equal to $\Delta z = 2.4$, 0.8 and 0.2 mm for each forcing frequency $f = 10$, 51 and 102 Hz.

It is then possible to apply this procedure to the different configurations. Figure 3.26 presents temporal samples of velocity measurements (solid line) on the burner axis for two locations on the burner axis $z = 7$ mm and $z = 13$ mm, as well as acoustic (squares) and convective (disks) components extracted from these measurements for three forcing frequencies $f = 10$, 51, 102 Hz in the inert configuration. It has been checked that the sum of both acoustic and convective components corresponds exactly to the measured data.

One clearly notices that the convective component is prevailing at $f = 10$ Hz (figures 3.26a and 3.26b). At higher forcing frequencies at $f = 102$ Hz, the situation is different and the acoustic component is dominant (figures 3.26e and 3.26f). For intermediate frequencies, at $f = 51$ Hz (figures 3.26c and 3.26d), the behaviour is different. At $z = 7$ mm, the convective component is dominant, but at $z = 13$ mm, a transfer of energy operates and the acoustic component becomes half of the convective component amplitude.

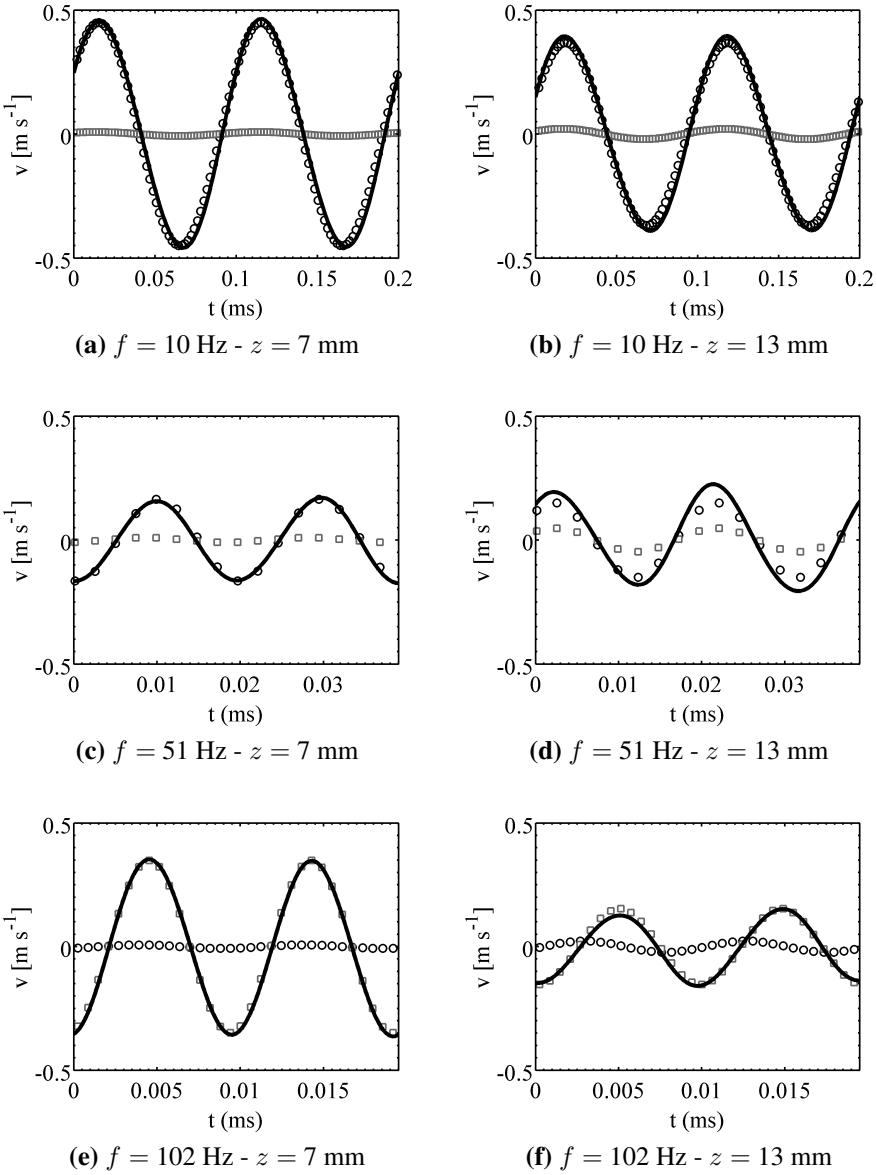

(a) $f = 10$ Hz - $z = 7$ mm

(b) $f = 10$ Hz - $z = 13$ mm

(c) $f = 51$ Hz - $z = 7$ mm

(d) $f = 51$ Hz - $z = 13$ mm

(e) $f = 102$ Hz - $z = 7$ mm

(f) $f = 102$ Hz - $z = 13$ mm

Figure 3.26: Time traces of relative velocity fluctuations measured by LDV (solid line), and their convective (circles) and acoustic contributions (squares) in the inert configuration. $f = 10$, 51 and 102 Hz, $(v_{rms}/\overline{v})_R = 0.20$.

This method is used to extract values of the amplitude A_{cv} of the convective wave, the amplitude of the acoustic wave A_{ac}, and the convective wavenumber k_{cv} for the forcing frequencies $f = 10$, 35, 51, 63, 75 and 102 Hz in the inert configuration and for flame P. These values slightly depend on the axial location z where they are determined (see figures 3.26c and 3.26d). However, only mean values averaged over the burner centreline axis are presented in this analysis. This is used to estimate the relative contribution between the acoustic and convective modes.

f (Hz)	A_{cv}	A_{ac}	A_{cv}/A_{ac}	k_{cv} (m^{-1})	$\overline{v}_{cv}$ (m s^{-1})
cold configuration					
10	0.42	0.02	18.7	42	1.5
35	0.32	0.02	15.5	200	1.5
51	0.20	0.06	3.31	374	1.1
63	0.21	0.17	1.22	-	-
75	0.11	0.18	0.64	-	-
102	0.02	0.23	0.07	-	-
flame P					
10	0.58	0.02	21.3	38.7	1.6
35	0.37	0.02	14.5	173	1.3
51	0.31	0.07	4.35	228	1.4
63	0.02	0.18	0.16	-	-
75	0.03	0.22	0.18	-	-
102	0.31	1.43	0.21	-	-

Table 3.5: Mean values of amplitudes A_{cv} of the convective wave, amplitudes A_{ac} of the acoustic wave, the ratio of amplitudes A_{cv}/A_{ac}, the convective wavenumber k_{cv} and the corresponding mean convective velocity $\overline{v}_{cv} = 2\pi f/k_{cv}$. These values are obtained using the mode decomposition procedure for forcing frequencies $f = 10$, 35, 51, 63, 75 and 102 Hz in the inert configuration and for flame P.

Values for the parameters k_{cv} and $\overline{v}_{cv}$, not reported in the table 3.5, correspond to cases where the results are not significant when the convective component is negligible. Except in some cases where the method is too approximate, this method yields interesting estimations of the relative importance of acoustic and convective components as function of the forcing frequency. It is clear that the convective mode is predominant for frequencies lower than $f = 51$ Hz, whereas the acoustic mode is predominant at high frequencies typically for $f = 102$ Hz. In the mid-range frequencies, the influence of both modes is comparable.

These results are consistent with the different evolutions observed for the phase of the velocity transfer function. It was however shown that convective and acoustic fluctuation components can be of the same order of magnitude. This means that destructive or constructive interferences may take place between these two components along the axis. The present decomposition is not robust enough to analyse the interference phenomenon that occurs for example at $f = 51$ Hz. This results mainly because strong interferences take place and the resulting fluctuation takes a so small level that the decomposition in convective and acoustic propagation modes is not possible. This method is also less reliable when the convective component becomes negligible because the determination of the circle radius becomes inaccurate. This model yields however general trends with success.

As a first conclusion, the processing of velocity measurements and imaging of the chemiluminescence of the flame enabled to draw some interesting conclusions on the flow and flame dynamics in this experimental configuration. The flame behaves as a low-pass filter for incoming flow velocity perturbations (Candel (2002)). The flame front location features large fluctuations at $f = 10$ Hz which reduces as the forcing frequency is increased. The flame front in the center region remains nearly around its steady location at $f = 51$ Hz and features no motion at $f = 102$ Hz. The modulation of the flow velocity generates vortex rings at burner outlet for forcing frequencies $f = 51$ and 102 Hz. These vortices are convected with the flow and mainly interact with the flame tips.
Analysis of the propagation modes of these velocity perturbations along the burner centreline highlights different behaviours at low and high Strouhal numbers. For a modulation $f = 10$ Hz, i.e for $\mathrm{St}_D < 0.5$, velocity perturbations propagate with a convective speed which value remains close to the flow velocity on the axis. For $f = 102$ Hz, i.e for $\mathrm{St}_D > 0.5$, velocity perturbations propagate at sound celerity. These propagation modes have been interpreted relative to the size of vortex ring shed at the burner lip. For $f = 10$ Hz, the formation of a large vortex at the burner outlet imposes its velocity along the burner axis. For $f = 102$ Hz, vortex rings shed at burner lips are too small to have a significant impact on burner centreline velocity and perturbations are dominated by acoustic waves. For intermediate forcing frequencies, convective and acoustic waves of similar amplitudes coexist. A decomposition of the velocity into its convective and acoustic contributions has been carried out to support this hypothesis.

3.4.5 Consequences for 1-D simulations

The consequences of these different propagation modes are now investigated for simulations of such a configuration with a 1-D numerical code. In numerical simulations, two formulations are classically adopted. It is possible to modulate the stretch rate (Im et al. (1996)) or to modulate flow velocity at the numerical domain boundaries (Kee et al. (1988); Dixon-Lewis (1991)). In the first formulation, it is assumed that the flow is generated infinitely far from the stagnation plane and therefore this type of simulations is difficult to use for comparisons with an experimental configuration where the distance between the burner outlet and the flame remains finite. The latter type of simulations with an imposed velocity at the domain inlet is thus considered in the present section.

In simulations carried out by imposing an unsteady flow velocity at boundaries (Ghoniem et al. (1992); Aguerre (1994); Lutz et al. (1996); Sun et al. (1996); Egolfopoulos and Campbell (1996)), the classical choice of boundary conditions consists in imposing the radial reduced velocity U_r at a constant null value, $U_r = 0$. One consequence of this choice of boundary condition is that velocity perturbations feature a plane wave structure and are uniform along the z-axis as shown later on in figure 3.27. In the mean time, the previous study showed that velocity perturbations may propagate at a convective velocity in some ranges of frequencies and are thus non uniform along the burner centreline. As a consequence, the classical choice of boundary condition is worth being discussed. Another possible choice of boundary condition is to impose also a modulated condition on the radial reduced velocity U_r. Consequences of this choice are investigated in this section.

Boundary conditions at the plate location are not affected by unsteadiness. They are the same as in the steady configuration presented in equation 3.3:

$$\begin{aligned} \frac{\partial T}{\partial z}(H,t) = \alpha(T - T_{plate}), \quad \frac{\partial Y_k}{\partial z}(H,t) = 0, \\ v(H,t) = 0, \quad U_r(H,t) = 0 \end{aligned} \tag{3.34}$$

with T the temperature, Y_k the mass fraction of the kth specie, v vertical velocity component and U_r the radial reduced velocity.

To simulate a pulsating flow, a uniform modulation is first considered at the

burner outlet at point R ($z_R = 3.5$ mm) and this takes the form:

$$\left\{ \begin{array}{rcc} v(z_R,t) & = & \overline{v}_R\left(1 + a\sin\left(2\pi f t\right)\right) \\ U_r & = & 0 \end{array} \right. \tag{3.35}$$

where $\overline{v}_R$ is the mean velocity, a the relative amplitude of oscillations and f the forcing frequency. These parameters are fitted to values obtained from velocity measurements at point R. The boundary condition in the radial direction is set to zero. This condition implies via the equation of mass continuity that velocity perturbations propagate uniformly within the numerical domain. This is shown in particular in simulations presented on the left side of figure 3.27.

Another possibility is to set a convective wave for velocity perturbations between the burner outlet and the plate (Baillot et al. (1992); Bourehla and Baillot (1998); Schuller et al. (2003b)). In this case, a convective wave on the burner axis featuring the following structure is imposed at point R:

$$v(z,t) = \overline{v}_R\left[1 + a\sin\left(2\pi f t - k_{cv}(z - z_R)\right)\right] \tag{3.36}$$

where $k_{cv} = 2\pi f/\overline{v}_R$ is the convective wavenumber. One can note that if $k_{cv}H \ll 1$, the previous equation is equivalent to equation 3.35. Equation 3.36 should also comply with mass continuity. This equation for an incompressible flow of constant mass density ρ can be written in the axisymmetric base (O,r,z):

$$\frac{\partial v}{\partial z} + \frac{1}{r}\frac{\partial}{\partial r}(r\ u) = 0 \tag{3.37}$$

Given the form of the velocity field introduced in equation 3.2, the mass continuity equation reads:

$$\frac{\partial v}{\partial z} + 2U_r = 0 \tag{3.38}$$

The radial component associated with axial fluctuations at the burner outlet is thus deduced by using the form proposed in equation 3.37 into this last expression. One obtains:

$$U_r(z_R,t) = \frac{1}{2}\ a\ k_{cv}\ \overline{v}_R\cos\left(2\pi f t\right) \tag{3.39}$$

This radial reduced velocity imposed at the point R location is compatible with a convective propagation of perturbations along the burner centreline.

Direction	Uniform boundary condition	Convective boundary condition
Axial	$v(z_R,t) = \overline{v}_R\,[1 + a\sin(2\pi f t)]$	
Radial	$U_r(z_R,t) = 0$	$U_r(z_R,t) = \dfrac{1}{2}\,a\,k_{cv}\,\overline{v}_R\cos(2\pi f t)$

Table 3.6: Two types of boundary conditions set at burner outlet at point R ($z_R = 3.5$ mm) in the axial and radial directions

Table 3.6 gathers the two sets of boundary conditions at the burner outlet in the axial and radial directions.

Simulations were carried out for the same flow conditions corresponding to the flame P configuration for these two types of boundary conditions by Dr. F. Laurent at Laboratoire EM2C. Figure 3.27 shows the results for the axial velocity profiles at different instants in the modulation cycle for three forcing frequencies $f = 10$, 51 and 102 Hz in case of the uniform or convective modulations at the inlet boundary.

Using the uniform modulation, simulations yield velocity perturbations which are in phase along the burner centreline for any forcing frequency investigated. The situation is different for the second type of boundary conditions. Velocity fluctuations along the burner centreline now feature a phase lag which increases with the forcing frequency. For a forcing frequency $f = 10$ Hz, the difference between simulations obtained with the convective and uniform models becomes negligible because the convective wavelength $\lambda_{cv} = \overline{v}_c/f$ becomes very large with respect to the burner to plate distance. At a mid forcing frequency $f = 51$ Hz, a discernible phase lag is clearly visible.

One can conclude that the choice of the type of boundary condition used to generate a perturbation has great consequences on the flow structure between the burner outlet and the plate. Differences between the predictions increase with the forcing frequency.

Figure 3.28 presents different axial velocity profiles obtained from simulations of flame P versus the z-coordinate with three forcing frequencies $f =$

10, 51 and 102 Hz. These simulations were carried out for convective and uniform models. There are no noticeable difference in the velocity profile and flame position between the two simulations at $f = 10$ Hz. This is in agreement with the previous discussion when the flow is in a bulk oscillation mode ($\lambda_{ac} \gg \lambda_{cv} \gg H$). At higher forcing frequencies, differences between the two simulations appear. The flow simulated with a uniform modulation at the boundary still features a bulk oscillation and the flame front executes an important oscillation along the z-axis. On the other hand, simulations obtained with the convective modulation exhibit waves in the different velocity profiles presented along the z-axis. The flame front located at $z \simeq 18$ mm remains almost steady. At $f = 51$ Hz, simulations yield intermediate results. The oscillation amplitude of the flame front motion is slightly higher with the uniform modulation than with the convective model. The instantaneous velocity profiles exhibit some fluctuations along the z-axis with the convective boundary condition while the flow moves as a bulk oscillation with the uniform boundary condition. These results should be compared with experimental results presented in figure 3.18.

We can note in these calculations that for any forcing frequency the flame position always features a slight oscillation of its location with the uniform or the convective model, except at $f = 102$ Hz for a convective modulation. This contrasts with measurements showing that the flame positions greatly fluctuates for $f = 10$ Hz, and does not fluctuate for higher forcing frequencies $f = 51$ and 102 Hz. This appears as a major limitation of these unsteady calculations that do not reproduce correctly the dynamical behaviour of the flame front location. This limitation prevents us from carrying out detailed comparisons between experimental results and simulations. However, the instantaneous velocity profiles (figure 3.28) show that a uniform boundary condition $U_r = 0$ can not be satisfactory both for low and high Strouhal numbers. This analysis shows that a convective boundary condition at domain inlet is necessary to better reproduce the flow and flame dynamics observed.

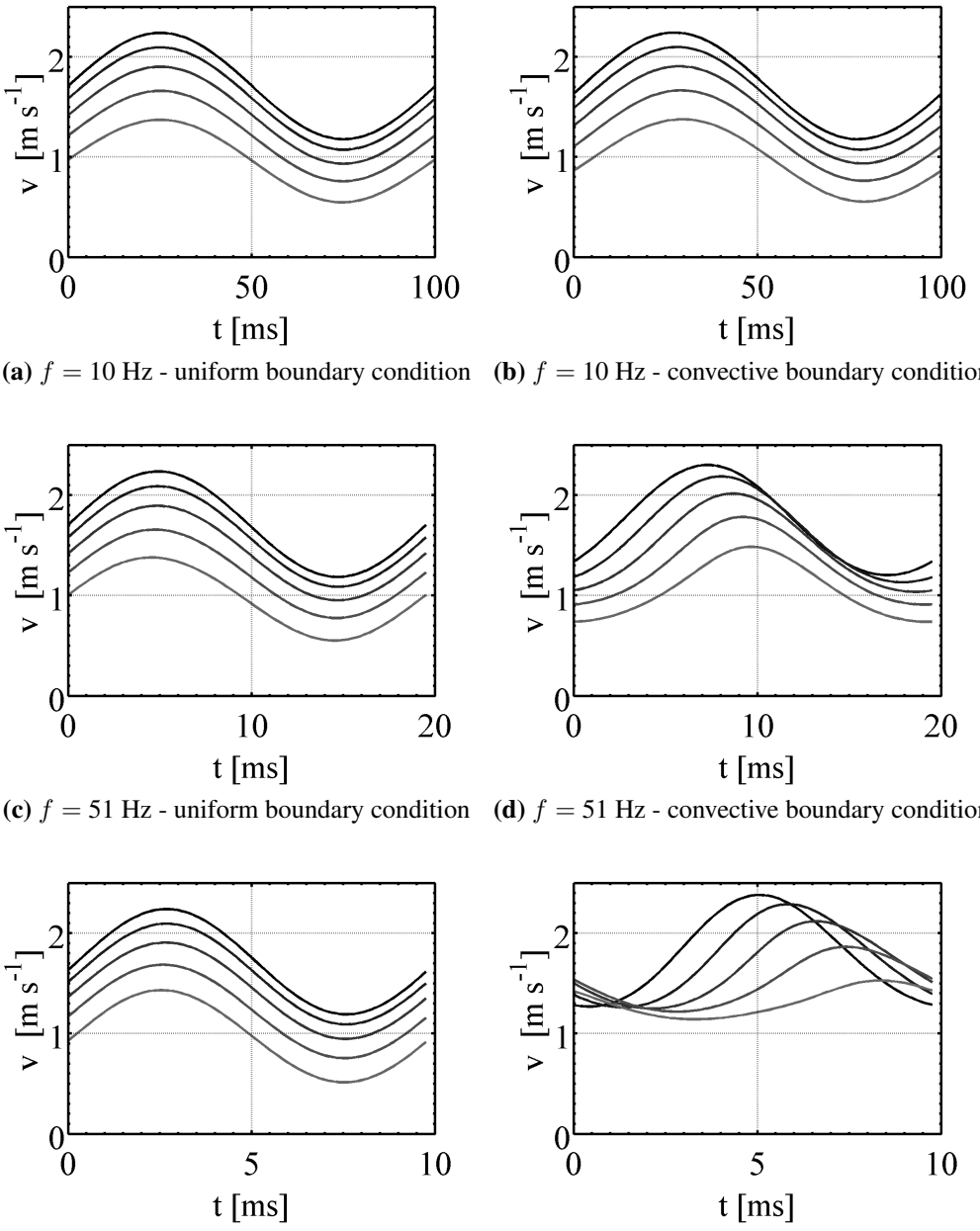

(a) $f = 10$ Hz - uniform boundary condition **(b)** $f = 10$ Hz - convective boundary condition

(c) $f = 51$ Hz - uniform boundary condition **(d)** $f = 51$ Hz - convective boundary condition

(e) $f = 102$ Hz - uniform boundary condition **(f)** $f = 102$ Hz - convective boundary condition

Figure 3.27: Axial velocities obtained from simulations of flame P along a time period with a fluctuation ratio at burner outlet of $(v_{rms}/\overline{v})_R = 0.20$ - Gray levels indicate different measuring locations on the burner centreline from point $z_R = 3.5$ mm (black curve) and at every $\Delta z = 2$ mm towards the plate (gray curves).

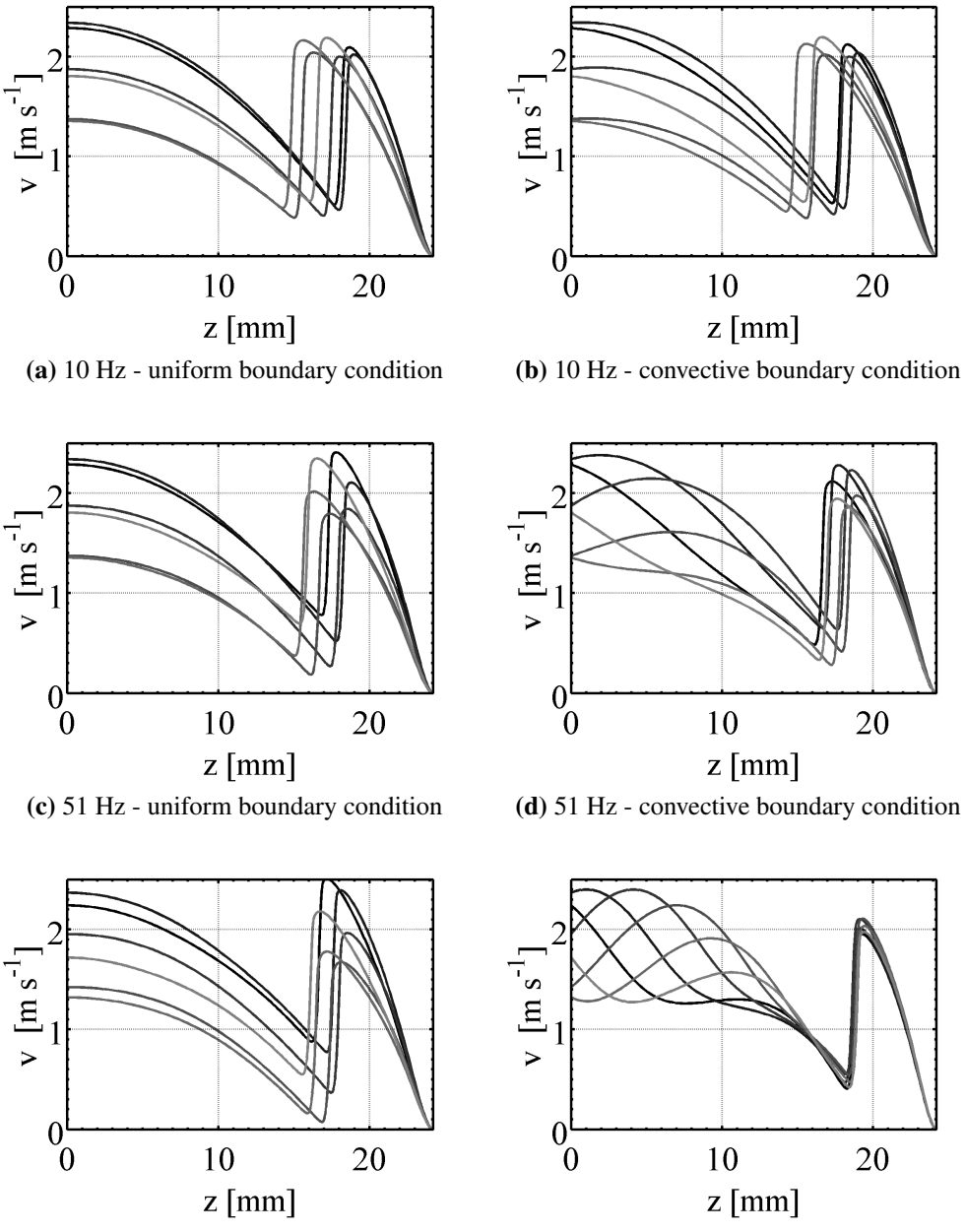

(a) 10 Hz - uniform boundary condition

(b) 10 Hz - convective boundary condition

(c) 51 Hz - uniform boundary condition

(d) 51 Hz - convective boundary condition

(e) 102 Hz - uniform boundary condition

(f) 102 Hz - convective boundary condition

Figure 3.28: Axial velocities obtained from simulations of flame P versus z-coordinate. $(v_{rms}/\overline{v})_R = 0.20$ - Gray levels indicate different instants in the time period.

3.5 Conclusion

The flow and flame responses of a premixed methane-air flame in a stagnation flow submitted to harmonic modulations have been studied. The modulation of the inlet flow velocity generates vortex rings at burner outlet which diameter depends on the forcing frequency. These vortices are convected with the flow and interact with the flame tips by enrolling the flame. The flame response behaves as a low-pass filter to incoming velocity perturbations. The flame position features large vertical oscillations at flow forcing frequencies ($f = 10$ Hz) while the flame front in the center region remains steady for higher modulation frequencies: $f = 51$ Hz and 102 Hz.
A detailed analysis of the propagation of velocity perturbations on the burner centreline highlights two different behaviours at low and high Strouhal numbers. At low frequencies, i.e at $\mathrm{St}_D < 0.5$, velocity perturbations propagate with a convective speed close to the steady flow velocity on the burner axis. At high frequencies, i.e at $\mathrm{St}_D > 0.5$, velocity perturbations propagate with the sound celerity. The origin of these different modes of propagation has been analysed relative to the size of vortex ring shed at the burner lip. At low Strouhal numbers, vortices shed from the burner mouth are large compared to the burner outlet diameter, and thus create velocity perturbations along the burner axis. At high Strouhal numbers, vortex rings shed at burner lips are too small to have a significant impact on burner centreline and perturbations are dominated by the acoustic fluctuations. For intermediate forcing frequencies, convective and acoustic waves of similar amplitudes coexist. A decomposition of the velocity fluctuations measured along the burner centreline into its convective and acoustic components has been carried out to support this explanation.

Finally, the choice of boundary conditions for 1-D simulations of these configurations has been reconsidered. Simulations conducted in previous works set a uniform propagation of perturbations. It was shown that this choice leads to large differences between predictions and measurements particularly at low Strouhal numbers. Another type of boundary conditions has been considered by imposing a convective propagation for fluctuations along the burner centreline. This latter type of boundary condition leads to predictions which feature a velocity field structure closer to that measured. This study globally points out the need of reconsidering velocity boundary conditions for unsteady simulations in a counterflow configuration. Further analysis are needed to conclude on the most relevant choice of boundary conditions in a general configuration.

Chapter 4

Flame response to flow modulations

Flame Transfer Functions (FTF) of laminar premixed strained planar flames submitted to flow perturbations are analysed. Flames are stabilized in a stagnation flow produced by a methane/air premixed jet impinging on a water-cooled plate as in the previous chapter. FTF are determined experimentally between heat release rate fluctuations and harmonic velocity perturbations produced at the burner outlet for a fixed modulation level. Heat release rate is estimated using the chemiluminescence emission from the entire combustion region or the flame emission restricted to a small region around the burner axis. These measurements are used to infer the local flame response around the stagnation streamline axis and the global flame response accounting also for the dynamics at the reactive front periphery. It is shown that the global and local FTF differ. The phase of the FTF approaches zero at low frequencies for the global response and tends towards π in the local measurements. This is also confirmed by a set of experiments in steady regimes. The phase lag then increases in both cases with increasing frequency. For the global response, it is associated with the travel time of vortices shed in the shear layer and impinging on the reactive front periphery. For the local response, the phase evolution is controlled by a constant time lag for flames featuring different equivalence ratios but the same flow velocity. In both cases, the FTF cut-off frequency is much lower than the inverse of the characteristic flame time scale α/S_L^2, where α is the thermal diffusivity and S_L the flame speed.

4.1 Introduction

The dynamics of premixed laminar strained flames in stagnation flows is investigated by determining their Flame Transfer Function (FTF) to velocity disturbances. The response of planar flames to external strain rate modulations is not well documented. Most studies consider this aspect using theoretical analysis or numerical simulations. Darabiha (1992) consider the response of a diffusion flame and Egolfopoulos (1994) consider the case of a premixed flame. They show that flames behave like low-pass filters when the perturbed strain-rate fluctuations do not exceed the extinction value. This has been confirmed by experiments and the cut-off frequency is often associated to a chemical or diffusion time scale (Renard et al. (2000)). With exception of data reported by Aguerre et al. (1993) for the response of a diffusion planar flame, there is no systematic analysis of the flame transfer function over the range of frequencies where the flame features a response. These elements are important to determine the stability of some laminar burners (Bourehla and Baillot (1998); Schuller et al. (2003a); Fernandes and Leandro (2006)), to validate numerical simulation tools and are also needed at the fundamental level to improve the modelling of unsteady flow interactions with turbulent flames.

Analysis of unsteady strained planar flames were mainly conducted using unidimensional numerical simulations along the stagnation streamline axis (Stahl and Warnatz (1991); Egolfopoulos (1994)). The response of laminar and diffusion flames to strain rate oscillations were examined by imposing periodic velocity fluctuations at the numerical domain boundaries (Rutland and Ferziger (1990); Stahl and Warnatz (1991); Ghoniem et al. (1992); Darabiha (1992); Egolfopoulos (1994); Sung and Law (2000)). This technique was also used to investigate the response of strained flames to mixture composition oscillations (Lauvergne and Egolfopoulos (2000); Konig et al. (2009)). A few sets of experiments have been conducted in unsteady regimes. It was shown that the dynamics of strained flames submitted to flow modulations notably differs near extinction (Decroix and Roberts (1999); Sardi and Whitelaw (1999); Luff et al. (2003)). Flames are more sensitive to unsteadiness close to the extinction limits (Im et al. (1995)). Away from these limits, it was suggested that the flame response is dominated by the fluid dynamics. Fluctuations of PAH concentrations in the burnt gases, variations of the flame width and of the flame temperature were examined for laminar hydrocarbon/air stretched diffusion flames submitted to acoustic forcing (Santoianni et al. (2001); Welle et al. (2003); Cuoci et al. (2008)). These flames respond quasi-steadily at low frequencies, but feature a phase offset between the strain rate oscillation and the

flame width or the temperature fluctuations at higher frequencies (Welle et al. (2003)). It is found that the flame frequency response is limited due to diffusion processes and the data obtained for flames submitted to different mean strain rates collapse roughly on a single curve when the forcing frequency is normalized by the mean cycle strain rate K. Aguerre et al. (1993) determined the frequency response of the OH^* chemiluminescence signal from a stretched hydrogen/air diffusion flame for forcing frequencies lower than 100 Hz. Data indicate large OH^* emission fluctuations at low frequencies that are filtered out at higher frequencies, but no attempt was made to normalize the results.
On contrast to diffusion flames, premixed flames can adjust their location in response to changes in the flow field. Away from the extinction limit, the structure of strained premixed flames is weakly affected by strain rate variations (Law et al. (1994)). It was also shown that the local instantaneous burning speed becomes less and less sensitive to hydrodynamic straining with increasing frequency (Joulin (1994)). This led to the hypothesis that the characteristic time for the flame response should be based on the local flow time, instead of the inverse of the mean strain rate $\tau_k = K^{-1}$, which describes the hydrodynamics of the bulk flow. This was confirmed by several numerical studies, where the flame frequency response is shown to scale with the characteristic flame time $\tau_f = \alpha/S_L^2$ (Law et al. (1994); Egolfopoulos (1994); Lauvergne and Egolfopoulos (2000); Bansal and Im (2007)). In this expression, α is the mixture thermal diffusivity and S_L the laminar flame speed. For premixed flames featuring Lewis numbers greater than unity $\mathrm{Le} \gtrsim 0.7$ (Sung and Law (2000)), low frequency heat release rate fluctuations are found out of phase with strain rate oscillations due to velocity oscillations imposed at the domain inlet. At higher frequencies, the flame response is reduced and the cut-off frequency is found of the order of τ_f^{-1} (Egolfopoulos (1994)). In a recent numerical analysis, it was however shown that velocity and mixture composition perturbations generated at the cold boundaries are convected by the flow and propagate with a wavelength $\lambda = v/f$, where v is the local flow velocity (Konig et al. (2009)). The perturbation amplitude reaching the flame thus decreases for increasing frequency and might be completely levelled before the reaction zone.
The conclusion from the preceding analysis is that the FTF of strained premixed flames submitted to flow perturbations must be governed by at least two dimensionless numbers :

$$FTF = FTF\left(f\alpha/S_L^2, fl/v\right) \tag{4.1}$$

where f is the forcing frequency, K the mean strain rate during a cycle, α/S_L^2 the characteristic flame time and l/v the characteristic flow time scale, l be-

ing the distance between the perturbation input and the reactive zone location. One objective of the present chapter is to identify which mechanism prevails for strained flames submitted to harmonic velocity modulations. Another is to document the gain and the phase evolution of the FTF in this configuration and to provide data for validation of unsteady numerical simulations. These elements are investigated using an original experimental setup enabling optical access to the center flame region around the stagnation streamline axis.

The experimental setup and the diagnostics used to characterize the flame response are presented in the next section (section 4.2). Time series of the global and local flame intensity emission signals together with the velocity perturbation imposed at the burner outlet are analysed in section 4.3. These signals are then used to determine the global and local FTFs presented in section 4.4.

4.2 Experimental setup

Measurements are carried out with the second setup presented in chapter 1 for gaseous reactive mixtures. The conditions investigated are the inert flow and flames P, Q and R also defined in chapter 3 in table 3.1. It is worth recalling that for the three reactive configurations P, Q and R, the sum of central mass flowrates of air and methane is kept constant and equal to $q_c = 1639$ nL h^{-1} with mixtures of different equivalence ratios. Flame P is near a stoichiometry condition, flame R is a rich and flame Q is a lean flame. Note that flames Q and R have the exact same laminar burning velocity $S_L = 0.27$ m s^{-1} (Vagelopoulos and Egolfopoulos (1998); Dong et al. (2002))..

The burner is equipped with two lateral loudspeakers to modulate the flow at the burner outlet. A signal synthesizer followed by a stereo amplifier is used to generate harmonic perturbations. The modulation level is controlled by the synthesizer gain and the resulting velocity perturbation level was adjusted with hot wire measurements in the inert configuration. This hot wire was placed on the burner axis at $z_R = 3.5$ mm below the nozzle outlet as schemed in figure 4.1a. The fluctuation level at point R was kept in these experiments at a constant value of $(v_{rms}/\overline{v})_R = 0.20$.

Heat release rate fluctuations are estimated from the chemiluminescence emission of CH^* or OH^* radicals present in the reaction front. This is now well established and has been verified in many studies on laminar flame dynamics (see for example Keller and Saito (1987); Schuller et al. (2002); Hardalupas

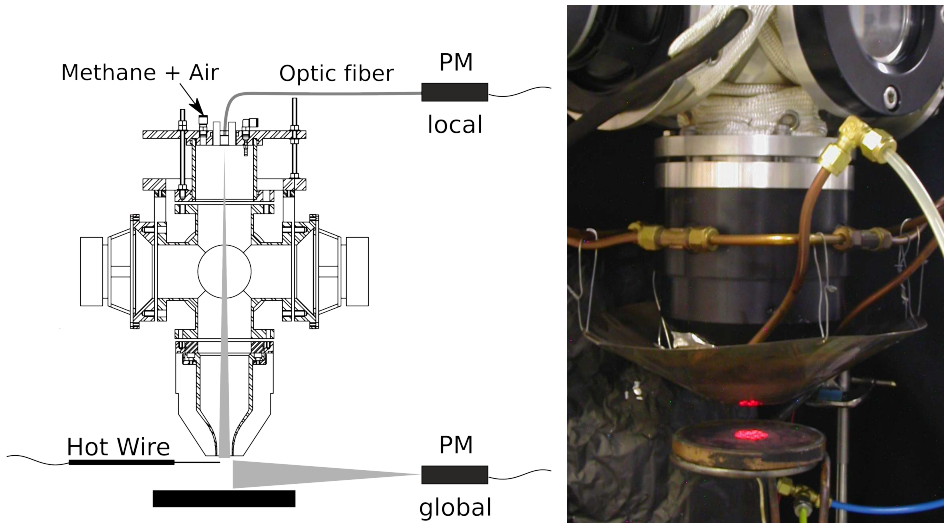

(a) Scheme of the whole setup - Gray zones show the imaged areas

(b) Area imaged by the photomultiplier (red disk)

Figure 4.1: Experimental setup used to obtain strained planar flames in a pulsated stagnation flow.

and Orain (2004); Duchaine et al. (2009) for planar stretched flames). Chemiluminescence images of pulsated flames were first recorded using a CCD camera at different instants in the modulation cycle. These images were presented in figures 3.7, 3.8 and 3.9 for flame P modulated at $f = 10$, 51 and 102 Hz. Images for flames Q and R are not shown here but they feature the same type of interactions identified in these figures. The only significant difference is that the flames Q and R stay a bit further from the burner outlet due to their lower flame velocity. These images can be used to reconstruct the flame surface area evolution assuming an axisymmetric configuration (Schuller et al. (2002)). However since the present interest is to compare chemiluminescence from the flame center to the emission resulting from the whole flame, it is preferable to conduct these measurements with the same photomultiplier PM placed at two different locations (see figure 4.1a). Emission from the entire combustion region is collected when the PM is placed on the side of the setup in front of the flame 300 mm away from the burner z-axis. This position of the PM is referred as "global" and the chemiluminescence intensity is noted I_g.
Part of the chemiluminescence emission originating from the flame region in the vicinity of the z-axis can also be recorded using a 600 μm diameter optical fiber made of quartz and mounted on a collimating lens placed on the top of the burner 350 mm away from the plate. The PM placed at the end of the

optical fiber delivers a signal proportional to the light intensity emitted from radicals present in the flame center region. This position of the PM is referred as "local" and the chemiluminescence intensity is noted I_l.
A laser placed at the end of the optical fiber was used to get an estimate of the viewfield. This produces a disk of light with a radius of about 8 mm at the plate location and this can be roughly estimated as the distance from the burner z-axis over which the flame chemiluminescence is integrated (see figure 4.1b). The converging unit is anodized in black to avoid spurious light reflection inside the burner and the copper plate surface is dark due to oxidation. Two different narrow band filters centred on $\lambda = 308$ and 431 nm (± 10 nm) can be placed in front of the PM to collect OH^* or CH^* radicals emission.
Flame Transfer Functions (FTF) were determined by modifying the forcing frequency from $f = 5$ to 150 Hz by 10 Hz increments and for a relative modulation level fixed to $(v_{rms}/\overline{v})_R = 0.20$ at the hot wire location. Effects of the amplitude level are not investigated in this study (Durox et al. (2009)). It was also checked that the small added co-flow has barely no impact on the flame dynamics in these experiments.

4.3 Analysis of chemiluminescence signals

It is now interesting to analyse the resulting chemiluminescence signals measured by the PM placed at the different locations. The fluctuating component v' (bold line) of the axial velocity signal measured by the hot wire, the corresponding global fluctuating intensity I'_g (filled symbols) resulting from the radicals emission of the whole reaction region and the local fluctuating intensity I'_l (empty symbols) originating only from the center flame region are plotted in figure 4.2 for two modulation frequencies $f = 10$ Hz and $f = 100$ Hz.
The signal I'_l has a much lower amplitude than the global emission I'_g and has been artificially multiplied by a factor 10 in these plots. There was also no filters in front of the PM in these experiments to improve the signal-to-noise ratio. In the bulk oscillation mode at $f = 10$ Hz, the global intensity fluctuation I'_g closely follows the velocity oscillation v'_R imposed at the burner outlet with the same period and with a small phase lag. These two signals are almost in phase, contrarly to the local intensity fluctuation I'_l which also features the same oscillation period but is out-of-phase with the velocity oscillation v'_R imposed at the nozzle outlet. When the axial velocity increases, the flame chemiluminescence near the burner axis drops and conversely. This behaviour ceases however at higher frequencies. For a harmonic modulation

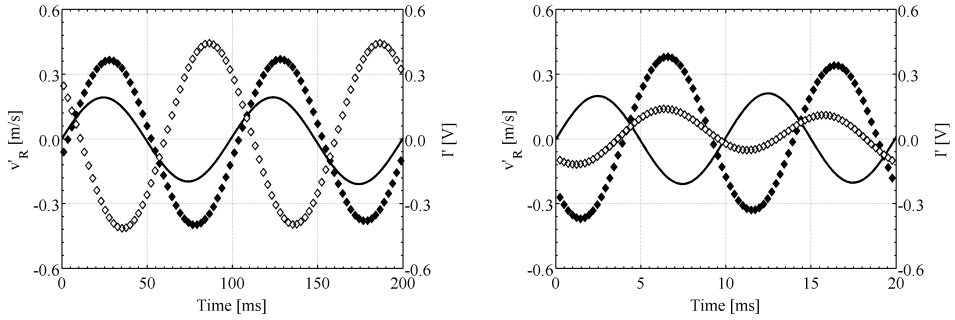

(a) $f = 10$ Hz **(b)** $f = 100$ Hz

Figure 4.2: Time traces of the fluctuating components of the axial velocity perturbation v' at the burner outlet (bold line), the resulting global I'_g (filled symbols) and local $10 \times I'_l$ (open symbols) chemiluminescence responses from the flame for an harmonic modulation at $f = 10$ Hz (left) and $f = 100$ Hz (right).

at $f = 100$ Hz, the two fluctuating signals feature now comparable phase lags with respect to the velocity input. It should also be noted that the amplitude of the local intensity fluctuation I'_l is considerably reduced at $f = 100$ Hz compared to that at $f = 10$ Hz for the same input level. This reduction remains moderate for the global intensity signal I'_g.

The different behaviours identified at low frequency can be further investigated. In the bulk oscillation mode at $f \simeq 10$ Hz, the flame and the flow interaction can be treated in a quasi-steady approach. A set of steady experiments is then conducted by varying the bulk velocity around the nominal operating regime obtained for $V_0 = 1.55$ m s^{-1} and by recording the evolution of the global and local emission intensities. Results plotted in figure 4.3 are normalized by the intensity I_0 in the nominal regime versus the ratio of the bulk flow velocity divided by this quantity V_0 in the nominal regime. The global intensity I_g emitted from the entire reaction zone increases linearly when the flow velocity is augmented with a constant rate $(I_g/I_{0,g})/(V/V_0) \simeq 0.6$. Deviation occurs for large modifications of the flowrate for $|V - V_0|/V_0 \geq 0.18$ where saturation effects appear. The local emission intensity I_l remains also proportional to the bulk flow velocity V around the nominal regime V_0, but the reactivity in the center flame region decreases when the flow velocity increases with a reduction rate roughly equal to $(I_l/I_{0,l})/(V/V_0) \simeq -0.4$. This value is less reliable than the one obtained for the global intensity measure-

ments because the light originating from the flame region around the burner axis remains weak. These data however confirm the observations made in pulsated configurations at low forcing frequencies. The global flame reactivity integrated over the whole flame surface area follows the mixture flowrate oscillation at very low frequencies, but the local flame reactivity restricted to a region located near the burner axis is out-of-phase with the velocity input. The evolution of the global flame intensity is easy to interpret. The global flame intensity increases with the bulk flow velocity, because the global heat release rate follows the supply of reactants to maintain combustion. The evolution of the local flame intensity decreasing with increasing the bulk flow velocity is also in agreement with previous findings for reactive mixtures featuring a Lewis number $\mathrm{Le} \gtrsim 0.7$ (Sung and Law (2000)).

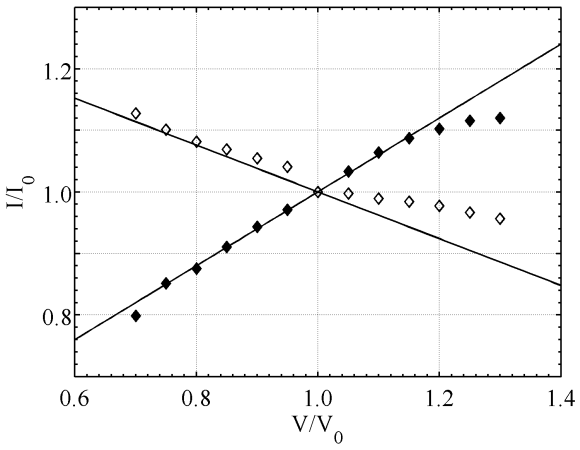

Figure 4.3: Global I_g (filled symbols) and local I_l (open symbols) chemiluminescence intensity in steady configurations normalized by the nominal regime characterized by a flow velocity V_0 and a corresponding intensity I_0. $V_0 = 1.55$ m s^{-1}, $\phi = 0.99$.

These findings are compared with 1D simulations. Figure 4.4 presents the normalized heat release rate versus normalized flow velocity for flames P, Q and R. Heat release rate fluctuations slightly decrease with the flow velocity in these three configurations. These results are in agreement with the measurements in figure 4.3 and also with previous studies (Egolfopoulos (1994); Sung and Law (2000)). The rate of decrease takes however different values: $(\dot{Q}/\dot{Q}_0)/(V/V_0) \simeq -0.01$ in the simulations and $(I_l/I_{0,l})/(V/V_0) \simeq -0.4$ in the experiments for flame P. This difference between experimental and nu-

merical results might be explained by the fact that the chemiluminescence measurements are carried out on an extended region around the burner axis. It can also be pointed out that Hardalupas and Orain (2004) showed that the chemiluminescence signal can be affected by the stretch rate. This means that the proportionality between heat release rate and chemiluminescence signal can be locally affected by varying stretch rates.

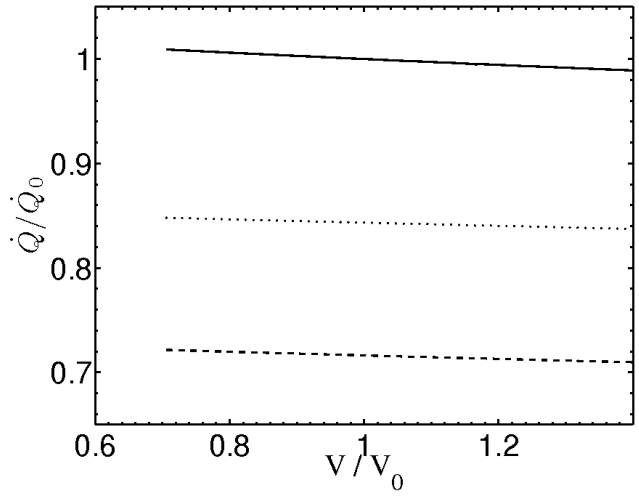

Figure 4.4: 1D simulations of normalized heat release rate $\dot{Q}/\dot{Q}_0$ versus normalized bulk flow velocity V/V_0 for flame P (solid line), flame Q (dashed line) and flame R (dotted line). Results are normalized by the mean heat release rate $\dot{Q}_0$ and mean flow velocity measured V_0 corresponding to flame P

4.4 Flame Transfer Functions

In the present configuration, a flame transfer function H relating the relative heat release rate fluctuation to the velocity oscillations at one location upstream the flame is defined. This location may be chosen as point R at the burner outlet or point S located at $z_S = 13$ mm just upstream of the flame front. The response is only examined at the forcing frequency f for a fixed perturbation level:

$$H_R(f) = \frac{\dot{Q}'/\overline{\dot{Q}}}{v'_R/\overline{v}_R} \qquad H_S(f) = \frac{\dot{Q}'/\overline{\dot{Q}}}{v'_S/\overline{v}_S} \tag{4.2}$$

with $\dot{Q}$ referring to the heat release rate signal and v to the velocity at the chosen location upstream the flame on the burner axis.

For premixed flames, in the case of a complete combustion of the incoming mixture, it has been shown that the heat release rate $\dot{Q}$ is proportional to flame surface A (Candel et al. (2004)) and to light emission from free radicals like CH^* or OH^* (Keller and Saito (1987); Schuller et al. (2002)). It is thus possible to determine the flame transfer function from one of the following expressions:

$$H(f) = \frac{\dot{Q}'/\overline{\dot{Q}}}{v'/\overline{v}} \simeq \frac{A'/\overline{A}}{v'/\overline{v}} \simeq \frac{I'/\overline{I}}{v'/\overline{v}} \tag{4.3}$$

with A referring to the flame surface and I to CH^* or OH^* chemiluminescence intensity originating from the flame region.

One then writes:

$$H(f) = \frac{I'/\overline{I}}{v'/\overline{v}} = |H(f)|e^{i\varphi_H(f)} = Ge^{i\varphi_H(f)} \tag{4.4}$$

where $G = |H(f)|$ and φ_H respectively designate the transfer function gain and phase.
There is a clear link between the transfer functions defined by H_R and H_S and the velocity transfer function F relating velocity fluctuation ratio at the burner outlet $(v'/\overline{v})_R$ and at the base of the flame $(v'/\overline{v})_S$ defined in chapter 3. One can write $H_R = H_S.F$ as presented in figure 4.5. The transfer function H_R represents the response of the flame to a velocity modulation at burner outlet and the transfer function H_S represents the same response of the flame but for a velocity modulation just upstream the reactive front. By examining the results obtained for the velocity transfer functions F described in chapter 3, one can infer that the transfer functions H_R and H_S may differ. The present work focuses on the determination of the transfer function H_R.

The flame response to incoming velocity disturbances is now investigated for frequencies ranging from 5 to 150 Hz. Relative heat release rate fluctuations can be directly obtained from the chemiluminescence signals $\dot{Q}'/\overline{\dot{Q}} \simeq I'/\overline{I}$ from one of the CH^* or OH^* radical emission intensity. The contribution I'/v'_R is then deduced from the velocity v_R and intensity I time traces using the operator S_{xy}/S_{xx}, where S_{xy} is the cross spectral density and S_{xx} the power spectral density examined at the forcing frequency f between the input

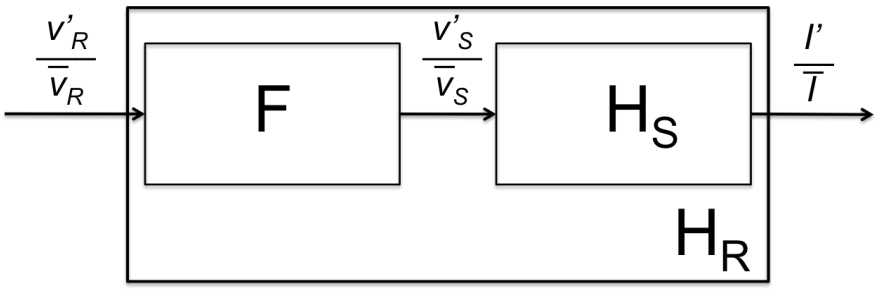

Figure 4.5: Schematic representation of the link between the different transfer functions F, H_S and H_R. $v'_R/\overline{v}_R$ and $v'_S/\overline{v}_S$ represent respectively the relative velocity fluctuation ratio at point R ($z_R = 3.5$ mm) and point S ($z_S = 13$ mm) on the burner centreline and $I'/\overline{I}$ represents flame chemiluminescence signal fluctuation ratio recorded locally or globally.

$x = v_R$ and the output $y = I$ signals. The global and local measurements of flame chemiluminescence yield respectively a global and local FTF representing the flame response of the entire reaction zone or uniquely that of the central region of the flame.

The global FTF in figure 4.6 was determined using three different filters in front of the PM collecting the light from the whole combustion region. Square symbols indicate results obtained with the CH^* filter, the disks those obtained with an OH^* filter and the diamonds denote data obtained without any filter. In this last case, the light is collected over the near UV and the visible spectral bandwidths and is filtered by the bell shape response curve from the detector. Figure 4.6 clearly shows that there is no difference between the FTFs determined with the OH^* and CH^* filters. It is also shown that the gain and the phase evolutions fit quite well for the FTF obtained without any filter. The gain eventually features slightly lower values, but the phase perfectly matches data obtained with filters over the entire frequency range explored. It can already be concluded that fluctuations of the flame chemiluminescence emission recorded by this type of photo-detector without any filter are roughly proportional to heat release rate fluctuations and can be used with confidence to determine FTFs for these premixed flames. In the following experiments, measurements presented without filter are preferred because the signal level is improved.
Analysis of the gain in figure 4.6 indicates that the flame response features different humps. The first hump exceeds the unit value indicating a strong amplification of incoming perturbations with violent heat release rate fluctu-

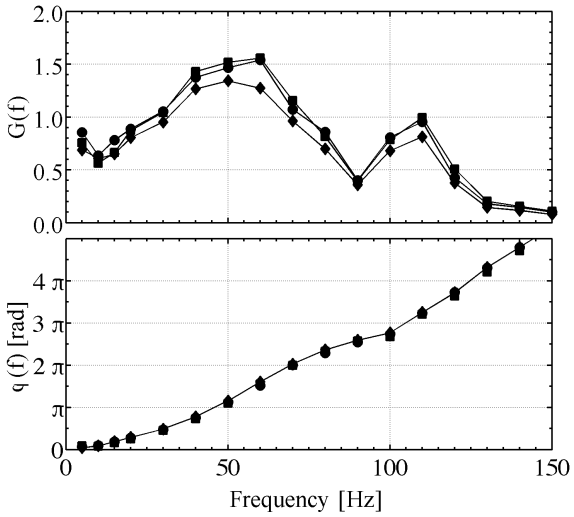

Figure 4.6: Global FTF determined using the CH^* filter (square), OH^* filter (disk) and no filter (diamond) in front of the PM placed on the side of the setup. Flame P : $V_0 = 1.55$ m s^{-1}, $\phi = 0.99$, $v_{rms}/\overline{v} = 0.20$.

ations. The maximum is reached for a forcing frequency around $f = 50$-60 Hz ($\mathrm{St}_D \simeq 0.5$) and corresponds to a situation where one large vortex enrols at the flame edges and produces periodic large and sudden flame extinctions at the flame periphery (see figure 3.8). The gain then drops for higher frequencies to reach a minimum at $f = 90$ Hz. This is followed by a second hump with a maximum approaching unity for a forcing frequency $f = 120$ Hz. Tomographies realized for a forcing frequency at $f = 102$ Hz show that a second vortex is following the first one in the fresh reactants. The second hump is then associated with this two vortices-flame roll-up mechanism. The new gain peak value is reached for a frequency $f = 120$ Hz corresponding to twice the peak frequency for a single vortex interaction found at $f \simeq 60$ Hz, but the interaction is weaker because the vortex size and consequently the vortex strength decreases as the frequency is increased. For higher frequencies the gain finally drops rapidly to reach 0.1 at $f = 150$ Hz.

In conclusion, these observations show that mechanisms governing the FTF of the global flame response result mainly from interactions taking place at the flame periphery because small perturbations at this location induce large heat release rate variations (Schuller et al. (2002); Duchaine et al. (2009)). Though, one should note that heat release rate mainly results from two mechanisms. The first one is associated with variations of the local consumption rate, which locally modifies the flame chemiluminescence. The second mechanism

corresponds to variations of the flame surface area, which does not modify the flame chemiluminescence. At the flame periphery, the latter mechanism dominates. Small flame surface area fluctuation induces large heat release rate variations without significant change in the local flame luminosity. This is emphasized by large coherent structures impinging the flame periphery and modifying the flame surface area.
The phase φ_g of the FTF takes vanishingly small values at low frequencies because the global chemiluminescence signal is in phase with the velocity input for low frequency bulk oscillations (see figure 4.2). It then increases regularly with the forcing frequency and can be described by the following relation:

$$\varphi_g = \varphi_{0,g} + 2\pi f \tau_g \tag{4.5}$$

where $\varphi_{0,g} = 0$ and $\tau_g(f)$ is the time required by the vortices to impinge the flame periphery. It is given by $\tau_g = l/v_t$ where l denotes the curvilinear distance swept by the vortices from the burner rim to the flame periphery and v_t is the mean vortex velocity along this path. This time lag increases also with the forcing frequency, because vortices follow all the same path but their size reduces for increased frequency. In the case explored in figure 4.6, this time lag equals $\tau_g = 12$ ms at $f = 50$ Hz and $\tau_g = 14$ ms at $f = 100$ Hz.

Figure 4.7 shows the evolution of the gain and the phase of the global FTF obtained for the three flames P (diamonds), Q (circles) and R (squares) without any filters in front of the PM. As a reminder, these flames correspond all to the same nominal flow velocity $V_0 = 1.55$ m s^{-1} but feature different equivalence ratios : $\phi = 0.99$, $S_L = 0.38$ m s^{-1} (diamonds), $\phi = 0.80$, $S_L = 0.27$ m s^{-1} (squares), and $\phi = 1.22$, $S_L = 0.27$ m s^{-1} (circles).
It is worth noting that the gain and phase evolutions for flames P, Q and R are of the same type. The gain presents a hump around $f = 40$ Hz and a second smaller hump around $f = 100$ Hz. The phase lag is globally linear with the forcing frequency: $\varphi_g = \varphi_{0,g} + 2\pi f \tau_g$.
Transfer functions of flames Q and R have indeed very close behaviours while flame P transfer function exhibit slightly different features. The local maxima of the gain of flames Q and R occur at smaller frequencies ($f \simeq 30$ Hz and $f \simeq 90$ Hz) and are weaker than the maxima observed for flame P. Concerning the phase evolution, the time lag is a bit greater for flames Q and R than for flame P: $\tau_g = 14$ ms at $f = 50$ Hz and $\tau_g = 18$ ms at $f = 100$ Hz. The similarities between flames Q and R can be explained by the fact that these two flames have the same laminar burning velocity $S_L = 0.27$ m s^{-1} but differ only by the equivalence ratio $\Phi < 1$ for Q and $\Phi > 1$ for R. In the present case, this induces for instance that flames Q and R stand at the exact same

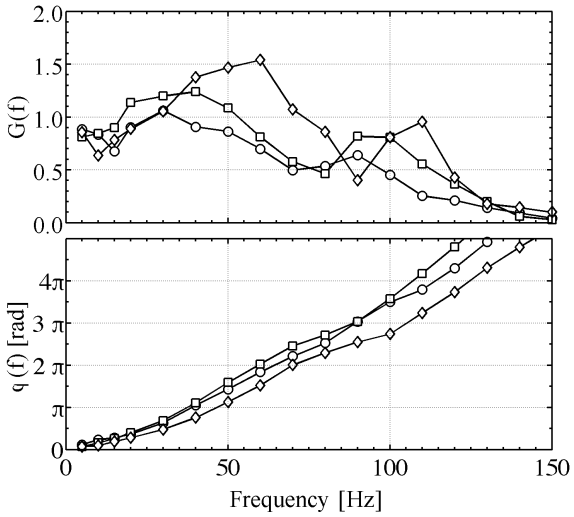

Figure 4.7: Global FTF for three configurations featuring the same plug flow velocity $V_0 = 1.55$ m s^{-1} and a nearly stoichiometric $\phi = 0.99$ (flame P - diamonds), lean $\phi = 0.80$ (flame Q - circles) and rich $\phi = 1.22$ (flame R - squares) mixtures. $(v_{rms}/\overline{v})_R = 0.20$.

position, a bit further away from burner outlet compared to flame P position. As a consequence, vortices shed at the burner lips require larger travel times to impact the flame periphery. This explains the larger time lags τ_g observed in the phase of the transfer functions.

The local FTF based on the chemiluminescence emission restricted to the region close to the stagnation streamline axis are now examined in figure 4.8 for the three different operating conditions. It was not possible to determine these FTF using the CH^* or OH^* emissions due to the weak signal to noise ratio and results are only presented without filter in front of the PM.

Data for the gain are first examined. The three curves follow roughly the same trend approaching a value of 0.4 for vanishingly small modulation frequencies. This value is consistent with the steady experiments conducted at different flow velocities in the previous section for the stoichiometric mixture case (see figure 4.3). It was found that the change of chemiluminescence decreases linearly with the change of velocity $(I_l/I_{0,l})/(V/V_0) \simeq -0.4$. The gain then drops to reach zero at $f \simeq 40$ Hz and features a rebound up to $f \simeq 120$ Hz with a maximum located around $f \simeq 80$ Hz. Extrema of the local flame response are found at the same locations for the three investigated flames.

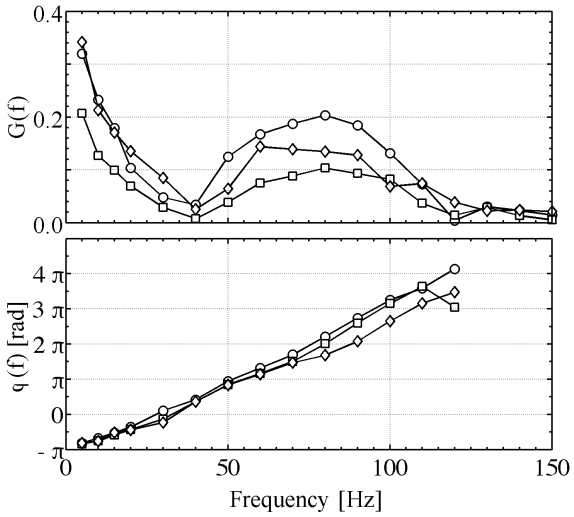

Figure 4.8: Local FTF for three configurations featuring the same plug flow velocity $V_0 = 1.55$ m s^{-1} and a nearly stoichiometric $\phi = 0.99$ (flame P - diamonds), lean $\phi = 0.80$ (flame Q - circles) and rich $\phi = 1.22$ (flame R - squares) mixtures. $(v_{rms}/\overline{v})_R = 0.20$.

This evolution is clearly different than the one found for the global FTF gain and suggests a different governing mechanism than the one identified for the global FTF. A main conclusion, is that the cut-off frequency $f_c \simeq 100$ Hz is found at a significantly lower value than the characteristic frequency $f_c = S_L^2/\alpha \simeq$ 10,000 Hz suggested in previous numerical investigations of this configuration (Egolfopoulos (1994)).
Results can also be analysed by examining the phase of the FTF. The phase evolution for the lean, stoichiometric and rich mixtures cases collapse on a single curve :

$$\varphi_l = \varphi_{0,l} + 2\pi f \tau_l \tag{4.6}$$

In this expression, $\varphi_{0,l} = -\pi$ because the local flame intensity is out-of-phase with the perturbation velocity at the burner outlet as shown in figure 4.3. Note that the choice of the value $-\pi$ or π is arbitrary. These results are also consistent with previous numerical simulations for the stoichiometric, lean and rich mixtures all featuring Lewis numbers greater than 0.7 (Egolfopoulos (1994); Sung and Law (2000)). The time lag is equal to $\tau_l =$ 11 ms and is found independent of the mean flame location on the burner axis for the three cases explored. A mechanism based on the travel time of perturbations between the nozzle outlet and the reactive flame front cannot be evoked to interpret

these behaviours because it would be a function of the position of the flame with respect to the burner outlet. A more detailed investigation of the pulsated flowfield would be necessary to determine the main parameters influencing this time lag.

4.5 Conclusion

Flame Transfer Functions (FTF) of laminar premixed strained methane/air flames were determined experimentally for harmonic velocity perturbations generated at the burner outlet. It was first shown that relative heat release rate fluctuations can be estimated using relative fluctuations of the chemiluminescence signal from the flame without specific interference filter. The flame frequency responses were determined using the chemiluminescence emission from the entire combustion region (global FTF) or the light emission restricted to a small area around the stagnation streamline axis (local FTF). The analysis of these transfer functions yielded different responses in terms of gain and phase. Mechanisms governing the global FTF were identified and result mainly from disturbances generated at the burner outlet, transported by the mean flow and interacting with the flame periphery. The local FTF responses collapse for a lean, stoichiometric and rich mixtures. They feature a phase-offset $\varphi = \pm\pi$ at low frequencies and a constant slope independent of the flame location with respect to the nozzle outlet. Results clearly indicate that the characteristic flame time scale α/S_L^2 cannot be invoked to interpret these data.

Chapter 5

Sound production mechanisms

While combustion noise from turbulent premixed flames is well documented, less is known for partially premixed systems. Fundamental analysis are required to determine the main mechanisms of sound generation resulting from combustion of non perfectly mixed reactants. To this purpose, an experimental study is conducted to investigate sound production during the interaction of a vortex train impinging on the periphery of a planar laminar methane-air flame in a stagnation flow. In response to these flow disturbances, the flame enrols around vortices and gases from the surrounding are entrained in the combustion region. Sound production is characterized for different compositions of the central and annular flows. Seven configurations are explored under the same mean flow and perturbation conditions using nitrogen, air and a diluted methane-air mixture for the surrounding flow. Time traces of radiated sound pressure and CH^* chemiluminescence emission signals during these interactions are characterized and compared together with detailed imaging of the flame and flow motions. It is shown that classical combustion noise relations based on CH^* emission used to analyse sound production from perfectly premixed flames are still valid in these partially premixed systems under a wide variety of operating conditions. The main mechanisms of sound production are identified in the seven configurations and correspond to entrainment of hot combustion products burning in the fresh mixture leading to a positive pressure peak and destruction of flame elements by vortex interaction leading to a negative pressure peak. The strength of these mechanisms depends on the surrounding gases composition. Entrainment of air leads to slightly louder noise levels than entrainment of premixed reactants because flame destruction takes place on a shorter period. It can be inferred that the fundamental mechanisms of sound production in premixed and partially premixed flames are essentially the same and may be analysed using simple optical diagnostics.

This chapter is an extension of the study published by Duchaine et al. (2009). It brings up complementary measurements and an analysis of the role of the central flow on noise production.

5.1 Introduction

Reduction of combustion noise emission is becoming an important issue for Diesel automotive engines at idle, jet engines and to a lesser extent for gas turbines applications at low speed engine operating conditions. While car engines are insulated with external acoustic absorbing materials to reduce noise annoyance, technologies are already available to silence jet engines or gas turbines with the use of acoustic absorbers inside the combustion chamber. These systems rely mainly on resonator devices put at judicious locations inside the engine and can damp efficiently pure tones sounds, but usually fail in broad band noise reduction. In an effort to tackle sound production at the source locations, studies were undertaken to understand fundamental mechanisms leading to intense noise production in turbulent burners. Many flame interactions were identified as potential important noise sources in premixed systems, but some fundamental mechanisms are still not yet understood (Candel et al. (2004); Candel et al. (2009)). Among them prediction of sound production from partially premixed systems is still a challenging issue, mainly because the combustion itself and its dynamics are more complicated than in perfectly premixed configurations because mixing phenomena should also be accounted for (Mahan J.R. (1991)).
Experimental studies were carried out to characterize sound radiation from non-premixed and partially premixed turbulent flames in open and close configurations and were recently reviewed by Singh et al. (2005). The main conclusions are the followings. Turbulent premixed fuel rich flames are noisier than fuel lean flames (Kilham and Kirmani (1979); Kotake and Takamoto (1990)). Turbulent non premixed flames are noisier than premixed flames for similar flow velocities (Singh et al. (2003)). Predominant sound sources are distributed in the rear region of the reaction zone in the case of turbulent non premixed jet flames (Price et al. (1969)), whereas they are located closer to the flame tip for premixed flames (Smith and Kilham (1963)). The output of these studies is useful scaling laws for the prediction of noise radiation levels and the frequency peak of the radiated noise spectrum. This has for example been reviewed by Rajaram et al. (2006) for premixed flames. Non premixed flames have however not been studied extensively using optical techniques. Attempts to investigate noise production from these flames were thus carried out using

numerical tools with RANS and more recently LES calculations (Klein and Kok (1999); Bui et al. (2007)). Underlying mechanisms at the origin of sound production were however not considered in these studies.
As in turbulent flows eddies with different scales and strengths develop and interact with the flame, a central issue is their impact on the noise generation process. Influence of coherent structures on the noise output was investigated at Laboratoire EM2C (Candel et al. (2004); Durox et al. (2005)) for laminar premixed flames and in turbulent diffusion flame configurations (Ohiwa et al. (1993)). Flame enrolment and rapid destruction were shown to be key processes of sound production. In partially premixed systems, the flame vortex dynamics should be modified depending whether hot combustion products, air, fuel or a mixture of both are entrained in the reaction region. These different interactions may have consequences on the sound output (Mahan J.R. (1991)). Detailed experiments are conducted in this chapter on laminar flat flames to investigate the role of the surrounding gas on the combustion generated noise during flame-vortex interaction. The objective is to identify if there is a hierarchy between entrainment of fresh air or premixed gases on the sound level output. Main elements on combustion noise sources identification are briefly discussed in the next section. The experimental setup and results for seven flames submitted to well controlled large vortices are then presented together with conclusions on mechanisms of sound production.

5.2 Combustion noise sources

Interactions with large scale vortices, annihilation of neighbouring flame elements and flame extinctions at cold boundaries were identified as significant noise sources in premixed flames submitted to incident flow perturbations (Schuller et al. (2002); Candel et al. (2004); Durox et al. (2005); Fernandes and Leandro (2006)). Acoustic pressure fluctuations resulting from these interactions always fit predictions from classical combustion noise theory (Strahle (1985)):

$$p'(r,t) = k_1 \left[\frac{d\dot{Q}'}{dt} \right]_{t-\tau} \tag{5.1}$$

The far field sound pressure signal p' is proportional to the rate of change of heat release rate fluctuations $\dot{Q}'$ delayed by a period $\tau = \int dr/c(r)$ corresponding to the time required for sound waves to cover the distance r at the sound speed $c \simeq 340\,\mathrm{m\,s^{-1}}$ from the compact combustion region to the mi-

crophone location. The coefficient k_1 depends on the microphone location and the reactive gases under consideration (Schuller et al. (2002)).
In the case of premixed flames kept at a constant equivalence ratio, the far field sound wave p' is also proportional to the light emitted by the free radicals present in the reaction region :

$$p' = k_2 \left[\frac{dI'}{dt}\right]_{t-\tau} \tag{5.2}$$

where I' corresponds to fluctuations of the chemiluminescence signal from the reaction region based on OH^*, C_2^* or CH^* radicals emission and k_2 is another real constant (Schuller et al. (2002); Hurle et al. (1968); Shivashankara et al. (1975); Katsuki et al. (1986)). Expressions (5.1) and (5.2) derived in the far field of a compact source region remain also valid in the near-field of the reaction zone because sound sources are mainly of monopole type without specific near-field structure (Candel et al. (2009)).
In a study of self-induced instabilities of a V-flame stabilized on a bluff body which flame tip is delimited by the mixing layer between the reactants jet and the surrounding air (Durox et al. (2005)), the equation 5.2 ceased to be verified and the following relation was instead observed $p' \simeq k_3 \left[I'\right]_{t-\tau}$ where k_3 is a real constant and I' is the fluctuation signal of CH^* radicals emission. It was observed that vortices created in the shear layer between the premixed reactants and the surrounding medium induce flame enrolment and flame surface annihilation at the flame tip. These mechanisms were already described in premixed systems, but the net sound output in this work ceases to be proportional to the rate of change of CH^* radicals emission. It was argued that dilution with entrained air changes locally the mixture composition at the flame tip periphery and as a consequence the light emitted from this region cannot be considered proportional to the heat release rate. This point was investigated deeper in Candel et al. (2004) and it was shown that the proportionality between sound pressure signal p' and the rate of change of heat release rate fluctuations $\dot{Q}'$ is recovered when the level of incident perturbations is increased.

As relation 5.1 was derived without restriction on the combustion regime, the sound pressure signal should remain proportional to the rate of change of the total heat release rate, but mixture composition inhomogeneities due to air entrainment may affect the chemiluminescence signal. It is thus not clear whether or not the relation 5.2 could be used to describe noise production from partially premixed flames and what is the role of the gases trapped during flame-vortex interaction on the radiated sound field. These points are investigated using a setup where the flame vortex interaction with the surrounding

flow is well controlled. The chosen configuration corresponds to a modulated premixed flame impinging on a water cooled plate because much is already known on the flame dynamics and sound emission in this simplified configuration (Roberts et al. (1993); Schuller et al. (2002); Fernandes and Leandro (2006)).

5.3 Experimental setup

Experiments are carried out on the first experimental setup described in chapter 1. A schematic representation of the setup is given in figure 5.1. The central part of the burner is fed with a methane-air-nitrogen mixture and produces a central reactive jet. The external part of the burner can be fed with the same reactive mixture, air or nitrogen. It is used to produce a coflow with different gases composition to modify the mixing layer between the central reactive jet and the annular flow. A set of grids and a honey comb produce a laminar flow at the central and annular outlets. A water cooled plate made of copper with a diameter $D = 100$ mm can be approached close to the burner outlet using a micrometric displacement system. The plate to burner outlet distance was fixed to $H = 24.2$ mm. Its temperature was kept roughly constant at about 70 °C.

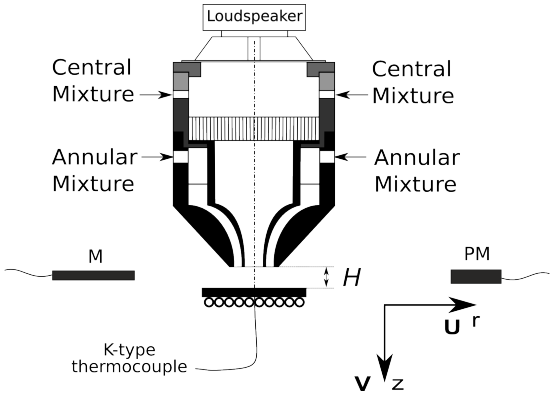

Figure 5.1: Experimental setup. Central flow diameter $D = 20$ mm, Burner to plate distance $H = 24.2$ mm. Photomultiplier PM to burner axis distance = 660 mm, Microphone M to burner axis distance $r = 320$ mm

In this chapter, flowrates were adjusted to yield always the same mean bulk velocities $V = 1.33\,\mathrm{m\,s^{-1}}$ in the central outlet and $V = 0.19\,\mathrm{m\,s^{-1}}$ in the

annular outlet. Seven flames A, B, C, D, E, F and G are defined for this analysis and the different cases are presented in table 5.1.

nL h^{-1}	Central flow			
Flames	A - E - F - G	B	C	D
CH_4	128	128	112	112
Air	1280	1120	1120	1280
N_2	0.0	160	176	16
Φ	0.95	1.09	0.95	0.83

nL h^{-1}	Annular flow			
Flames	A	B - E	C - F	D - G
CH_4	0.0	0.0	16	16
Air	0.0	160	160	0
N_2	494	334	318	478
Φ	x	0.00	0.95	x

Table 5.1: Definition of flames A, B, C, D, E, F and G

The same overall flowrate of air, plus nitrogen and methane in the central and the annular flows are used for flames A, B, C and D. Sound production is thus compared between flames A, B, C and D that only differ by the gases composition distribution between the central and the annular flows. Since only volumetric flowrates were kept constant, impulsion ratios J between central and annular flows differ. But differences are lower than 2% between these four configurations and one can consider that these different cases correspond to stagnation flows featuring the same shear layer between the central and the annular flows but with different mixing layers between these coflows. Flame A features an annular non-reacting flow (with 100 $\%$ nitrogen), flame B to an air diluted with nitrogen annular flow (with 32 $\%$ of air and 68 $\%$ of nitrogen), flame C to a methane-air-nitrogen mixture annular flow with the same equivalence ratio $\Phi = 0.95$ as in the central jet and flame D to a methane-nitrogen annular flow with the same quantity of methane as in case C.

Flames E, F and G are defined with central flow of flame A, and with respectively annular flowrates of flames B, C and D. As a consequence, overall flowrates of air, plus nitrogen and methane in the central and the annular flows do not remain exactly the same as for flames A, B, C and D. These last cases enable to investigate effects of the annular flow on sound production for a fixed central flow.

To sum up, flames A, B, C and D are used to investigate effects on sound production of the gas repartition between the annular and central flows and flames A, E, F and G are used to study effects on sound production of the gas composition of the annular flow. All of these experiments are carried out for the same flow velocity inlet conditions and for flames submitted to the same perturbation, so that only sound produced by combustion is hereby investigated. During steady operations, flames take typical strained flat shapes presented in figure 5.2. Images were obtained using CH^* chemiluminescence emission after Abel transform to get the trace of the flame front in the symmetry plane of the burner. The velocity flowfield in this figure is represented in this figure by black arrows. For clarity reason, only one vector for every 9 cells is represented in these plots.

A difference of gas composition in the central flows leads to different flame velocities and therefore the flame fronts lie at different distances from the burner outlet. Flames A, E, F and G stand around $z = 16$ mm whereas flames B, C and D stand significantly closer to the plate (18 mm $\lesssim z \lesssim 21$ mm). These differences in location can be put into relation with flame speed calculations conducted with the Chemkin package using the detailed GRI Mech 3.0 kinetic scheme. Using $T = 25$ °C and $P = 1$ atm, the flame speed calculations are given in table 5.2 for central flowrates of flames A, B, C and D.

Central flow	S_L [m s^{-1}]
A, E, F, G	0.363
B	0.264
C	0.251
D	0.284

Table 5.2: Flame speed calculations performed for the different central flow compositions.

Flames A, E, F and G stand close to the burner outlet because the flame speed S_L is high. This contrasts with flames B, C and D which lie closer to the plate because the associated flame speed is smaller.

The central and the annular outlets are both fed with the same ratio of oxidizer and fuel flowrates and the region where gases are well premixed spreads over its maximal radial extension (figures 5.2c, Flame C). The flame remains planar over a large radial distance. When the annular outlet is fed with air or nitrogen, a mixing layer is formed (figures 5.2a 5.2b, Flames A and B). The flame remains premixed and planar in its central part, but it is radially

shortened because of progressive dilution with the annular gases. Flame A is shorter than B, C and D. Flames E, F and G look very similar to flame A except at the periphery region because they have the same composition of the central flowrates.

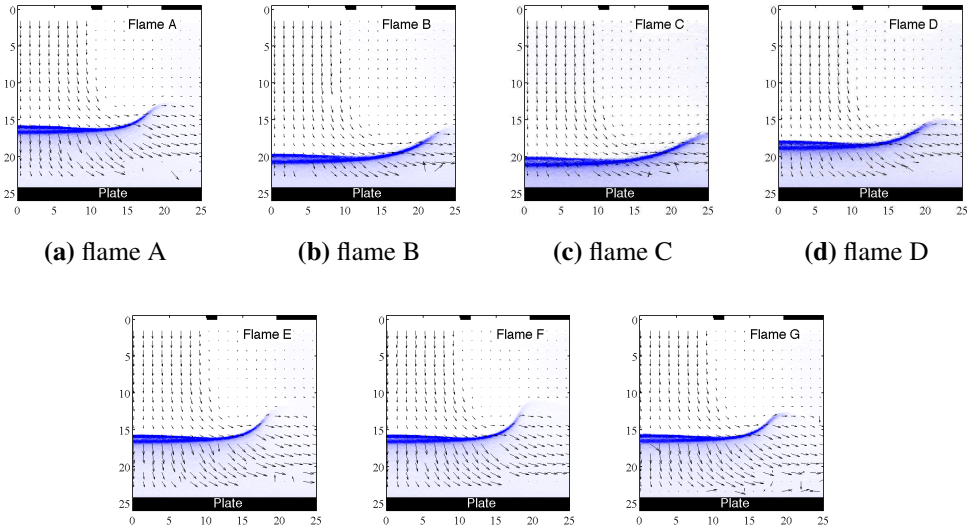

(a) flame A **(b)** flame B **(c)** flame C **(d)** flame D

(e) flame E **(f)** flame F **(g)** flame G

Figure 5.2: Steady flame shapes. Chemiluminescence signal obtained after Abel transformation represented in blue. The bottom of each image corresponds to the position of the plate. At the top are indicated the position of the central and the annular burner outlets. Available velocity flowfield obtained by PIV is represented by black arrows (1 vector out of 9 represented). The scale is given by velocity vectors at burner outlet.

A loudspeaker placed at the top of the burner is used to produce harmonic modulations of the central flow at fixed forcing frequencies. The annular flow was not modulated in these experiments. For certain frequencies, a vortex is formed in the shear layer between the central and the annular flows and is transported towards the flame. For a modulation frequency $f = 55$ Hz, the size of the vortex produced is large enough to detail its interaction with the flame. The velocity field in the central and annular flows were characterized using Particle Imaging Velocimetry (PIV) on solid particles of oxide of zirconium (ZrO_2) seeded within flow to get access to the velocity field in the fresh and hot burnt gases. A single point measurement at $z_R = 3.5$ mm below the burner outlet section on the burner axis was used to control the modulation level using LDV. All experiments have been carried out in the same pulsating

conditions. Relative velocity fluctuation rate on the axis at $z_R = 3.5$ mm from burner outlet is constantly equal to 20%, $v_{rms}/\overline{v} =$ 0.20. Transport and interaction with the flame of the large structures produced at the burner outlet were characterized using PIV (figures 5.4 and 5.5). Induced flame motions were recorded using an intensified CCD camera equipped with a CH^* filter. Conditional phase averaged images of these interactions were obtained with an integration time of 20 µs over 100 snapshots. Integrated chemiluminescence emission and noise radiation signals were also recorded during unsteady operations using a photomultiplier (PM) equipped with a narrow band filter centred on CH^* radical emission and a microphone M located at $r = 320$ mm away from the burner axis (figure 5.1). A TTL output from the signal synthesizer recorded to drive the loudspeaker is used to synchronize all the diagnostics together (LDV, PIV, ICCD camera, photomultiplier PM and microphone M). Further details on these diagnostics are given in chapter 2.

5.4 Noise radiation

The noise radiated and the light emitted by the flame were recorded for the seven configurations investigated when the flow is submitted to harmonic modulations. These experiments were conducted with a sampling frequency of 8,192 Hz and signals were recorded over 8 seconds to allow statistical spectral analysis. The time lag τ (equation (5.2)) between sound source in the reacting region and the pressure signal recorded by the microphone M was estimated assuming uniform acoustic propagation over 30 mm at the flame temperature and the rest remaining at an ambient temperature. Cyclic evolutions of the sound pressure p' and the time derivative of the PM signal dI'/dt are plotted over a forcing period after conditional average over 440 periods in figure 5.3. The pressure signal p' is shifted in time in these plots using the estimated value for the time lag $\tau = 0.91$ ms. These conditional averages were obtained with a reference corresponding to the rising edge of the TTL signal from the synthesizer output at $f = 55$ Hz. The phase 0 corresponds to a vortex generation at the burner outlet. These signals were also low pass filtered with a cut-off frequency $f_c = 2$ kHz to remove high frequency noise.

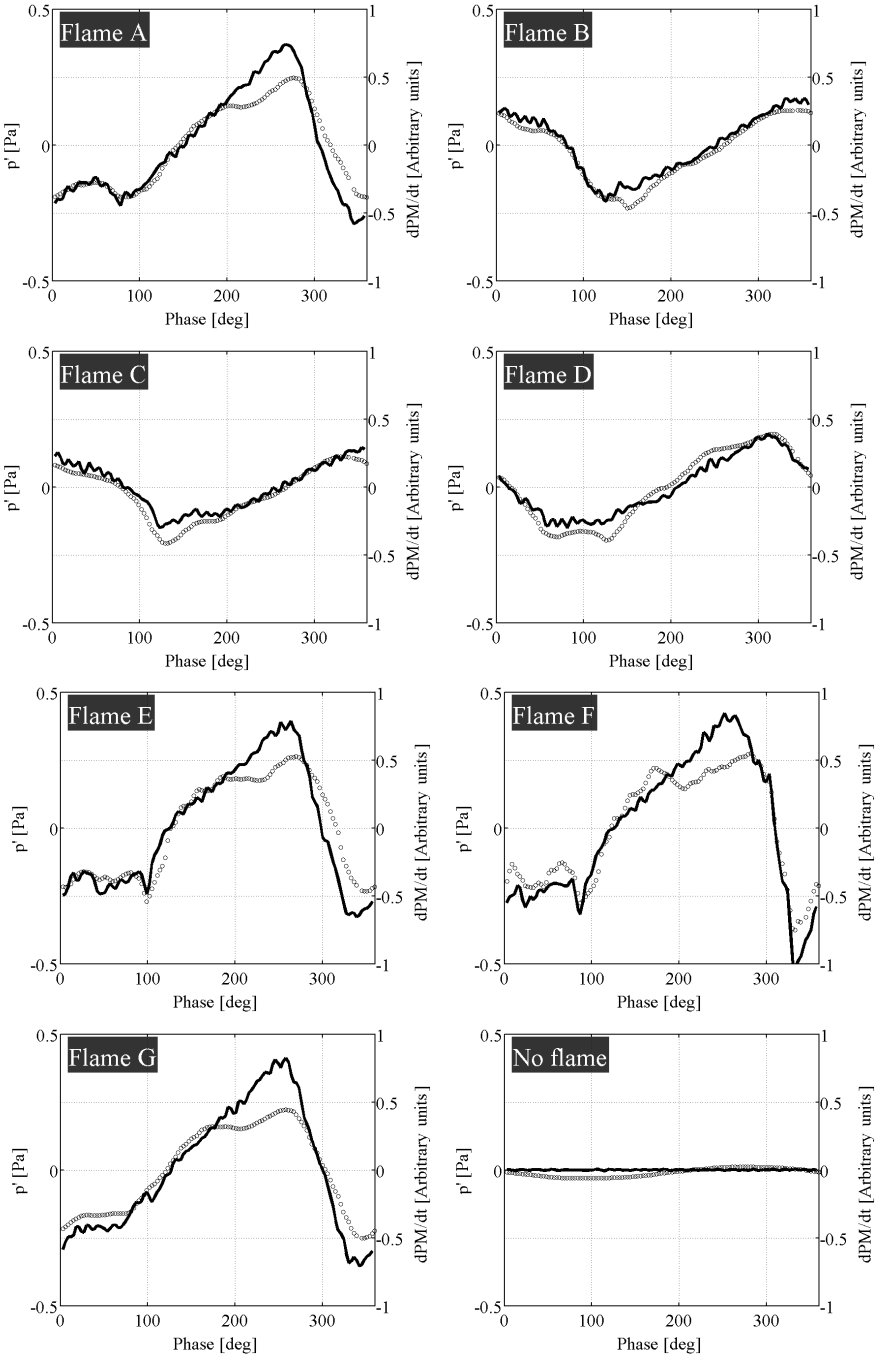

Figure 5.3: Time rate of change of the chemiluminescence signal dI'/dt plotted with the sound pressure $p'(t-\tau)$ recorded by the microphone M. τ corresponds to the propagation time from the compact source to the microphone location. Signals are low-pass filtered (2 kHz) and the phase is defined relative to vortex generation at the burner mouth. $f = 55$ Hz, $(v_{rms}/\overline{v})_R = 0.20$.

It is worth noting that the radiated sound pressure and the time derivative of the PM signals always satisfy reasonably well equation 5.2 even if these flames are partially premixed at their periphery with different surrounding gases. This first shows that the relation between the pressure and the time ratio of change of chemiluminescence is also valid for the configurations explored which are not perfectly premixed.

Table 5.3 gathers some elements on the sound pressure signals. It is indicated the phases corresponding to sound pressure extrema in the cycle within an accuracy of 12 deg. The overall sound pressure level integrating all frequencies and the narrowband noise SPL@ 55Hz corresponding to the sound level radiated at the forcing frequency $f = 55$ Hz are also indicated. The sound pressure level (SPL) is defined in decibel (dB) by $20\ \log_{10}(p_{rms}/p_{ref})$ with $p_{ref} = 20.10^{-6}$ Pa.

Flame	no flame	A	B	C	D	E	F	G
Phase [deg] of p'_{max}		279	339	336	315	270	280	261
Phase [deg] of p'_{min}		0	150	129	128	348	333	345
SPL [dB]	70.8	78.5	76.8	76.1	77.5	80.1	80.8	79.0
SPL@ 55 Hz [dB]	55.0	74.0	71.8	70.1	73.2	75.5	75.9	74.5
sound rank		4	6	7	5	2	1	3

Table 5.3: Sound emission characteristics by flames A, B, C, D, E, F and G for a modulation at $f = 55$ Hz and $(v_{rms}/\overline{v})_R = 0.20$. Phases are relative to the generation of a vortex at the burner outlet. The overall SPL and the narrowband SPL@55 Hz are also indicated. With loudspeaker off, the SPL is about 72.7 dB and SPL@55 Hz equals about 44 dB

Under steady operations without loudspeaker, the SPL measured in the laboratory is identical for all the flames. It is equal to SPL = 72.7 dB and SPL@55 Hz = 44 dB. The overall SPL measured for a modulated non-reacting mixture under the same flow and forcing conditions is 70.8 dB. With combustion and under modulation, the overall SPL increases of about 5 to 10 dB depending on the configuration considered compared to the non reactive flow. It is thus clear that noise due to combustion is produced in the present configuration. The same conclusion is valid for the sound produced at the forcing frequency (SPL@ 55Hz). It is found that flames E, F, G are noiser than flame A which is itself slightly louder than flames D, B and C.

Figure 5.3 shows that the noisy flames A, E, F and G have different sound

emission signatures compared to flames B, C and D. Flames B, C and D signatures are characterized by relatively smooth shapes approaching that of a sine wave. Flames A, E, F and G have steeper gradients, especially in the negative part of the signal. In addition to the larger amplitudes of fluctuations, a phase lag between the sound signatures of flames A, E, F, G and flames B, C, D is also noticeable. This phase shift has no consequence on sound production and is only due to differences in flame position inducing a time shift in flame/vortex interactions. It can be observed that for flames A, E, F and G, the radiated sound pressure and the time derivative of the PM signals do not match exactly for phases comprised between 200 and 300 deg. This difference might be due to the composition of central flow or to an acoustic effect of the plate close to these flames. It would be interesting to further investigate this point in a future study.

The same type of experiments were conducted for different modulation levels $v_{rms}/\overline{v} =$ 0.15 - 0.10 - 0.05. They yielded similar results which are presented in Duchaine et al. (2009). It is however difficult to remove background noise from the signals when the modulation level is reduced.

5.5 Flow and flame dynamics

The evolution of both the flame and the flow dynamics are presented in figures 5.4 and 5.5. To study the strength and position of the vortices, the swirling strength criterion λ_{ci}, defined as imaginary portion of the complex eigenvalue of the local velocity gradient tensor, is calculated. This criterion is not sensitive to shear stress and therefore is representative of the swirling motion induced by coherent structures as already discussed in chapter 3. The swirling strength λ_{ci} is represented by magenta iso-lines in figures 5.4 and 5.5. The flame contour after inverse Abel transformation and a filtering procedure using a 3x3 pixels^2 Wiener filter is represented with a blue scale. Only half burner has been imaged to improve the precision of the measurements. A previous analysis conducted by Duchaine et al. (2009) has shown that the configuration is symmetric with respect to the burner axis. Velocity measurements were obtained using an averaged correlation on 100 pairs of images with windows of 16x16 pixels^2, representing a physical interrogation zone of 1x1 mm^2. Velocity vectors with a SNR, defined as the ratio of the first and second cross-correlation peaks, below 3 have been removed. These latter vectors indeed correspond to poorly seeded areas.

It is important to note that the initial vortex generated is identical, both in space and strength, in all the seven configurations explored. This is illustrated on the top of figures 5.4 and 5.5 for a phase of 0 deg. This again shows that experiments were carried out under the same forcing conditions and for the same initial flow perturbations. It is clearly visible that the flow is dominated by large coherent structures shed from the central burner lip and impinging the flame periphery further downstream. As the vortex travels downstream, it takes gases from the annular flow to the central flow.

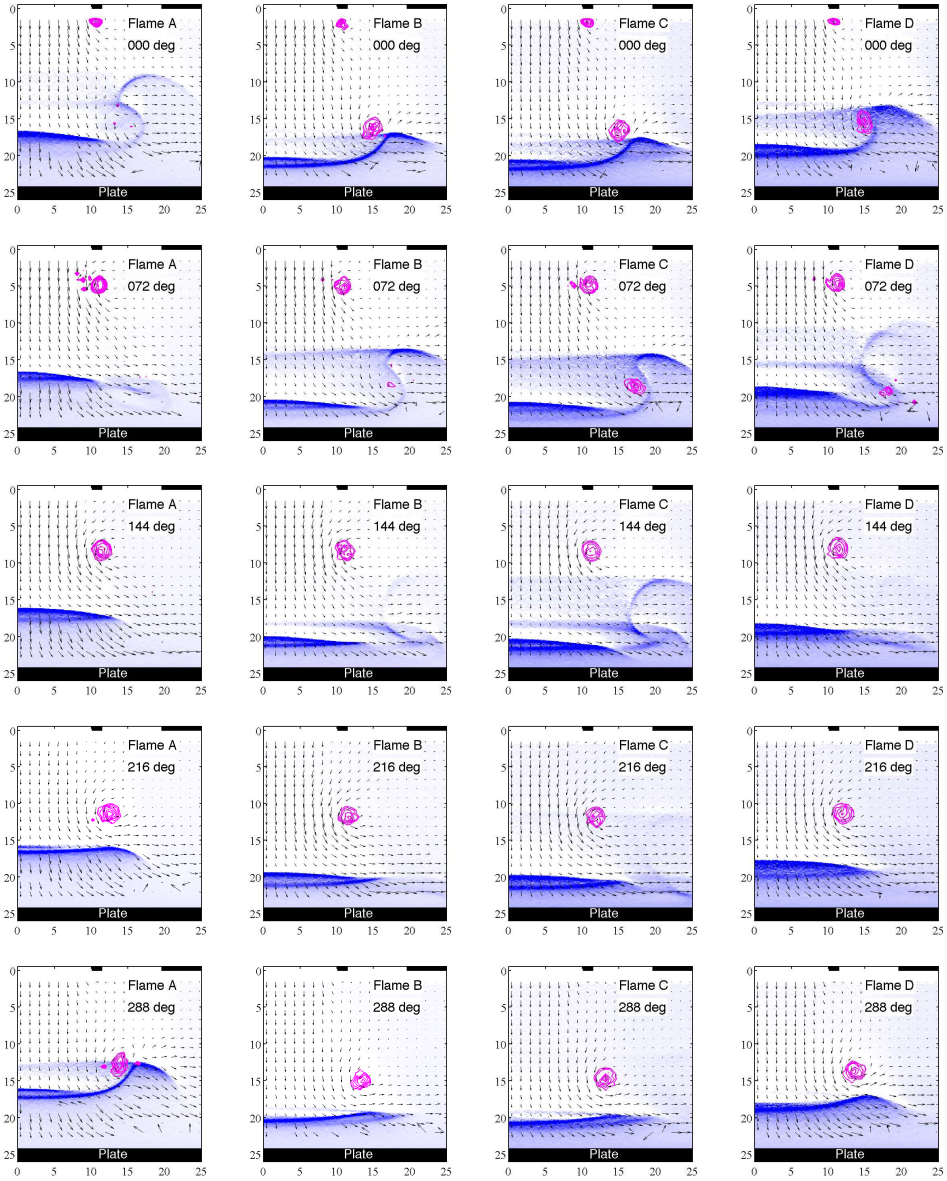

Figure 5.4: Flames A, B, C and D (from left to right). Frequency of excitation $f = 55$ Hz with 20 % of velocity fluctuations level $(v_{rms}/\overline{v})_R = 0.20$. Vectors represent phased locked PIV (1 vector over 9). Swirling strength λ_{ci} is represented as magenta contour. Chemiluminescence signal obtained after inverse Abel transformation is represented by a blue scale. The bottom of each image corresponds to the position of the plate

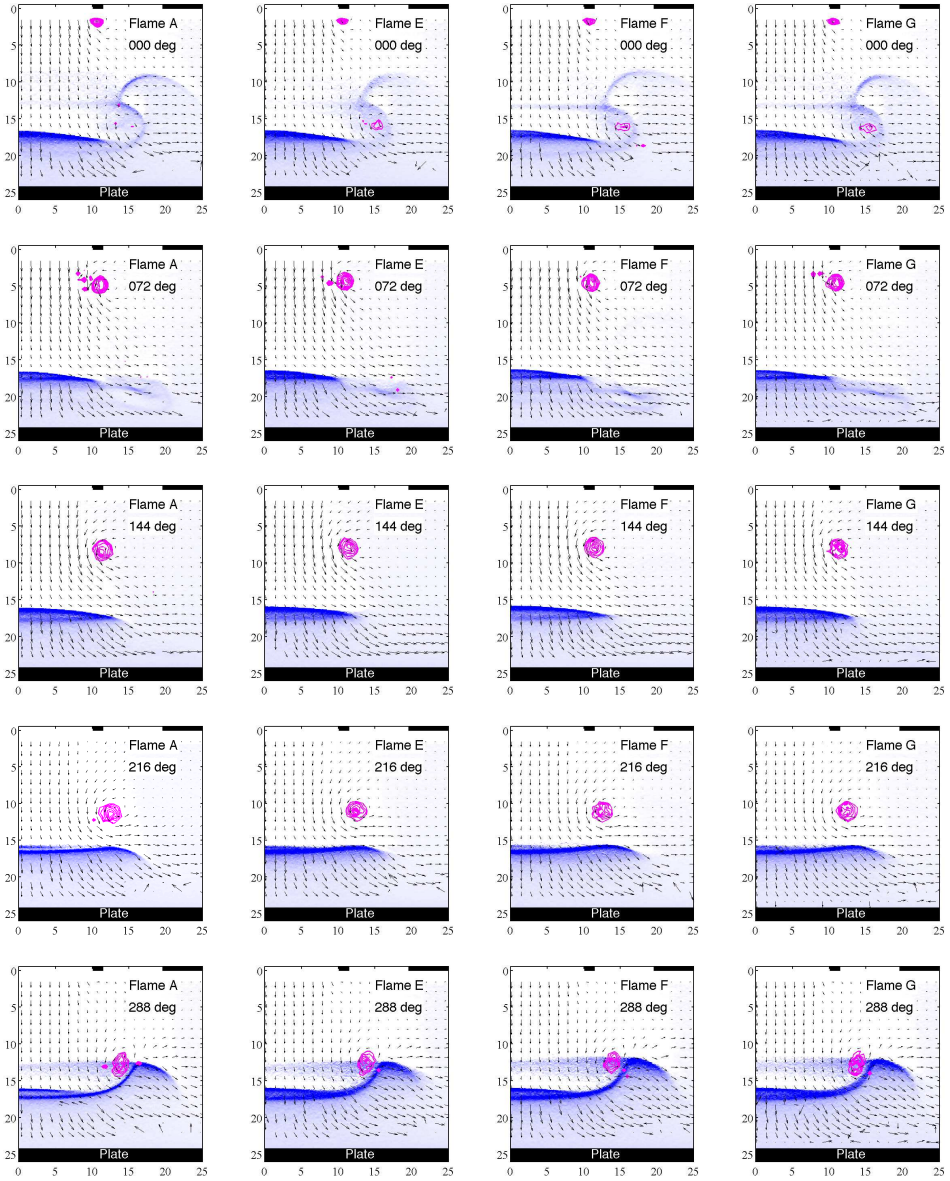

Figure 5.5: Flames A, E, F and G (from left to right). Frequency of excitation $f = 55$ Hz with 20 % of velocity fluctuations level $(v_{rms}/\overline{v})_R = 0.20$. Vectors represent phased locked PIV (1 vector over 9). Swirling strength λ_{ci} is represented as magenta contour. Chemiluminescence signal obtained after inverse Abel transformation is represented by a blue scale. The bottom of each image corresponds to the position of the plate

Figure 5.6 presents trajectories of vortices during a forcing period. Positions of local maxima of swirling strength λ_{ci} are plotted on the right for flames A, B, C, D and on the left for flames A, E, F and G.

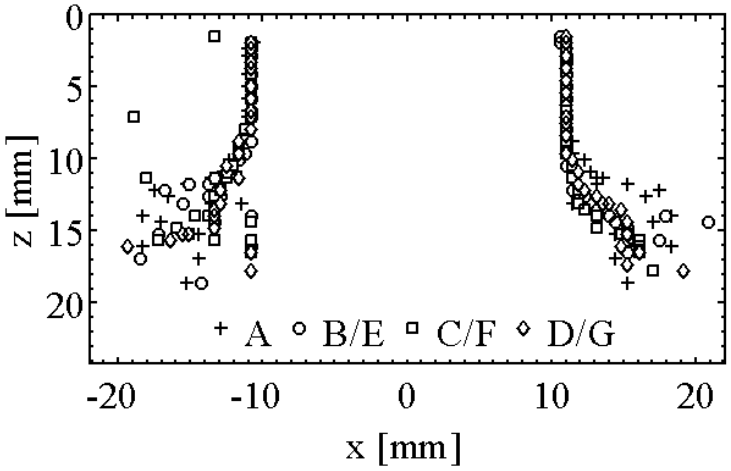

Figure 5.6: Trajectories of maxima of swirling strength λ_{ci} - on the right, flames A, B, C and D - on the left, flames A, E, F, G

It is first shown that the vortex ring is generated at the same location for the seven flames. Two parts can be identified in these trajectories. Between $z =$ 3 mm and $z = 12$ mm for flames A, E, F G and between $z = 3$ mm and $z = 16$ mm for flames B, C, D, the vortex ring is generated and convected along the flow. Beyond these values, the vortex ring interacts with the flame and its trajectory is deviated towards the periphery due to the expansion of the burnt gases, before disappearing. These trajectories are as expected very similar between all these flames, because the mean flowfield conditions and the perturbation conditions are the same and only the flame position might vary between the different cases.

Figure 5.7 presents the evolution of the swirling strength λ_{ci} over two forcing periods. The microphone signal p' is also plotted on the top of these graphs. The minima of p' correspond to important flame surface destructions instants, i.e. to instants where a vortex ring cuts the flame tips.

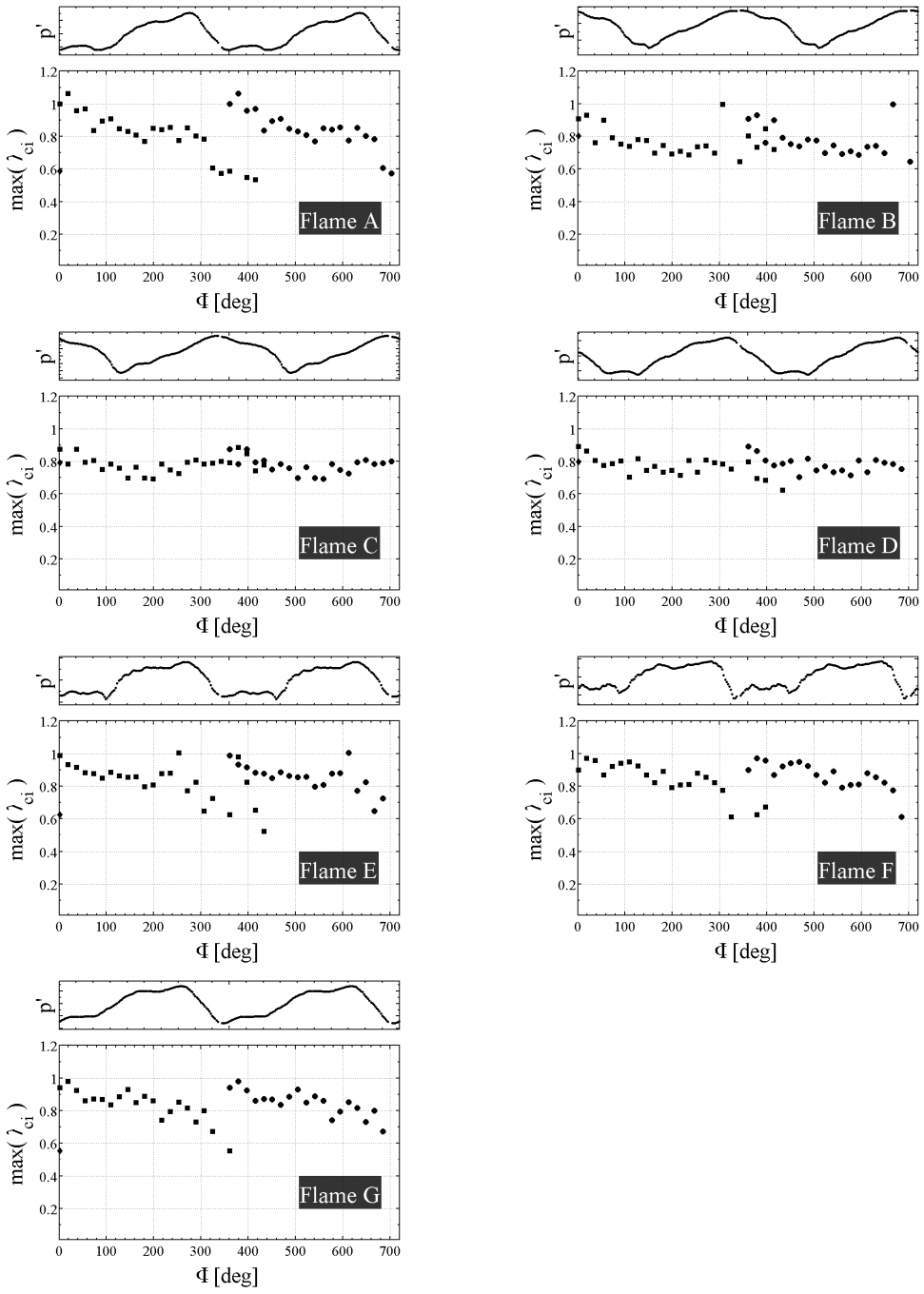

Figure 5.7: Representation of the maxima of swirling strength λ_{ci} in arbitrary units over two periods of excitation (normalized by initial value of flame A). Diamond, square and disk symbols are used for vortex rings successively shed at burner mouth. Shape of microphone signal p' (shifted to account for the propagation delay from the flame to the microphone) is reminded on top sub-plot. The phase is defined relative to vortex generation at the burner mouth. $f = 55$ Hz, $(v_{rms}/\overline{v})_R = 0.20$.

The features of the seven flames are successively commented and analysed relative to the previously introduced tables and figures. The focus is placed on analysing the differences in vortex/flame interactions and their consequences on sound production.

Flame A

A vortex is approaching the flame front for a phase of 216 deg. It then enrols the flame at its periphery (phase 288 deg). One can then notice a change in the shape of the flame front, from concave to convex. This event corresponds to a positive pressure peak in table 5.3 and figure 5.3. Further downstream, the vortex interacts with the flame front, which tends to expand in the radial direction under its influence. However, only nitrogen is available in the annular flow and therefore, the flame cannot penetrate inside this co-flow. The flame is then moved upstream due to available fresh mixture. The vortex still follows its initial direction and finally, for a phase comprised between 360+0 deg and 360+72 deg, flame elements formed at the periphery are cut from the central part due to the vortex strength. These instants correspond to the largest negative pressure peak observed in figure 5.3. The instant of sudden extinction of the flame by the vortex creates a large deficit of heat release rate because this occurs at the flame periphery. This constitutes an important source of noise. The maximal positive pressure peak for flame A is found for a phase around 279 deg, which corresponds to the initial influence of the vortex stretching the flame. The heat release rate is then increased due to a sudden burning of fresh reactants with the creation of a new flame front and leads also to a maximum of radial expansion of the fresh gases. As shown in figure 5.7, the vortex strength remains roughly constant from its generation to the flame, then suddenly, the vortex intensity decreases constantly between 300 deg and 360+20 deg. As a conclusion, the positive pressure peak has been identified as being the consequence of the combustion of fresh reactants by entrainment of hot gases (Mahan J.R. (1991)) and the negative pressure sink for the extinction of the flame due to the vortex travelling through the flame front (Durox et al. (2005)). These are the two predominant mechanisms of noise production for this flame.

Flame B

The dynamics of this interaction follows that described for flame A during the first part of the cycle. However, the interaction with the flame front occurs later in the cycle for phases larger than 288 deg. The curvature at the flame periph-

ery is less pronounced compared to flame A. The fresh mixture that is trapped within the vortex is pushed on the outer part of the flow. As air is available in the annular flow, combustion can take place because the mixture of the central flow is relatively rich. The flame changes from flat to a cup shape with a relatively intense combustion taking place at the edge (360+70 deg). The vortex still containing fresh gases is finally able to disrupt the flame and a secondary flame is formed in the outer part (360+72 deg). This secondary flame finally disappears for a phase comprised between 360+144 and 360+216 deg. When comparing those events with peaks and sinks of the sound pressure signals in figure 5.3, it can be seen that the sink is again linked with a local extinction due to vortex/flame interaction (360+144 deg). The positive peak is found for the initial influence of the vortex, which is stretching the flame surface and hence increasing the heat release rate (360 deg). The main sources of sound are thus similar to those prevailing in the case of flame A. The phases and intensities are different due respectively to a change in the position of the flame front and to the modification of the gases composition of the surrounding flow. Addition of oxygen in the annular flow leads to a flame-vortex interaction which last a longer period during the cycle reducing the net sound output compared to a neutral gas. This is exemplified by phase differences between pressure extrema in table 5.3. Flame B features extrema separated almost by half a period, whereas this delay is reduced to 81 degrees for flame A. One also notices in figure 5.7 that the vortex strength remains roughly constant from its generation to its extinction. Unlike flame A, a decrease in vortex strength is not noticeable, which proves that the vortex lives a bit longer.

Flame C

The flow and flame patterns are relatively similar to the case of flame B, but the flame has a wider radial expansion, certainly because a methane-air mixture is now also available in the annular flow. The phenomena of flame surface destruction and flame stretch do not seem to feature any phase delay between flame B and C responses. They exhibit only small differences as far as radial expansion is concerned. Addition of methane in the annular flow leads to pressure or time derivative of the PM signal (figure 5.3) featuring almost the same shape as for a co-flow of air-nitrogen (figure 5.3), with extrema events separated by the same phase differences in the cycle (table 5.3). However, amplitudes of fluctuations are slightly lower for this last interaction. For phases comprised between 360+24 and 360+124 degrees, the time rate of change of the PM signal in figure 5.3 decreases faster for flame B than for flame C, denoting that flame destruction due to entrainment of air takes place over a

shorter time period than entrainment of methane-air mixture under the same vortex strength influence. This mechanism may explain the slightly lower SPL radiated by flame B.

Flame D

The dynamics of the flow and flame are relatively similar to the cases of flames B and C during the interaction with the vortex. The presence of methane and nitrogen in the annular flow leads to a sound signature or a time derivative of the PM signal (figure 5.3) featuring almost the same shape as for a co-flow of air-nitrogen, with extrema events separated by the same phase differences in the cycle (table 5.3). The flame position is a bit closer to the burner exhaust than for flames B and C, therefore the interaction is slightly shifted in time during the cycle (figure 5.3). The lifetime of the vortex generated in this case is larger than for flame A, leading to a smoother fluctuation of the flame intensity signal and to a lower sound level than for flame A. This interaction is very similar to flame B. The vortex strength stays roughly constant during its lifetime (figure 5.7). As a conclusion, the addition of methane in the annular flow seems to support combustion when the vortex ring cuts the flame tips and as a consequence it tends to reduce combustion noise production.

Flames E, F and G

These flames are characterized by different global quantities of methane, air and nitrogen than the other four previous configurations explored. As a consequence, one should be extremely careful making comparisons of sound production since the configuration can be affected not only by sound production mechanisms but also by total quantity of reactants. However, these configurations can be very helpful to understand the role of the annular flow composition in the sound production mechanisms.
It is interesting to note that the evolutions of chemiluminescence signal and pressure fluctuations (figure 5.3) are very similar to flame A, probably due to the same position of these flames with respect to the burner outlet. These three flames are all louder than flame A, showing that an addition of air or methane in the shroud, keeping the central flow identical, increases production of sound. Interestingly, the loudest flame is F with a mixture of methane and air in the annular flow which is the mixture the most likely to bring some more combustion and therefore noise. In the meantime, flame C with the same annular mixture as flame F is the quietest flame. It is difficult to directly compare flames C and F since the total quantity of methane and air is not kept constant.

However, two counter-effects can be identified in the mechanisms of sound production in case of flame C. On one hand, the addition of air and methane in the annular flow increases the sound output, as observed when comparing flames A and F. On the other hand, the depletion of air and methane in the central flow reduces the sound output, as observed when comparing flames A and C. Since flame C is the quietest flame, it seems that the latter phenomenon prevails. One can also note that a sharp decrease in vortex intensity for flames E, F and G is observed in figure 5.7 from a phase of 300 deg showing that vortex ring sharply cuts the flame and thus induces a high noise level.

5.6 Conclusion and Perspectives

The sound generated by seven different partially premixed flames interacting with a train of vortices of controlled strength has been studied. No striking differences in the sound production mechanisms could be found between a methane-air mixture encompassed by pure nitrogen compared to configurations where oxygen, methane or methane-air were also added to the co-flow. The flame having a co-flow of pure nitrogen produces the loudest sound output due to the sudden extinction of the flame that was enrolled over the vortex. Methane or air trapped within the vortex was found to lead to slightly higher noise levels than entrainment of methane-air mixture because this interaction leads to shorter interaction delays in these specific cases. Considering partially premixed turbulent flames, one may conjecture that regions of air entrainment into the reaction zone may be at the origin of larger noise output than perfectly premixed regions.

It was also found that the proportionality between the radiated sound pressure and time derivative of the emission signals from CH^* radicals established for perfectly premixed systems remains reasonably well satisfied for the partially premixed configurations explored. This is an interesting result that may be useful to study noise production from other partially premixed combustion systems. The conclusions found in this chapter should however first be validated by other experiments over wider operating conditions, including an investigation at different forcing frequencies to vary the size of the impinging vortex and an analysis of modifications induced by different equivalence ratios within the annular and the central flows.

In future works, it would be interesting to quantify precisely the gas composition within the vortex during its interaction with the flame tips. Experiments

based on Acetone LIF were carried out. Data obtained in these configurations can however not be used to clearly conclude on the local concentration of combustible within the vortex. This type of measurement required to reach a precision level for the quantification of the combustible concentrations greater than the actual relative differences between annular flowrates of different flames.

To investigate further sound production by partially premixed flames, one suggests to slightly modify the experimental configuration. Indeed, one major progress would be to get rid of the influence of the plate whose acoustic role is difficult to take into account. For this purpose one possibility would be to study flames being at the same distance of the plate. In this case, the plate would have the same role for the different cases explored. This is however difficult to comply with keeping simultaneously the total flowrates and flame-plate distance constant. Another possibility would be to work with an inert counterflow instead of a plate and analyse the differences observed with and without the plate. The counterflow would play a minor role in the acoustics, and it would thus enable the study of combustion noise production without the plate reflections.

Part III

Dynamics of a spray in a jet and in a reactive flow

As mentionned in the introduction, in many practical burners, such as gas turbines for example, the fuel is introduced in liquid phase. It is first atomized to form a cloud of droplets and interacts with the air flow which is generally swirled to obtain compact flames (see figure 1). Modelling of two-phase reactive flows plays therefore a key role in progress of combustion science. Many challenges are associated with the modelling of such two-phase configurations because complex physical phenomena like the evaporation of sprays and the spray interaction with the turbulent flow and flame should be taken into account. In this case again, detailed experiments come as a key input in the understanding of fundamental physical mechanisms, and as a benchmark for comparisons with simulations in well-controlled configurations.

Fundamental experiments are therefore valuable to collect quantitative data on interactions of sprays with vortices and flame. This kind of simple and well controlled configurations also enables a better understanding of the different contributing mechanisms. Among them, the interaction of a vortex with a laminar flat flame can be used to investigate a number of features that are common in turbulent combustion such as stretch or extinction effects. In the experimental field, efforts have been made in the last decades to reach rapid and reliable measurements of vapour concentration around droplets, together with concentration around droplets, together with information on the droplets dynamics. Numerous laser-based techniques have been developed for the separate characterization of either vapour or droplets. These vapour sensing techniques include laser Rayleigh scattering (Zhao and Ladommatos (1998)), spontaneous Raman spectroscopy (Zhao and Ladommatos (1998)), laser-induced fluorescence (Zhao and Ladommatos (1998); Thurber and Hanson (2001); Lavieille et al. (2001); Orain et al. (2005)), spectrally resolved absorption spectroscopy (Ma et al. (2002)). Characterization of the droplet dynamics includes the measurement of laser extinction (Dobbins and Jizmagian (1966)), laser phase Doppler anemometry (Bachalo (1994)) and interferometric particle imaging (Damaschke et al. (2005)). Each technique has its own advantages and disadvantages and is useful for a certain domain of applications. However, these techniques are generally not transferable to the simultaneous monitoring of both vapour and liquid droplet properties. Some vapour sensing techniques, based on elastic scattering such as the Rayleigh scattering or based on fluorescence such as LIF, can be extended to measure both vapour and droplet concentrations. But, usually light scattering from droplets greatly exceeds that from the vapour, therefore jeopardizing or even prohibiting accurate estimates on the vapour measurements. A similar analysis makes tough the direct combination of two measurement techniques, each dedicated to a specific phase, for

simultaneous vapour and droplet characterization. Despite these challenges, a few laser-based diagnostic techniques have been attempted for simultaneous characterization of the vapour and liquid phases originating from droplets. Laser Induced Exciplex Fluorescence (LIEF) developed by Melton (Melton (1983)) enables simultaneous two-dimensional imaging of the vapour and liquid phase distribution in a light sheet, under limited conditions. Besides implementation difficulties, the LIEF signal is difficult to quantify, and quenching from oxygen limits most of the LIEF applications to nitrogen environments (Desantes et al. (2005)). Also, Chraplyvy (1981) proposed an alternative technique and applied a method based on a two-wavelengths laser extinction strategy to measure vapour concentration and droplet volume fraction simultaneously in an evaporating fuel spray.

The scope of the present experimental study is to analyse effects of unsteadiness on the fuel vapour distribution originating from liquid droplets injected in a flow either released in a free environment, or impinging on a planar diffusion flame. These configurations feature controlled conditions where large coherent vortices can be created by modulation of the outlet flow which are then convected with the flow. These interactions encompass furthermore many challenges for numerical simulations with a polydisperse spray interacting with an unsteady reactive flow. Simulations have already been envisaged in a non reactive configuration where the distribution of evaporating droplets in a pulsated jet has been calculated using Eulerian multi-fluid models (Laurent and Massot (2001)) and predictions were shown in good agreement with detailed experiments (Freret et al. (2009)).

Two experimental configurations were explored in this part. The first is described in chapters 6 and 7 and consists in an hexane spray carried away by a nitrogen flow which can be modulated. The second configuration described in chapter 8, enables the study of a two-phase diffusion flame of heptane. In both cases, studies are conducted for steady and pulsated flow configurations.

In chapter 6, the focus is put on the study in the steady conditions, a first necessary step for the characterization of the inert spray properties.The following chapter 7 focuses on the study of the pulsated inert spray. In chapter 8, a dilute two-phase diffusive heptane flame is studied thanks to a set of diagnostics including Laser Induced Fluorescence.

Chapter 6

Steady inert two-phase jet

In this chapter, the dynamics of an inert hexane spray in a gaseous jet flow is characterized in steady conditions. For this purpose, a collection of diagnostics are used to investigate the flow velocity, the droplets velocity and droplets size distribution in these flows, as well as the distribution of the vapour and liquid of the fuel. Among them, a Laser Induced Exciplex Fluorescence (LIEF) technique has been used to discriminate the fluorescence emitted by the vapour and the liquid phases. This method is applied here to obtain quantitative fields of concentration of vapour and liquid phases in a laminar two-phase flow. In the next chapter, the same two-phase flow will be studied under external flow modulations.

6.1 Experimental setup

Experiments are carried out on the two-phase bench described in chapter 1. A schematic view of this setup and notations used this part are reminded in figure 6.1. In this section, the velocity flowfield will be characterized using cylindrical coordinates (O, r, z), where r is the distance to the burner axis and z is the vertical distance measured from the burner outlet and O is located at the burner outlet on its axis. When needed, the planar coordinates (O, x, z) are also used where x is the algebraic distance to the burner axis along a given diameter of the burner. A honey comb and the converging unit are used to obtain a perfectly laminar flow at burner outlet.

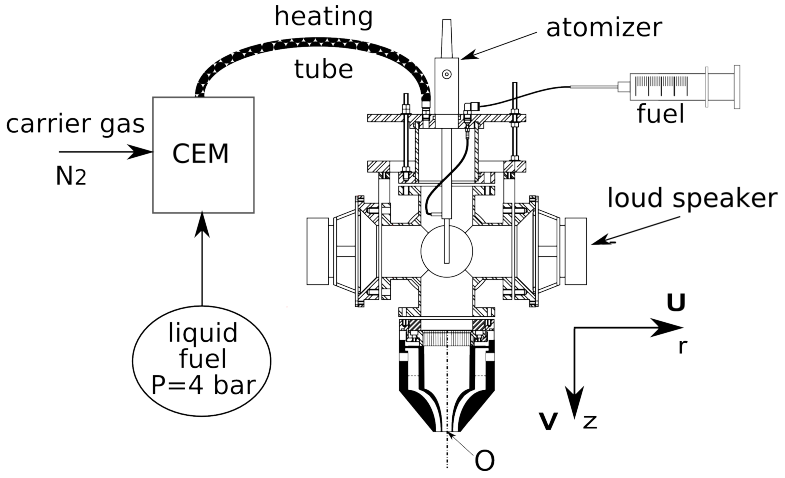

Figure 6.1: Experimental setup used to generate the two-phase flow. The mixture of fuel and tracer is pushed either via a syringe into an ultrasonic atomizer generating a cloud of micronic droplets, or via an evaporator - A central flow of nitrogen N_2 carries away the cloud of droplets to the nozzle - An inert annular flowrate of nitrogen N_2 encompasses the central flow - The origin O of the local coordinate system (O, r, z) is fixed on burner axis at the outlet

An inert two-phase flow at ambient temperature is investigated in the chapters 6 and 7. All the traced fuel is injected through the atomizer in these experiments. Flowrates of hexane C_6H_{14} and nitrogen N_2 in the central and annular outlets are indicated in Table 6.1. The flowrates conditions of the two-phase diffusion flame will be presented in chapter 8. The evaporating system (CEM in figure 6.1) is only used in chapter 8 for the study of a two-phase diffusion flame.

	Fluid	Flowrate	
Central	traced C_6H_{14}	218 mL/h	153 g/h
	N_2	636 nL/h	795 g/h
Annular	N_2	500 nL/h	625 g/h

Table 6.1: Liquid and gaseous flowrates in the two-phase inert configuration - A liquid flowrate of n-hexane C_6H_{14} is atomized in inert N_2 central flow. No fuel is sent to the evaporator. An annular inert flow encompasses the latter - Experiments are done at ambient temperatures

Injection of N_2 with the liquid phase results in gaseous mean flow velocity $V = 0.64$ m s^{-1} in the central flow and $V = 0.19$ m s^{-1} in the annular flow

with plug flow profiles at burner outlet. The liquid mixture is composed of 89% n-hexane, 9% DEMA and 2% FB in volume. The choice of n-hexane as liquid fuel and FB and DEMA as tracers is justified by an extensive bibliographic study presented in chapter 2. The mixture is prepared in advance and stored in hermetically closed glass containers. The fuel is only injected via the atomizer, the evaporating system being not used for the studies conducted in chapters 6 and 7.

A preliminary parametric study has been performed to choose the best experimental conditions to generate the spray interacting with an unsteady jet flow. It was found that the amplitude of voltage supplying the loudspeaker for the modulated experiments had to be chosen in a limited range to get well defined vortices. This study was thus carried out for a unique value of the modulation amplitude. It was also verified that changes of the modulation frequency f lead to the generation of vortices of different sizes. In this study, the focus is put on the investigation of large vortex rings. As a consequence, the forcing frequency was fixed to $f = 28.125$ Hz yielding a Strouhal number $\mathrm{St_D} = fD/V$ equal to the unity.
The fluctuation level of velocity was controlled with LDV near the burner outlet on the axis (point R, $z_R = 3.5$ mm). It was fixed at a relatively high value to ensure the generation of strong vortex rings at burner lips: $(v_{rms}/\overline{v})_R = 0.30$. It was also found that the liquid flowrate had only a minor influence on the droplet size distribution. As a result, the liquid flowrate was kept constant throughout these experiments. Adjustement of the value used for the annular flowrate results from a compromise to ensure a good protection of the central flow from the external oxidant and to yield a nice shape of the vortex rings generated at the burner outlet.

In these conditions, the Reynolds number of the central gaseous flow is equal to Re = 715. Axial velocity profiles measured at burner outlet of the purely gaseous flows in the steady flow feature very low temporal fluctuation level (less than 2 %) which is partly due to the presence of the honey comb and the converging unit.

6.2 Settings of measurement methods

6.2.1 PDA setup

A Phase Doppler Anemometry (PDA) system is used for measurements of diameters and velocities of droplets generated in the flow by the ultrasonic atomizer at burner outlet. These measurements are useful in particular to provide boundary conditions for simulations and are used as a benchmark for the analysis of Interferometric Particle Imaging (IPI) size measurements.
Details on the system are given in chapter 2 in particular on the calibration procedure via an internal diode. With the chosen set of parameters, the range of possible diameter measurements spans from 0.5 to 80 µm. The optical propagation index of n-hexane $n_{C_6H_{14}} = 1.375$ is used for diameter calculations. The measurement data rate of validated droplets is about 150 Hz. The acquisition lasts a sufficiently long time to collect information over more than 20,000 droplets at each position in the steady and pulsated conditions. Measurements are carried out every 2 mm along a diameter in steady and pulsated configurations. In pulsated conditions, the TTL signal from the wave generator is recorded simultaneously enabling phase-conditioned processing of the measurements.

6.2.2 PIV and PTV setups

Particle Imaging Velocimetry (PIV) measurements were done on the pure gaseous flow in the steady configuration and for 20 phases in the modulation cycle in the pulsated configuration. These measurements are needed for the simulation of the configuration and to build up typical trajectories of the vapour phase fluid particles.
For this purpose, the central and annular flows of pure nitrogen are seeded with micronic oil droplets with the system presented in chapter 3. A PIV system is set up as described in chapter 2 (scheme 2.2). In the steady configuration and for 20 phase positions in the pulsated configuration at $f = 28.125$ Hz, one hundred pairs of images have been recorded. The delay between the two laser shots is set to $\delta t = 193$ µs so that the mean displacement is about 8 pixels. The pairs of Mie scattering images have been cross-correlated on windows of 32x32 pixels^2 with an overlap of 25% with the Dantec software FlowManager v.4.71.05. Only the average of the cross-correlation results is finally considered providing smooth velocity fields without requiring the use of filters to remove outliers. The precision of the displacement measurement,

knowing that peak locking has been prevented, can be estimated at about 0.1 pixel (Westerweel (1997)). This corresponds to relative incertitude on velocity measurement of about 1.25%. PIV measurements yield velocity fields in the zone defined by $-20 \leq x \leq 20$ mm and $2 \leq z \leq 36$ mm. It is important to note that these measurements correspond to a pure nitrogen flow without fuel vapour. However since the maximum quantity of fuel represents only 5.8% of the total central flowrate (by assuming a complete evaporation), one can consider that PIV measurements yield also with a good accuracy the velocity field of the studied configuration with the spray.

The liquid velocity field is determined via Particle Image Velocimetry (PTV) on the images taken by the focused camera B of the IPI setup. The determination of the droplets velocity via the PTV algorithm is done with interrogation windows of 128 pixels and an overlap ratio of 50 %. A filter based on the possible range of velocities is applied to improve the quality of the results. Velocities above 1 m s^{-1} are rejected because they are considered as non representative of real droplets velocities. For the calculation of mean trajectories of liquid particles, another kind of processing from the Mie scattering images has been used because the velocity fields obtained by PTV always contain some wrong vectors prohibiting the correct reconstruction of the droplets trajectories. For this purpose, the pairs of Mie scattering images have been processed with an average correlation and interrogation windows of 32x32 $pixels^2$. Details on this average correlation are given in chapter 2.

6.2.3 Mie scattering and LIEF setups

A system composed of a laser and an ICCD camera is set up around the experimental bench to carry out measurements of Mie scattering signal and measurements on vapour and liquid phases via Laser Induced Exciplex Fluorescence (LIEF) as presented in chapter 2 (scheme 2.11). An identical setup is used for FB fluorescence measurements on pure vapour flow of hexane in chapter 8. The complete setup and fundamental principles of the exciplex fluorescence are presented in details in chapter 2.
As indicated in table 2.4, adequate filters were used in front of the camera and measurements are averaged over a large number of acquisitions. In the following, some experiments conducted to determine the regime of vapour LIF measurements and the spectra of vapour and liquid fluorescences are presented. The calibration procedure leading to the absolute quantification of the vapour concentration from LIF measurements is also presented in details.

LIF regime versus laser energy density

In chapter 2, the fundamental principles of fluorescence were presented. It appears that the fluorescence signal features different regimes, namely linear, saturated or intermediate regimes, depending on the duration and the energy of the laser pulse (Eckbreth (1996)). It is important to determine in which regimes the experiments were carried out to know if laser shot fluctuations lead to fluctuations of the fluorescence signal recorded on instantaneous acquisitions. In the present experimental configuration, given the long duration of the laser pulse, it is certain that the fluorescence signal is saturated versus the duration of the laser pulse. This is not so obvious when considering the energy density. The evolution of the fluorescence signal versus the energy of the laser pulse needs to be characterized to determine the fluorescence regime versus laser energy. These experiments are hereby presented.

Traced n-hexane is injected into the burner as vapour with the same flowrates conditions as in the real experiment. Measurements were conducted by setting successively the power of laser from its normal operating conditions (35 mJ per pulse) to the lowest available energy operating conditions (5 mJ per pulse) by steps of 5 mJ per pulse. An averaged image is calculated from one hundred instantaneous acquisitions with the HP266 and BP290 filters mounted on. The fluorescence signal averaged in regions of 10x10 mm^2 versus the energy per pulse is presented in figure 6.2.

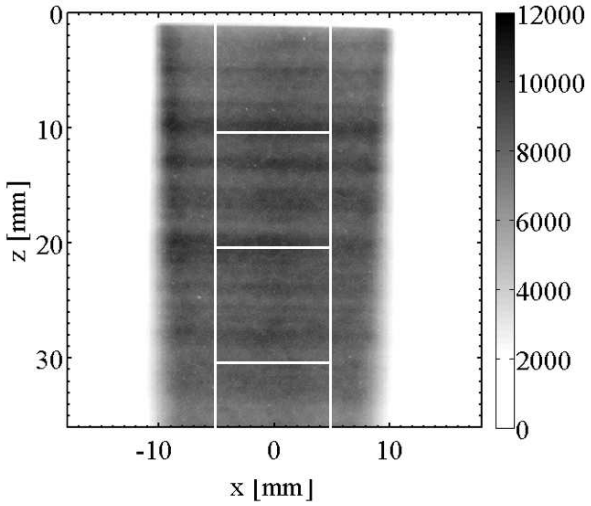

(a) Mean acquisition image in counts. White squares indicate areas over which signal is averaged.

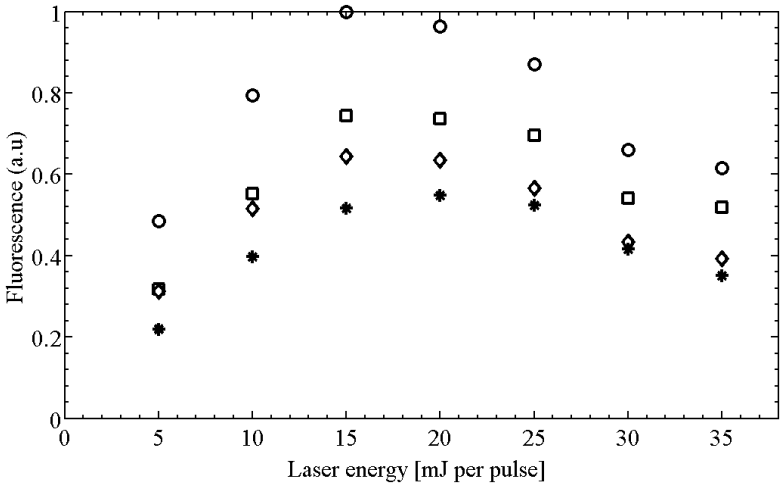

(b) Behaviour of mean fluorescence image versus energy density

Figure 6.2: Mean LIEF vapour signal versus energy per pulse in mJ per pulse - Signal is averaged on the axis for respectively regions of 10x10 mm^2 centred around $z \simeq 5$ mm (square), $z \simeq 15$ mm (circle), $z \simeq 25$ mm (diamond), $z \simeq 35$ mm (star) from 100 acquisitions

The vapour fluorescence signal averaged on regions centred on the burner centreline follows always the same types of evolution depending on the laser energy deposit. The signal increases from 5 to 20 mJ per pulse before slightly

decreasing from 20 to 35 mJ per pulse. This evolution suggests that the fluorescence signal emitted by the vapour does not truly reach saturated conditions relative to the energy deposit. As a consequence, shot to shot measurements can not be relied on for quantification since fluctuations in laser energy shots would lead to variations of the collected vapour fluorescence signal. In the present study, only averaged measurements over a large number of measurements, typically 100 acquisitions, are considered. It has been verified that an average over a set of 100 images of the fluorescence signal with the ICCD camera is sufficient to reach a dispersion of the results lower than 1% of the measured signal (similarly to the study presented in figure 6.9).
The differences in fluorescence signals at different z-coordinates, indicated by square, circle, diamond and star symbols, put into evidence a non-homogeneity of the laser sheet in the vertical direction. These vertical inhomogeneities are corrected by a calibration procedure for measurements of vapour concentrations.

Spectra of vapour and liquid fluorescences

A special care is taken to measure vapour and liquid fluorescence spectra of the traced fuel in order to validate the use of the presented interference filters. This is conducted with a spectrometer to characterize the fluorescence spectra of signals emitted from the vapour and liquid phases. A grating of 600 lines mm^{-1} has been used leading to a spectral resolution of 0.25 nm on a domain covering 130 nm with a slit aperture of 150 µm. The aperture parameters corresponding to the gate width gw and gate delay gd of the spectrometer were set to equivalent values as for the ICCD camera collecting the fluorescence signal. Spectra in this section were established from measurements on three separate windows. The spectrometer has been calibrated with a Mercury lamp.

Vapour fluorescence spectrum An optical fibre mounted on the spectrometer images the atomized flow coming out from the burner. The bare laser beam cuts the viewfield in order to obtain the best signal to noise ratio. Since the spray is very dilute, the major part of the fluorescence signal results from the vapour and this experiment is thus well suited to characterize the vapour spectrum. Figure 6.3 presents measured spectra right after the laser pulse (black line) and for acquisition windows delayed respectively of 10 ns (successive gray lines). The signal obtained in the same conditions without any tracer is also plotted (black dotted line) indicating the noise level in these measurements.

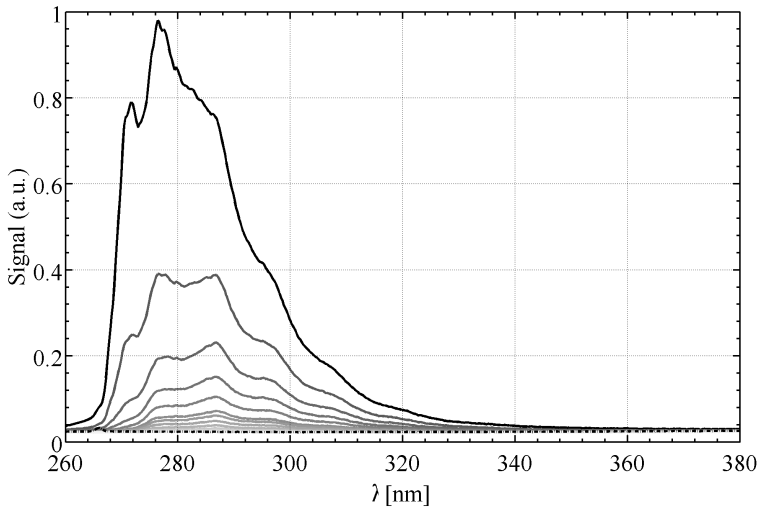

Figure 6.3: Vapour fluorescence spectrum collected while imaging the atomized flow of a mixture of n-hexane traced with 9% DEMA and 2 %FB in volume. The black curve corresponds to the signal measured right after a laser pulse. Each other gray curve corresponds to data collected delayed by 10 ns. Black dotted line corresponds to measurements within a pure nitrogen flow. Data are averaged over 100 shots.

A strong fluorescence signal is measured on a wave band centred around 290 nm. This observation is in agreement with the analysis of the literature (Duewel et al. (2009)) and corresponds to the fluorescence signal of the Fluorobenzene (FB) tracer excited at 266 nm. The temporal evolution of fluorescence over 100 ns shows that the fluorescence signal lasts about 40 ns. The fluorescence signal level measured 50 ns after the laser pulse has diminished to the background noise level. The use of BP290 filter is adapted because the maximum of fluorescence signal lies close to 290 nm. It is also worth noting the absence of any spurious light at 266 nm, which shows that the signal only corresponds to the fluorescence emission.

Liquid spectrum The liquid fluorescence spectrum could not be obtained in the same conditions because the liquid volume fraction of the studied spray remains globally too small even if the liquid signal can be very strong locally. Another experiment was conducted to infer the liquid fluorescence spectrum. A 10x10 mm^2 quartz cell is filled with the mixture of hexane and tracers. The

optical fibre connected to the spectrometer images now the quartz cell. A special care was paid to the positionning of the liquid cell to minimize absorption effects. Since absorption through the liquid is very strong, a correct signal can only be measured if the optical fibre images an interrogation zone close to the entry of the laser beam into the liquid.

Figure 6.4 presents the measured spectrum right after the laser pulse. The liquid fluorescence signal spans over a large waveband between 350 and 450 nm. One also notices two strong peaks of the laser light at 532 and 266 nm.

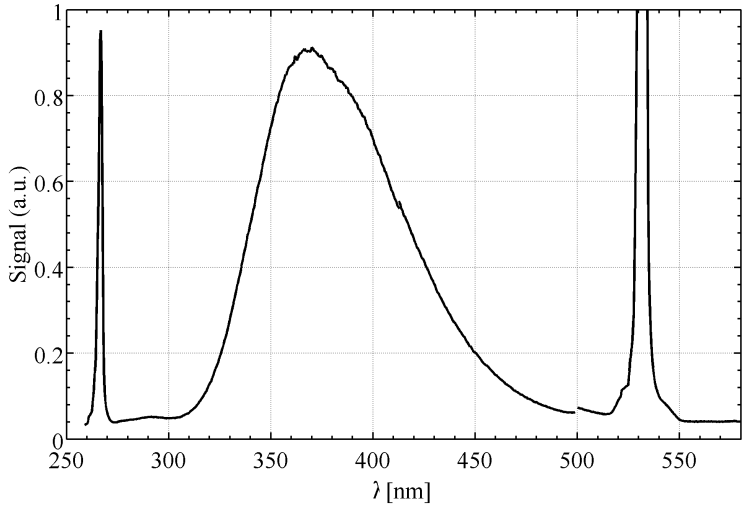

Figure 6.4: Liquid spectrum collected while imaging a quartz cell filled with a liquid mixture of n-hexane traced with 9% DEMA and 2% FB in volume.

Calibration for vapour concentration measurements

A calibration procedure was conducted to get access to the absolute concentration of the fuel vapour via fluorescence measurements. This calibration of the fluorescence signal is carried out in a test cell which composition is precisely controlled. The calibration cell is equipped with four quartz windows of 100 mm diameter to enable optical access to the laser sheet and visualization of the fluorescence signal. The whole calibration procedure is carried out at ambient temperature. Figure 6.5 presents the corresponding experimental configuration. The cell is filled with a given concentration of mixture of hexane and tracers and placed in the viewfield of the camera. The conditions at which the

laser and the camera are operated are exactly the same as the ones used for in-situ measurements.

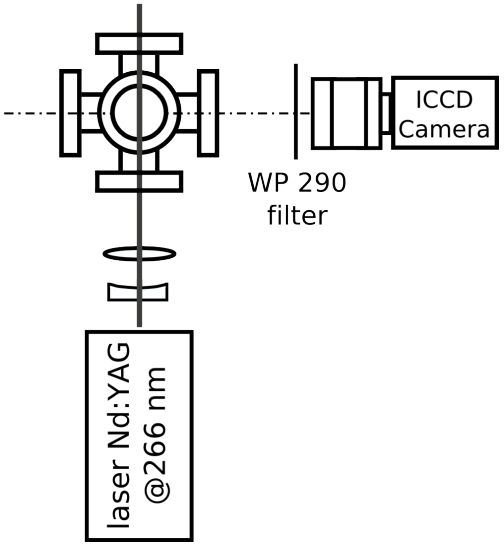

Figure 6.5: Experimental setup for the calibration of vapour fluorescence signal: the cell is filled with a given concentration of hexane and tracers and placed in the viewfield of the camera. The laser and acquisition parameters are the same as for in-situ measurements

Mixtures of different concentrations below the dew point of hexane are prepared in 5 litre-cylinders at ambient temperature. First a vacuum pump is used to empty completely the cylinder down to a pressure of 100 Pa. Then a quantity of traced hexane corresponding to the desired concentration is injected into the empty cylinder using a micro-syringe. Pure nitrogen is then injected into the cylinder up to a pressure above the ambient value. All the mixtures injected in the cylinder remain strictly below the saturation pressure of hexane to ensure that no liquid may appear in the cylinder. A pressure of 1.5 bar in the cylinder has been chosen in these experiments. This pressure enables investigation over 66% of the range below saturation pressure once injected into the cell at ambient pressure. In order to ensure a well-homogenized mixture before the injection into the calibration cell, a procedure is cautiously respected. The cylinders are stored in the horizontal position in the lab. Five minutes before use, the cylinder is put in the vertical position in a hot water bucket, so that the temperature gradients help to the mixing of the content of the cylinder. The content of the cylinder is then injected into the calibration cell, up to a pressure of 1 bar measured with a manometer with an accuracy of 200 Pa.

In order to prevent the liquid formation of hexane in the cylinder, the partial pressure of hexane $P^{cyl}_{C_6H_{14}}$ should stay below the saturation pressure of hexane $P^{sat}_{C_6H_{14}}$ at the corresponding temperature $T_a = 20$ °C.

$$P^{cyl}_{C_6H_{14}} \overset{def}{=} \frac{n_{C_6H_{14}}}{n_{N_2} + n_{C_6H_{14}}}.P_{cyl} \tag{6.1}$$

$$\overset{ideal\ gas}{=} \frac{\rho_{C_6H_{14}} V_{inj}}{M_{C_6H_{14}}} \frac{RT}{V_{cyl}} < P^{sat}_{C_6H_{14}} \tag{6.2}$$

with V_{inj} represents the injected volume of traced hexane in the volume V_{cyl} of the cylinder, P_{cyl} is the pressure in the cylinder. At $T_a = 20$ °C, the saturation pressure of hexane is $P^{sat}_{C_6H_{14}} = 4700$ Pa.

Considering a perfect mixing process in the cylinder, the mixture injected from the cylinder induces a concentration of traced hexane $[C_6H_{14}]_{cell}$ in the cell, which can be written as:

$$[C_6H_{14}]_{cell} = \underbrace{\frac{n_{C_6H_{14}}}{V_{cyl}}}_{(1)} \underbrace{\frac{P_{atm}}{P_{cyl}}}_{(2)} = \frac{V_{inj}\ \rho_{C_6H_{14}}}{M_{C_6H_{14}}} \frac{P_{atm}}{V_{cyl}.P_{cyl}} \tag{6.3}$$

The term (1) represents the concentration of hexane in the cylinder and the term (2) corresponds to the dilution ratio of the cylinder content into the calibration cell and P_{atm} is the ambient pressure.

The injected volume of traced hexane V_{inj}, the partial pressure of hexane in the cylinder $P^{cyl}_{C_6H_{14}}$, the corresponding concentration of hexane once injected in the calibration cell $[C_6H_{14}]_{cell}$ and the partial pressure of hexane in the calibration cell $P^{cell}_{C_6H_{14}}$ are reported in table 6.2 for the six mixtures used in the calibration procedure.

In these six tests, the partial pressure of hexane $P_{C_6H_{14}}$ remains always below the saturated level $P^{sat}_{C_6H_{14}}$ inside the cylinder and inside the calibration cell. This ensures that no liquid may appear due to condensation both inside the cylinder and the cell. The cylinder is prepared at a pressure higher than the ambient value to allow the filling of the calibration cell. This process enables the investigation of only 66% of the pressure range below saturation. The calibration curves will be extrapolated linearly in the non investigated domain. Several sets of one hundred acquisitions are recorded in the exact same con-

n°	V_{inj} µL	$P^{cyl}_{C_6H_{14}}$ Pa	$[C_6H_{14}]_{cell}$ mmol L^{-1}	$P^{cell}_{C_6H_{14}}$ Pa
0	0	0	0	0.0
1	300	998	0.27	665
2	600	1,996	0.55	1,330
3	900	2,994	0.82	1,996
4	1200	3,927	1.11	2,661
5	1400	4,658	1.32	3,105

Table 6.2: Characteristics of the six tests used in the calibration procedure: the injected volume of traced hexane V_{inj}, the partial pressure of hexane in the cylinder $P^{cyl}_{C_6H_{14}}$, the corresponding concentration once injected in the calibration cell $[C_6H_{14}]_{cell}$ and the partial pressure of hexane in the calibration cell $P^{cell}_{C_6H_{14}}$

ditions as for in-situ measurements. Fluorescence images obtained without injection and the calibration cell filled with five mixtures of different concentration are presented in figure 6.6.

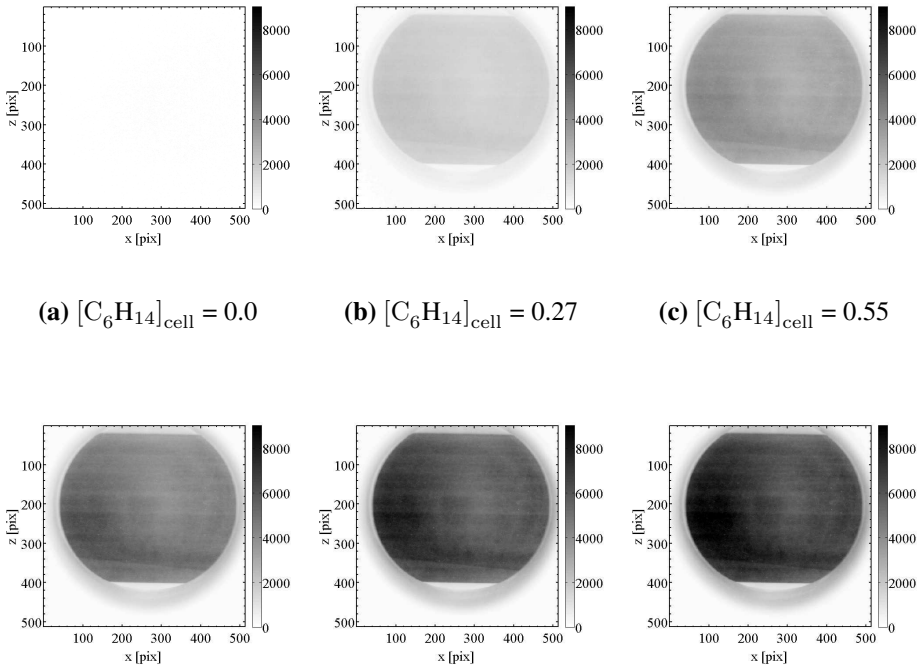

(a) $[C_6H_{14}]_{cell} = 0.0$ **(b)** $[C_6H_{14}]_{cell} = 0.27$ **(c)** $[C_6H_{14}]_{cell} = 0.55$

(d) $[C_6H_{14}]_{cell} = 0.82$ **(e)** $[C_6H_{14}]_{cell} = 1.1$ **(f)** $[C_6H_{14}]_{cell} = 1.3$

Figure 6.6: Mean images over 100 acquisitions of the calibration cell for different values of the concentration $[C_6H_{14}]_{cell}$ of traced hexane (in mmol L^{-1}).

These data are used to obtain calibration curves interpolated between the six measurement points for each pixel of the ICCD camera. Figure 6.7 indicates results obtained for a particular pixel (left) and for the set of all pixels imaging the cell (right). The interpolation curves are also plotted up to the vapour saturation pressure. The plot on the right gives an idea of the dispersion of the response between different pixels. The precision of pressure determined with the manometer ensures an incertitude of ± 0.067 mmol L^{-1} in concentration of hexane. This incertitude is represented with a horizontal error bar.

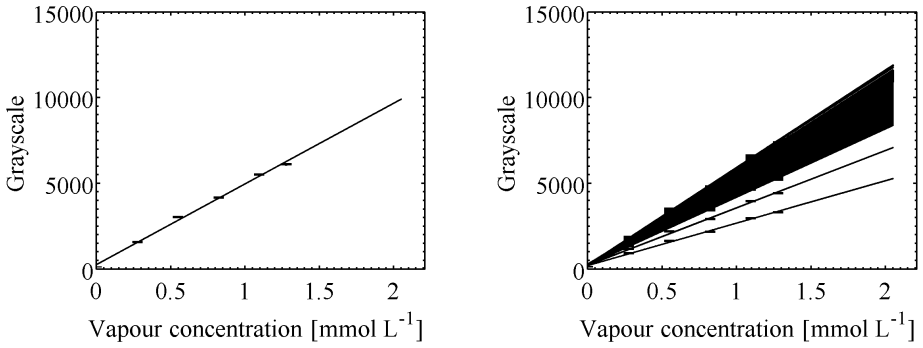

(a) Signal received by a particular pixel

(b) Signal received by all pixels of the view-field

Figure 6.7: Fluorescence signals measured for mixtures with six different concentrations and for pure nitrogen (black cross). The calibration curve is deduced for each pixel by linear interpolation (black line) up to the saturation condition. Each measurement point is represented with an horizontal and a vertical error bar

This calibration procedure enables to free the technique from inhomogeneities of the laser sheet, as well as non homogeneity of the response of the pixels from the camera. After this calibration, some horizontal streaks remained in the image. These streaks only appear for images obtained with the burner and not on images taken with the calibration cell. A second step in the calibration process has been added to minimize effects of these streaks. A 20 liter cylinder has been filled up with a concentration $[C_6H_{14}]$ = 0.82 mmol L^{-1} of doped fuel and diluted in nitrogen up to 1.5 bar. This mixture has then been injected directly into the burner and acquisitions were taken thirty seconds after the mixture contained in the cylinder is flowing through the burner. The data collected are used to carry out a correction on the preceding calibration curves obtained. This correction is used to get rid of the horizontal stripes on the ICCD fluorescence images. It was also verified that the application of the whole calibration procedure including this new correction to the calibration images obtained within the cell yields, uniform images with a grayscale level corresponding to the injected concentration.

The whole calibration process described above enables to relate the intensity of the vapour fluorescence signal to the absolute concentration of the C_6H_{14} vapour phase. A typical raw image obtained after average over 100 acquisitions and its conversion via the calibration procedure into absolute concentrations map is presented in figure 6.8.

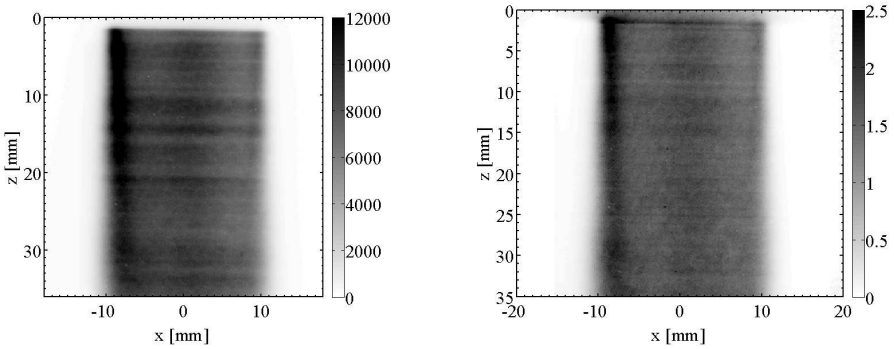

(a) Raw fluorescence signal displayed in counts

(b) Post-processed signal in absolute concentration in mmol L^{-1}

Figure 6.8: Raw and post-processed images of the steady flow jet obtained after averaging over 100 shots.

Convergence study of vapour fluorescence measurements

A study on the convergence of vapour fluorescence measurements is performed to quantify the precision of vapour concentration measurements. Figure 6.9 shows results obtained from the convergence analysis of the mean fluorescence images from the calibration cell over 100 shots on a particular pixel in the central flow close to the burner centreline. For the six concentrations injected in the calibration cell, the cumulative moving average over the 100 shots is reported (black disks). Moreover for the concentration $[C_6H_{14}]_{cell} = 0.82$ mmol L^{-1}, the instantaneous values of the fluorescence signal are reported with black crosses.

The cumulative moving average curves obtained for the six injected concentrations are very flat except for the 30 first shots. This shows that convergence has been reached after averaging over 100 acquisitions. The fluctuation level of the instantaneous values is about 10% as indicated from black crosses. As the vapour fluorescence measurements are performed from averaged values over 100 acquisitions, one can estimate the precision of concentrations determined with 1% of the measured value. This value includes uncertainty due to laser shots and to camera acquisition.

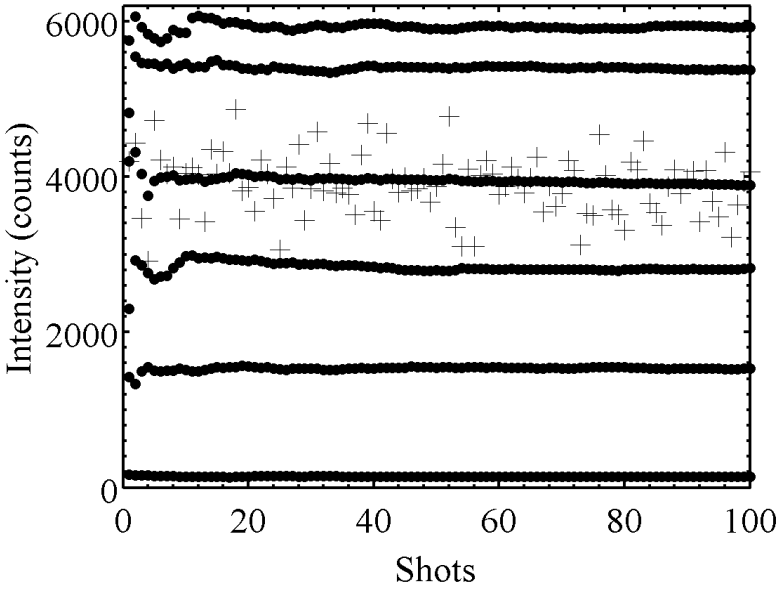

Figure 6.9: Convergence analysis of the mean images from the calibration cell over 100 shots for a particular pixel in the central flow close to the burner centreline. For the six concentrations injected into the calibration cell, the cumulative moving average over 100 shots, i.e. the average between the first and the current shot, is reported (black disks). For the concentration $[C_6H_{14}]_{cell} = 0.82$ mmol L^{-1}, the instantaneous values of the fluorescence signal are reported with black crosses.

6.2.4 IPI setup

The experimental setup for Interferometric Particle Imaging (IPI) comprises a Nd:YAG laser with a doubled crystal yielding a coherent beam at 532 nm and two CCD cameras equipped with 105 mm lenses (figure 6.10). The camera A is placed perpendicular to the laser sheet and records defocused images of the flow. The camera B is placed parallel to the laser sheet and views the scene through a semi-reflective blade. This camera records focused images which are automatically mirrored in the horizontal direction by the driving software. The cameras are tuned to image precisely the same scene, both cameras have been set at a distance of 225 mm perpendicular to the laser sheet. With the chosen geometrical parameters and the defocusing of the lens, the apparent diameter of droplets on the defocused image spans over 35 pixels and each vertical fringe in the droplet represents an equivalent diameter of 6 μm, as already presented in figure 2.6.

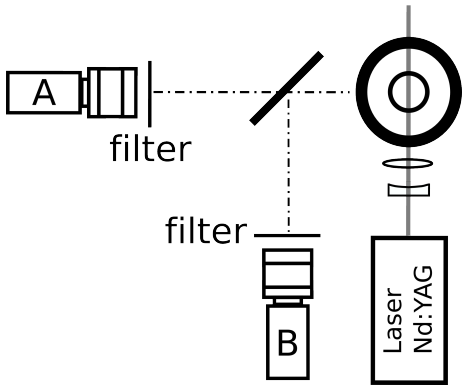

Figure 6.10: Experimental setup for the IPI measurements: CCD camera A records defocused images of the scene directly - CCD camera B records focused images of the scene through a semi-reflective blade

IPI processing requires to set values for different parameters in the Dantec Flowmanager software. These parameters are relative to the the optical setup, the calculation of Fast Fourier Transform (FFT), the velocity settings (PTV) and the validation of droplet diameters.
A parametrical analysis based on images with 16 different droplets has been carried out. This is presented in details in appendix A. A synthesis of the main parameters which have been chosen for the present study are summarized below. A detailed explanation of these choices is given in the appendix.

- the minimal and maximum sizes of defocused particles are respectively set to 30 and 40 pixels. The step size for FFT calculation was set to its minimal value, i.e. to 1 pixel.
- the ratio between the frequencies along the horizontal and vertical directions is set to a minimum value of $F_x/F_z = 5$.
- an allowable overlap of 60% between two droplets was set.
- no criterion based on the minimal distance between two droplets and no image filter were used.

A detailed study from synthetic images on focused and defocused droplets was carried out to investigate the precision of IPI measurements with emphasis on droplet images overlapping effects. This analysis, presented in detail in appendix A, concludes that measurements for diameters from 6 to 60 µm of isolated synthetic droplets are performed with an accuracy of 7% in the present setup. Concerning the effects of overlapping, results show that the software deals with it with a relative precision better than 20% on the measured diameter for an overlap ratio below 60%. For an overlap ratio greater than 60%,

the software does not reach a reliable measurement, therefore the maximum allowable overlap was set to 60%. In the case of droplets overlapping, the relative precision on the determination of droplets diameter is deteriorated from 7% to 20%. Overall, given that the overlap of droplets is not considerable in the studied spray, the precision on droplets diameters measured in these experiments can be estimated at about 10%.

It should also be noted that the droplets with measured diameters on both frames differing of more than 10% are eliminated in the post-processing.

6.3 Measurements in steady conditions

In this section, results for a steady nitrogen jet with a n-heptane spray are presented and commented. First, the central and annular flow structures are presented. The gaseous and liquid velocity fields, the droplets size distribution, the trajectories of gaseous and liquid phases are then presented together with planar visualizations of vapour and liquid phases.

In the following figures relative to the distribution of the droplets sizes, the vertical scale in the plots always represents the percentage of the total number of measured droplets. The droplets are distributed in classes of diameter of 1 μm width.

6.3.1 Flow structure

Figure 6.11 shows mean Mie scattering images of the flow seeded alternatively in the central (left) and in the annular (right) flows with oil particles. The grayscale is normalized and chosen so that level 0 corresponds to the background noise level and 1 corresponds to the maximum pixel intensity.

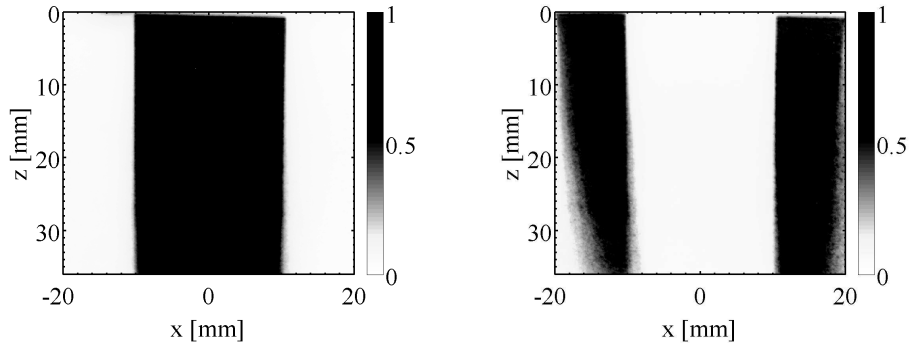

(a) Seeded central flow **(b)** Seeded annular flow

Figure 6.11: Mean Mie scattering images of the flow seeded alternatively in the central (left) and in the annular (right) flows with oil particles.

These two images highlight the position of the central and annular flows. They show that the flow is steady because the central flow remains strictly between $-10 \leq x \leq 10$ in the whole viewfield. One can notice that the annular flow is a bit disturbed for $x \leq -15$. This shows the importance of an annular flow encompassing and protecting the central flow from external flow disturbances. These images also show that ambient air from the environment is not mixed to the central flow, and this guarantees that the exciplex fluorescence signal will not be quenched by molecules of oxygen.

6.3.2 Gaseous and liquid velocity fields

Vapour velocity field

PIV measurements provide velocity fields of the gaseous phase in the whole viewfield with a relative accuracy of 1.25%. LDV measurements were also carried out at burner outlet at $z_R = 3.5$ mm along a radius to characterize the axial velocity profile at this location. Velocity measurements are presented in figure 6.12 where the mean (circle) and the rms fluctuation level of the velocity (squares) obtained from LDV (open symbols) and PIV (filled symbols) are represented. PIV processings only provide a velocity vector per interrogation window with no information on the fluctuation level.

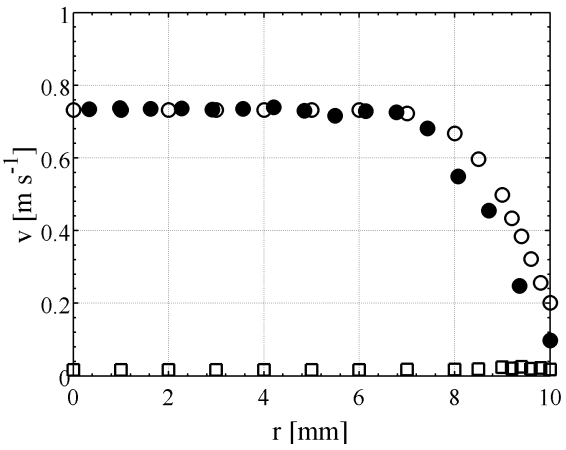

Figure 6.12: Mean (circle) and rms fluctuation level of the axial velocity (square) along the burner radius at $z_R = 3.5$ mm obtained by LDV (open symbols) and PIV (filled symbols)

This axial velocity profile takes a very flat shape for $0 \leq r \leq 8$ mm and rapidly reduces in the shear layer between $8 \leq r \leq 10$ mm. The fluctuation level remains low and is typical of a laminar flow. There is a very good match between LDV and PIV measurements except for $r \geq 8$ mm where PIV measurements decrease a bit faster. This difference is probably due to the fact that PIV measurements are spatially averaged over an interrogation window in the measurement plane (0.7x0.7 mm^2) while LDV measurements are integrated over the collection volume where the two laser beams cross.

Liquid velocity field

Figure 6.13 presents the statistics for the mean axial velocities (circles) and the corresponding rms fluctuation levels (squares) measured for all droplets in the steady flow at $z_R = 3.5$ mm along the burner radius. These data were obtained by PDA every $\Delta r = 2$ mm (open symbols) and by PTV every $\Delta r = 1$ mm (filled symbols).

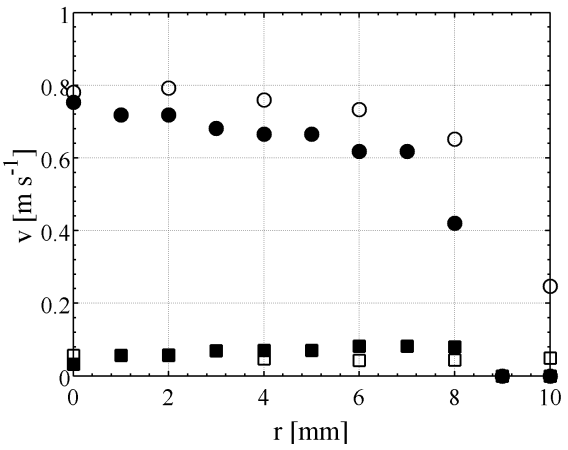

Figure 6.13: Mean axial velocities (circles) and rms fluctuation levels (squares) of droplets of all diameters in the steady flow at $z_R = 3.5$ mm along the burner radius. PDA (open symbols) and PTV (filled symbols)

Both techniques yield roughly the same result. The profile measured via PDA seems a bit more flat over $0 \leq r \leq 8$ mm than the profile measured via PTV. It is worth remembering that PTV results are spatially-averaged on windows (0.7x0.7 mm^2) whereas PDA measurements are pointwise.

The distribution of the vertical droplet velocity v versus the droplet diameter d for PDA measurements along a burner radius is presented in figure 6.14. This plot shows that no significant correlation between sizes and velocities of droplets at the burner outlet can be established.

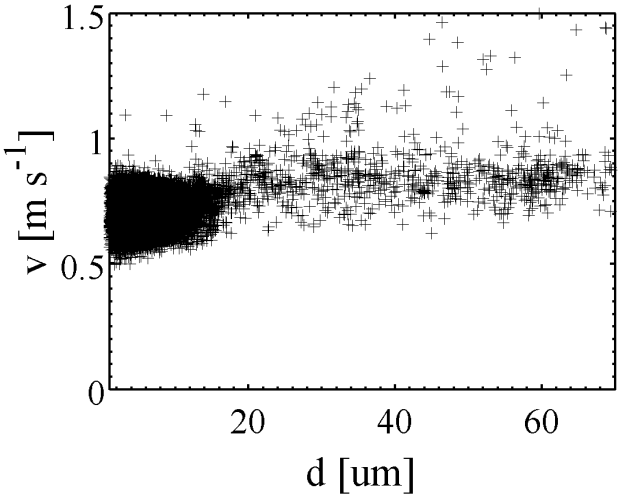

Figure 6.14: Distribution of vertical droplet velocity versus the droplet diameter for measurement via PDA along a burner radius

6.3.3 Droplet size distribution

The statistics of the droplets size distribution can be examined using global describing parameters like the arithmetic diameter d_{10}, the surface diameter d_{20} and the volumetric diameter d_{30}. These diameters are defined for a collection of N droplets of respective diameters $d_i, i \in [1, N]$ as:

$$d_{10} = \frac{1}{N}\sum_{i=1}^{N} d_i \, , \, d_{20} = \left(\frac{1}{N}\sum_{i=1}^{N} d_i^2\right)^{1/2} \, , \, d_{30} = \left(\frac{1}{N}\sum_{i=1}^{N} d_i^3\right)^{1/3} \tag{6.4}$$

The arithmetic diameter is the mean diameter of the set of droplets. The surface diameter d_{20} corresponds to the diameter of N identical droplets yielding the same total droplet area as a spray of N droplets with respective diameters d_i. Similarly, N identical droplets of diameter d_{30} would yield the same total droplets volume as a spray of N droplets with respective diameters d_i. Surface and volume diameters are particularly interesting as global describing parameters for a spray when dealing with physical interactions dependent on the surface or the volume of droplets.
It is also interesting to calculate the Sauter mean diameter d_{32} for evaporating and combusting sprays. It corresponds to the ratio of the total volume of the spray to the total surface of the spray.

$$d_{32} = \frac{\sum_{i=1}^{N} d_i^3}{\sum_{i=1}^{N} d_i^2} \tag{6.5}$$

$\forall$ d $\in$ [6 ; 90]	d_{10}	d_{20}	d_{30}
at burner outlet	13.5 µm	18.2 µm	25.1 µm
in the whole viewfield	15.0 µm	20.9 µm	28.7 µm

Table 6.3: Arithmetic d_{10}, surface d_{20} and volume d_{30} diameters estimated with data via IPI from 6 to 90 µm

IPI size measurements

IPI size measurements are presented in figure 6.15 respectively in a region close to the burner outlet (left) and in the whole viewfield (right). The relative distributions of the droplets diameters, surfaces and volumes are successively presented.

The distribution of diameters shows two main peaks, the first one for droplets diameter $d = 6$ µm and the second one around $d = 15$ µm. A significant number of droplets are detected with a diameter up to 30 µm. Values for the mean arithmetic d_{10}, surface d_{20} and volume d_{30} diameters are estimated from the IPI measurements and are averaged over a diameter at burner outlet and in the whole viewfield. Results are reported in table 6.3. No significant differences between values obtained at the burner outlet and in the whole viewfield are noticed. This may indicate that no significant evaporation takes place between the nozzle outlet and the rest of the viewfield.

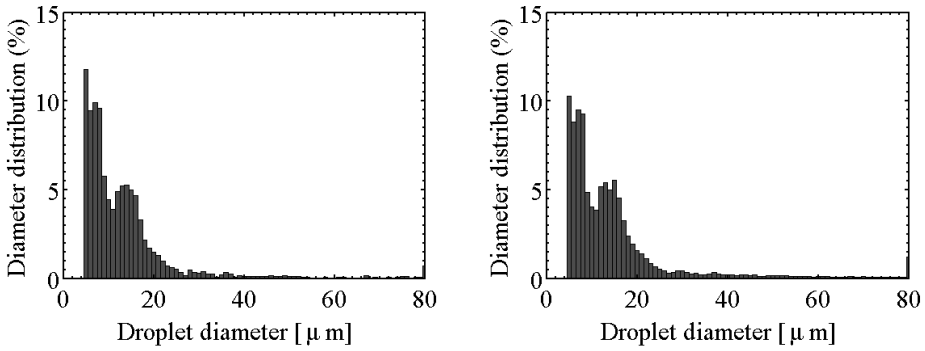

(a) Diameter distribution

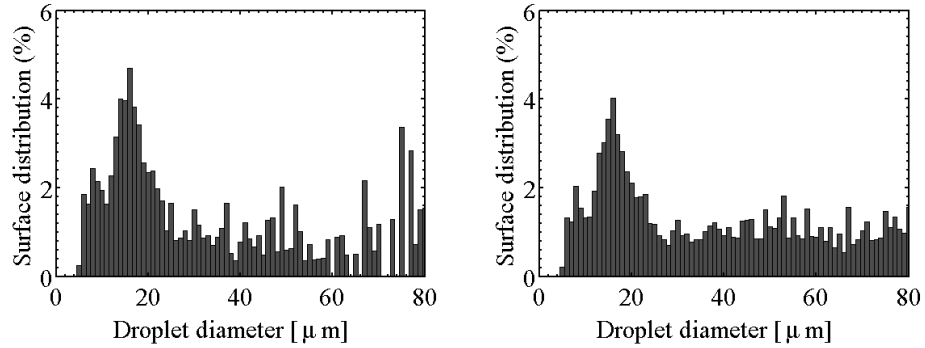

(b) Surface distribution

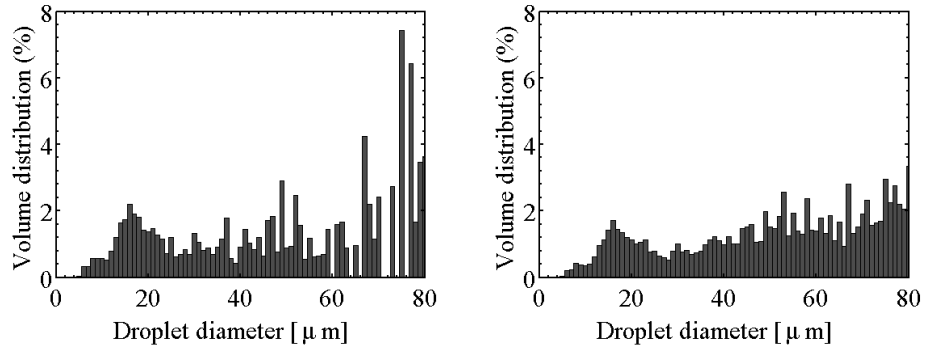

(c) Volume distribution

Figure 6.15: Droplet diameter, surface and volume distribution measured by IPI. Data on the left are averaged along a diameter at burner outlet. Data on the right are averaged in the whole viewfield

Three classes of droplets are defined with equivalent population distribution based on their diameters. These classes are defined as follows:

class A comprises droplets of diameters ranging between 6 to 9.6 µm
class B comprises droplets of diameters ranging between 9.6 to 15.4 µm
class C comprises droplets of diameters ranging between 15.4 to 90 µm

The Stokes number Stk corresponding to the ratio of the response time of the droplet divided by the response time of the flow can be estimated for each class of droplets. This dimensionless number was introduced earlier in chapter 2 and writes.

$$\mathrm{Stk} = \frac{\tau_p}{\tau_{flow}} = \frac{\rho_p d_p^2 v}{18 \mu_{air} \rho_{air} L} \tag{6.6}$$

where ρ_p and d_p are respectively the volumetric mass and the diameter of the droplets, v is the velocity of the flow ($\simeq$ 0.75 m s^{-1}), μ_{air} is the dynamic viscosity of air (18.10^{-6} kg m^{-1}s^{-1} for temperatures between ambient and 1300 °C) and L_c is a characteristic length of the system ($\simeq$ 20 mm in the present case, which corresponds to the nozzle outlet diameter).

Estimations of the Stokes number for the three previously defined classes of droplets are presented in table 6.4.

Class	d (µm)	Stk (x10^{-3})
A	6 to 9.6	2.3-4.9
B	9.6 to 15.4	4.9-14.9
C	15.4 to 90	14.9-521

Table 6.4: Estimations of the Stokes number for the three classes of droplets in the steady flow.

The Stokes number remains always below unity for all droplets classes, so all droplets are expected to follow quite well the gaseous flow.

Figure 6.16 presents of droplets densities cartographies determined via IPI for all droplets (a), for droplets belonging to class A (b), class B (c) or class C (d) in the whole viewfield in steady conditions. To build these images, all droplets measured over 500 shots are distributed in a grid of cells of 1x1 mm^2. A spatial Gaussian filter 3x3 cells^2 is applied to remove high-frequency noise. The results are only presented in the region of interest (ROI), 3 mm $\leq z \leq$ 29 mm , corresponding to the homogeneous part of the laser sheet. Map (a) is indeed the sum of maps (b), (c) and (d).

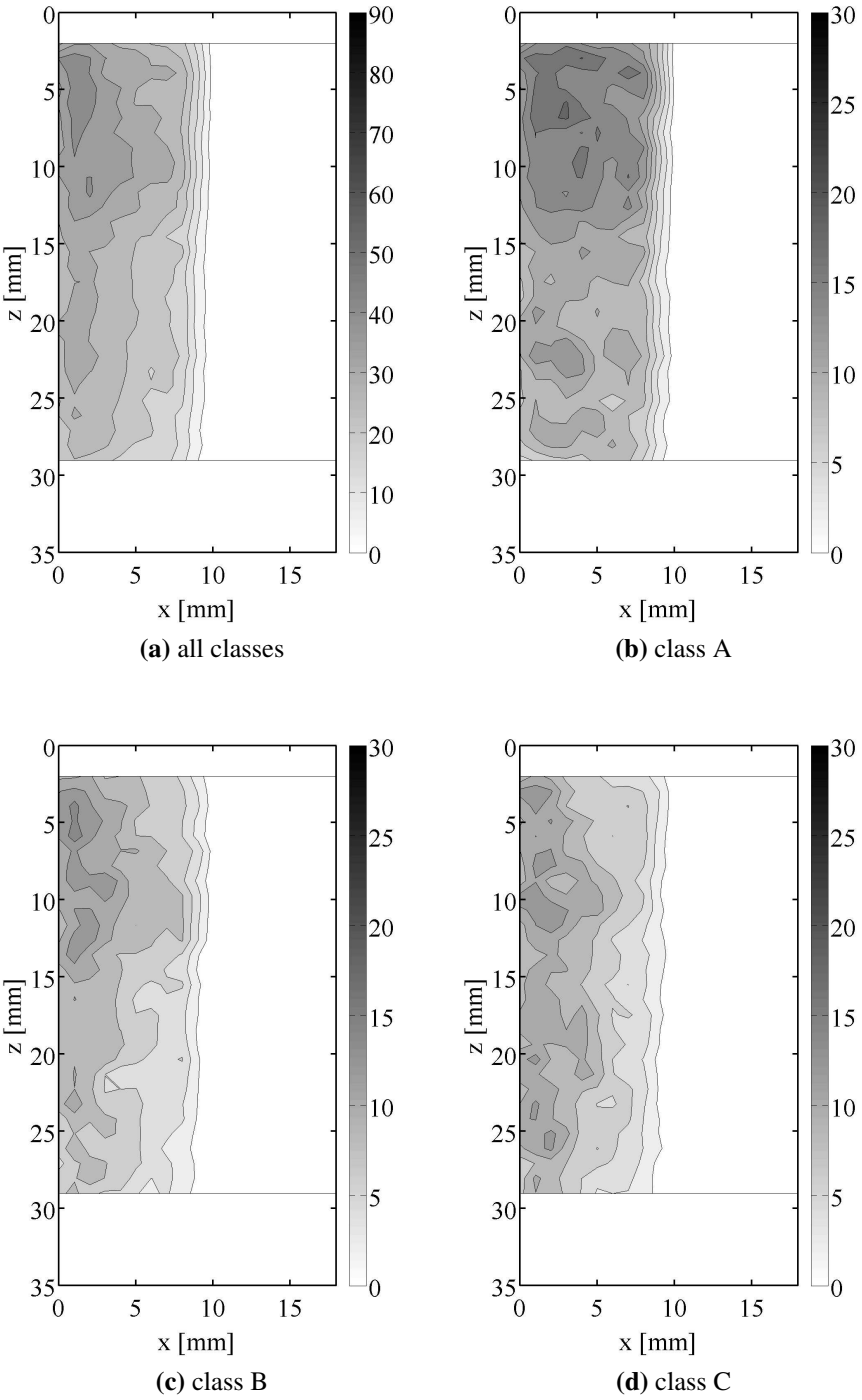

(a) all classes **(b)** class A

(c) class B **(d)** class C

Figure 6.16: Density distribution of validated droplets via IPI in the steady configuration averaged over 500 acquisitions. Results are presented successively for droplets of all diameters, then for class A, class B and class C on a grid of 1x1 mm^2. A spatial Gaussian filter 3x3 $cells^2$ is applied to remove high frequency noise

These density maps show a relatively homogeneous distribution of droplets in the viewfield. One can however notice that the density of droplets increases on the top of these images. This is particularly true for class A. This phenomenon may indicate evaporation from droplets mainly belonging to the smallest class. It should however be noted that this may also be attributed to inhomogeneities between the top and the bottom parts of the laser sheet leading to a better detection of droplets in the top part of the image. Furthermore, the spray seems more dense close to the burner centreline while the droplets concentration vanishes for $x \geq 10$ mm.

PDA size measurements

Size droplets measurements with PDA are carried out every 2 mm along a diameter at the burner outlet at $z_R = 3.5$ mm. No significant differences were observed in the distributions of droplet diameters along the radial direction. As a consequence, results presented in this section were averaged along this direction. The relative population distribution of diameter, surface and volume versus the droplets diameter from 3 to 80 µm are presented in figure 6.17. Droplets are distributed in classes of diameter separated by 1 µm width. These distributions are presented in percentage of the total number of droplets.

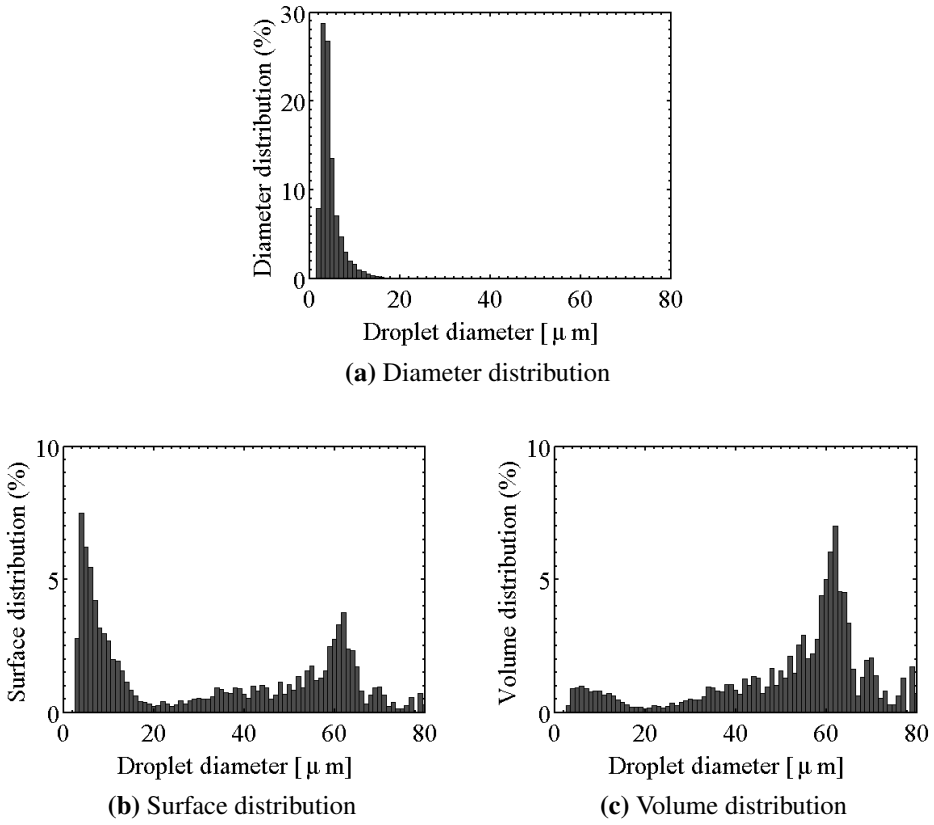

(a) Diameter distribution

(b) Surface distribution

(c) Volume distribution

Figure 6.17: Droplet diameter, surface and volume distribution measured by PDA - The results are measured are averaged along a diameter at $z_R = 3.5$ mm - The distributions are presented in percentage of the total number of droplets

The distribution of droplets diameter shows a predominant peak around $d = 5$ µm. The distributions of droplet surface and volume also exhibit a second peak centred around a diameter $d = 60$ µm.

Mean arithmetic d_{10}, surface d_{20} and volume d_{30} diameters are reported in table 6.5 for all droplets sizes (first line) and for diameters restricted to the measurement range of IPI (second line). A significant difference between values calculated over the whole range and those limited to the IPI range can be observed due to the large number of droplets featuring a diameter below 6 µm.

	d_{10}	d_{20}	d_{30}
$\forall$ d $\in$ [2.5 ; 90]	5.5 µm	8.2 µm	13.3 µm
$\forall$ d $\in$ [6 ; 90]	12.8 µm	17.6 µm	23.6 µm

Table 6.5: Arithmetic d_{10}, surface d_{20} and volume d_{30} diameters from PDA measurements calculated on all measured diameters (first line) and restricted to diameters comprised between 6 to 90 µm (second line) corresponding to the IPI range.

Comparisons between IPI and PDA size measurements

A comparison between PDA and IPI size measurements can be carried out at burner outlet. Figure 6.18 presents distributions of diameters from measurements averaged along the burner diameter at burner outlet for droplets diameters comprised between 6 to 30 µm.

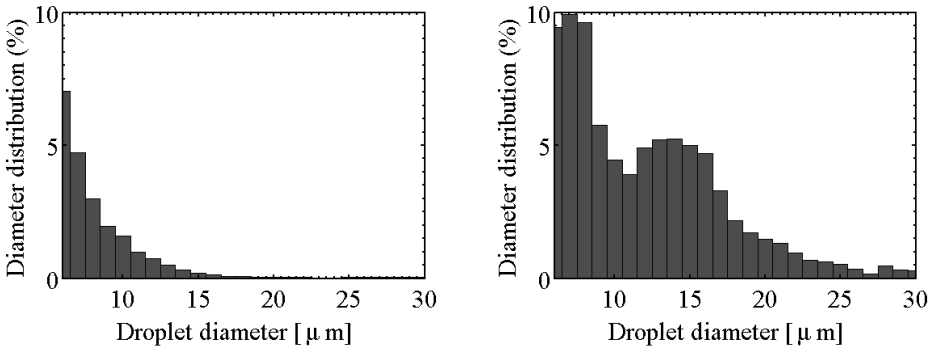

(a) Droplets diameter distribution from PDA **(b)** Droplets diameter distribution from IPI

Figure 6.18: Droplet diameter distribution in the range from 6 to 30 µm measured at burner outlet with PDA (a) and IPI (b)

Mean values of diameters d_{10}, d_{20} and d_{30} reported in tables 6.3 and 6.5 are very similar between PDA and IPI measurements over 6 to 90 µm. However it seems that the distribution of diameters is quite different between PDA and IPI measurements as shown in figure 6.18. The diameter distribution deduced from IPI measurements features a bimodal shape with a relatively important population of droplets with a diameter comprised between 10 and 20 µm. This contrasts with the distribution of diameters deduced from PDA measurements which exhibits an exponentially decreasing profile for diameters ranging from 6 to 30 µm. One can also note a noticeable quantity of droplets measured via PDA around $d = 60$ µm as shown for instance in figure 6.17c.

Before commenting these differences, one should keep in mind that measurement volumes are quite different between the two measurement technique: droplet diameters are measured in a laser sheet of about 1 mm width with IPI, while PDA measurement volume correspond to an ellipsoid of 3 mm long and 1 mm width. The differences observed between PDA and IPI size distributions may be attributed to the limitations in size of the IPI apparatus. Small droplets are less likely to get measured via IPI because the scattered light remains small, and thus the detection of stripes becomes difficult. This fact might cause a bias in diameter detection. A comparison between diameters measured by PDA and IPI in this configuration does not seem achievable due to this bias. As a consequence, the size measurements results presented in this thesis will be analysed in terms of relative evolution, and not in quantitative terms.

6.3.4 Planar visualization of vapour and liquid phases

LIEF signal from the vapour phase

Figure 6.19 shows images of hexane the vapour fluorescence signal. Two single shot images (a) and two averaged images over 100 acquisitions (b) are presented. It is worth noting that the laser sheet originates from the left in these images.

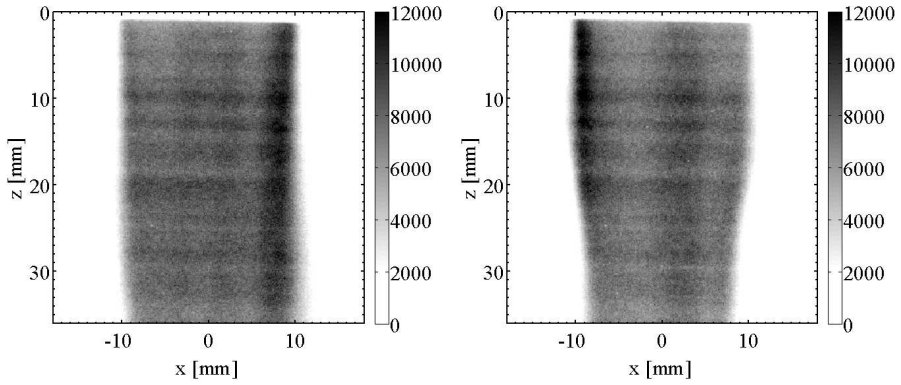

(a) Single shot images

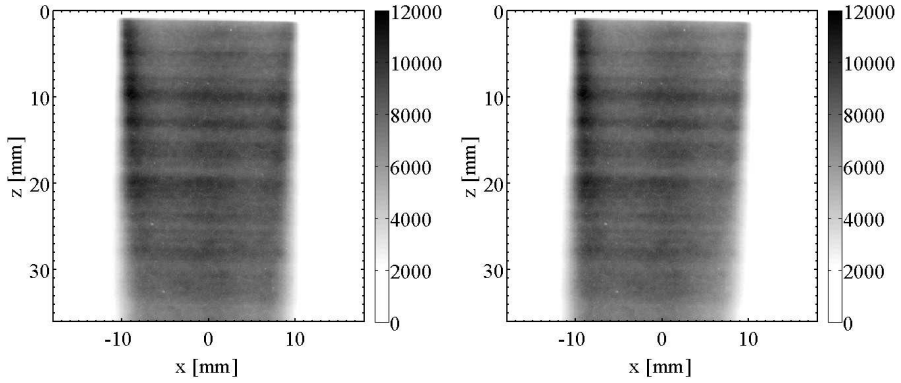

(b) Mean images over 100 acquisitions

Figure 6.19: Images of hexane vapour fluorescence - the grayscale representing intensity in an arbitrary unit spans between 0 and 12,000 - Two single shot images (a) and two averaged images over 100 acquisitions (b) are presented

The snapshots resulting from individual shots shot images present vertical streaks which origins are investigated in appendix B. The position of these streaks vary from shot to shot. They seem to be due to inhomogeneities of the vapour resulting from the evaporation of droplets. The mean images also con-

tain some horizontal streaks which are less significant. In the following, all presented vapour fluorescence images are averaged over 100 acquisitions to reduce the impact of these inhomogeneities. The fluorescence signal collected is then converted into combustible vapour concentration thanks to the calibration procedure described in 6.2.3. The postprocessed image yields a map of vapour concentration in mmol L^{-1} (i.e. 10^{-3}.mol L^{-1}) as presented in figure 6.20.

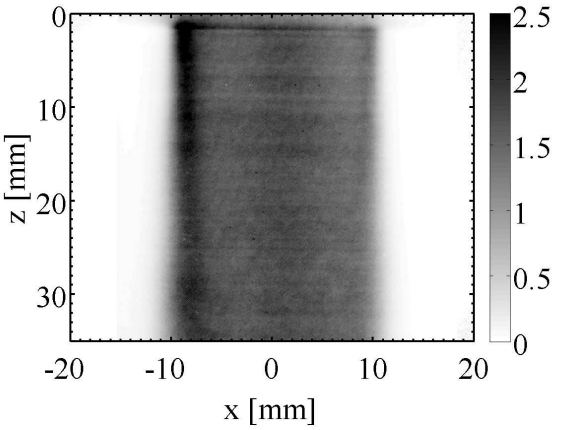

Figure 6.20: Concentration in mmol L^{-1} of vapour of hexane deduced after averaging over 100 vapour fluorescence images

One can observe an homogeneous concentration of the vapour phase along the vertical direction. The mean measured concentration of hexane is about 1.7 10^{-3} mol L^{-1}. Knowing the mean flow velocity and assuming a constant and homogeneous concentration of vapour, the mean concentration measured in figure 6.20 induces that 65% of the initial quantity of hexane pushed into the atomizer is vaporized at the burner outlet. Moreover the homogeneous levels observed in the viewfield show that the vapour concentration remains roughly constant along the z-axis. One can also note that the measured concentration of hexane corresponds to a partial pressure of hexane $P_{C_6H_{14}} = 4130$ Pa, i.e. to 88% of the saturation pressure of hexane $P^{sat}_{C_6H_{14}} = 4700$ Pa at room temperature. In conclusion, many droplets originating from the atomizer are evaporating inside the burner and the combustible vapour concentration at the burner outlet reaches a level close to saturation in these experiments.

Mie scattering

Instantaneous images of the Mie scattering signal coming from the hexane droplets presented in this flow typically comprise between 10 to 30 individual droplets. Each of these droplets scatters a signal which impresses the 16 bits ICCD camera with intensity levels comprised between 1,000 to 50,000 counts. The noise level is about 120 counts. The size of the trace of light scattered by these droplets spans over 1x1 pixels^2 to 3x3 pixels^2 onto the CCD camera. Two thousands images are recorded without external forcing and images are presented in figure 6.21. The first image (a) is obtained after averaging over 2,000 acquisitions. The grayscale spans from the background noise level ($\simeq$120 counts) to the maximum pixel value ($\simeq$250 counts). Since the Mie scattered signal from the droplets is proportional to the square of droplet diameter, this image constitutes a map representing the distribution of the surface diameter d_{20}. In the second image (b), each of the 2,000 acquisitions of Mie signal are first thresholded at a level significantly higher than the background noise level (250 counts). This operation modifies the initial instantaneous image into binary image featuring a level of 1 for pixels where at least one droplet has been detected and a level of 0 where no droplet has been detected. The average of these 2,000 thresholded images yields an information on the spatial distribution of the liquid phase from the spray averaged over a long time with no information relative to the droplets size. The grayscale corresponds to a probability density function of the presence of liquid phase.

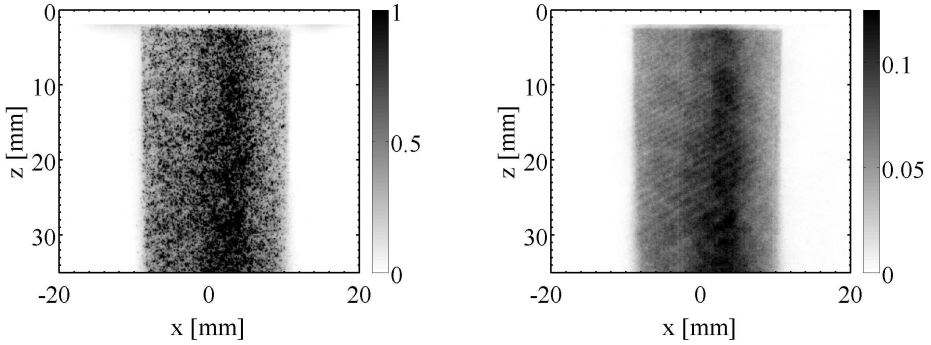

(a) Mean image

(b) Spatial distribution (pdf) of the liquid phase from Mie scattering

Figure 6.21: Images of Mie scattering processed from 2,000 acquisitions

The averaged image and the thresholded image feature the highest gray levels and maximal probability around the burner centreline. A slight asymmetry

is noticed in both images. The maximum seems to be located slightly on the right of the burner axis. This asymmetry lies on the opposite side to the one noticed for the distribution of the combustible vapour concentration. It is worth remembering that the laser sheet originates from the left side of the image. No significant absorption is noticed between the left and right parts of the spray. This is a piece of evidence that absorption phenomena can be neglected in these configurations and cannot be evoked to interpret the observed asymmetry .

LIEF signal from the liquid phase

Instantaneous images of the liquid fluorescence signal emitted by the droplets typically comprise between 5 to 20 individual droplets. Each of these droplets emits a signal which impresses the 16 bits ICCD camera with levels comprised between 500 to 50,000 counts. The noise level is about 120 counts. This yields spots of light that span over 1x1 pixels^2 to 3x3 pixels^2 onto the CCD camera. Figure 6.22 presents an example of image obtained after averaging over 4,000 shots of the fluorescence signal from the droplets. Similarly to the mean Mie scattering acquisitions, the first image (a) in figure 6.22 is obtained after averaging over 4,000 acquisitions. The grayscale spans from the background noise level (120 counts) to the maximum pixel intensity (150 counts). The fluorescence signal from the droplets is proportional to the cube of the droplet diameter, and this mean image constitutes a map of volume diameter d_{30}. For the second image (b), the 100 acquisitions of liquid fluorescence are first thresholded at a level significantly higher than the noise level (250 counts). This operation modifies the initial instantaneous image into binary image featuring a level of 1 for pixels where at least one droplet has been detected and a level of 0 where no droplet has been detected. The average of these 4,000 thresholded images yields an information on the spatial distribution of the liquid phase with no information relative to the droplets sizes. The grayscale corresponds to a probability density function of the presence of liquid phase.

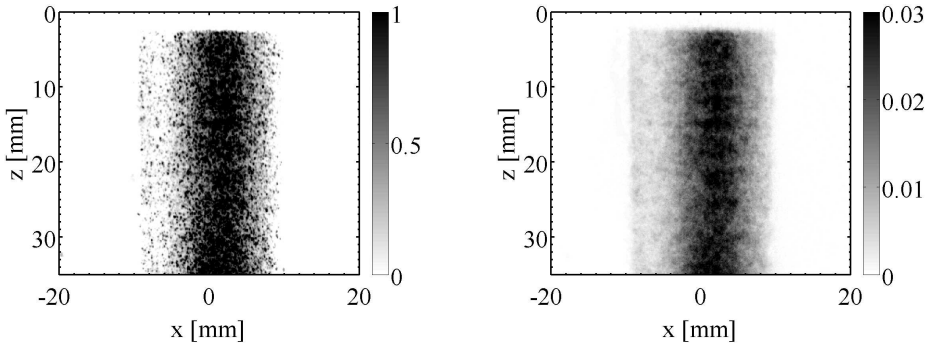

(a) Mean image

(b) Spatial distribution of the liquid phase from fluorescence

Figure 6.22: Images of liquid fluorescence signal processed from 4,000 acquisitions

The averaged image and the thresholded image clearly exhibit a maximum level around the burner centreline. A slight asymmetry is noticed again in both images. The maximum pixel intensity of the fluorescence signal is located slightly on the right of the burner axis. This asymmetry is in agreement with that observed for Mie scattering images. Here again, no absorption phenomena can be observed between the left and right parts of these liquid fluorescence averaged images. This asymmetry may be attributed to a slight offset of the atomizer tip with respect to the burner centreline symmetry axis. This is because the ultrasonic atomizer cannot be tight to the setup and is only placed on a rubber. Contact between the vibrating atomizer tip and the burner body should be avoided for correct operation of the atomizer.

6.3.5 Trajectories of gaseous and liquid fluid particles

Calculation of trajectories

Mean trajectories of vapour and liquid fluid particles are reconstructed respectively from PIV and PTV fields. The same algorithm is used to reconstruct the mean trajectories of fluid particles from both phases. The following reconstructed trajectories correspond to the statistically mean trajectories from the vapour and liquid fluid particles because they are obtained after averaging over a large set of instantaneous PIV and PTV velocity fields. These data cannot be evoked to interpret instantaneous trajectories. These trajectories are clearly different to streamlines when dealing with a pulsated flow. These results are used to interpret the dynamics of the droplets in the vicinity of the vortex and to compare it with the gaseous flow dynamics.

The reconstruction procedure is now presented in details. A starting point is chosen close to the burner outlet at $z = 4$ mm. The radial distance from the starting point to the burner axis is chosen so that it is located within the central flow at the position Φ_0 in the modulation cycle when dealing with pulsated flow. Twenty phase positions separated by a constant temporal step $\Delta t = 1/(20f) = 1.78$ ms are considered. For each time step, the velocity at the particle location is determined from the velocity field using an Adaptive Gaussian Window (AGW) method (Agui and Jimenez (1987)). The velocity (u,v) at a given point P in the viewfield is determined from available PIV or PTV vectors distant of x_i and y_i in the horizontal and vertical directions using:

$$(u, v) = \sum_{i=1}^{n} (u_i, v_i) \frac{\exp\left(-\dfrac{x_i^2 + y_i^2}{h^2}\right)}{\sum_{j=1}^{n} \exp\left(-\dfrac{x_j^2 + y_j^2}{h^2}\right)} \tag{6.7}$$

where the distance h is a constant. The position at the next time step is deduced from the original position translated by the vector $\Delta t.(u, v)$. This method can be applied on structured velocity fields (PIV) as well as on non-structured fields (PTV). The distance h is set equal to 1 mm which is a value ensuring that a sufficient number of vectors in the vicinity of the particle (between 5 and 10) contributes to the calculation of the reconstructed velocity. In the AGW method, the vectors located at a distance greater than $2h$ do not contribute significantly to the calculation of the particle velocity.

This reconstruction procedure yields well defined trajectories for the vapour fluid particles determined from PIV measurements. This is not the case for the liquid fluid particles which trajectories are estimated from PTV measurements. The measurements feature a high background noise level with many wrong vectors which may lead to diverging results. In order to tackle this issue, the liquid droplets trajectories presented in this thesis were calculated from the average correlations of pairs of focused images of fuel droplets taken with IPI setup. The correlation over 32x32 pixels^2 interrogation windows with 25% overlap between neighbouring windows were averaged to yield structured liquid droplets velocity fields of good quality but without possibility of discrimination with respect to the droplet diameter (see details in chapter 2). The same global postprocessing technique used to estimate the vapour and liquid fluid particles trajectories was used.

Trajectories of vapour and liquid particles

Figure 6.23 shows the results obtained for the trajectories of the vapour and liquid fluid particles based respectively on PIV and PTV measurements. The white disks and squares represent respectively the starting points of the calculation reconstruction procedure for vapour and liquid particles trajectories. The five initial positions are located vertically at $z = 4$ mm, and horizontally at 80% and 60% of the maximal radial extension of the central flow on the left part of the flow with respect to the burner axis location and at 30% and 80% of the maximal radial extension of the central flow on the right part of the flow and on the burner axis. The extreme positions enable to investigate the trajectories of vapour or liquid particles carried away into the vortex rings when the flow is modulated. These external symmetric positions also enable to check the symmetry of the trajectories. The gray line represents the calculated trajectory. The mean Mie scattering image of the central flow seeded with micronic oil particles (figure 6.11a) serves as a background image.

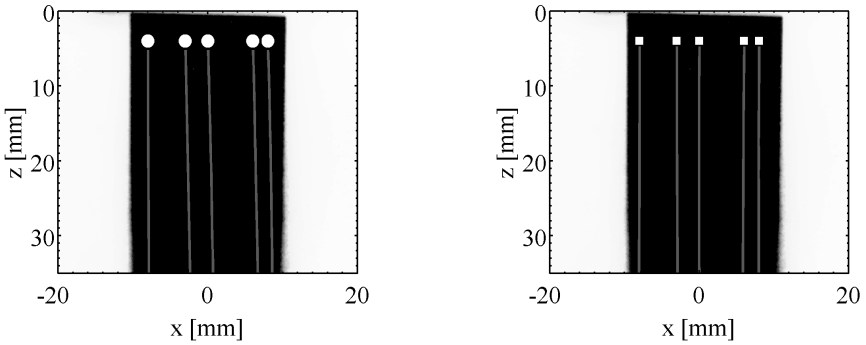

(a) Trajectories of vapour fluid particles **(b)** Trajectories of liquid fluid particles

Figure 6.23: Trajectories of vapour and liquid fluid particles in the steady flow (gray line). White circles and squares indicate the starting points of trajectories. The mean Mie scattering image of the central flow seeded with micronic oil particle serves as background image

As expected, the vapour and liquid fluid particles trajectories in this steady flow are parallel to the z-axis. A detailed examination of the successive positions shows that the trajectories of vapour and liquid have almost the same velocity equal to $V = 0.75$ m s^{-1} for $4 \leq z \leq 35$ mm.

6.3.6 General considerations on flow conditions

The whole set of measurements conducted in steady conditions highlights some interesting features of the studied flow.

First, one can deduce from the measurements of vapour fluorescence signals and from the calibration procedure presented in section 6.3.4 that the vapour concentration remains roughly constant along the z-axis with a mean concentration of 1.7 10^{-3} mol L^{-1}. Knowing the mean flow velocity and assuming a constant and homogeneous concentration of vapour, this implies that 65% of the initial quantity of liquid hexane pushed through the atomizer is vaporized at the burner outlet. The partial pressure of hexane corresponding to this concentration is equal to 88% of the hexane vapour saturation pressure at ambient temperature. The vapour pressure of hexane is thus close to the saturation point. Given the uncertainty of the absolute quantification of vapour, the vapour pressure could be even closer to the saturation point while remaining strictly below. No liquid flow along the burner walls was observed in these experiments.

One can also estimate from the vapour concentration estimates the liquid volumetric mass α_p inside the flow. This dimensionless parameter is defined as the ratio of volumes respectively occupied by the liquid and by the vapour phases. This quantity is important to evaluate the possible influence of liquid phase on the vapour phase (two-way interactions) or the influence of droplets one to each other (four-way interactions). The liquid volumetric mass α_p is evaluated considering the part 35% of the initially injected hexane volume still remaining in the liquid phase in the viewfield:

$$\alpha_p = \frac{Q^{liquid}_{[C_6H_{14}]}}{(Q^{vapour}_{[C_6H_{14}]} + Q^{vapour}_{[N_2]})} \simeq 1.1\ 10^{-4} \tag{6.8}$$

This value for α_p shows that the spray regime is found at the frontier between a mode of pure one-way coupling where vapour influences the liquid phase with no influence of the liquid phase on the vapour phase, and a mode of two-way coupling where the vapour and liquid phases influence each other (Elghobashi (1994); Freret et al. (2009)). However, given the fact that the studied flow is laminar, one can basically conclude that coalescence should not take place in this spray and that droplets should not affect the vortex evolutions.

It is also worth noting the very weak evaporation of droplets present in the viewfield. There is indeed no measurable deviation from the mean vapour

concentration between the top and the bottom of the viewfield. The maximum concentration of vapour corresponds to the saturation point of hexane vapour and the actual measured concentration is found close to this value. This two-phase flow is almost saturated (88% of the hexane vapour saturation pressure). This fact, combined to the short residence time $\tau_{res} \simeq 54$ ms of the droplets in the viewfield, explains the difficulty to analyse the evaporation mechanism in this setup.

The distribution of droplets found by IPI measurements is also found very homogeneous in the entire viewfield. It is however difficult to conclude if evaporation takes place with these images because inhomogeneities of the laser sheet are not fully corrected.

One last observation can be made on the distribution of droplet sizes in the viewfield. The PDA and IPI techniques used to measure droplets diameters do not yield the same results for the mean droplet diameter and the size distribution. It was however shown that the full width at half maximum of distribution of droplet diameter is less than 10 µm. This means that the great majority of droplets in the viewfield have a diameter comprised between 6 and 20 µm, corresponding respectively to Stokes numbers of 2 10^{-3} to 2.6 10^{-2} in the steady flow. The majority of droplets corresponds therefore to Stokes number much smaller than unity. These droplets are thus expected to follow the gaseous flow.

Chapter 7

Pulsated inert two-phase jet

In the present chapter, an experimental analysis is conducted on the two-phase flow configuration presented in the previous chapter where the flow is submitted to external modulations. The central flow is now modulated at $f = 28.125$ Hz with a constant fluctuation level at the burner outlet $(v'/v_{rms})_R = 0.30$. Mean phased-conditioned images of the spray taken at four equally separated instants in the modulation cycle enable the study of the interaction of large periodic vortices shed from the burner lip with the spray. In section 7.1, the analysis focuses on the differences observed between the steady and the pulsated configurations. For this purpose, results obtained from the different measurements techniques are presented for a particular phase $\Phi = 0$ deg in the modulation cycle. In section 7.2, the evolution of the spray characteristics along the modulation cycle is then investigated in details. Measurements are presented at four phase positions in the modulation cycle: $\Phi = 0$, 90, 180 and 270 deg. Signals evolutions along the modulation cycle are commented and analysed thoroughly.

7.1 Analysis of a particular phase

7.1.1 Flow structure

Figure 7.1 presents the mean Mie scattering images of the flow which was alternatively seeded with small oil droplets inside the central and the annular flows. The seeding is made with the perfume atomizer presented in chapter 2.

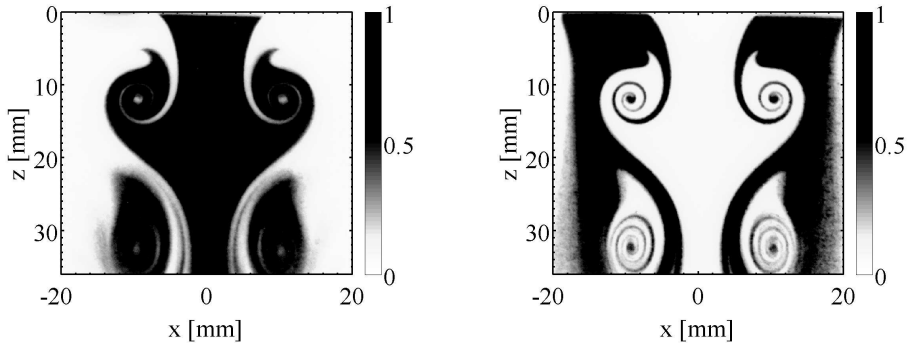

(a) Seeded core flow **(b)** Seeded annular flow

Figure 7.1: Mean Mie scattering images of the flow with alternatively seeded core and seeded annular flows at phase $\Phi_0 = 0$ deg.

The Mie scattering images are obtained after averaging over 100 acquisitions. The boundary between the central and annular flow is well defined in these average images and shows the good reproducibility of the flow structure between different modulation periods. The two images are almost complementary images one to each other, showing that there is little mixing between the two coaxial flows. Note that little mixing does not mean that there is no molecular diffusion between the central and annular flows, which cannot be reproduced by the micronic seeders.

These images are used to understand the structure and the development of vortices when the flow is submitted to a harmonic modulation at the burner outlet. One can refer to figure 7.5 to follow the formation of the vortex ring along a modulation period. It originates from the mutual rolling up of the central and annular flows around each other. The black and white arms are wrapping together along the time period and are entrained by the mean flow.

These images can be used to locate the center of the vortex ring defined as the mass center of the core region of the vortex. This region always corresponds to a pocket of gas originating from the annular flow which is trapped by the vortex as shown in figure 7.1.

7.1.2 Gaseous and liquid velocity fields

The strength and trajectory of these vortices are analysed using a criterion based on the swirling strength λ_{ci} estimated from the complex eigenvalues of

the tensor of velocity gradients (Adrian et al. (2000)) introduced in chapter 3. Figure 7.2 presents contours of the swirling strength λ_{ci} represented by gray iso-lines calculated from the vapour (left) and from the liquid droplets (right) velocity flow fields. Data obtained for the droplets were obtained by averaging the correlation of the Mie signal images using the technique described in details in chapter 2. The grayscale of the contour of λ_{ci} spans from 100 to 300 s^{-1} with steps of 50 s^{-1}.

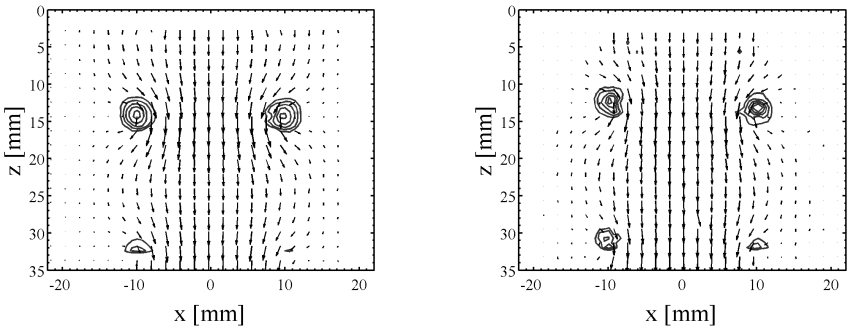

(a) Vapour field **(b)** Liquid field

Figure 7.2: Contours of swirling strength λ_{ci} calculated from vapour (left) and liquid (right) velocity flowfields at phase $\Phi_0 = 0$ deg. The scale is the same for both images and spans from 100 to 300 s^{-1} with 50 s^{-1} increments. Velocity vectors are superimposed in black (only one vector out of 9 is represented for clarity reasons) - The velocity field from the vapour phase is deduced from PIV measurements. The velocity field from the liquid phase is deduced from an average correlation of Mie scattering images of droplets taken for IPI measurements. Spatial resolution: 24x24 $pixels^2$

The vapour and liquid velocity fields exhibit nice structured and defined pockets of swirling strength, symmetric to the burner centreline. One can note that the two velocity fields of vapour and liquid fluid particles are very similar. The vorticity pockets exhibit the same shapes and levels of swirling strength. However a gap of 2 mm along the vertical axis between the vapour and liquid positions of pockets of swirling strength can be observed between the two images indicating that droplets lag the vapour fluid particles during the modulation.

The inverse of the swirling strength λ_{ci}^{-1} can be taken as being the time required for the local streamlines to have one turnover (Adrian et al. (2000)). This enables to estimate a Stokes number $\text{Stk} = \tau_p/\tau_{flow}$ for droplets in the pulsated flow. The response time of the flow τ_{flow} is here taken as the inverse of the

swirling strength from the vapour velocity gradient tensor. At 1 mm from the vortex center, the swirling strength λ_{ci} is about 200 s^{-1}, so that the response time of the flow can be estimated roughly equal to $\tau_{flow} \simeq \lambda_{ci}^{-1} \simeq 1/200 \simeq$ 0.005 s. This response time corresponds to an azimuthal velocity at 1 mm from the vortex center of $v_\theta = 2\pi r/\tau_{flow} \simeq 1.25$ m s^{-1}, a value seemingly reasonable. The response time of the particles τ_p remains the same as the one calculated in chapter 6, i.e. $\tau_p = \dfrac{\rho_p d_p^2}{18\mu_{air}\rho_{air}}$. This can be used to estimate the Stokes numbers for the three defined classes of droplets presented in table 7.1.

Class	d (µm)	Stk (x10^{-3})
A	6 to 9.6	12-26
B	9.6 to 15.4	26-79
C	15.4 to 90	79-2800

Table 7.1: Estimations of the Stokes numbers for the three classes of droplets in the pulsated flow.

These values are about 5 times greater than the ones found in the steady flow due to the differences in flow response time. However for a large number of droplets with a diameter limited to 30 µm, the Stokes number remains low, Stk $\leq 0.3 \leq 1$, and the droplets follow the vapour flow. For a small minority of droplets featuring a large diameter $d > 54$ µm, inertia effects overwhelm viscous forces and the Stokes number becomes larger than 1. These droplets lag the vapour flow perturbations.

7.1.3 Droplet size distribution

The analysis of the overall size distribution of droplets at the burner outlet showed no significant difference in comparison to results presented for the steady condition in section 6.3.3. Therefore, no results in pulsated conditions are presented in this section.

Figure 7.3 presents the density of droplets estimated from IPI for respectively droplets of all diameters (a), droplets belonging to class A [6-9.6 µm] (b), to class B [9.6-15.4 µm] (c) and to class C [15.4-90 µm] (d) on a grid of cells of 1x1 mm^2. A spatial Gaussian low-pass filter 3x3 $cells^2$ with standard deviation 0.6 is applied to remove the high frequency noise. The gray scale is indicated on the right side of the plot and represents the number of droplets locally measured by IPI in the corresponding class of diameters. The map (a) is the

sum of maps (b), (c) and (d). The region of interest (ROI) is situated between $3\,\text{mm} \leq z \leq 29\,\text{mm}$ corresponding to the homogeneous part of the laser sheet. Each measurement in the pulsated configuration is averaged over 100 phase-locked acquisitions.

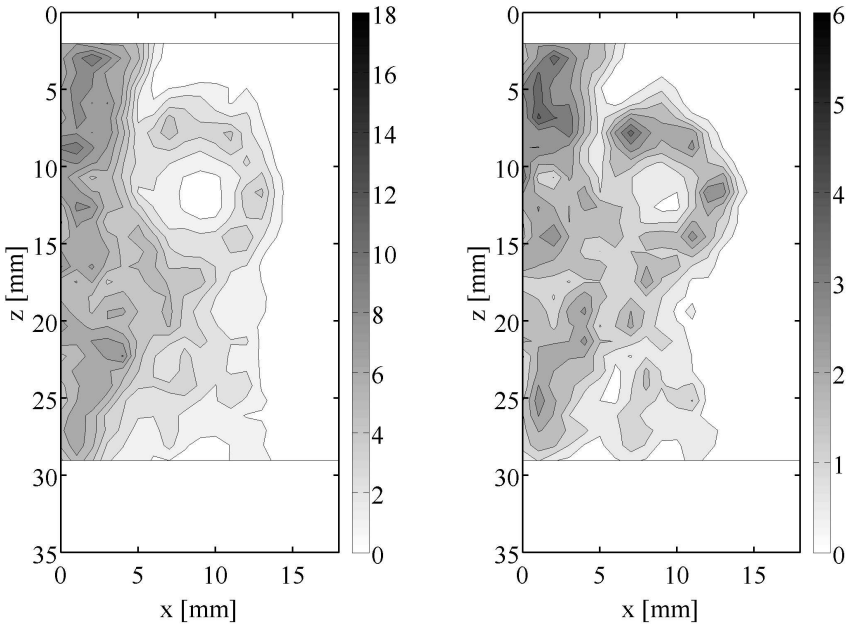

(a) all diameters

(b) class A (6-9.6 µm)

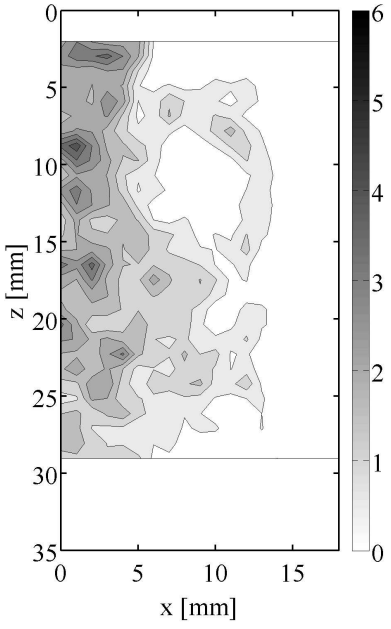

(c) class B (9.6-15.4 µm)

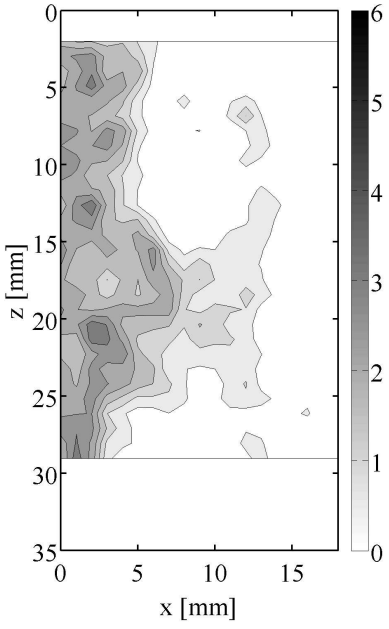

(d) class C (15.4-90 µm)

Figure 7.3: Density of validated droplets via IPI in the pulsated configuration at $\Phi = 0$ deg averaged over 100 acquisitions. Results are presented successively for droplets of all diameters, then for small droplets (class A), intermediate dropltes (class B) and large droplets (class C) on a grid of cells of 1x1 mm^2. A spatial Gaussian filter 3x3 $cells^2$ is applied to remove high frequency noise

The analysis of these maps lead to the following conclusions. First, the density of droplets is greater close to the burner axis than in the vortex ring. This is particularly visible for droplets featuring a large diameter as can be seen in figure 7.3d where almost all droplets are detected in a region within 5 mm of the burner centreline.
The vortex rings free of droplets are well defined with a center located at about $z = 12$ mm. Droplets belonging to class A are almost homogeneously distributed around the vortex center. This is in contrast with droplets belonging to class C which are only present in the bottom part of the vortex and not in the external and top parts. This can be explained by the fact that large droplets are less likely to be entrained within the vortex due to the centrifugal force exerted, whereas small droplets are less sensitive to centrifugal forces and closely follow the flow in the vortex ring.
The central hollow of the vortex ring has a size which clearly depends on the size of the droplets. For droplets of classes A, B and C, the size of this hollow disk corresponds respectively to 3 mm, 6 mm and 8 mm diameter. This is again due to centrifugal forces where the largest droplets are ejected from the vortex ring core.

7.1.4 Planar visualization of vapour and liquid phases

Figure 7.4 presents six plots relative to the vapour and liquid phase distribution inside the viewfield at phase $\Phi = 0$ deg in the modulation cycle. The plot (a) presents the annular flow structure as already introduced in figure 6.11, plot (b) presents the absolute vapour concentration in mol L^{-1} obtained from the LIF signal, plot (c) presents the normalized mean Mie scattering signal from the spray and plot (d) presents the spatial distribution of the liquid phase from the Mie scattering as introduced in figure 6.21. Finally plot (e) presents the normalized mean liquid fluorescence signal from the spray and plot (f) presents the spatial distribution of the liquid phase from the liquid fluorescence signal as introduced in figure 6.22

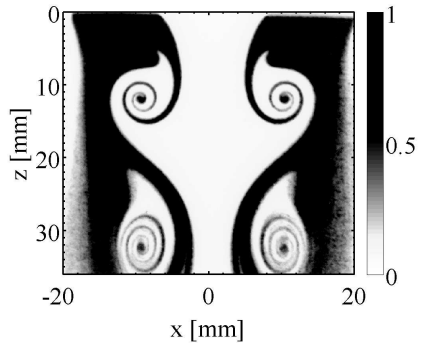

(a) Flow structure

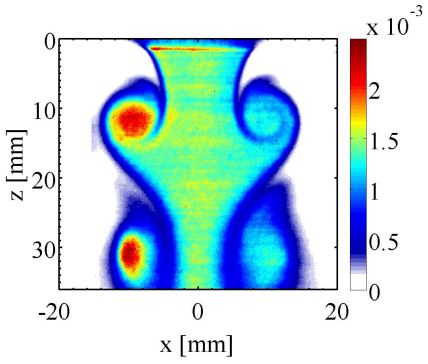

(b) Vapour concentration in mol L^{-1}

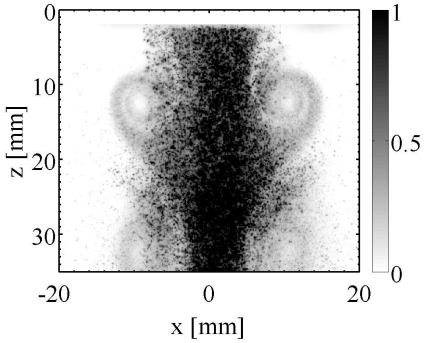

(c) Normalized mean Mie scattering signal

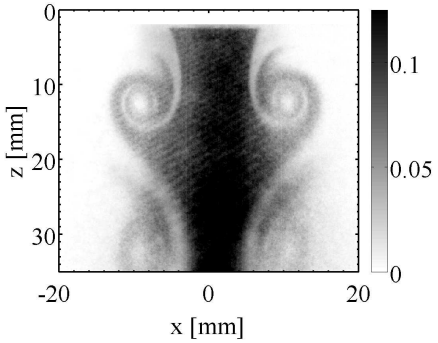

(d) Spatial distribution (pdf) of the liquid phase from Mie scattering

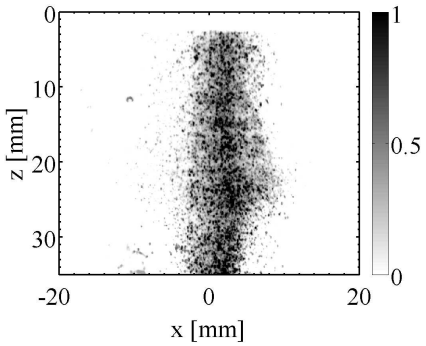

(e) Normalized mean LIEF liquid signal

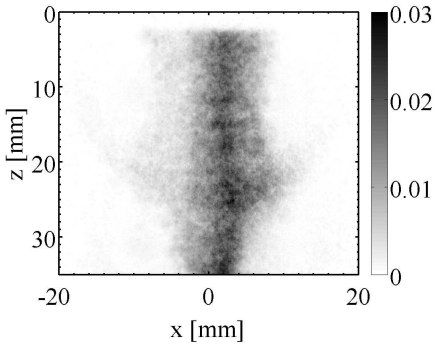

(f) Spatial distribution (pdf) of the liquid phase from fluorescence

Figure 7.4: Vapour and liquid phase visualizations at phase $\Phi = 0$ deg. (a): annular flow structure, (b): absolute vapour concentration in mol L^{-1}, (c): mean Mie scattering signal of the spray, (d): spatial distribution (pdf) of the liquid phase from Mie scattering, (e): mean liquid fluorescence signal of the spray, (f): spatial distribution (pdf) of the liquid phase from LIEF

One can note that the vapour concentration map exhibits an average value $[C_6H_{14}] \simeq 1.7$ mmol L^{-1} over the core flow region. On the boundary between the central and annular flows, the vapour signal slowly drops within 2-3 mm. This shows that the vapour from the central flow has diffused in the surrounding coflow. Moreover, one cannot distinguish q precise internal structure of the vortex ring as in figure 7.4a indicating that vapour has diffused in the vortex center where gas are originally trapped from the surrounding coflow.

The map of mean Mie scattering signal exhibits the highest pixel values within 5 mm from the burner centreline. These values are about 250 counts on a 16-bit camera. This low level is due to the fact that only a few droplets are imaged at each laser shot, typically from 10 to 30 droplets. These mean images show that most droplets are located close to the axis and that only a few are carried away into the vortex rings. This is confirmed by the analysis of the spatial distribution in figure 7.4d, where large clear vortex rings can be recognized.

The liquid fluorescence signal map also exhibits high pixel values within 5 mm from the burner centreline. These maxima are even lower (150 counts) than for Mie scattering mean images. This is due to the dependence of fluorescence signal on the cubic power of the diameter of the droplets, implying that even less droplets can be imaged with the same 16-bit camera (typically from 5 to 20 droplets per image). The visualization of fluorescence thus favours large droplets whereas small droplets are swallowed up in the background noise. One can also note that the fluorescence signal is not present in the external parts of the vortex ring. This is also due to the fact that small droplets are not detected by this LIEF technique. As a consequence, the large droplets, which are unlikely to be carried away in the vortex rings (see for example the density map in figure 7.3d), only radiate some signal along the burner axis.

7.1.5 Trajectories of vapour and liquid fluid particles

Figure 7.5 presents mean trajectories of vapour (left) and liquid (right) particles as a gray line. White disks and squares indicate the locations of the fluid particles in the trajectories. The five initial positions are located respectively vertically at $z = 4$ mm and horizontally at 80% and 60% of the maximal radial extension of the central flow on the left part of the flow with respect to the burner axis, at 30% and 80% of the maximal radial extension of the central flow on the right part of the flow and on the burner axis.

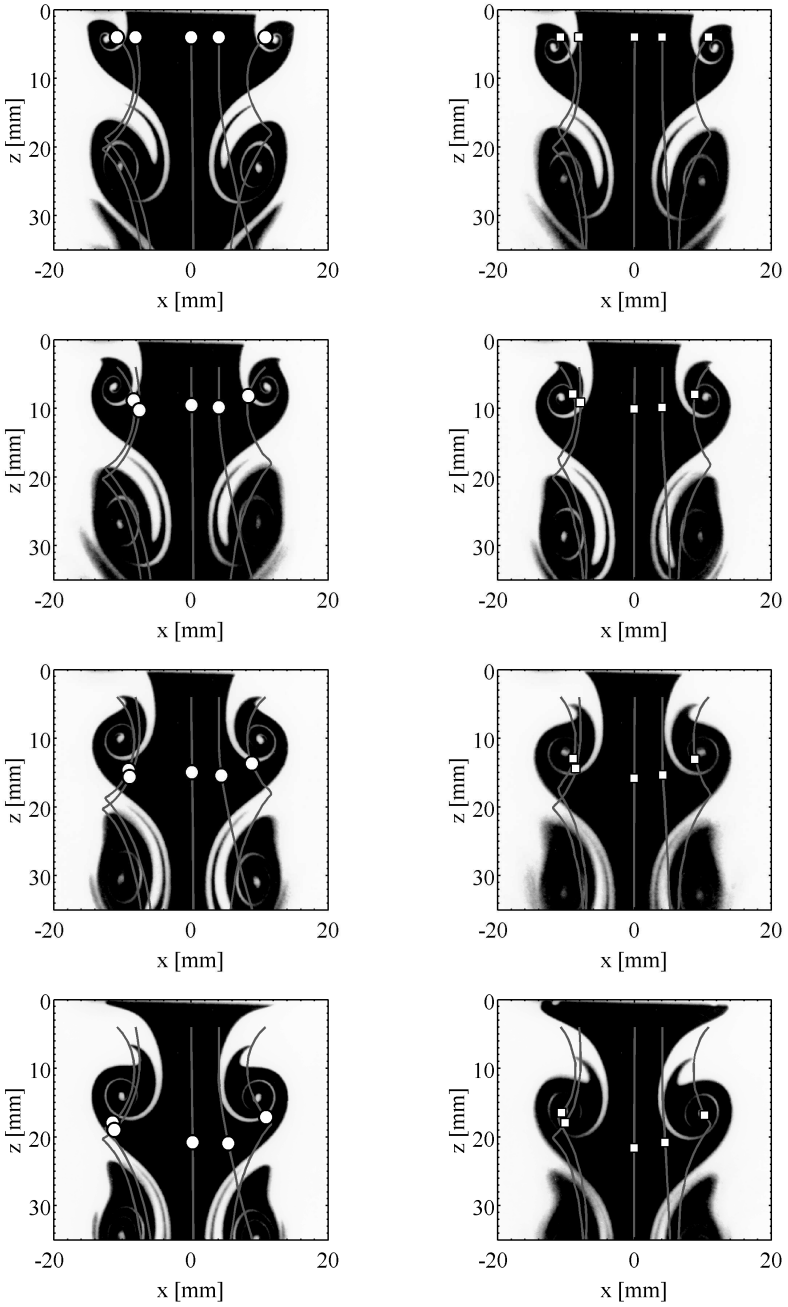

Figure 7.5: Trajectories of vapour (left) and liquid (right) particles (gray line) - white disks and squares indicate the starting points of trajectories. The mean Mie scattering image of the seeded central flow is placed as a background. The phase of vortex shedding is $\Phi_0 = 180$ deg - left : vapour - right : droplets of all diameters. Four phase positions each separated by a fifth of a modulation period are represented (from top image to bottom image)

The droplets are shed at a starting phase $\Phi_0 = 180$ deg. Four phase positions regularly separated in the modulation period are represented from the top images to the bottom images in figure 7.5. Calculations were conducted over more phases and are based on 18 deg steps.

It is particularly interesting to look into details at the trajectories of droplets shed in the external part of the core flow on the left side of the figure. The first vapour fluid particle is released at the boundary of the core and annular flows and follows roughly the corresponding trajectory indicated by the gray line along the pulsation period. This vapour fluid particle gets trapped inside the vortex ring and deviated from the burner centreline. The second particle released starts inside the vortex ring and remains located close to the boundary with the annular flow. This vapour fluid particle is carried away in the vortex ring and rolls up again around the vortex center. These two fluid particles get closer to each other in the vortex ring. One can notice that the external particle, originally released in the central flow (black area) crosses the part of the vortex arm composed of annular flow (white area). This scenario is obviously a mistake. This shows somehow the limitations of the reconstruction procedure from PIV measurements.
The same analysis is conducted for two droplets located at the same initial positions. They follow nearly the same trajectories as the vapour fluid particles. Here again, one of the trajectory seems to cross the vortex arm composed of annular flow (white area). This scenario is obviously wrong again. This also shows another limitation for the determination of trajectories relying on an iterative process. A slight error during one time step is amplified in subsequent calculations. Comparing liquid and vapour fluid particles trajectories, there are only small differences. This is probably due to the fact that the mean droplets Stokes number is too small to put into evidence noticeable differences in trajectories. The only significant difference is observed for a liquid droplet released between the burner axis and the vortex rings. The trajectory for the vapour fluid particle is more influenced by the presence of the vortex ring than the trajectory of the liquid droplet particle. This effect can be attributed to the greater inertia of liquid particles.

7.2 Evolutions over a modulation cycle

In this part, the analysis focuses on the dynamical behaviour of the spray over the modulation cycle. For this purpose, the figures 7.6, 7.7, 7.8 and 7.9 gather

the results of measurements performed at different instants in the modulation cycle, respectively at $\Phi = 0$ deg, $\Phi = 90$ deg, $\Phi = 180$ deg and $\Phi = 270$ deg. On each of these figures are successively presented phase conditionned mean images of:

(a) the annular flow structure obtained by averaging the Mie scattering of the core flow seeded with micronic oil droplets

(b) the mean Mie scattering signal emitted by the liquid droplets from the spray

(c) the mean liquid fluorescence signal emitted by the spray

(d) the vapour concentration in mol L^{-1} deduced from vapour fluorescence measurements via calibration

(e) the spatial distribution (pdf) of the liquid phase from Mie scattering

(f) the spatial distribution (pdf) of the liquid phase from the fluorescence signal

(g) to (j) the density of droplets deduced from IPI measurements respectively for droplets of all diameters and for droplets belonging to classes A, B and C

(k) the mean trajectories of vapour fluid particles for a starting phase Φ_0 successively equal to 0 deg, 90 deg, 180 deg and 270 deg. The background image is the core flow structure at the starting phase Φ_0. The five initial positions are located respectively vertically at $z = 4$ mm and horizontally at 80% and 60% of the maximal radial extension of the central flow on the left part of the flow, at 30% and 80% of the maximal radial extension of the central flow on the right part of the flow and on the burner axis.

(l) the mean trajectories of liquid particles of all diameters for a starting phase Φ_0 successively equal to 0 deg, 90 deg, 180 deg and 270 deg. The background image is the core flow structure at the starting phase Φ_0. The initial positions are the same as for vapour fluid particles trajectories.

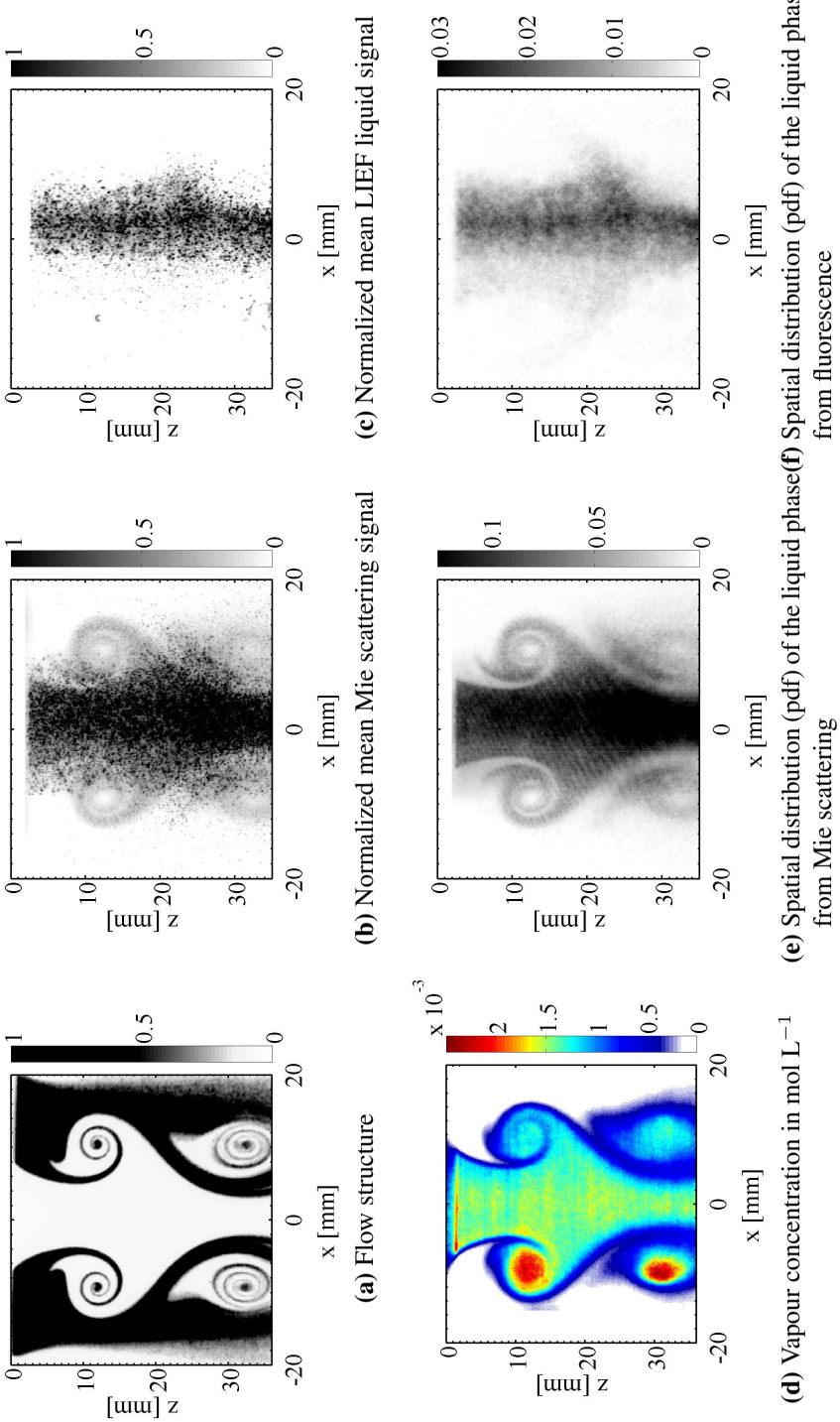

(a) Flow structure **(b)** Normalized mean Mie scattering signal **(c)** Normalized mean LIEF liquid signal

(d) Vapour concentration in mol L^{-1} **(e)** Spatial distribution (pdf) of the liquid phase from Mie scattering **(f)** Spatial distribution (pdf) of the liquid phase from fluorescence

(g) Density of droplets via IPI - all classes

(h) Density of droplets via IPI - class A (6-9.6 µm)

(i) Density of droplets via IPI - class B (9.6-15.4 µm)

(j) Density of droplets via IPI - class C (15.4-90 µm)

(k) Trajectories of vapour fluid particles

(l) Trajectories of liquid particles

Figure 7.6: Overview of results in the pulsated configuration at $f = 28$ Hz and $\Phi = 0$ deg

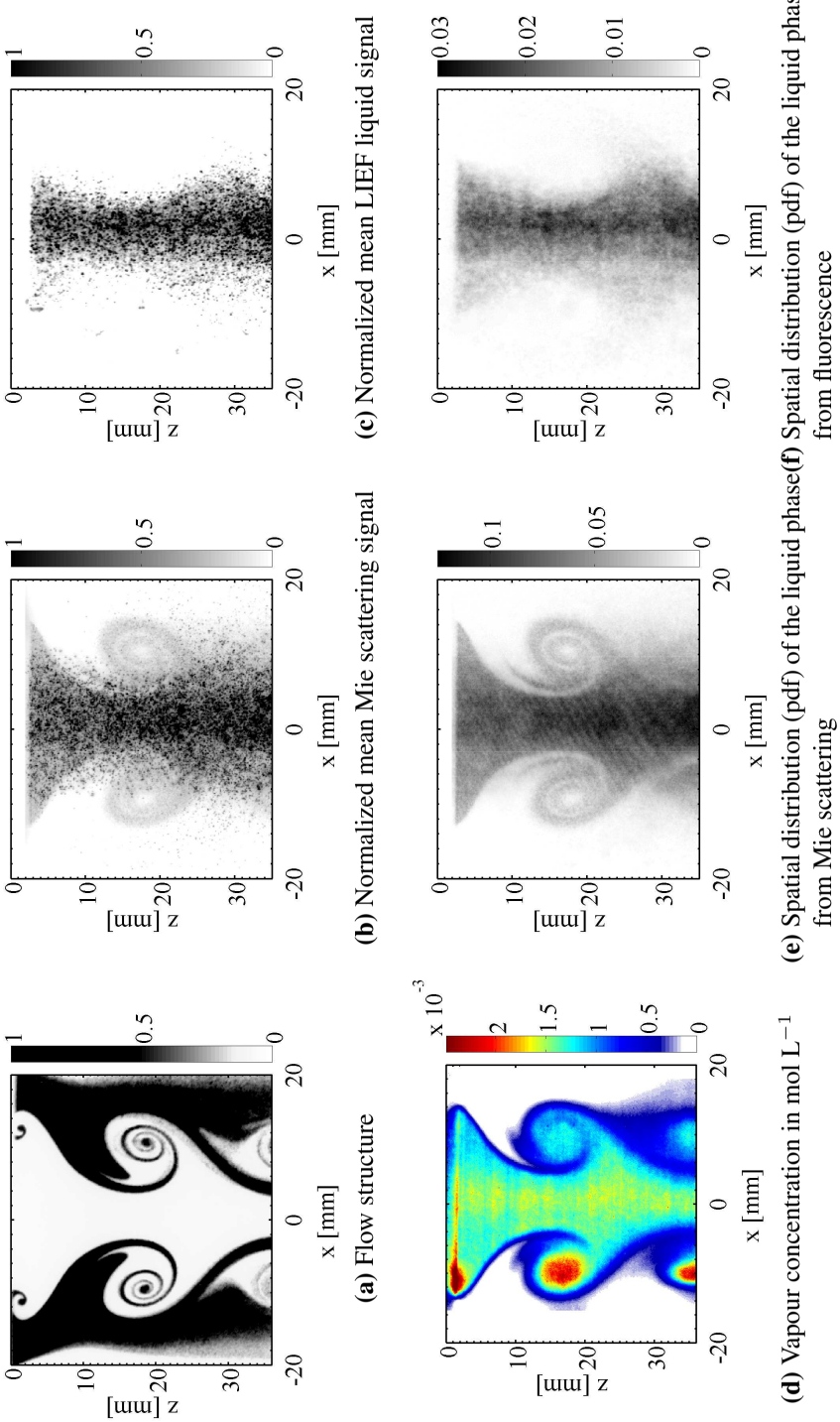

(a) Flow structure **(b)** Normalized mean Mie scattering signal **(c)** Normalized mean LIEF liquid signal

(d) Vapour concentration in mol L^{-1} **(e)** Spatial distribution (pdf) of the liquid phase from Mie scattering **(f)** Spatial distribution (pdf) of the liquid phase from fluorescence

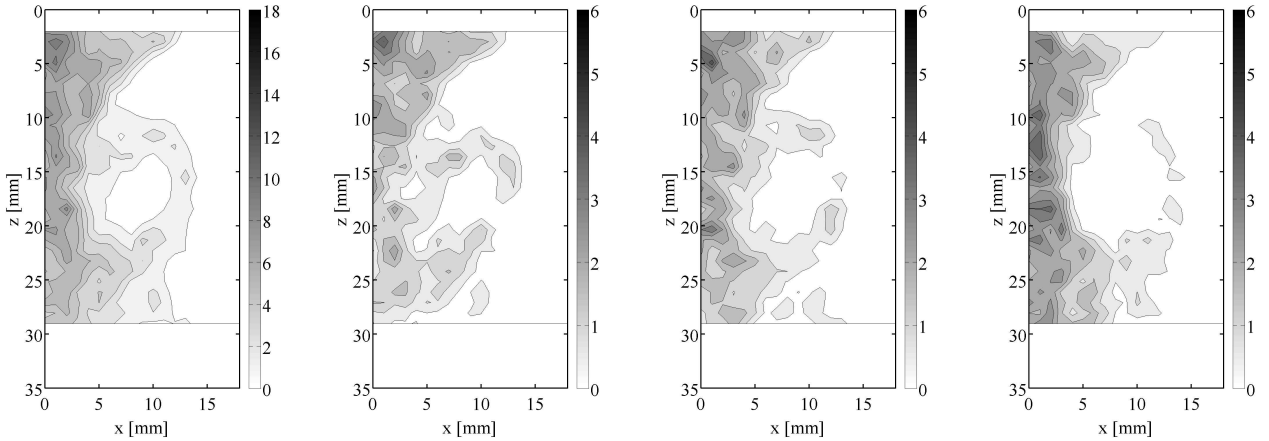

(g) Density of droplets via IPI - all classes

(h) Density of droplets via IPI - class A (6-9.6 µm)

(i) Density of droplets via IPI - class B (9.6-15.4 µm)

(j) Density of droplets via IPI - class C (15.4-90 µm)

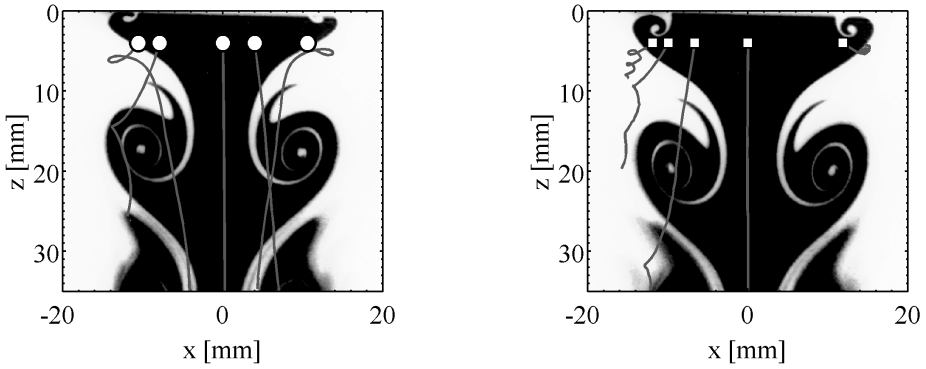

(k) Trajectories of vapour fluid particles

(l) Trajectories of liquid particles

Figure 7.7: Overview of results in the pulsated configuration at $f = 28$ Hz and $\Phi = 90$ deg

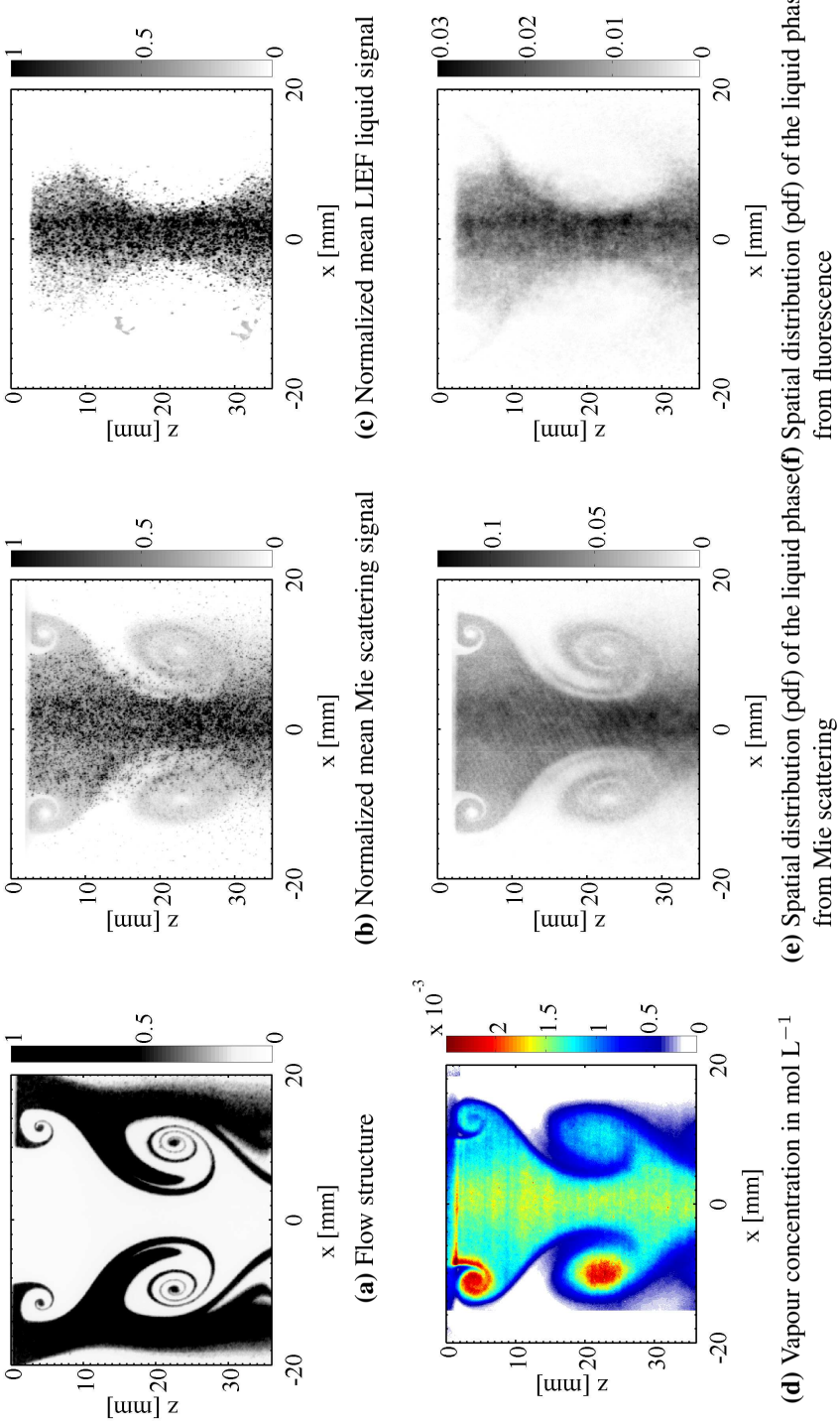

(a) Flow structure **(b)** Normalized mean Mie scattering signal **(c)** Normalized mean LIEF liquid signal

(d) Vapour concentration in mol L^{-1} **(e)** Spatial distribution (pdf) of the liquid phase from Mie scattering **(f)** Spatial distribution (pdf) of the liquid phase from fluorescence

(g) Density of droplets via IPI - all classes

(h) Density of droplets via IPI - class A (6-9.6 µm)

(i) Density of droplets via IPI - class B (9.6-15.4 µm)

(j) Density of droplets via IPI - class C (15.4-90 µm)

(k) Trajectories of vapour fluid particles

(l) Trajectories of liquid particles

Figure 7.8: Overview of results in the pulsated configuration at $f = 28$ Hz and $\Phi = 180$ deg

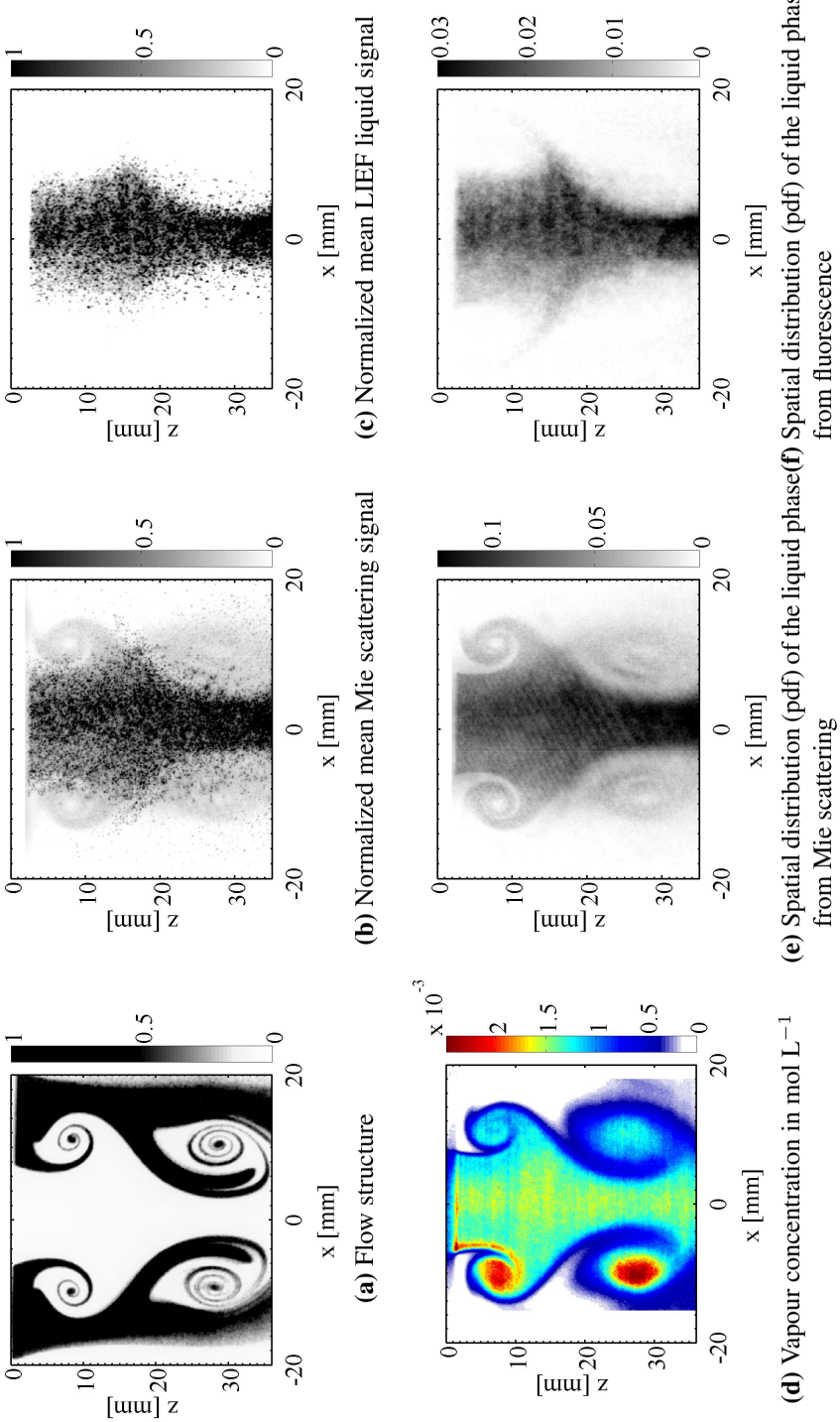

(a) Flow structure **(b)** Normalized mean Mie scattering signal **(c)** Normalized mean LIEF liquid signal

(d) Vapour concentration in mol L^{-1} **(e)** Spatial distribution (pdf) of the liquid phase from Mie scattering **(f)** Spatial distribution (pdf) of the liquid phase from fluorescence

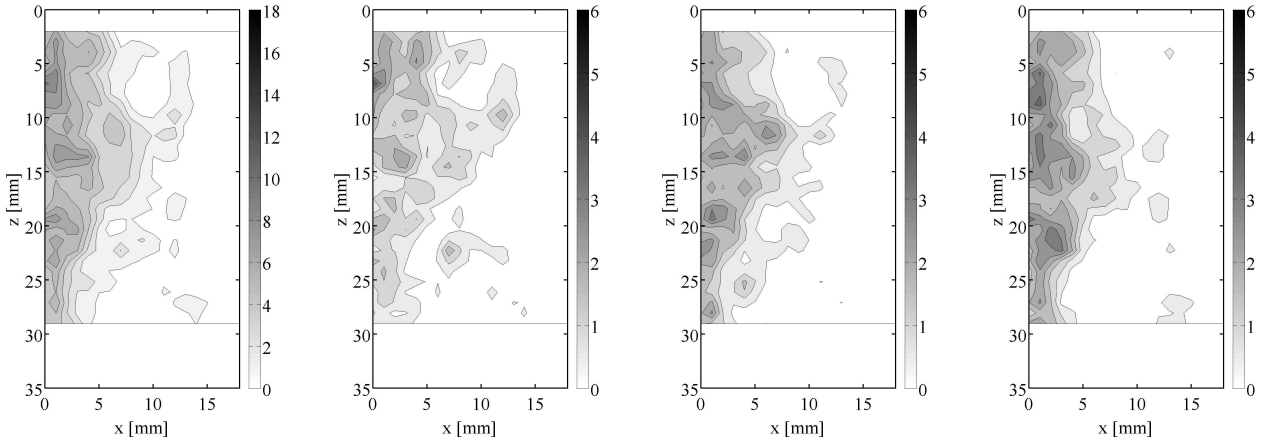

(g) Density of droplets via IPI - all classes

(h) Density of droplets via IPI - class A (6-9.6 µm)

(i) Density of droplets via IPI - class B (9.6-15.4 µm)

(j) Density of droplets via IPI - class C (15.4-90 µm)

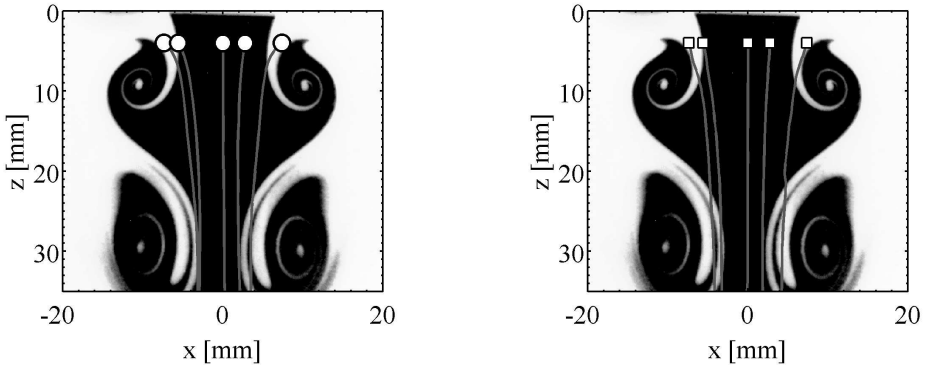

(k) Trajectories of vapour fluid particles

(l) Trajectories of liquid particles

Figure 7.9: Overview of results in the pulsated configuration at $f = 28$ Hz and $\Phi = 270$ deg

These data are now used to analyse the spray dynamics along a modulation cycle.

Flow structure (a) The images of the flow structure enable to follow the formation of a vortex ring. The vortex ring is generated at the burner outlet slightly before $\Phi = 180$ deg. One can then observe the successive rolling up of the central and annular flows leading to a wrap of white and black arms corresponding respectively to central and annular flows. These images also enable to estimate the trajectory and growth of vortex rings. The size and shape of the vortex rings evolve from the burner outlet to the bottom of the viewfield. It starts from a disk of a diameter of about 4 mm and grows to an ellipsoid with a major diameter of 10 mm and a minor diameter of 6 mm.

Spatial distribution of vapour phase (d) Images of fluorescence are used to analyse the spatial distribution of the vapour phase along the modulation cycle. The images of vapour fluorescence exhibit a nearly constant pixel value in the region occupied by the central flow along the modulation cycle. The boundary between the central and the annular flows is a region where diffusion from the fuel into the inert coflow takes place. This can be observed on the vapour concentration maps where an intermediate concentration zone, marked in blue, separates the central flow from the annular flow. The size of this zone gets indeed wider along the z-axis, with the increasing duration of diffusion of fuel in its environment.
Results for the concentration inside the vortex core are striking. There are regions of high concentrations, that increase with the vortex growth in the left part of the flow whereas the vapour concentration determined in the right vortices presented in the image remains low. These observations are difficult to explain because of the strong asymmetry in vapour images. The uncertainties on vapour concentration measurements unfortunately do not lead to a clear conclusion on vapour concentration evolution within these vortex rings.

Spatial distribution of liquid phase (b), (c), (e) and (f) The Mie scattering and liquid fluorescence maps highlight the dynamics of the liquid phase. The mean Mie scattering images (b) yield a map of surface diameter d_{20} of the spray while mean fluorescence images (c) yield a map of volume diameter d_{30} of the spray. Images (e) and (f) obtained after processing with a thresholded value on instantaneous images yield the spatial distribution of the liquid droplets sufficiently large to be detected by the camera.
The shape of the central flow and the vortex rings are very similar to the previ-

ously depicted gaseous flow structure. A small part of the Mie scattering signal is detected in vortex rings. The low level of signal in the vortex rings denotes a low concentration of droplets in the external parts of the spray compared to the burner centreline. After processing, the spatial distribution obtained from Mie scattering (e) shows a better definition of the vortex ring than the mean image. This observation is another proof that the droplets present in the vortex rings are on average of smaller diameters than the droplets present along the burner centreline. The definition of the vortex rings is enough refined to detect the successive enrolments of the spray around the vortex core. The structures are once again very similar to the ones highlighted in the gaseous flow visualizations (a).
The mean fluorescence images (f) exhibit signal only close to the burner axis. No signal is detected in the outer parts of the spray. This difference with the visualizations based on the Mie scattering can be explained by the dependence of fluorescence signal. In order to prevent saturation on the camera, the gain is reduced and only the largest droplet are thus detected. One consequence is that the available range of droplets diameters measurable is reduced. This observation shows that large droplets are concentrated around the burner axis. No additional information can be deduced from liquid fluorescence visualizations. LIEF would bring more information with a less dilute spray, inducing a higher signal to noise ratio.

Size distribution droplets via IPI (g) to (f) The determination of the spray diameters via IPI yield also interesting features for the spatial distribution of the droplets belonging to different diameter classes. The vortex ring is shed at a phase $\Phi = 180$ deg from the burner mouth with a diameter of about 4 mm (Figure 7.8g). The vortex ring is composed mainly of droplets of small diameters (class A) while droplets of larger diameters (classes B and C) are only entrained in the lower part of the vortex ring and not in the external part (see for instance figure 7.8j). The vortex is then convected with the flow and grows up. The distribution of droplets belonging to different diameter classes inside the vortex ring remains globally the same during the vortex lifetime. Droplets of class A are distributed uniformly along the vortex ring while larger droplets of classes B and C are not trapped within the vortex.
The central hollow of the vortex ring is also dependent on the droplets classes and on the phase position in the modulation cycle. Right after the generation of the vortex at a phase $\Phi = 180$ deg, the hollow from the vortex is quite small. It spans over 2 mm for droplets of class A and over 4 mm for droplets of class B. Along the modulation cycle, this central hollow becomes larger. The same trend can be observed for small and large droplets. For example, $3/4^{th}$

of a modulation cycle later, at phase $\Phi = 90$ deg, the hollow in the vortex ring spans from 5 mm for droplets of class A to 9 mm for droplets of class C. These evolutions can be understood relative to the inertia of droplets. Droplets are submitted to a centrifugal force when entraind in the vortex ring. Due to this external force, droplets are likely to be thrown out of the vortex ring depending on their sizes.

Trajectories of vapour and liquid fluid particles (h) and (l) The vapour and liquid trajectories are plotted for different starting phases $\Phi_0 = 0$, 90, 180 and 270 deg. It appears that the starting phase $\Phi_0 = 180$ deg is the only one implying a strong interaction of vapour and liquid fluid particle trajectories with the vortex rings. For any other starting phase, the vapour and liquid particles are little influenced by the vortex ring and they are basically carried away with the flow describing an almost straight trajectory. For the starting phase $\Phi_0 = 180$ deg, the liquid and vapour trajectories interact strongly with the vortex ring. These trajectories were commented and analysed in details in section 7.1.5.

7.3 Conclusion

Interaction of a hexane spray with a modulated jet has been studied using advanced diagnostics. The size distribution of the droplets of the spray has been characterized via Interferometric Particle Imaging (IPI). The spatial distribution of vapour and liquid phases has been investigated with exciplex laser induced fluorescence (LIEF).

A LIEF technique has been used for measurement on the two-phase jet. First, the spectra of fluorescence of vapour and liquid were determined and adapted interference filters were chosen to avoid any crosstalking between the fluorescence wavebands of vapour and liquid phases. The fluorescence of the vapour signal originating from the spray showed an asymmetry, presumely due to inhomogeneities of the vapour distribution at burner outlet from droplets already evaporated inside the burner. This vapour signal was converted into an absolute concentration thanks to a calibration process. The measurements of absolute concentration of vapour appear to be fairly constant along the z-axis. No significant evaporation could be noticed along the burner axis in steady and pulsated configurations.
The liquid phase was characterized by imaging Mie scattering and liquid fluo-

rescence signals. These signals also exhibit a slight asymmetry. The Mie scattering signal was used to obtain maps approaching the distribution of the surface diameter d_{20} and shows the presence of a significant quantity of droplets inside the vortex rings. The images of liquid fluorescence enabled to analyse the distribution of the volume diameter d_{30} and showed the absence of droplets in the vortex rings. This latter observation is due to the fact that LIF imaging favours the visualization of large droplets.

The size distribution of droplets was characterized at the burner outlet using Phase Doppler Anemometry (PDA) and in the whole viewfield via Interferometric Particle Imaging (IPI). Differences between PDA and IPI diameter measurements were observed, in particular IPI measurements exhibit a bimodal distribution. The spatial distributions of droplets show differentiated behaviours depending on the droplet diameters. For instance, the central hollow in the vortex ring increases with the diameter of droplets. This observation can be interpreted because large droplets have more inertia and are pushed to the outer parts of the vortex due to the centrifugal force. There is overall no significant difference in density between the top and bottom parts of the image, suggesting that evaporation remains moderate.

Mean trajectories of vapour and liquid fluid particles were reconstructed from PIV and PTV velocity fields in the steady and pulsated configurations. The vapour trajectories helped to the understanding of the vortex rings formation. The trajectories of liquid particles yield results of poor quality when processed from PTV data. Post-processing of pairs of Mie scattering images of droplets with an averaging correlation procedure led to better results enabling to estimate mean trajectories of droplets of all diameters. In particular, one observed very little differences between the vapour and the liquid fluid particles trajectories, certainly due to the low Stokes number from the majority of the droplets.

Chapter 8

Steady and pulsated diffusive two-phase flame

An experimental study on a two-phase counterflow diffusion flame is conducted in this chapter with the same diagnostics used in the two preceding chapters. A flame is stabilized in the vicinity of a stagnation plane where two counterflows are impinging. They are formed by a heptane spray impinging on an air jet. The dynamics of the spray and the flame are analysed using measurements in steady and pulsated conditions.

8.1 Experimental setup

In the present chapter, a n-heptane/air planar stretched diffusion flame is stabilized on a twin counter-flow burner. The top part of the burner is the same as the one used in chapters 6 and 7 and is represented schematically in figure 1.2. The bottom part is similar to the one used in part II for the investigation of pure vapour flows. A distance $H = 24.2$ mm is set between the two burners. The bottom burner is fed with air. The top burner is fed with a mixture of nitrogen, pre-vaporized n-heptane and with a polydisperse liquid n-heptane spray. The whole setup, the evaporating system generating the prevaporized flow of n-heptane and the atomizer generating the spray are described in details in chapter 1.

Experiments initiated with a steady two-phase flame originating from an hexane spray were unsuccessful because the high temperature reached at the top burner caused the entire evaporation of the hexane spray before the burner outlet. Heptane was thus preferred in these experiments because its higher boiling

point enabled to operate the system with a liquid spray at the burner outlet. A parametric study has been conducted to choose the different flow conditions so that a steady two-phase flame can settle between the twin-burners interspace. The different flowrates used in these experiments are reported in table 8.1. Two top and bottom annular flows of nitrogen are used to prevent disturbances from the external environment on the flame and to prevent the presence of oxygen molecules in the top central flow. The liquid heptane fuel feeding the atomizer is traced with the couple of tracers FB/DEMA while heptane sent to the evaporating system is free of tracers. These systems are used to generate a two-phase stream of heptane vapour seeded with a liquid heptane spray. At this point it is worth noting that heptane is not perfectly coevaporative with the couple of tracers FB/DEMA due to its higher boiling point (see table 2.2 in chapter 2). The FB/DEMA couple cannot be used for quantitative concentration measurements of the heptane vapour distribution originating from the liquid droplets and only qualitative results will be presented in this chapter using LIF images.

Using the settings indicated in table 8.1, a planar flame can be stabilized with and without the atomized n-heptane spray. It is also possible to modulate the flow with a forcing frequency $f = 30$ Hz for a velocity fluctuation at burner outlet of $v_{rms} = 0.36$ m s^{-1} and a mean velocity of $\overline{v}_R$ =0.49 m s^{-1}. Note that the fluctuation level is in these experiments much higher than that typically applied for the premixed gaseous flames explored. It corresponds nearly to a reverse flow condition at the fuel stream outlet.

Top Burner		
Core	C_7H_{16} vaporized	120 g h^{-1}
	C_7H_{16} atomized	39.6 g h^{-1}
	N_2	280 nL h^{-1}
Shroud	N_2	800 nL h^{-1}

Bottom Burner		
Core	Air	324 nL h^{-1}
Shroud	N_2	800 nL h^{-1}

Table 8.1: Flowrates definition at the top and bottom outlets.

The top burner used for the two-phase fuel stream is thermalized and the temperature was controlled at different locations to avoid overheated or cold points. The burner temperature was fixed to 85 °C and this corresponds to a flow temperature of 65 °C at the burner outlet. The bottom part of the burner

used for the air stream remains at ambient temperature.
A 50 mL syringe mounted on a syringe pump supplies the atomizer with a constant liquid fuel flowrate. The velocity and size distribution of heptane droplets produced at burner outlet are characterized by PDA measurements at a distance $z_r = 3.5$ mm from burner outlet and at radial distances $r = 0$ mm, 4 mm and 8 mm from burner centreline. Measurements on the axis at point R ($z_R = 3.5$ mm, $r = 0$ mm) indicate a volume diameter $D_{10} = 8.2$ µm and a Sauter mean diameter $D_{32} = 45$ µm. No noticeable correlation between the droplet size and their corresponding velocity could be observed. This means that all droplets enter the viewfield with similar velocities.
Figure 8.1 presents an image of the planar heptane/air diffusion flame fed by the liquid spray in steady conditions. The spray is illuminated in this image by the laser for LDV measurements. One clearly sees the laser light scattered by droplets at burner outlet. This gives an idea of the droplets density of the spray. Some droplets also cross the main planar flame front and burn behind. The largest droplets create disturbances of the flame front. Some droplets partially pass through the flame front and bend the flame shape. These phenomena are transient and depend on the number and position of the largest droplets impacting the flame. One can also identify that the largest droplets form soot particles and emit red light as shown in the present picture.

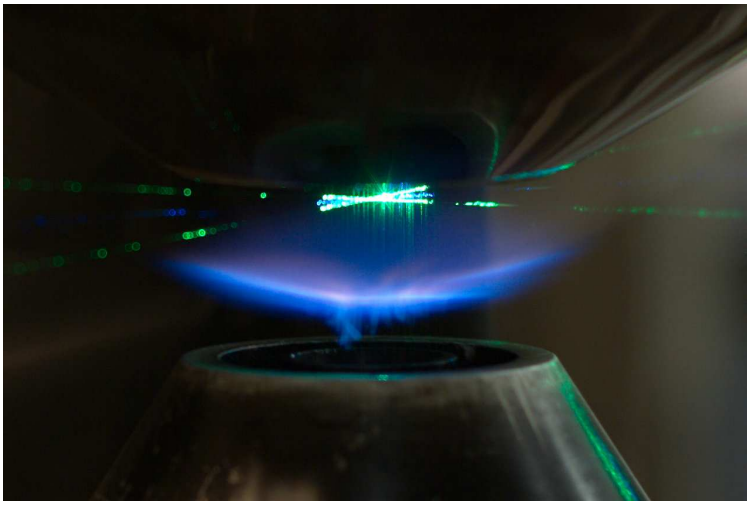

Figure 8.1: Image of the heptane/air two-phase planar flame in steady conditions with the LDV beams. One clearly sees the laser light scattered by hexane droplets at the burner outlet and the impacts of droplets on the flame.

The position and the response of the flame were characterized with 200 snapshots of CH^* chemiluminescence recorded with an ICCD camera equipped

with a band-pass filter (centred at 431 nm with a full width at half maximum (FWHM) of 25 nm) in steady conditions and for 8 phase positions in the modulation cycle. In addition to this, images of vapour fuel fluorescence and Mie scattering were recorded in the fuel stream. Note that for the vapour fluorescence visualisations, the calibration procedure presented in chapter 6 was not applied here for two main reasons. First, since hexane had been replaced by heptane, the fuel is not truly coevaporative with the tracers, so the measured vapour signal does not correspond precisely to the concentration of fuel but only to the concentration of tracers. Secondly, the incoming flow could not be kept at a constant temperature and features temperatures gradients. Quantification of vapour concentration would have required a calibration procedure under varying temperatures. This calibration procedure was not carried out in this thesis. However, a correction of the laser sheet inhomogeneities has been performed on vapour fluorescence images. For this purpose, a mean image over 200 acquisitions of a calibration cell filled with an homogeneous mixture of tracers was taken. This image yields the relative sensitivity of the fluorescence signal of each pixel in the viewfield. This sensitivity is used as a corrective factor during the processing of vapour fluorescence images, and enables to free oneself from inhomogeneities of the laser sheet in the vertical direction, as well as from differences in pixels responses. Mean Mie scattering measurements relative to the liquid phase are also presented in section 8.3.

8.2 Fluorescence signal from the evaporating droplets

Figure 8.2 presents an example of the fluorescence signal originating from the droplets vapour phase averaged over 200 acquisitions. The results are presented in arbitrary units between level 0 corresponding to the mean background noise signal and level 1 corresponding to the maximum counts in the viewfield. Inhomogeneities from the laser sheet have been corrected in these images. Images feature a symmetry with respect to the burner axis, so only half images are displayed. The left image is taken in the reactive configuration and the right image corresponds to the same flow and thermodynamic operating conditions without the flame. One should keep in mind that only atomized heptane is traced and the pre-vaporized heptane is not traced. The fluorescence signal in the waveband centred around $\lambda = 290$ nm is only due to the vapour coming from the evaporation of the spray. This image is accompanied by the trace of the flame front in the vertical plane.
The reaction zone is heavily disturbed by individual droplets impacting the

flame. Single shot images of the flame chemiluminescence yield an information on the shape taken by the flame front which is changing between the different snapshots and features different locations in the vertical direction with an amplitude of about 8 mm along the burner centreline. Images of the flame chemiluminescence was therefore also recorded for a flow fed with the same total flowrate of heptane completely prevaporized, in order to get an insight on the flame position without disturbances introduced by the presence of droplets. The resulting mean image averaged over 200 acquisitions is superimposed in black in figure 8.2. No Abel transformation was performed because the shape of the flame remained quite flat.

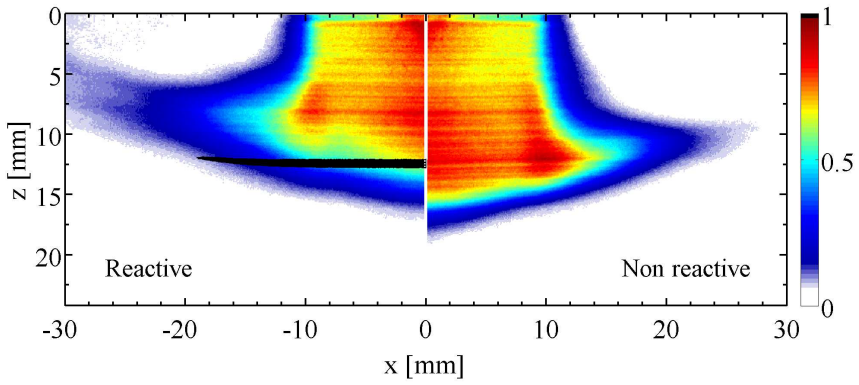

Figure 8.2: Vapour fluorescence signal in the steady flow averaged over 200 acquisitions. On the left: reactive case. On the right: non reactive case. Results are presented in arbitrary units between level 0 corresponding to the mean value of the background noise signal and level 1 corresponding to the maximum counts in the viewfield. The flame CH^* chemiluminescence trace is also indicated for a flow fed only with heptane vapour.

For steady operating conditions, the CH^* chemiluminescence trace indicates that the flame front lies at a distance $z = 12.4$ mm from the burner outlet in absence of spray. The flame is planar and remains steady when the fuel flow is only fed with heptane vapour, but it is strongly disturbed when the spray is added. As can be inferred from figure 8.1, droplets regularly impact and bend locally the flame, and as a consequence the mean flame front trace is much thicker (3-3.5 mm) with the spray than when only heptane vapour is used (1 mm, figure 8.2).

The fluorescence signal resulting from the vapour presented in figure 8.2 indicates that the signal remains quite homogeneous and is almost identical be-

tween the non-reactive and reactive cases in the major part of the viewfield. This shows that the flame has only a significant impact on the heptane vapour distribution originating from the droplets in the vicinity of the flame front and does not affect the flow field originating from the burner outlet. The fluorescence images are also perfectly symmetrical with respect to the burner axis. This explains why only half of the burner is represented in each configuration. The symmetry of the images also indicates that the LIF technique is adapted to investigate such dilute two-phase flows.
The main difference between the non-reactive and reactive configurations lies in the fact that the vapour distribution characterized by the LIEF signal vanishes earlier in the reactive case. This shows that the fuel is consumed through the flame. In the non-reactive case, the fluorescence signal disappears further away from the plate at the position of the stagnation plane. The fluorescence signal is quenched below the stagnation plate due to the diffusion and mixing of oxygen coming from the bottom part of the burner with the tracer.

One can also notice in the reactive case that there is a fluorescence signal beyond the mean CH^* chemiluminescence trace. This can be understood by considering that in the steady flow, the flame is significantly disturbed by single droplets impacts. As a consequence, the flame position fluctuates greatly on instantaneous images around its mean value and when averaging over many acquisitions, one is likely to detect fluorescence signal beyond the flame mean position.

Figure 8.3 presents phase-conditioned results in the pulsated regime at $f = 30$ Hz with a fluctuation level at burner outlet of $(v'/v_{rms})_R = 0.73$. A whole period of excitation is presented. One easily follows the evolution of a large vortex shed at burner outlet (image 1). The vortex ring slowly develops and move downwards (images 2-4), it then interacts with the flame front (left images) or the stagnation plane (right images) (images 5-8). The phase conditioned position of the fame front is also plotted in these figures. The flame front remains nearly at the same location $z = 18.4$ mm along the burner centreline during the modulation cycle. Only the flame periphery slightly moves in the radial direction. These motions are less important than for premixed flames presented in part II. Indeed, in the case of non premixed flows, the flame is not likely to burn the upcoming vortex rings and consequently the flame moves significantly less than for premixed flows.
Similar comments as for the steady case can be made here too. The unsteady flow structures and maps of fluorescence signals are very similar between non-reactive and reactive configurations on the upper part of the viewfield. On the

lower part of the field, some major differences appear. In the reactive configuration, the fluorescence signal vanishes 2 to 3 mm before the reaction zone while in the inert case the fluorescence signal diminishes further downstream. Moreover, no significant fluorescence signal can be detected beyond the main reaction zone. Instantaneous images indeed show that the pulsated flame is less perturbed by the incoming spray than the steady flame.

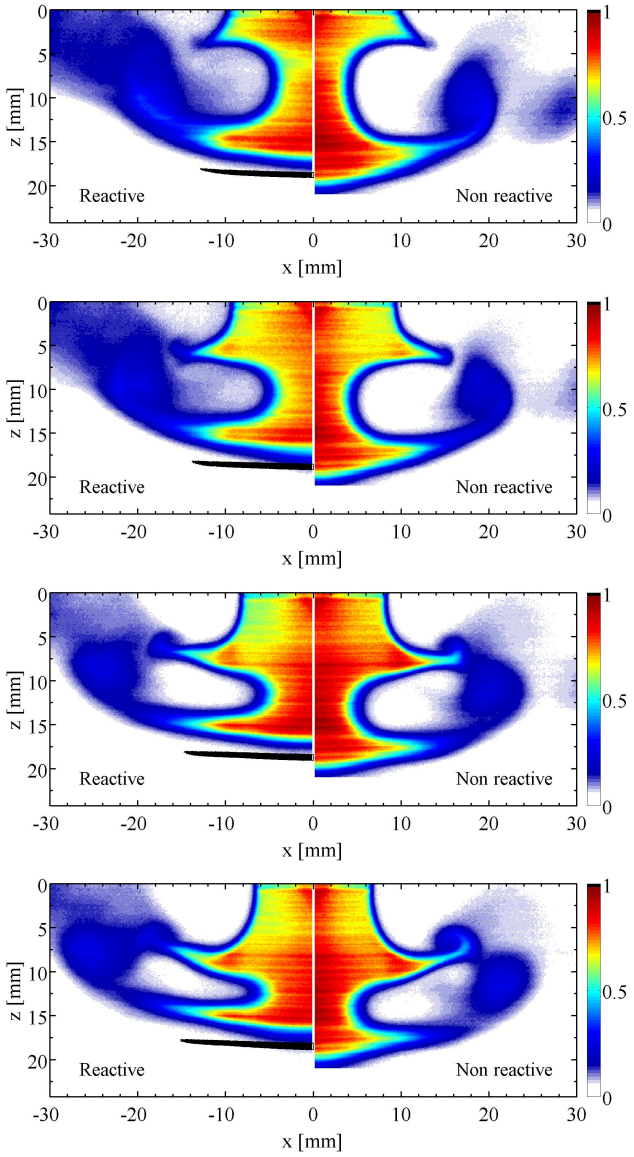

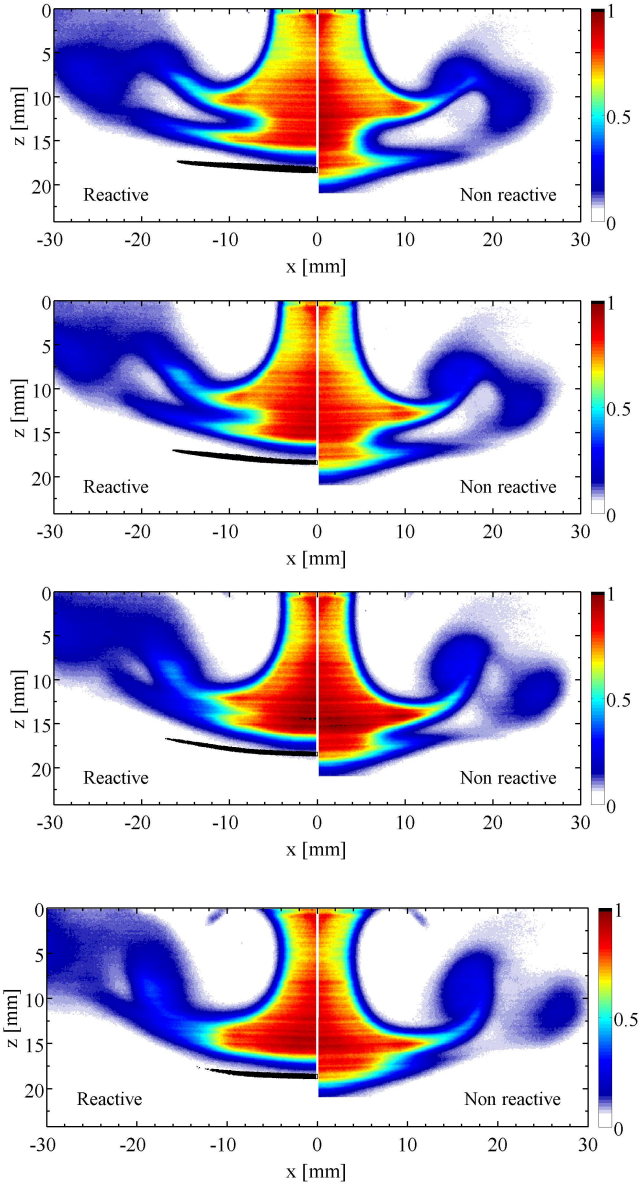

Figure 8.3: Vapour Fluorescence signal in the pulsated flow. Phase conditioned images at eight instants in the pulsation period over 200 acquisitions. On the left: reactive case. On the right: non reactive case. Results are presented in arbitrary units between level 0 corresponding to the mean value of the background noise signal and level 1 corresponding to the maximum counts in the viewfield. The flame CH^* chemiluminescence trace is also indicated for a flow fed only with heptane vapour.

Figure 8.4 shows the temporally-averaged profiles along the radial coordinate

of heptane vapour signal for three values of z-coordinates - from dark to light curves $z = 4$ mm, 8 mm, 12 mm - respectively in steady and pulsated flows. Results relative to the non-reactive and reactive configurations are presented respectively on the left and on the right parts of the figure. The signal levels are normalized relative to the maximum of the signal on the steady viewfield.

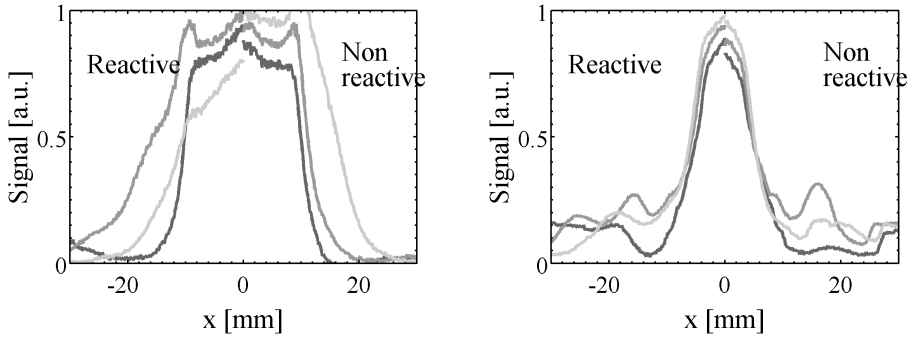

(a) steady configuration **(b)** pulsated configuration at $f = 30$Hz

Figure 8.4: Profiles of vapour fluorescence signal along the radial coordinate in the steady (left) and pulsated (right) configurations of heptane counterflow flame. Dark to light curves respectively refer to profiles at $z = 4$ mm, 8 mm, 12 mm averaged over 200 acquisitions

The curves of figure 8.4 confirm the first observations done from fluorescence maps. The flame seems to have almost no influence on heptane evaporation upstream of the flame as the two dark curves are identical between the non reactive and reactive cases. Closer to the flame front, an influence of the flame is noticeable in the steady case (figure 8.4a) as the lightest curve is noticeably lower than in the non reactive case.
In the pulsated configuration, the flame stands a bit lower than in the steady case. As a consequence, no influence of the flame is noticeable down to $z =$ 12 mm in plot 8.4b. One can also notice some local maxima in the outer part of the flow for $10 \lesssim |x| \lesssim 20$. These maxima correspond to the trajectories of vortex rings, rich in vapour of fuel. In all the plots, one notices a slight increase of vapour fluorescence signal along the z-axis. Since the signal has not been calibrated it is difficult to interpret this evolution which could be due to evaporation of the spray along the z-axis, as well as to an inhomogeneity of the laser sheet.

Figure 8.5 presents different profiles of the heptane vapour fluorescence signal

along the burner centreline originating from the spray droplets. Results obtained in the steady configuration are plotted as black bold curves and data are also presented for four regularly separated instants in the modulation cycle at $f = 30$ Hz as gray lines. These data show that the signal resulting from the vapour phase on the burner centreline is very similar in steady and pulsated configurations for distances lower than $z = 10$ mm. The fluorescence vapour signal then drops earlier in the steady case because the flame stands closer to the top burner in this configuration. The decrease of the fluorescence signal is steeper in the pulsated configuration. In the steady configuration, the signal decreases continuously over $\Delta z = 7$ mm. This difference can be attributed to the flame position that significantly fluctuates under the impact of droplets during steady operation and is less disturbed in the pulsated flow.

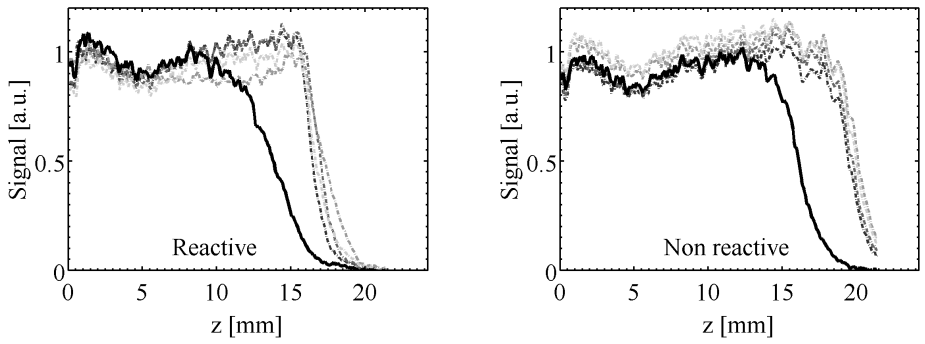

(a) Reactive **(b)** Inert

Figure 8.5: Profiles of vapour fluorescence signal along the burner centreline in the steady (black bold curve) and pulsated (gray curves) configurations. Different gray curves represent phase-conditioned measurements at four positions in the modulation cycle. Measurements for the inert (left) and reactive (right) configurations are averaged over 200 acquisitions

8.3 Visualisation of Mie scattering from the liquid phase

The signal emitted from the liquid phase (Mie scattering and fluorescence) has been recorded in the same conditions as in previous chapters 6 and 7. The spray was very dilute in these experiments, the signal resulting from the liquid phase was very low and difficult to capture. The liquid fluorescence signal was for instance not significant, and is therefore not presented in this

section. Figure 8.6 shows the spatial distribution of the liquid phase from Mie scattering signal obtained after averaging over 500 acquisitions. Each single acquisition has been converted into binary images using to a threshold value set at 250 counts. The steady reactive flow is plotted on the left side and the pulsated reactive flow at phase $\Phi = 0$ deg (corresponding to first plot in figure 8.3) is plotted on the right side.

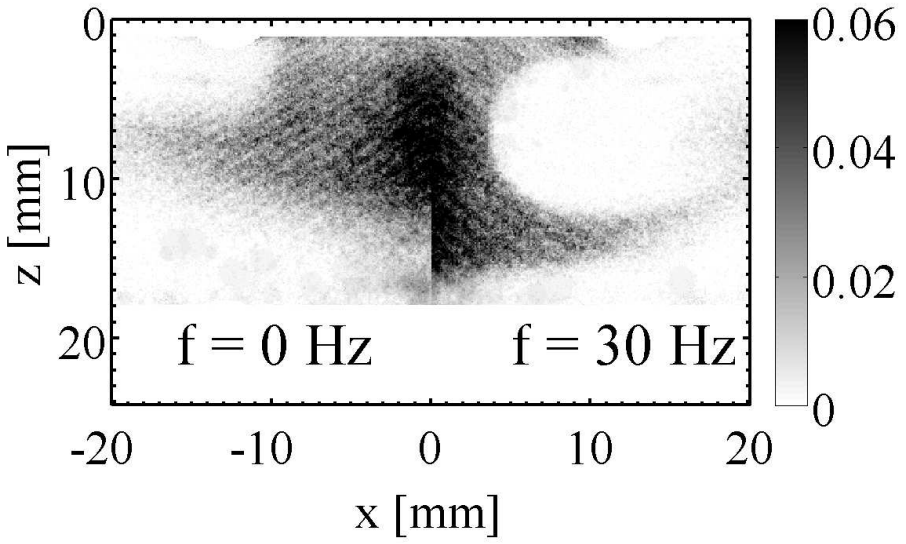

Figure 8.6: Spatial distribution of the liquid phase from Mie scattering signal obtained after averaging over 500 acquisitions. The steady reactive flow is plotted on the left side while the pulsated reactive flow at phase $\Phi = 0$ deg is plotted on the right side.

This image yields the structure of the spray. The density is much lower than what was observed in chapters 6 and 7 for the inert two-phase jet, showing again that the spray is very dilute in these experiments. The steady spray has a spatial distribution similar to the vapour one presented in figure 8.2. The pulsated spray exhibits also structures about the same as the ones determined for the vapour distribution at this particular phase (figure 8.3, first plot). One can notice slanting stripes on the image which origin was not identified.

8.4 Conclusion

Lighting up a two-phase diffusion flame which was stable and which could be pulsated was indeed a difficult task. The first difficulty was to obtain a stable flame while impacted by droplets and submitted to flow modulations. Moreover, some minutes after ignition, the temperature of the upper burner increased up to 90 to 100 °C even if radiative panels and a cooling water system were used. This rise of temperature vaporizes partially the cloud of droplets before they reach the burner outlet. For this reason, experiments could not be carried on with more dense sprays. The study of a steady two-phase reactive flow under wider flowrates conditions would indeed require the inversion of the configuration with the two phase flow and the loudspeakers on the lower part and the counterflow of air in the upper part. In this case, the two-phase flow and the loudspeakers would stay at cooler temperatures. In the scope of this thesis, the focus was put on the study of a dilute two-phase diffusive heptane flame.

The exciplex laser induced fluorescence technique was used to investigate a dilute two-phase diffusion flame of heptane. Qualitative visualisations of the fluorescence signal emitted by the vapour were obtained. Quantitative data could not be obtained and would have required a calibration of the fluorescence signal with the temperature. This calibration procedure was difficult to setup, and thus not performed in this work. The maps and profiles of fluorescence signal yield though some first interesting results on the structure of a stagnation non reactive flow and a stagnation diffusion flame submitted to flow modulations. It is shown in particular that the vapour concentration is fairly constant except in the vicinity of the flame. The diffusion flame is also less sensitive to flow perturbations than what was observed on premixed flames in part II.

Conclusion

The investigation was concerned with collecting knowledge on fundamental aspects of combustion in laminar flows submitted to upstream modulations. The objective was both to characterize the flame dynamics in a premixed counterflow configuration, and to experimentally study via advanced diagnostics a two-phase flow in an inert and reactive configurations. Experimental studies were carried out on two different experimental configurations. The first setup comprises a gaseous reactive flow impinging a plate (Part II) and the second setup comprises a fuel spray entrained by an inert free jet or by a reactive counterflow (Part III).

- In chapter 3, the flow and flame dynamics of a premixed methane-air stagnation flow was investigated under modulation. The modulation of the flow inlet velocity generated vortex rings at burner outlet whose diameter depends on the forcing frequency. These vortices are convected with the flow and greatly interact with the flame tips. The flame behaves as a low-pass filter to incoming flow velocity modulations: the flame position greatly fluctuates at $f = 10$ Hz, while the flame front in the center region remains steady at $f = 51$ and 102 Hz.
  Analysis of the propagation of velocity perturbations on the burner centreline highlights very different behaviours at low and high Strouhal numbers. At low frequencies, i.e at $\mathrm{St}_D < 0.5$, the velocity perturbations propagate at a convective speed close to the flow velocity on the axis. At high frequencies, i.e at $\mathrm{St}_D > 0.5$, velocity perturbations propagate at sound celerity. The origin of these modes of propagation were analysed relative to the size of the vortex ring shed at the burner lip. At low Strouhal numbers, the vortex shed at burner outlet is large compared to burner outlet diameter, and so imposes its velocity perturbation along the burner axis. At high Strouhal numbers, vortex rings shed at burner lips are too small to have a significant impact on burner centreline and perturbations are dominated by an acoustic wave. For intermediate forc-

ing frequencies, convective and acoustic waves of similar amplitudes coexist. A decomposition of velocity into convective and acoustic components has been carried out to support this explanation.
The choice of boundary conditions in 1-D simulations was discussed relative to the latter findings. The classical choice of boundary conditions sets a uniform propagation of perturbations. This leads to inaccuracies in 1D simulations of flow and flame, in particular at low Strouhal number. Another set of boundary conditions imposing a convective propagation of fluctuations along the burner centreline was investigated. This latter boundary condition led to more accurate simulations in some cases. This study globally points out the need of reconsidering velocity boundary conditions in a counterflow configuration, especially at low Strouhal numbers. A deeper analysis would though be needed to conclude on the most relevant choice of boundary conditions in a general configuration.

- In chapter 4, Flame Transfer Functions (FTF) were determined experimentally for laminar premixed strained methane/air flames with different equivalence ratios submitted to harmonic velocity perturbations generated at the burner outlet. It was first shown that relative heat release rate fluctuations can be estimated using relative fluctuations of the chemiluminescence signal from the flame without specific interference filter. The flame frequency responses were determined using the chemiluminescence emission from the entire combustion region (global FTF) or the light emission restricted to a small area around the stagnation streamline axis (local FTF). The analysis of these transfer functions yielded different responses in terms of gain and phase. Mechanisms governing the global FTF were identified and result mainly from disturbances generated at the burner outlet, transported by the mean flow and interacting with the flame periphery. The local FTF responses collapse for a lean, a stoichiometric and a rich mixtures. They feature a phase-offset $\varphi = -\pi$ at low frequencies and a constant slope independent of the flame location with respect to the nozzle outlet. Results clearly indicate that the characteristic flame time scale α/S_L^2 cannot be invoked to interpret these data. Further experiments with a varying stretch rate ε would be necessary to know if the flame response is governed by the characteristic flow time scale l/v.

- In chapter 5, the sound generated by seven different partially premixed flames interacting with a train of vortices of controlled strength was in-

vestigated. No striking differences in the sound production mechanisms could be found between a methane-air mixture encompassed by pure nitrogen compared to configurations where oxygen, methane or methane-air were also added to the co-flow. The flame having a co-flow of pure nitrogen produces the loudest sound output due to the sudden extinction of the flame that was enrolled over the vortex. Methane or air trapped within the vortex was found to lead to slightly higher noise levels than entrainment of a methane-air mixture because this interaction leads to shorter interaction delays in these specific cases. Considering partially premixed turbulent flames, one may conjecture that regions of air entrainment into the reaction zone may be at the origin of stronger noise output than perfectly premixed region.
It was also found that the proportionality between the radiated sound pressure and time derivative of the emission signals from CH^* radicals established for perfectly premixed systems remains reasonably well satisfied for the partially premixed configurations explored in this work. This is an interesting result that may be useful to study noise production from other partially premixed combustion systems. The conclusions drawn hereby require a validation by other experiments over wider operating conditions, including investigations at different forcing frequencies to vary the size of the impinging vortex. It would be also interesting to vary the equivalence ratios within the annular and the central flows and study their effects on noise production.

- In chapters 6 and 7, a two-phase flow of hexane was investigated via the use of advanced diagnostics. The size distribution of the droplets of the spray were characterized via Interferometric Particle Imaging (IPI). The spatial distribution of vapour and liquid phases was investigated using Laser Induced Exciplex Fluorescence (LIEF). This technique is particularly suited for the investigation of flow with two distinct phases. It has been successfully set in a well-controlled inert configuration.
  The vapour signal showed a clear asymmetry due to an asymmetry of vapour at burner outlet evaporated from droplets. This might be due to an injecton of the spray slightly out off the burner axis. The vapour concentration was though quantified thanks to a calibration procedure. No evaporation was noticeable along the burner axis in steady and pulsated configurations.
  The liquid phase distribution was characterized by Mie scattering and fluorescence imaging. The signal exhibited a slight asymmetry. The Mie scattering signal enabled to draw maps yielding the spatial distribution

of surface diameter d_{20} and showed the presence of a significant quantity of droplets in the vortex rings. The images of liquid fluorescence enabled to draw maps representing the spatial distribution of volume diameter d_{30} and showed the absence of droplets in the vortex rings. This latter observation was due to the fact that LIF imaging favours the visualisation of large droplets.
The size distribution of droplets were characterized using Phase Doppler Anemometry (PDA) and Interferometric Particle Imaging (IPI) was also used to estimate diameters and velocities of droplets in the whole viewfield. An important discrepancy between PDA and IPI diameter measurements was identified. These differences might be to bias on IPI measurements. The plots of spatial distributions of droplets show differentiated behaviours depending on diameters. For instance, the hollow in the vortex ring increases with the diameter of the droplet. This is logical because large droplets have inertia and are pushed to the outer part of the vortex. A high density of droplets was also found in the top part of the vortex. There was indeed no significant difference in density between the top and bottom parts of the image, meaning that the spray was non evaporative in the viewfield.

- In chapter 8, a two-phase diffusion flame of heptane was studied using vapour LIEF. Only qualitative visualisations of the fluorescence signal emitted by the vapour were obtained because quantitative data for concentration estimations would have required a calibration of the fluorescence signal as a function of the temperature. The obtained maps and profiles of fluorescence signal yielded the structure of flow and flame under velocity modulations.

These studies could be pursued in various directions. The analysis of the flame dynamics in gaseous stagnation flow impinging a plate put into evidence that the velocity perturbations were likely to propagate as a convective wave or uniformly depending on the Strouhal number. The consequences of these two modes on the choice of velocity boundary conditions were explored. It has been shown that the usual set of boundary conditions with radial velocity component taken as null $U_r = 0$ is not satisfactory for low Strouhal numbers. It would be interesting to go deeper into this question. For this purpose, more detailed comparisons between measurements and calculations over wider operating conditions should be carried out in order to draw conclusions in a general case.

The study on sound production mechanisms could be carried on without a plate. Indeed, the conclusions reached in that study were interesting, but they somehow suffer from the presence of the plate which may influence the measured noise. The role of the plate may also depend on the distance to the flame, i.e. on the equivalence ratio of the central flow. One solution would be to conduct a similar study with an inert counterflow flame instead of the plate. This counterflow would play a minor role from an acoustic point of view, and thus it would enable an easier study of combustion noise production in premixed flames. In such a configuration, similar experimental investigations would lead to clarify the acoustic role of the plate and to draw wider conclusions.

Investigations on two-phase flows are also worth being pursued. The experimental configuration should be modified to enable the study of two-phase flames under wider conditions. For this purpose, the fuel spray should come from the bottom and the oxidizer stream from the top. In such a configuration, it would be possible to light up a steady two-phase diffusion flame under wider conditions than what has been done in chapter 8. The characterization of two-phase flows with the set of diagnostics used in part III was interesting. Nevertheless, one can point out that investigating the liquid phase with laser induced fluorescence requires that the spray is not too polydisperse, otherwise the dynamics of fluorescence diagnostic is not sufficient to measure all sizes of droplets. The LIF exciplex actually brought interesting pieces of information on both vapour and liquid phases. However, quantification of the liquid phase is quite difficult to reach. Future studies should be based on denser sprays to reach a higher signal to noise ratio on the liquid phase. The Interferometric Particle Imaging (IPI) revealed to be a trustworthy method to investigate size and position of droplets in a plane. A successful comparison with PDA size measurements has though not been completed. The efforts should be put on solving of potential biases in size measurements in order to achieve an accurate comparison with PDA measurements.

Appendix A

Parametrical study on Interferometric Particle Imaging (IPI) parameters

In this appendix, three parametrical studies investigating the settings and accuracy of IPI measurements carried out with Dantec software Flowsizer v4.71.05 are presented. In section A.1, a study investigating the most relevant set of parameters for IPI measurements is carried out. In section A.2, the accuracy of size measurement of droplets is determined thanks to synthetic images. In section A.3, the effect of overlapping between two droplets on the determination of droplet diameters is investigated in details. The accuracy of measurements in this case is also estimated.

A.1 Choice of set of IPI parameters

A parametrical study is carried out on the possible sets of parameters for IPI processing. The aim is to understand the effects of each of them and to choose the most relevant set of parameters to process the data. Dantec Flowmanager 4.71.05 software offers the possibility to choose the following parameters for post-processing of focused and unfocused droplets:
Optical setup parameters: scattering angle, refractive index medium , refractive index particle, aperture diameter and distance from lens to light sheet.
Fast Fourier transform parameters: size of FFT, minimum and maximum sizes of the droplet, step size, window type, direction and strength
Velocity set up parameters: interrogation size, overlap, background noise removal and maximum number of particles

Validation criteria: peak level, allowable overlap, the ratio of main detected frequencies in the horizontal direction to the vertical direction F_x/F_z, particle filter

The optical setup parameters are set as the following: the scattering angle is $\phi = 90$ deg, the refractive index medium is $n = 1$ (air), the refractive index particle of hexane is $n = 1.375$, the aperture diameter is $d_a = 21.43$ mm and the distance from lens to light sheet is $z_l = 225$ mm. The velocity setup parameters are set relative to mean droplet displacement: the interrogation size is 128 pixels and an overlap of 50% is chosen.

For other parameters, a parametrical study is performed to determine successively the most appropriate values. For example, for the determination of the minimum and the maximum sizes of droplet to be considered, different values centred on the apparent sizes of droplets (35 pixels in this case) are first chosen. The results of processing on some droplets are compared with an estimated size of droplets based on the number of visible vertical stripes. This work reveals that when the gap between minimum and maximum sizes of droplets to be considered is large, the software is likely to misinterpret the number of vertical stripes. On the contrary, when the gap between minimum and maximum sizes of droplets to be considered is small, the software is accurate in the determination of the number of vertical stripes. As a consequence, it is more appropriate to limit the search of a droplet diameter in regions of 30 to 40 pixels width. The same kind of reasoning is performed for the choice of other parameters.

The results of this study enable to choose the following set of parameters :

- minimal and maximum size of defocused particles are respectively set to 30 and 40 pixels. It is important to tighten as much as possible the apparent size of droplets to avoid any misinterpreting of the software on the accurate localisation of the droplet. Since the droplet apparent size is constant at about 35 pixels, the latter values are found as the most relevant ones. Step size is set to its most accurate value, i.e. 1 pixel.
- the size of fast Fourier transform has been set to the highest available value (512 pixels) to reach the best accuracy.
- a background noise removal of 11% and a maximum number of particles validated per image of 1000 were set.
- the ratio of main detected frequencies in the horizontal direction to the vertical direction $F_x/F_z = 5$ was considered as the most relevant. Values below 5 lead to validation of non existing droplets and values above 5

was too restrictive.
- an allowable overlap of 60% was set according to the study presented in section A.3.
- a peak level of 1% was chosen. It appeared that values above were too restrictive leading to the rejection of valid droplets, whereas values below 1% sometimes lead to validation of non-existing droplets.
- neither criterion on minimal distance between two particles, nor image filter have been used.
- X_{offset} and Z_{offset} are corrective offsets to apply in the x- and z-directions in case the set up has slightly moved between the calibration procedure and the measurements. Surprisingly, these two parameters may have a great influence on measured diameters. A special care needs thus to be taken in the chosen values so that the measured droplet exactly fits on unfocused image of the droplet. In some cases, it has been observed that even a discrepancy of some pixels can change dramatically the measured diameters. Since it is impossible to choose a correct value with an accuracy of one pixel, it is clearly a limiting factor of the measurements accuracy. The couple of values $\{X_{offset}; Z_{offset}\} = \{5; -2\}$ yields a very good match between the software identified droplet and the unfocused image of the droplet for the set of acquisitions we were working on. This couple has therefore been used for post-processing of all measurements.

This parametrical study shows that the IPI parameters need to be chosen very carefully since they have a great impact on the global distribution of droplets. Globally, the study yielded some logical results. For example, it makes sense that increasing the size of FFT makes the measurements more precise. It is also conceivable that narrowing the gap between minimum and maximum sizes would increase the reliability of measurements since the software is less likely to be mistaken on the apparent size of droplets. However there remains unclear influences of some parameters. For example, the X_{offset} and Z_{offset} values seem to have a great influence on measured diameters though they only indicate a spatial readjustment. To give a precise example, from a pair of focused/unfocused images, the same processing has been carried out changing only the value of the last parameters:
- $X_{offset} = 0$ pixel and $Z_{offset} = 0$ pixel
- $X_{offset} = 5$ pixels and $Z_{offset} = -2$ pixels yielding a perfect match of IPI circles and defocused images
- $X_{offset} = 2$ pixels and $Z_{offset} = -1$ pixel

It was found for a given droplet localized on the focused and unfocused images

that diameters can greatly vary from 13.4 µm (1^{st} case) to 39.6 µm (2^{nd} case) or 13.2 µm (3^{rd} case). The counting of the number of stripes with the eye gives an expected diameter of about 32 µm which tends to prove that the second set of parameters is the correct one. These great variations have been observed on many other droplets too. It underlines the importance of the choice of corrective offsets X_{offset} and Z_{offset} on the quality of measurements.

These conclusions are though balanced by the parametrical study presented in section A.2 showing that induced errors are moderate.
The set of parameters presented and explained in this section is used for the process of measurements data in chapter 6.

A.2 Estimation of the accuracy of the measurement of diameter via IPI

In order to estimate the accuracy of measurements, a calibration of IPI measurement procedure has been carried out from synthetic images. Synthetic images of focused and unfocused droplets are created in Matlab as shown in figure A.1. The images are then imported in Dantec Flowsizer software and processed in the same way as for in-situ measurements.

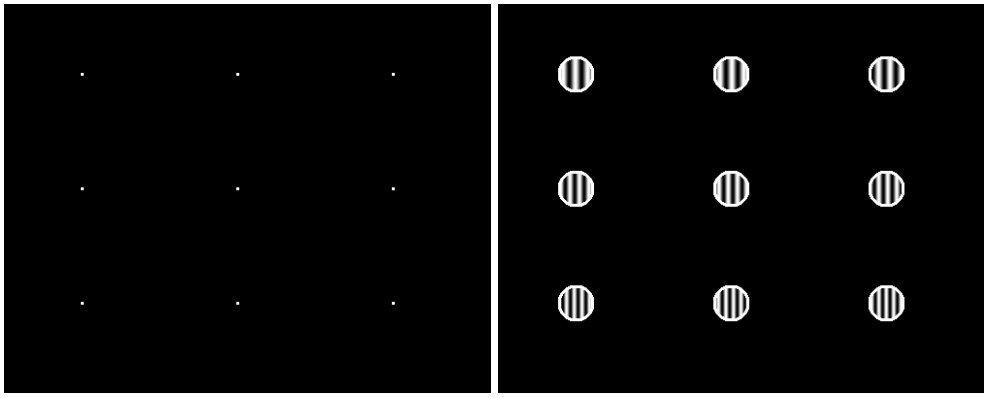

(a) focalized target **(b)** unfocalized target

Figure A.1: Example of focalized and non-focalized synthetic targets created in Matlab and loaded in Flowsizer Dantec software - The initial phase and the number of fringes per particle span the whole available range

The initial phase of stripe position in the unfocused droplet spans over range 0 to 2π. The number of fringes per particle spans from 0.2 to 10 fringes with

a step of 0.2 corresponding thus to all values of the measurement range. The calibration procedure is carried out with the exact same set of parameters as in-situ measurements except for X_{offset} and Z_{offset} which may vary for a detailed investigation. In the present case, the couple $\{X_{offset}; Z_{offset}\} = \{0\,;0\}$ yields a perfect match between the software identified droplets and the unfocused image of the droplets.

Results of processing of these synthetic images with the different sets of parameters is presented in figure A.2. The expected diameter d_P is also plotted versus the synthetic number of fringes N_f as a solid line:

$$d_P = \frac{N_f}{\kappa} \tag{A.1}$$

where N_f is the number of fringes in the unfocused droplet and κ is the proportionality coefficient introduced in chapter 2:

$$\kappa = \frac{\arcsin(d_a/2z_l)}{\lambda}\left(cos(\frac{\phi}{2}) + \frac{n\sin(\frac{\phi}{2})}{\sqrt{n^2+1-2n\cos(\frac{\phi}{2})}}\right) = 1.526210^5 \mathrm{m}^{-1} \tag{A.2}$$

The smallest measurable diameter is thus : $d_{min} = 1/\kappa = 6.5$ m.

This plot enables to estimate the importance of the role of the values of X_{offset}, Z_{offset} on the measured diameter. It shows that these values have moderate impact on measurements since the discrepancy between results is in most cases smaller than 5%. In addition, this plot enables to estimate the accuracy of measurements from synthetic droplets relative to theoretical diameters. Comparing the real measurements (symbols) to theoretical diameters (solid line), the accuracy of diameter measurement can be estimated at about 7%. Though it is important to note that during the real in-situ measurements, the accuracy might be a bit lower due to defaults in unfocused images since the present study is performed from synthetic images.

As a conclusion, this study gives a good estimate of the accuracy of these measurements which is estimated at about 7% in the range [6 µm ; 70 µm].

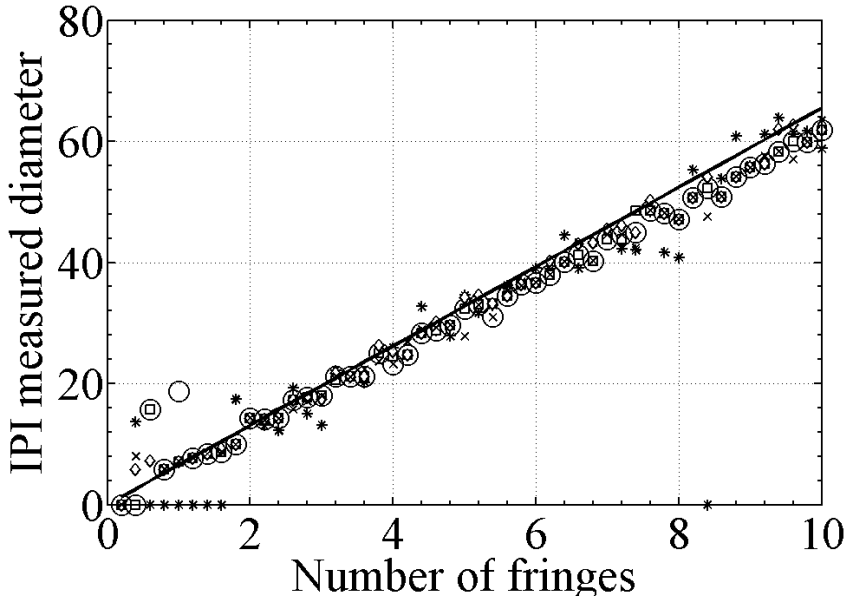

Figure A.2: Measured diameter (in μm) versus number of fringes of synthetic droplets. Solid line : theoretical relation - Symbols : measured diameters with Dantec IPI software on synthetic droplets - circle : (X_{offset}, Z_{offset}) = $(0, 0)$ - star : (X_{offset}, Z_{offset}) = $(10, 10)$ - square : (X_{offset}, Z_{offset}) = $(2, 0)$ - diamond : (X_{offset}, Z_{offset}) = $(-3, 1)$ - cross : (X_{offset}, Z_{offset}) = $(-1, 0)$

A.3 Effect of overlapping

In order to investigate the robustness of the software to droplets overlapping, a study is carried out from synthetic droplets. With the chosen set of parameters, synthetic images with different ratio of overlapping have been processed. Images of two droplets of respectively 14 and 26 μm are generated with Matlab with a relative overlap from 0% to 100%. These images are then imported in Dantec Flowsizer software and processed in the same conditions as in-situ measurements. Images of the droplets are presented in figure A.3 for overlap ratio of 0%, 30%, 60% and 90%.

Figure A.4 presents the results of processing of synthetic images. The processed diameters of two droplets with respective theoretical diameters of 14 and 26 μm are plotted versus a relative overlap ratio from 0% to 100%.

It appears that above an overlap ratio of 60%, the software does not succeed in distinguishing both droplets. Below an overlap of 60%, both droplets are correctly recognized with an accuracy of about 20%. As a consequence, the

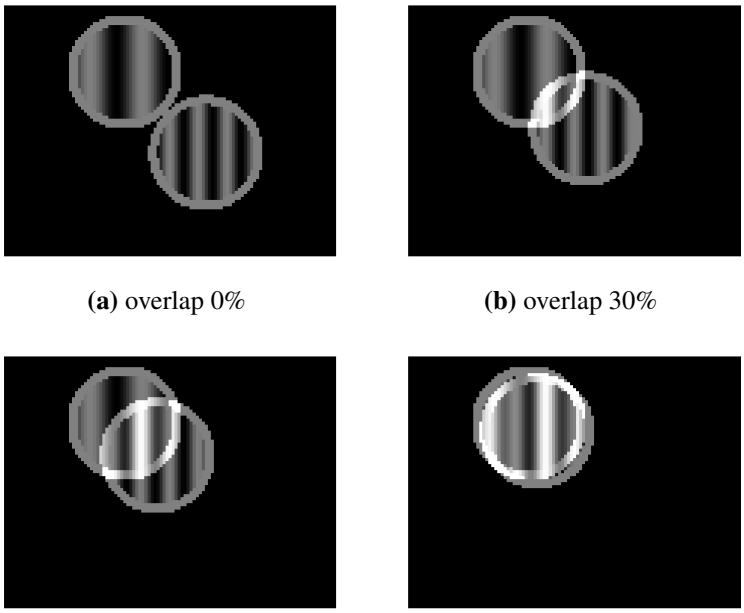

(a) overlap 0% **(b)** overlap 30%

(c) overlap 60% **(d)** overlap 90%

Figure A.3: Example of non-focalized synthetic targets with different overlapping ratios - the droplets on the left and the right have respectively theoretical diameters of 14 and 26 µm

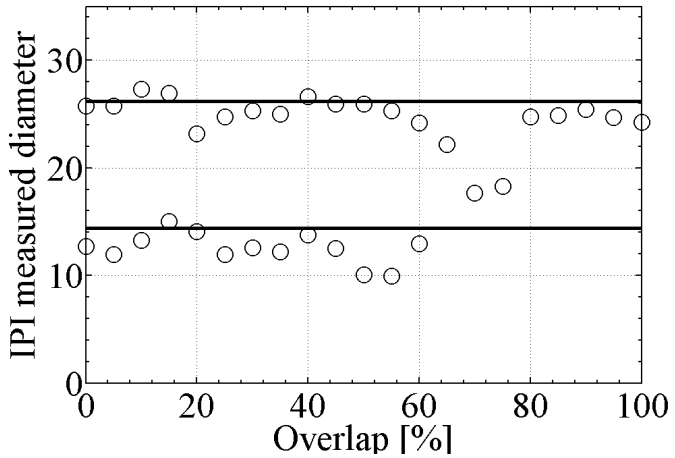

Figure A.4: Measured diameters (in µm) of two synthetic droplets (with respectively theoretical diameters of 14 and 26 µm) versus a relative overlap ratio from 0% to 100%

post-process of the study presented in chapter 6 will be carried out with a maximum overlap of 60 %. The droplets exhibiting an overlap ratio greater than 60% are rejected.

As a general conclusion to this appendix, a detailed parametrical study has been carried out to choose the most appropriate set of parameters for IPI processing. This set is used throughout the study presented in chapters 6 and 7. Another study from synthetic images ensures that the accuracy of diameter measurement is around 7% for isolated droplets and around 20% for non-isolated droplets. Since the overlap of droplets is not important in the studied spray, the overall accuracy of measurement of droplet diameter can be estimated at about 10%.

Appendix B

Investigations on the streaks on images of vapour fluorescence of two-phase flow

In this appendix, the reasons for the presence of vertical streaks on single shot images of vapour fluorescence signal are investigated. These vertical streaks are not expected, especially because these positions can vary significantly from shot to shot. To understand the presence of such vertical streaks, the visualisation of vapour fluorescence is successively performed on a pure vapour flow in section B.1 and on a the two-phase flow in section B.2 in the exact same conditions as in chapter 6.

B.1 Visualisation of a pure vapour flow

In this section, the fuel, traced only with FB, is entirely pushed via the evaporating system. The fuel is not traced here with DEMA since only the vapour phase is present and thus the exciplex can not be formed. This precaution is taken to prevent any spoiling of the liquid Coriolis flowmeter by DEMA, as well as for safety reasons since DEMA is quite irritating once released in the atmosphere. Figure B.1 presents six instantaneous images of vapour fluorescence images in stationary conditions (plots a) and three mean images of vapour fluorescence averaged over 100 acquisitions (plots b). The grayscale is identical between all images and spans between 0 and 12,000 counts. For information, one reminds that for all images presented in this thesis, the laser sheet comes from the left of the image.

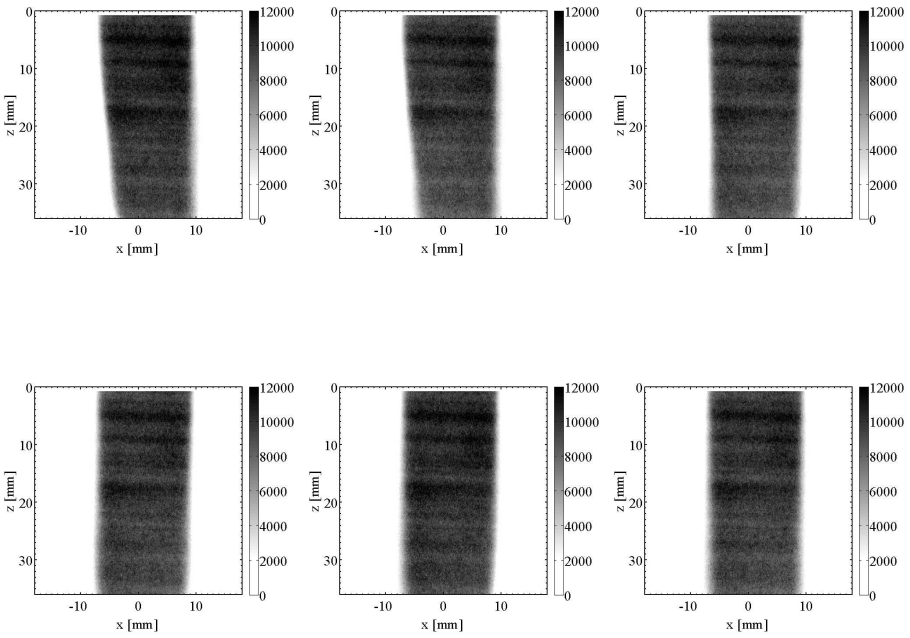

(a) Instantaneous images

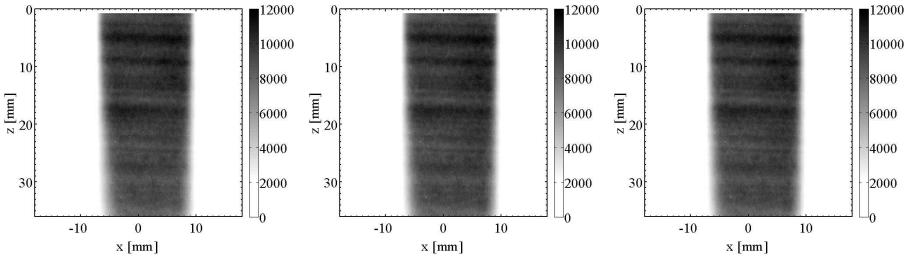

(b) Mean images averaged over 100 acquisitions

Figure B.1: Vapour fluorescence visualisations of a pure vapour flow - Grayscale spans from 0 to 12,000 counts

An almost perfectly homogeneous signal is measured in each of these images in the zone of the central flow even though weak horizontal stripes are present. These horizontal stripes might be due to inhomogeneities in the laser sheet since these are reproducible from shot to shot. However no inhomogeneity in the vertical direction and no absorption between the left and the right parts of the image are noticed.

B.2 Visualisation of a two-phase flow

Similar visualisations are now carried out with the same fuel flowrate injected into the atomiser. No fuel is here injected into the evaporating system. Figure B.1 presents six instantaneous images of vapour fluorescence in stationary conditions (plots (a)) and three mean images of vapour fluorescence averaged over 100 acquisitions (plots (b)). The grayscale is identical between all images and spans between 0 and 12,000 counts.

On the instantaneous images, one can notice strong asymmetries of the fluorescence signal with vertical streaks appearing at different positions. These streaks are clear and their positions can vary from left to right of the image. In addition, weak streaks along the x-axis similar to the one observed in section B.1 can be noticed.
In the averaged images, the vertical inhomogeneities are less significant even though well present.

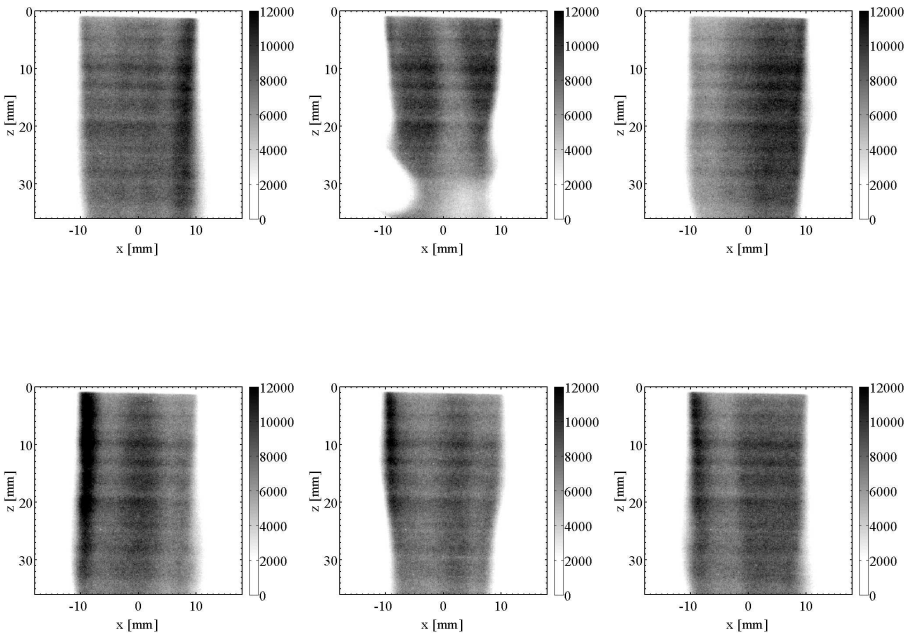

(a) Instantaneous images

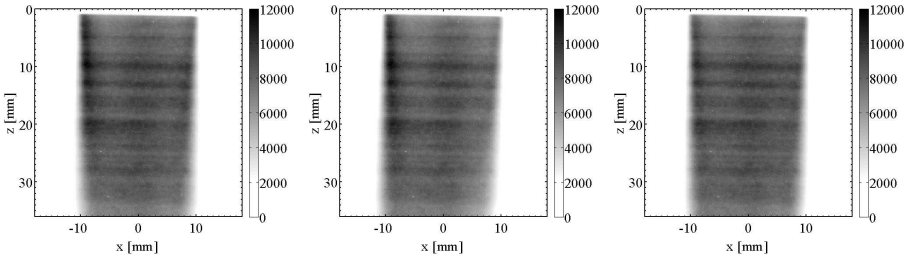

(b) Mean images averaged over 100 acquisitions

Figure B.2: Vapour fluorescence visualisations of a two-phase flow - Grayscale spans from 0 to 12,000 counts

B.3 Investigations

To understand the origin of vertical streaks, several specially designed experiments have been performed. The investigation follows several steps:

- one first investigates whether the vertical streaks can be due to vibra-

tions of the atomizer. For this purpose, visualisations of the pure vapour flow as in section B.1 are performed. No vertical streaks appear on the images that look exactly like figures B.1. One can thus conclude that the vibrations of the atomiser are not responsible for inhomogeneities in two-phase visualisations.

- one then investigates whether the absence of DEMA as a tracer in the experiments in section 6.3.4 can explain the absence of vertical streaks on visualisations of pure vapour flow as in section 6.3.4. For this purpose, a mixture of hexane and FB without DEMA is injected into the atomizer as in section B.2. The results are very similar to what has been presented in figure B.2: vertical inhomogeneities appear at positions varying from shot to shot. As a consequence, the absence of DEMA in the evaporating system can not be incriminated.
- it is then investigated whether vertical streaks could be due to the presence of liquid droplets which would absorb or scatter the vapour signal. For this purpose, the same quantity of traced hexane without DEMA is pushed through the evaporator and simultaneously pure hexane without any tracer is pushed into the atomizer. The visualisations performed in this configuration yield no vertical streaks but an homogeneous image. As a consequence, the presence of droplets should not be responsible for the presence of vertical streaks.
- the honey comb was also suspected to play a role in the presence of vertical streaks. The same visualisations of the two-phase flow were successively carried out with and without the honey comb. Similar results were obtained in particular relative to the presence of vertical streaks. The honey comb does not play any significant role in the presence of vertical streaks.
- the inhomogeneities of liquid phase was then investigated. The density maps of the liquid phase deduced from mean images of the Mie scattering or liquid fluorescence reveal no similar vertical inhomogeneities as the one observed vertically in the vapour visualisations.

The investigation process is summed up below:

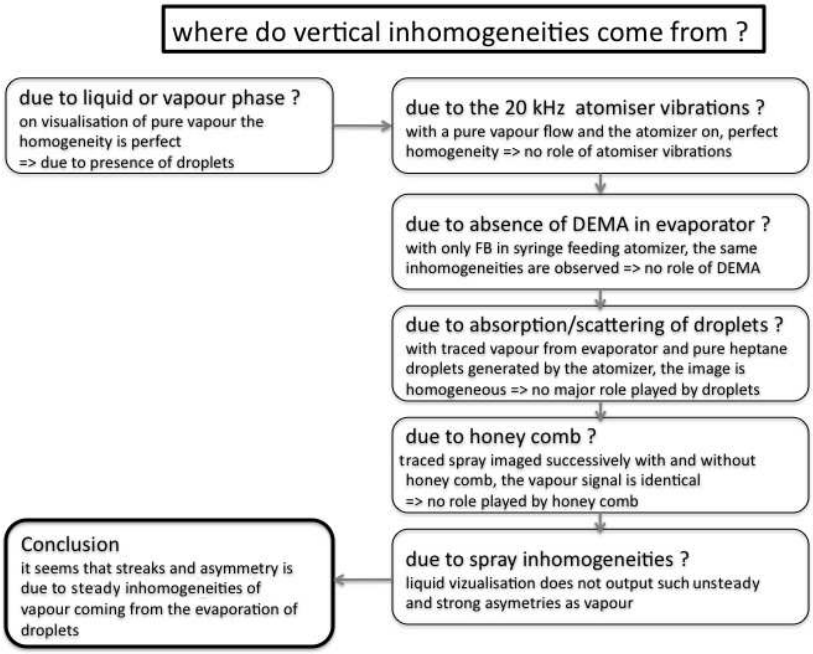

The only possible explanation are that vertical streaks are due to inhomogeneities of vapour coming from the evaporation of droplets at burner outlet. One can now estimate the characteristic diffusive time $\tau_{\mathcal{D}}$ of hexane in nitrogen on a distance of $L \simeq 35$ mm:

$$\tau_{\mathcal{D}} = \frac{L^2}{\mathcal{D}} \simeq 49 \text{ s}$$

where $\mathcal{D}$ is the diffusivity coefficient typically equal to 0.25 cm^2 s^{-1}
This characteristic time $\tau_{\mathcal{D}}$ is very large compared to the time step between two laser pulses (0.1 s) and the time needed for a particle to travel through the viewfield (0.04 s). This thus means that an inhomogeneity in the vapour concentration generated at burner outlet may be transported along the streamlines in the whole viewfield, thus creating a vertical streak. So, the hypothesis that vertical streaks are due to inhomogeneities of vapour coming from evaporation of droplets at burner outlet is in agreement with characteristic diffusion times, and thus realistic.

References

Adam, A., P. Leick, G. Bittlinger, and C. Schulz (2009). Visualization of the evaporation of a diesel spray using combined mie and rayleigh scattering techniques. *Experiments in Fluids 47*(3), 439–449.

Adrian, R. J., K. T. Christensen, and Z.-C. Liu (2000). Analysis and interpretation of instantaneous turbulent velocity fields. *Experiments in Fluids 29*(3), 275–290.

Aguerre, F. (1994). *Etude expérimentale et numérique des flammes laminaires étirees stationnaires et instationnaires*. Ph. D. thesis, Ecole Centrale Paris.

Aguerre, F., N. Darabiha, J. C. Rolon, and S. Candel (1993). Experimental and numerical study of transient laminar counterflow diffusion flames. *Combustion, Explosion, and Shock Waves 29*(3), 311–315.

Agui, J. and J. Jimenez (1987). On the performance of particle tracking. *Journal of fluid mechanics 185*, 447–468.

Albrecht, H.-E., N. Damaschke, M. Borys, and C. Tropea (2003). *Laser Doppler and Phase Doppler Measurement Techniques*.

Andersson, M., S. Hemdal, F. Persson, and A. Rosen (2006). Temperature determination based on spectral shift of exciplex fluorescence. In *ICLASS, Kyoto, Japan*, Number 06-165.

Bachalo, W. D. (1994). The phase doppler method: Analysis, performance evaluations, and applications. *Particle and Particle Systems Characterization 11*(1), 73–83.

Baillot, F., D. Durox, and R. Prudhomme (1992). Experimental and theoretical study of a premixed vibrating flame. *Combustion and Flame 88*(2), 149–168.

Bansal, G. and H. G. Im (2007). Time scales in unsteady premixed flame extinction with composition fluctuations. *Combustion and Flame 150*(4), 404–408.

Bardsley, Felton, and Bracco (1989). Two-dimensional visualization of a hollow-cone spray in a cup-in- head, ported, i.c. engine. *SAE Technical*

Papers 890315.

Bardsley, M., P. Felton, and F. Bracco (1988). 2-d visualization of liquid and vapor fuel in an i.c. engine. *SAE Technical Papers 880521*, 281–291.

Bazile, R. and D. Stepowski (1995). Measurements of vaporized and liquid fuel concentration fields in a burning spray jet of acetone using planar laser induced fluorescence. *Experiments in Fluids 20*(1), 1–9.

Birbaud, A. L., D. Durox, S. Ducruix, and S. Candel (2007). Dynamics of free jets submitted to upstream acoustic modulations. *Physics of Fluids 19*(1), 13602.

Bourehla, A. and F. Baillot (1998). Appearance and stability of a laminar conical premixed flame subjected to an acoustic perturbation. *Combustion and Flame 114*(3-4), 303–318.

Brown, T., R. Pitz, and C. Sung (1998). Oscillatory stretch effects on the structure and extinction of counterflow diffusion flames. *Proceedings of the Combustion Institute 27*(1), 703–710.

Bui, M., M. Ihme, W. Meinke, H. Schröder, and Pitsch (2007). Numerical investigation of combustion noise and sound source mechanisms in a non-premixed flame using les and ape-rf. In *13th AIAA/CEAS Aeroacoustics Conference*.

Campbell, Sinko, and Chehroudi (1995). Liquid and vapor phase distributions in a piloted diesel fuel spray. *SAE Technical Papers 950445*, 760–775.

Candel, S. (2002). Combustion dynamics and control: Progress and challenges. *Proceedings of the Combustion Institute 29*(1), 1–28.

Candel, S., D. Durox, S. Ducruix, A. Birbaud, N. Noiray, and T. Schuller (2009). Flame dynamics and combustion noise: progress and challenges. *International Journal of Aeroacoustics 8*, 1–56(56).

Candel, S., D. Durox, and T. Schuller (2004). Flame interactions as a source of noise and combustion instabilities. In *10th AIAA/CEAS Aeroacoustics Conference*, pp. 2928.

Castanet, G., P. Lavieille, M. Lebouche, and F. Lemoine (2003). Measurement of the temperature distribution within monodisperse combusting droplets in linear streams using two-color laser-induced fluorescence. *Experiments in Fluids 35*(6), 563–571.

Castanet, G., C. Maqua, M. Orain, F. Grisch, and F. Lemoine (2007). Investigation of heat and mass transfer between the two phases of an evaporating droplet stream using laser-induced fluorescence techniques: Comparison with modeling. *International Journal of Heat and Mass Transfer 50*(17-18), 3670–3683.

Chen, G. and A. Gomez (1992). Counterflow diffusion flames of quasi-monodisperse electrostatic sprays. *Proceedings of the Combustion Institute 24*(1), 1531–1539.

Chojnacki, K. T. and D. A. Feikema (1998). Exciplex fluorescence imaging for liquid mixing studies. *Applied Optics 37*(18), 4034–4038.

Chraplyvy, A. R. (1981). Nonintrusive measurements of vapor concentrations inside sprays. *Applied Optics 20*(15), 2620–2624.

Correa, S. M. (1998). Power generation and aeropropulsion gas turbines: From combustion science to combustion technology. *Proceedings of the Combustion Institute 27*(2), 1793–1807.

Crow, S. C. and F. H. Champagne (1971). Orderly structure in jet turbulence. *Journal of Fluid Mechanics 48*(03), 547–591.

Cuoci, A., A. Frassoldati, T. Faravelli, and E. Ranzi (2008). Frequency response of counter flow diffusion flames to strain rate harmonic oscillations. *Combustion Science and Technology 180*(5), 767–784.

Damaschke, N., H. Nobach, T. I. Nonn, N. Semidetnov, and C. Tropea (2005). Multi-dimensional particle sizing techniques. *Experiments in Fluids 39*(2), 336–350.

Darabiha, N. (1992). Transient behaviour of laminar counterflow hydrogen-air diffusion flames with complex chemistry. *Combustion Science and Technology 86*(1), 163–181.

Darabiha, N., F. Lacas, J. Rolon, and S. Candel (1993, November). Laminar counterflow spray diffusion flames: A comparison between experimental results and complex chemistry calculations. *Combustion and Flame 95*(3), 261–275.

Decroix, M. E. and W. L. Roberts (1999). Study of transient effects on the extinction limits of an unsteady counterflow diffusion flame. *Combustion Science and Technology 146*(1-6), 57–84.

Desantes, J., J. Pastor, J. Pastor, and J. Julia (2005). Limitations on the use of the planar laser induced exciplex fluorescence technique in diesel sprays. *Fuel 84*(18), 2301–2315.

Diwakar, R., T. Fansler, D. French, J. Ghandhi, C. Dasch, and D. Heffelfinger (1992). Liquid and vapor fuel distributions from an air-assist injector–an experimental and computational study. *SAE Technical Papers 920422*.

Dixon-Lewis, G. (1991). Structure of laminar flames. *Proceedings of the Combustion Institute 23*(1), 305 – 324.

Dobbins, R. and G. Jizmagian (1966). Particle size measurements based on use of mean scattering cross sections. *Journal of the Optical Society of America 56*(10), 1351–1352.

Domann, R., Y. Hardalupas, and A. R. Jones (2002). A study of the influence of absorption on the spatial distribution of fluorescence intensity within large droplets using mie theory, geometrical optics and imaging experiments. *Measurement Science and Technology 12*(3), 280–291.

Dong, Y., C. M. Vagelopoulos, G. R. Spedding, and F. N. Egolfopoulos (2002). Measurement of laminar flame speeds through digital particle image velocimetry: Mixtures of methane and ethane with hydrogen, oxygen, nitrogen, and helium. *Proceedings of the Combustion Institute 29*(2), 1419–1426.

Duchaine, P., L. Zimmer, and T. Schuller (2009). Experimental investigation of mechanisms of sound production by partially premixed flames. *Proceedings of the Combustion Institute 32*(1), 1027–1034.

Duewel, I., W. Koban, F. Zimmermann, T. Dreier, and C. Schulz (2009). Spectroscopic characterization of the fluorobenzene/dema tracer system for laser-induced exciplex fluorescence for the quantitative study of evaporating fuel sprays. *Applied Physics B: Lasers and Optics 97*(4), 909–918.

Duewel, I., C. Schulz, and J. Wolfrum (2007). *Spray combustion diagnostics with tracer-based laserinduced fluorescence imaging*. Ph. D. thesis.

Durox, D., S. Ducruix, and F. Lacas (1999). Flow seeding with an air nebulizer. *Experiments in Fluids 27*(5), 408–413.

Durox, D., T. Schuller, and S. Candel (2005). Combustion dynamics of inverted conical flames. *Proceedings of the Combustion Institute 30*(2), 1717–1724.

Durox, D., T. Schuller, N. Noiray, and S. Candel (2009). Experimental analysis of nonlinear flame transfer functions for different flame geometries. *Proceedings of the Combustion Institute 32*(1), 1391 – 1398.

Eckbreth, A. (1996). *Laser Diagnostics for Combustion Temperature and Species*. Taylor & Francis Ltd - Combustion Science and Technology.

Egolfopoulos, F. N. (1994). Dynamics and structure of unsteady, strained, laminar premixed flames. *Proceedings of the Combustion Institute 25*(1), 1365–1373.

Egolfopoulos, F. N. and C. S. Campbell (1996). Unsteady counterflowing strained diffusion flames: diffusion-limited frequency response. *Journal of Fluid Mechanics 318*(1), 1–29.

Einecke, S., C. Schulz, and V. Sick (2000). Measurement of temperature, fuel concentration and equivalence ratio fields using tracer lif in ic engine combustion. *Applied Physics B: Lasers and Optics 71*(5), 717–723.

Elghobashi, S. (1994). On predicting particle-laden turbulent flows. *Applied Scientific Research 52*(4), 309–329.

Epstein, A. H. (1977). Quantitative density visualization in a transonic compressor rotor. *ASME, Transactions, Series A-Journal of Engineering for Power. 99*, 460–475.

Felton, P., F. Bracco, and M. Bardsley (1993). On the quantitative application of exciplex fluorescence to engine sprays. *SAE Technical Papers 930870*.

Fernandes, E. and R. Leandro (2006). Modeling and experimental validation of unsteady impinging flames. *Combustion and Flame 146*(4), 674–686.

Freret, L., C. Lacour, S. de Chaisemartin, S. Ducruix, D. Durox, F. Laurent, and M. Massot (2009). Pulsated free jets with polydisperse spray injection: Experiments and numerical simulations. *Proceedings of the Combustion Institute 32*(2), 2215–2222.

Froba, A. P., F. Rabenstein, K. U. Munch, and A. Leipertz (1998). Mixture of triethylamine (tea) and benzene as a new seeding material for the quantitative two-dimensional laser-induced exciplex fluorescence imaging of vapor and liquid fuel inside si engines. *Combustion and Flame 112*(1-2), 199–209.

Fujimoto, M. and M. Tabata (1993). Effect of swirl rate on mixture formation in a spark ignition engine based on laser 2-d visualization techniques. *SAE Technical Papers 931905*.

Gervais, D. and P. Gastaldi (2002). A comparison of two quantitative laser-induced fluorescence techniques applied to a new air-guided direct injection si combustion chamber. *SAE Technical Papers 2002-01-0750*.

Ghandi, J., P. Felton, B. Gajdeczko, and F. Bracco (1994). Investigation of the fuel distribution in a two-stroke engine with an air-assisted injector. *SAE Technical Papers 940394*.

Ghoniem, A., M. Soteriou, O. Knio, and B. Cetegen (1992). Effect of steady and periodic strain on unsteady flamelet combustion. *Proceedings of the Combustion Institute 24*(1), 223–230.

Glover, A. R., S. M. Skippon, and R. D. Boyle (1995). Interferometric laser imaging for droplet sizing: a method for droplet-size measurement in sparse spray systems. *Applied Optics 34*(36), 8409–8421.

Gutmark, E. and C.-M. Ho (1983). Preferred modes and the spreading rates of jets. *Physics of Fluids 26*(10), 2932–2938.

Hanson, R. K., J. M. Seitzman, and P. H. Paul (1990). Planar laser-fluorescence imaging of combustion gases. *Applied Physics B: Lasers and Optics 50*(6), 441–454.

Hardalupas, Y. and M. Orain (2004). Local measurements of the time-dependent heat release rate and equivalence ratio using chemilumines-

cent emission from a flame. *Combustion and Flame 139*(3), 188–207.

Hiller, B. and R. K. Hanson (1988). Simultaneous planar measurements of velocity and pressure fields in gas flows using laser-induced fluorescence. *Applied Optics 27*(1), 33–48.

Hirasawa, T., T. Ueda, A. Matsuo, and M. Mizomoto (2000). Response of flame displacement speeds to oscillatory stretch in wall-stagnating flow. *Combustion and Flame 121*(1-2), 312–322.

Hodges, J., T. Baritaud, and T. Heinze (1991). Planar liquid and gas fuel and droplet size visualization in a di diesel engine. *SAE Technical Papers 910726*.

Hurle, R. B., T. M. Price, Sugden, and A. Thomas (1968). Sound emission from open turbulent premixed flames. *Proceedings of the Royal Society of London. Series A, Mathematical and Physical Sciences 303*, 409–427.

IAE, I. E. A. (2008). Key world energy statistics. Technical report, International energy agency.

Im, H., C. Law, J. Kim, and F. Williams (1995). Response of counterflow diffusion flames to oscillating strain rates. *Combustion and Flame 100*(1-2), 21–30.

Im, H. G., J. K. Bechtold, and C. K. Law (1996). Response of counterflow premixed flames to oscillating strain rates. *Combustion and Flame 105*(3), 358–372.

Im, H. G. and J. H. Chen (2000). Effects of flow transients on the burning velocity of laminar hydrogen/air premixed flames. *Proceedings of the Combustion Institute 28*(2), 1833–1840.

Joulin, G. (1994). On the response of premixed flames to time-dependent stretch and curvature. *Combustion Science and Technology 97*(1-3), 219–229.

Karlovitz, B., D. Denniston, D. Knapschaefer, and F. Wells (1953). Studies on tubulent flames. *Proceedings of the Combustion Institute 4*, 613–620.

Kashdan, J. and G. Bruneaux (2006). La préparation du mélange et de la combustion dans un moteur diesel, hcci à accès optique. *Oil & Gas Science and Technology - Rev. IFP 61*(1), 25–42.

Katsuki, Y. Mizutani, and M. Chitami (1986). Sound emission from a turbulent flame. *Proceedings of the Combustion Institute 21*, 1543–1550.

Kee, R. J., n. E. G. H. Miller, J. A. a, and G. Dixon-Lewis (1988). A computational model of the structure and extinction of strained, opposed flow, premixed methane-air flames. *Proceedings of the Combustion Institute 22*(1), 1479–1494.

Keller, J. O. and K. Saito (1987). Measurements of the combusting flow in

a pulse combustor. *Combustion Science and Technology 53*, 137–163.

Kilham, J.-K. and N. Kirmani (1979). The effect of turbulence on premixed flame noise. *Proceedings of the Combustion Institute 17*(1), 327–336.

Kim, J., B. Golding, H. Schock, P. Keller, and D. Nocera (1996). Exciplex fluorescence visualization systems for pre-combustion diagnosis of an automotive gasoline engine. *SAE Technical Papers 960826*.

Kim, J., W. K. Hartmann, H. J. Schock, B. Golding, and D. G. Nocera (1997). The electron donor-acceptor exciplex of n,n-dimethylaniline and 1,4,6-trimethylnaphthalene. *Chemical Physics Letters 267*(3-4), 323–328.

Kim, J.-U. and B. Hong (2001). Quantitative vapour-liquid visualization using laser-induced exciplex fluorescence. *Journal of Optics A: Pure and Applied Optics 3*(5), 338–345.

Kim, T., M. Beckman, P. Farrell, and J. Ghandhi (2002). Evaporating spray concentration measurements from small- and medium-bore diesel injectors. *SAE Technical Papers 2002-01-0219*.

Kim, T. and J. B. Ghandhi (2001). Quantitative 2-d fuel vapor concentration measurements in an evaporating diesel spray using the exciplex fluorescence method. *SAE Technical Papers 2001-01-3495*.

Klein, S. A. and J. B. W. Kok (1999). Sound generation by turbulent non-premixed flames. *Combustion Science and Technology 149*(1), 267–295.

Konig, G., K. Anders, and A. Frohn (1986). A new light-scattering technique to measure the diameter of periodically generated moving droplets. *Journal of aerosol science 17*(2), 157–167.

Konig, K., V. Bykov, and U. Maas (2009). Investigation of the dynamical response of methane/air counterflow flames to inflow mixture composition and flow field perturbations. *Flow, Turbulence and Combustion 83*(1), 105–129.

Kornmesser, C., T. Müller, V. Beushausen, W. Hentschel, and P. Andresen (2001). Applicability of different exciplex tracers and model fuels for investigation of mixture formation in direct injection gasoline engines. In *The Fifth International Symposium on Diagnostics and Modeling of Combustion in Internal Combustion Engines, Nagoya, Japan*.

Kotake, S. and K. Takamoto (1990). Combustion noise - effects of the velocity turbulence of unburned mixture. *Journal of Sound Vibration 139*(1), 9–20.

Kychakoff, G., R. D. Howe, and R. K. Hanson (1984). Quantitative flow visualization technique for measurements in combustion gases. *Applied Optics 23*(5), 704–712.

Lacour, C., D. Durox, S. Ducruix, and M.Massot (2010). Interaction of a polydisperse sparay with vortices. *Submitted to Experiments in Fluids*.

Laurent, F. and M. Massot (2001). Multi-fluid modeling of laminar polydispersed spray flames: Origin, assumptions and comparison of the sectional and sampling methods. *Combustion Theory and Modelling 5*(4), 537–572.

Laurent, F., V. Santoro, M. Noskov, M. D. Smooke, A. Gomez, and M. Massot (2004). Accurate treatment of size distribution effects in polydisperse spray diffusion flames: multi-fluid modelling, computations and experiments. *Combustion Theory and Modelling 8*(2), 385–412.

Lauvergne, R. and F. N. Egolfopoulos (2000). Unsteady response of c3h3/air laminar premixed flames submitted to mixture composition oscillations. *Proceedings of the Combustion Institute 28*(2), 1841–1850.

Lavieille, P., F. Lemoine, G. Lavergne, and M. Lebouche (2001). Evaporating and combusting droplet temperature measurements using two-color laser-induced fluorescence. *Experiments in Fluids 31*(1), 45–55.

Law, C., C. Sung, G. Yu, and R. Axelbaum (1994). On the structural sensitivity of purely-strained planar premixed flames to strain rate variations. *Combustion and Flame 98*(1-2), 139–154.

Le Coz, J. F., J. Cherel, and S. L. Mirronet (2003). Fuel/air mixing process and combustion in an optical direct-injection engine. *Oil & Gas Science and Technology - Rev. IFP 58*, 63–78.

Leach, B. (2004). Two-phase fuel distribution in an air assisted di gasoline engine. In *The sixth international symposium on diagnostics and modeling of combustion in internet combustion engines, Yokohama, Japan*.

Lee, U. D., H. D. Shin, K. C. Oh, K. H. Lee, and E. J. Lee (2006). Extinction limit extension of unsteady counterflow diffusion flames affected by velocity change. *Combustion and Flame 144*(4), 792–808.

Lemaire, A., T. R. Meyer, K. Zahringer, J. R. Gord, and J. C. Rolon (2004). Piv/plif investigation of two-phase vortex-flame interactions: effects of vortex size and strength. *Experiments in Fluids 36*(1), 36–42.

Li, S. C. (1997). Spray stagnation flames. *Progress in Energy and Combustion Science 23*(4), 303–347.

Lieuwen, T. and V. Yang (2005). *Combustion Instabilities in Gas Turbine Engines: Operational Experience, Fundamental Mechanisms, and Modeling*, Volume 210. Progress in astronautics and aeronautics.

Lozano, A., B. Yip, and R. K. Hanson (1992). Acetone: a tracer for concentration measurements in gaseous flows by planar laser-induced fluorescence. *Experiments in Fluids 13*(6), 369–376.

Luff, D., E. Korusoy, P. Lindstedt, and J. H. Whitelaw (2003). Counter-

flow flames of air and methane, propane and ethylene, with and without periodic forcing. *Experiments in Fluids 35*(6), 618–626.

Lutz, A., R. Kee, J. Grcar, and F. Rupley (1996). Oppdif: A fortran program for computing opposed-flow diffusion flames. *Sandia National Laboratories Report SAND96-8243*.

Ma, L., S. Sanders, J. Jeffries, and R. Hanson (2002). Monitoring and control of a pulse detonation engine using a diode-laser fuel concentration and temperature sensor. *Proceedings of the Combustion Institute 29*(1), 161–166.

Mahan J.R., A. K. (1991). *Aeroacoustics of Flight Vehicles: Theory and Practice. Volume 1: Noise Sources*, Chapter 9 : Combustion and core noise, pp. 483–517. NASA - Langley Research Center.

Massot, M., M. Kumar, M. D. Smooke, and A. Gomez (1998). Spray counterflow diffusion flames of heptane: Experiments and computations with detailed kinetics and transport. *Proceedings of the Combustion Institute 27*(2), 1975–1983.

McDaniel, J. C., B. Hiller, and R. K. Hanson (1983). Simultaneous multiple-point velocity measurements using laser-induced iodine fluorescence. *Optical Letters 8*(1), 51–53.

Meinhart, C. D., S. T. Wereley, and J. G. Santiago (1999, October). Piv measurements of a microchannel flow. *Experiments in Fluids 27*(5), 414–419.

Melton, L. A. (1983). Spectrally separated fluorescence emissions for diesel fuel droplets and vapor. *Applied Optics 22*(14), 2224.

Melton, L. A. and J. F. Verdieck (1985). Vapor/liquid visualization in fuel sprays. *Proceedings of the Combustion Institute 20*(1), 1283–1290.

Mikami, M., S. Miyamoto, and N. Kojima (2002). Counterflow diffusion flame with polydisperse sprays. *Proceedings of the Combustion Institute 29*(1), 593–599.

Modica, V., C. Morin, and P. Guibert (2007). 3-Pentanone LIF at elevated temperatures and pressures: measurements and modeling. *Applied Physics B-Lasers and Optics 87*(1), 193–204.

Morin, C., V. Modica, and P. Guibert (2008, OCT). Measurement of exhaust gas recirculation rate by laser-induced fluorescence in engine. *Measurement Science and Technology 19*(10).

Mounaim-Rousselle, C., B. Deschamps, E. Depussay, and V. Ricordeau (1999). Combined catalytic hot wires probe and fuel-air-ratio-laser-induced-exciplex fluorescence air/fuel ratio measurements at the spark location prior to ignition in a stratified gdi engine. *SAE Technical Papers 1999-01-3536*.

Munjal, M. (1987). *Acoustics Of Ducts And Mufflers With Application To Exhaust And Ventilation System Design*. John Wiley & Sons, New York.

Murray, A. M. and L. A. Melton (1985). Fluorescence methods for determination of temperature in fuel sprays. *Applied Optics 24*(17), 2783–.

Noiray, N., D. Durox, T. Schuller, and S. Candel (2009). Mode conversion in acoustically modulated confined jets. *AIAA Journal 47*(9), 2053–2062.

Ohiwa, N., K. Tanaka, and S. Yamaguchi (1993). Noise characteristics of turbulent diffusion flames with coherent structure. *Combustion science and technology 90*(1), 61–78.

Orain, M., X. Mercier, and F. Grisch (2005). Plif imaging of fuel-vapor spatial distribution around a monodisperse stream of acetone droplets: Comparison with modeling. *Combustion Science and Technology 177*(2), 249–278.

Orain, M., H. Verdier, and F. Grisch (2006). Equivalence ratio measurements in kerosene-fuelled lpp injectors using planar laser induced fluorescence. In *13th International Symposium on Application of Laser Techniques to Fluid Mechanics, Lisbon, Portugal*, Number 1120.

Pastor, J., J. López, J. Juliá, and J. Benajes (2002). Planar laser-induced fluorescence fuel concentration measurements in isothermal diesel sprays. *Optics Express 10*(7), 309–323.

Penner, J., D. Griggs, and D. Lister (1999). *Aviation And The Global Atmosphere*. Cambridge University Press.

Peters, N. (1986). Laminar flamelet concepts in turbulent combustion. *Proceedings of the Combustion Institute 21*(1), 1231–1250.

Price, I., T. Hurle, and Sudgen (1969). Optical studies of generation of noise in turbulent flames. *Proceedings of the Combustion Institute 12*(1), 1093–1102.

Raffel, M., C. Willert, and J. Kompenhaus (1998). *Particle Image Velocimetry*. Springer.

Rajaram, J., T. Gray, and Lieuwen (2006). Premixed combustion noise scaling : total power and spectra. *AIAA paper 1*, 2612.

Renard, P. H., D. Thevenin, J. C. Rolon, and S. Candel (2000). Dynamics of flame/vortex interactions. *Progress in Energy and Combustion Science 26*(3), 225–282.

Roberts, W. L., J. F. Driscoll, M. C. Drake, and L. P. Goss (1993). Images of the quenching of a flame by a vortex–to quantify regimes of turbulent combustion. *Combustion and Flame 94*(1-2), 58–69.

Rolon, J. C. (1988). *Etude théorique et expérimentale de la flamme de diffusion à contre courant*. Ph. D. thesis, Ecole Centrale Paris.

Rosner, D. (1986). *Transport processes in chemically reacting flow systems*. Dover Publications.

Rotunno, A. A., M. Winter, G. M. Dobbs, and L. A. Melton (1990). Direct calibration procedures for exciplex-based vapor/ liquid visualization of fuel sprays. *Combustion Science and Technology 71*(4), 247–261.

Rutland, C. J. and J. Ferziger (1990). Unsteady strained premixed laminar flames. *Combustion Science and Technology 73*(1-3), 305–326.

Saffman, P. (1995). *Vortex Dynamics*. Cambridge Monographs on Mechanics.

Santoianni, D., M. Decroix, and W. Roberts (2001). Temperature imaging in an unsteady propane-air counterflow diffusion flame subjected to low frequency oscillations. *Flow, Turbulence and Combustion 66*, 23–36.

Santoro, V. S., D. C. Kyritsis, and A. Gomez (2000). An experimental study of vortex-flame interaction in counterflow spray diffusion flames. *Proceedings of the Combustion Institute 28*(1), 1023–1030.

Sardi, K. and J. H. Whitelaw (1999). Extinction timescales of periodically strained, lean counterflow flames. *Experiments in Fluids 27*(3), 199–209.

Scarano, F. (2002). Iterative image deformation methods in piv. *Measurement Science and Technology 13*, 1–19.

Schafer, S. R., H. J. Schock, and T. R. Stuecken (1994). Development of an improved quantitative calibration for an exciplex liquid/vapor fuel visualization system. In *Proceedings of SPIE*, Volume 2122, Los Angeles, CA, USA, pp. 61–71. SPIE.

Schuller, T., D. Durox, and S. Candel (2002). Dynamics of and noise radiated by a perturbed impinging premixed jet flame. *Combustion and Flame 128*(1-2), 88–110.

Schuller, T., D. Durox, and S. Candel (2003a). Self-induced combustion oscillations of laminar premixed flames stabilized on annular burners. *Combustion and Flame 135*(4), 525–537.

Schuller, T., D. Durox, and S. Candel (2003b). A unified model for the prediction of laminar flame transfer functions: comparisons between conical and v-flame dynamics. *Combustion and Flame 134*(1-2), 21–34.

Seitzman, J. M., G. Kychakoff, and R. K. Hanson (1985). Instantaneous temperature field measurements using planar laser-induced fluorescence. *Optical Letters 10*(9), 439–441.

Senda, J., Y. Fukami, Y. Tanabe, and H. Fujimoto (1992). Visualization of evaporative diesel spray impinging upon wall surface by exciplex fluorescence method. *SAE Technical Papers 920578*.

Shimizu, R., S. Matumoto, S. Furuno, M. Murayama, and S. Kojima (1992). Measurement of air-fuel mixture distribution in a gasoline engine using lief technique. *SAE Technical Papers 922356*.

Shivashankara, B., W. Strahle, and J. Handley (1975). Evaluation of combustion noise scaling laws by an optical technique. *AIAA Journal 13*, 623–627.

Singh, K., S. Frankel, and J. Gore (2003). Effects of combustion on the sound pressure generated by circular jet flows. *AIAA Journal 41*, 319–321.

Singh, K. K., C. Zhang, J. P. Gore, L. Mongeau, and S. H. Frankel (2005, January). An experimental study of partially premixed flame sound. *Proceedings of the Combustion Institute 30*(2), 1707–1715.

Smith, J. and K. Kilham (1963). Noise generation by open turbulent flames. *Journal of the Acoustical Society of America 35*, 715–724.

Stahl, G. and J. Warnatz (1991). Numerical investigation of time-dependent properties and extinction of strained methane- and propane-air flamelets. *Combustion and Flame 85*(3-4), 285–299.

Strahle, W. C. (1985). *A more modern theory of combustion noise*. Recent advances in the aerospace sciences, Plenum Press, New York.

Stufflebeam, J. H. (1989). Exciplex fluorescence thermometry of liquid fuel. *Applied Spectroscopy 43*(2), 274–278.

Sun, C. J., C. J. Sung, L. He, and C. K. Law (1999). Dynamics of weakly stretched flames: quantitative description and extraction of global flame parameters. *Combustion and Flame 118*(1-2), 108–128.

Sun, C. J., C. J. Sung, D. Zhu, and C. Klaw (1996). Response of counterflow premixed and diffusion flames to strain rate variations at reduced and elevated pressures. *Proceedings of the Combustion Institute 26*(1), 1111–1120.

Sung, C. J. and C. K. Law (2000). Structural sensitivity, response, and extinction of diffusion and premixed flames in oscillating counterflow. *Combustion and Flame 123*(3), 375–388.

Tabata, M., M. Kataoka, M. Fujimoto, and Y. Noh (1995). In-cylinder fuel distribution, flow field, and combustion characteristics of a mixture injected si engine. *SAE Technical Papers 950104*.

Thurber, M. C. and R. K. Hanson (2001). Simultaneous imaging of temperature and mole fraction using acetone planar laser-induced fluorescence. *Experiments in Fluids 30*(1), 93–101.

Vagelopoulos, C. M. and F. N. Egolfopoulos (1998). Direct experimental determination of laminar flame speeds. *Proceedings of the Combustion Institute 27*(1), 513–519.

Van de Hulst, H. C. (1981). *Light scattering by small particles*. Dover Publications Inc.

Welch, P. (1967). The use of fast fourier transform for the estimation of power spectra: A method based on time averaging over short, modified periodograms. *IEEE Transactions on Audio Electroacoustics AU-15*, 70–73.

Welle, E. J., W. L. Roberts, C. D. Carter, and J. M. Donbar (2003). The response of a propane-air counter-flow diffusion flame subjected to a transient flow field. *Combustion and Flame 135*(3), 285–297.

Westerweel, J. (1997). Fundamentals of digital particle image velocimetry. *Measurement Science and Technology 8*(12), 1379–1392.

Wieske, P., S. Wissel, G. Gruenefeld, and S. Pischinger (2006). Improvement of lief by wavelength-resolved acquisition of multiple images using a single ccd detectors simultaneous 2d measurement of air/fuel ratio, temperature distribution of the liquid phase and qualitative distribution of the liquid phase with the multi-2d technique. *Applied Physics B: Lasers and Optics 83*(2), 323–329.

Wolfrum, J. (1998). Lasers in combustion: From basic theory to practical devices. *Proceedings of the Combustion Institute 27*(1), 1–41.

Wyzgolik, A. and F. Baillot (2007). Response of the non-premixed lifted flame to coaxial jet mixing layers. *Proceedings of the Combustion Institute 31*(1), 1583–1590.

Yeh, C., T. Kamimoto, S. Kosaka, and H. Kobori (1994). Quantitative measurement of 2-d fuel vapor concentration in a transient spray via a laser-induced fluorescence technique. *SAE Technical Papers 941953*.

Yeh, Y. and H. Cummins (1964). Localized fluid flow measurements with a he-ne laser spectrometer. *Applied Physics Letters 4*(1), 176.

Zhao, H. and N. Ladommatos (1998). Optical diagnostics for in-cylinder mixture formation measurements in ic engines. *Progress in Energy and Combustion Science 24*(4), 297–336.

Zimmer, L., R. Domann, Y. Hardalupas, and Y. Ikeda (2003). Simultaneous laser-induced fluorescence and mie scattering for droplet cluster measurements. *AIAA Journal 41*(11), 2170–2178.